SYNTHESIS AND CHARACTERIZATION OF COBALT FERRITE POWDERED MATERIALS

LIU BINGHAI

(*M. Eng. WUST*)

A THESIS SUBMITTED

FOR THE DEGREE OF DOCTOR OF PHILOSOPHY

DEPARTMENT OF MATERIALS SCIENCE AND ENGINEERING

NATIONAL UNIVERSITY OF SINGAPORE

2008

Table of Content

Chapter 3 Synthesis of cobalt ferrite powdered materials

Acknowledgements

Firstly, I would like to express my deepest gratitude to my supervisor, Prof. Ding Jun for his kind guidance, supports and helps in many respects throughout past years. His efforts in imparting the theoretical knowledge and experimental skills in the field of magnetism and materials science are greatly appreciated. I am deeply impressed by his everlasting passion and conscientious attitude to the research, which are invaluable to me and I should treasure forever.

Sincere appreciation should be extended to Dr. Dong Zhili in Nanyang Technological University for his precious guidance in the field of transmission electron microscopy (TEM). His profound knowledge and expertise in TEM deeply impressed me and has been benefitting me so much. I would also thank Dr. Chris Boothroyd for his advices and helpful discussions in the TEM analysis for this thesis work.

I would also like to express my sincere appreciation to all my fellow colleagues in the Magnetic Materials Group, like Jiabao, Yu Shi, Zeliang, Lezhong, Jianhua, Lihui and Kae who have been providing me friendly helps and supports throughout years. Special thanks should also go to some Professors, colleagues and fellow students in the Department of Materials Science and Department of Chemistry for their helps and encouragements rendered to me from time to time.

Last but not the least, I am most grateful to my wife for her constant supports, encouragements and understanding during past years.

Summary

This thesis research dealt with the synthesis and characterization of cobalt ferrite ($CoFe_2O_4$) powdered materials, and studied the influences of phase, microstructure and cation distribution on magnetic properties. The major research efforts were devoted to the exploration of the ways for coercivity enhancement and the investigations of associated coercivity mechanisms.

$CoFe_2O_4$ powdered materials were synthesized by both the modified co-precipitation and mechanochemical processes. The results indicated that the average particle/grain size and size distribution greatly affected coercivity of resultant nanocrystalline powdered samples. On the other hand, for mechanochemical process, different post-annealing processes resulted in different cation distribution and thus different magnetic properties. It was found that the cation distribution in spinel lattice played a key role in saturation magnetization and coercivity as well as magnetocrystalline anisotropy of the samples.

Mechanical milling was demonstrated to be an effective way for introducing high-level strain and high-density defects in $CoFe_2O_4$ powdered materials. The results indicated that the initial grain/particle size greatly affected the microstructure evolution and thus magnetic properties of the milled samples. A high coercivity of 5.1 kOe was achieved in the sample with large grain size after milling for a short time. Our results clearly indicate that the milling-induced high coercivity is closely related to milling-induced high-level strain and high-density defects. Detailed magnetic

studies indicate that the domain-wall pinning controlled mechanisms are responsible for the milling-induced high coercivities.

The Ni^{2+} substituted cobalt ferrites ($Ni_xCo_{1-x}Fe_2O_4$) powdered materials were synthesized by mechanochemical process with post thermal annealing process. The magnetic studies indicated that Ni^{2+} substitution directly led to decrease in both saturation magnetization and coercivity of the $Ni_xCo_{1-x}Fe_2O_4$ samples. The results confirmed the key role of Co^{2+} in the magnetocrystalline anisotropy of $Ni_xCo_{1-x}Fe_2O_4$.

The mechanical milling of $Ni_xCo_{1-x}Fe_2O_4$ samples also led to notable enhancement in both coercivity and magnetic anisotropy. It was found out that such coercivity and anisotropy enhancement was also closely related to the milling-induced high-level residual strain and high-density defects. The most noteworthy is the significant mechanical hardening of the soft $NiFe_2O_4$ with milling and a high coercivity of 2.1 kOe was achieved.

List of Publications

A. The publications directly related to the research project of the thesis:

1. Liu BH, Ding J, *Strain-induced high coercivity in cobalt ferrite*, Applied Physics Letters 88 (2006) 042506

2. Liu BH, Ding J, Dong ZL, Boothroyd CB, Yin JH, Yi JB, *Microstructure evolution and its influence on magnetic properties of $CoFe_2O_4$ powders during mechanical milling,* Physics Review B 74 (2006)184427

3. Yin JH, Liu BH, Ding J, Wang YC, *High coercivity in nanostructured Co-ferrite thin films,* Bulletin of Materials Science 29 (2006) 573

4. Liu BH, Ding J, Yi JB, Yin JH, *Magnetic Anisotropies in Cobalt-nickel Ferrites ($Ni_xCo_{1-x}Fe_2O_4$)*, Journal of the Korean Physical Society (accepted)

B. The publications directly related to the research project of the thesis:

1. Wang YC, Ding J, Liu BH, Shi Y, *Magnetic Properties of Co-ferrite and SiO_2-Doped Co-ferrite Thin Films and Powders by Sol-Gel*, International Conference on Materials for Advanced Technologies 2003 (ICMAT 2003), July 2003, Singapore

2. Wang YC, Ding J, Yi JB, Liu BH, *High-coercivity Co-ferrite thin films on (100)-SiO_2 substrate*, Applied Physics Letter 84 (2004) 2596

3. Wang YC, Ding J, Yi JB, Liu BH, Yu T, Sheng ZX, *High coercivity Co-ferrite thin films on SiO2(100) substrate,* Journal of Magnetism and Magnetic Materials 282 (2004)211

C. The publications related to the synthesis technique (mechanical milling) employed in the thesis research.

1. Liu BH, Ding J, Zhong ZY, Dong ZL, White T, Lin JY, *Large-scale preparation of*

carbon-encapsulated cobalt nanoparticles by the catalytic method, Chemistry Physics Letter, 358 (2002) 96

2. Liu BH, Zhong ZY, Ding J, Lin JY, Shi Y, Si L, *Growth of multi-walled carbon nanotubes on mechanical alloying-derived Al_2O_3-Ni nanocomposite powder,* Journal of Materials Chemistry, 11 (2001) 2523

3. Ding J., Liu BH, Dong ZL, Zhong ZY, Lin JY, White T, *The preparation of Al_2O_3/M (Fe, Co, Ni) nanocomposites by mechanical alloying and the catalytic growth of carbon nanotubes,* Composite Part B, 35 (2004) 103

4. Liu BH, Ding J, Dong ZL, Zhong ZY, Lin JY, White T, *Mechanochemical synthesis of Fe-based nanocomposites and their application in the catalytic formation of carbon nanostructures,* Solid State Phenomena, 111 (2006) 183

List of Tables

List of Figures

CHAPTER 1

Introduction and Literature Review

1.1 Background

The history of ferrite materials can be traced back to centuries ago with the discovery of stones that attracted iron.[1] Plentiful deposits of these stones were found in the district of *Magnesia* in Asia Minor, and hence the mineral's name became magnetite (Fe_3O_4).[2,3] The naturally formed ferrites such as magnetites are magnetically soft. The research efforts at that time for producing the analogue soft magnetic materials were not successful until in 1930's when the first synthetic ferrites were developed independently in Japan and Netherlands.[4,5] Since then, intensive efforts have been devoted to this research area, which led to the remarkable developments in both science and technologies of ferrite materials. The unique electric and magnetic properties of ferrite materials enable them to have a wide range of applications, such as high-frequency devices, microwave components,[5-8] magnetic fluids[9-12] and magnetic data storage[13-20] as well as potential biomedical applications (e.g. drug delivery).[21,22]

In terms of crystal structures, ferrites can be classified into three groups, namely, spinel, garnet and magnetoplumbite.[23] The details of these three types of ferrites are shown in Table 1.1. As an important member in the family of spinel ferrites, cobalt ferrite ($CoFe_2O_4$) materials have been accepted as the promising candidates for a wide variety of applications including magnetic and magneto-optical data storage due to their good chemical stability and magnetic properties such as the high Curie temperature, relatively high saturation magnetization and high magnetic anisotropy.[13-20] In terms of these unique properties and promising applications, cobalt ferrite ($CoFe_2O_4$) is chosen as the research subject of this thesis research.

Table 1.1 Crystal types of ferrites

Type	Structure	General Formula	Example
Spinel	Cubic	$M^{II}Fe_2O_4$	M^{II}=Fe, Cd, Co, Mg, Ni and Zn
Garnet	Cubic	$M^{III}{}_3Fe_2O_{12}$	M^{III}=Y, Sm, Eu, Gd, Tb, and Lu
Magnetoplumbite	Hexagonal	$M^{II}Fe_{12}O_{19}$	M^{II}=Ba, Sr

For hard magnetic applications such as high-density magnetic recording, the coercivity is a key parameter. However, the practical applications, cobalt ferrite are often limited by its relatively low coercivity. It is well known that high coercivity is generally achieved in magnetic materials with uniaxial anisotropy and high magneto-crystalline energy.[24] Although cobalt ferrite has large magnetocrystalline anisotropy, the coercivity achieved in cubic cobalt ferrite is usually lower than 2 kOe.[15,18] Therefore, achieving high coercivity in cobalt ferrite is not only practically important for the potential applications, but also scientifically interesting for the investigation of the mechanisms behind the high coercivity in materials with a cubic structure.

Many research groups in the world are investigating how to improve magnetic properties by controlling the microstructure or doping with different elements.[13-15,18-20,25,26] In recent years, our group has made great achievements in coercivity enhancement of cobalt ferrite materials. High coercivities of up to 12.5 kOe have been achieved in $CoFe_2O_4$ thin film materials.[18,26] Our studies indicated that the microstructure played a key role in the coercivity of the thin film materials. Thus, the high coercivities achieved in thin films can be ascribed to the combination of modern film deposition technologies and the strategies which facilitate the structural tailoring of the thin film materials. This includes the controlling of grain/particle size, the building up of the texture structure and internal residual stress. However, to further understand detailed coercivity mechanisms and the relationship between properties

and structures, systematic studies are still necessary, especially for the effects of the defects and the associated residual strain. In addition, the study on cation redistribution is also necessary in order to understand the intrinsic anisotropy of cobalt ferrites. However, for cobalt ferrite thin films, the materials are too thin to be applicable for the cation distribution analysis by Mossbauer spectroscopy. Therefore, in order to understand the coercivity mechanisms in cobalt ferrite materials, in this thesis research, cobalt ferrite powdered materials are chosen. Although the formation of a textured structure in powdered materials is impossible in terms of the random assembly of the magnetic particles, the phase and microstructure tailoring will be the effective ways for the purpose of coercivity enhancement. In addition, cation distribution analysis will be convenient for powdered materials with Mössbauer analysis.

In terms of the above arguments, this thesis research focuses on the synthesis of cobalt ferrite powdered materials and the investigation of the effects of the phase and microstructure on their magnetic properties. The major research efforts are devoted to the strategies for achieving high magnetic coercivity and to studies on the mechanisms behind coercivity enhancement in cobalt ferrite materials.

1.2 Crystal structure of spinel cobalt ferrite

The general chemical formula of spinel ferrites is $M^{II}Fe_2O_4$ where M^{II} represents divalent ions, as indicated in Table 1.1. The crystal structure of spinel ferrites is similar to that of the spinel mineral $MgAl_2O_4$, which is illustrated by Fig.1.1. For this type of structure, the unit cell contains eight formula units. The cubic closely packed arrays of oxygen ions result in the two kinds of interstitial sites denoted by tetrahedral sites (or A sites) and octahedral sites (or B sites), as shown in Fig.1.1. The unit cell

contains 64 A sites and 32 B sites, and only 8 A sites and 16 B sites are occupied by metallic ions. [27]

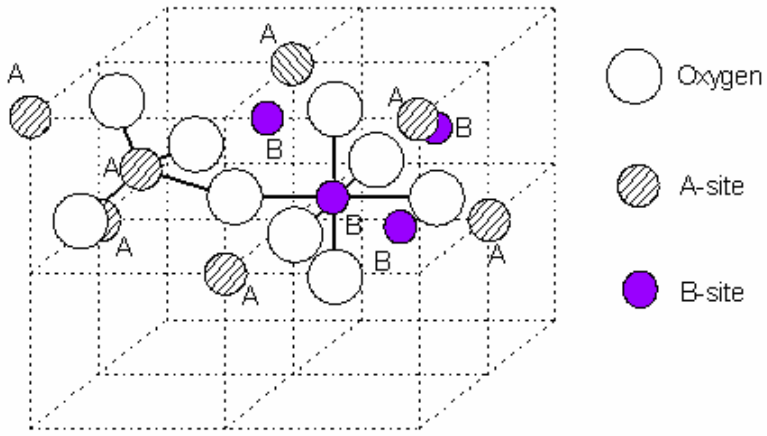

Figure 1.1 The crystal structure of spinel ferrites. The unit cell consists of octants and the ions in tetrahedral site A (shadowed circles) and octahedral site B (solid circles) as well as oxygen (open circles) are shown in two octants[27]

Spinel ferrites show remarkable variations of atomic arrangements in terms of the site occupation of metallic ions and thus the molecular formula of the spinel ferrites can be expressed as[23,27,28]

$$[M^{II}_{1-\delta}Fe^{III}_{\delta}]_{tetra}[M^{II}_{\delta}Fe^{III}_{2-\delta}]_{octa}O_4.$$

If δ=0, the structure formula becomes $[M^{II}]_{tetra}[Fe^{III}_2]_{octa}O_4$, in which case all trivalent Fe^{3+} ions occupy B sites, and then the spinel is said to have "normal" cation distribution. The opposite extreme occurs if δ=1, corresponding to the structure formula of $[Fe^{III}]_{tetra}[M^{II}Fe^{III}]_{octa}O_4$, in which case the trivalent Fe^{3+} ions are evenly distributed on both A and B cation sites, and then the spinel has the so-called fully "inversed" cation arrangements. In view of these, δ is defined as the inversion parameters. The factors that influence the distribution of the cations on A and B sites include the radii of the metal ions, the matching of the electronic configuration of the metal ions to the surrounding oxygen ions, and electrostatic energies of the lattice. The nearest neighboring ions to those on the A sublattice are the ions on the B

sublattice. A typical spinel with an inversed structure is nickel ferrite ($NiFe_2O_4$) whose molecular formula can be expressed as[27]

$$[Fe^{III}]_{tetra}[Ni^{II}Fe_2^{III}]_{octa}O_4,$$

where all Ni^{2+} ions occupy the octahedral sites (B sites) and Fe^{3+} ions are evenly distributed in A and B sites. For cobalt ferrite ($CoFe_2O_4$) materials, they usually have partially inversed spinel structure and the molecular formula can be expressed as [27,29,30]

$$[Co_{1-\delta}^{II}Fe_{\delta}^{III}]_{tetra}[Co_{\delta}^{II}Fe_{2-\delta}^{III}]_{octa}O_4,$$

i.e., both Co^{2+} and Fe^{3+} ions are distributed in both A and B sites. The inversion extent is dependent on the sample preparation processes and the heat treatment processes. Since Co^{2+} has a major contribution to the magnetocrystalline anisotropy of cobalt ferrites, the inversion extent greatly affects the magnetic properties of the material, i.e. coercivity and saturation magnetization. This could be understood based on the ferrimagnetism and magnetic anisotropies of spinel ferrites which will be elucidated in the following.

1.3 Magnetism in spinel ferrites

1.3.1 Ferrimagnetism in spinel ferrites

Ferrimagnetism was proposed by Néel for describing the magnetization behaviors of ferrite materials in which the magnetic ions occupy two different crystallographic positions. He made the assumption that the exchange force acting between an ion on A site and an ion on B site was negative.[27,31] Thus the lattice of A ions is spontaneously magnetized in one direction and the lattice of B ions is spontaneously magnetized in the opposite direction, namely antiparallel to each other as shown in

Fig.1.2 (a). However, the different magnitudes of magnetization of A site and B site lead to the net spontaneous magnetization without external field.[27,31] Therefore, just as ferromagnetic materials, ferrimagnetic materials exhibit substantial spontaneous magnetization at room temperature which makes them industrially important. With temperature increasing, the arrangement of the spins is disturbed by thermal agitation, which is accompanied by a decrease of spontaneous magnetization. At a certain temperature, called the Curie point (T_C), thermal agitation leads to the random arrangement of the spins and the spontaneous magnetization vanishes, as shown in Fig.1.2 (b). Above the Curie point (T_C), the substance exhibits paramagnetism, and the susceptibility (χ) decreases with an increase of temperature (Fig.1.2 (b)).

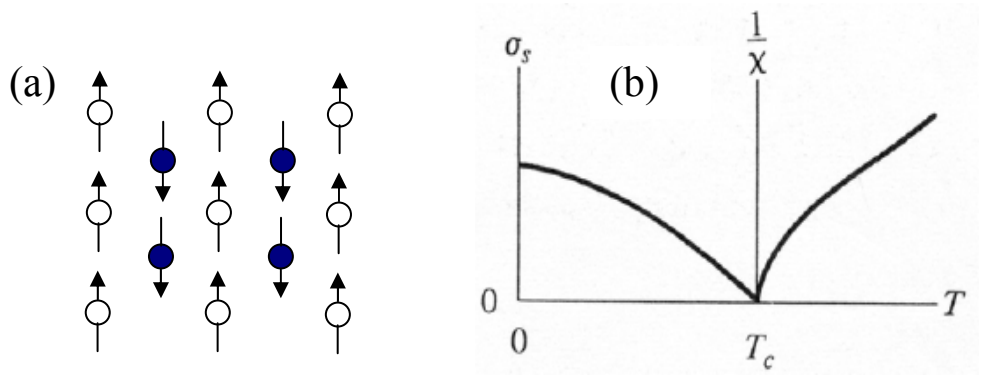

Figure1.2 The schematic drawing for ferrimagnetism: (a) spin configuration in two sublattices; (b) The variation of magnetization (σ_S) with the temperature

Based on the Néel ferrimagnetism, the saturation magnetization of ferrite materials at 0 K can be calculated, if knowing the moment of each ions and the distribution of ions in both A and B sites. Table 1.2 shows some examples of the calculated net magnetic moment for two typical ferrites, i.e. $NiFe_2O_4$ and $CoFe_2O_4$. Given $3\mu_B$ moments per Co^{2+} and $5\mu_B$ moments per Fe^{3+}, the calculated saturation magnetization of the completely inversed $CoFe_2O_4$ is 3 μ_B per molecule. However, $CoFe_2O_4$ usually has a partially inversed structure. In this case, if the inversion extent is δ, the calculated saturation magnetization is 7-4 δ per molecule of $CoFe_2O_4$.

Table 1.2 Ion distribution and net moment per molecule of $CoFe_2O_4$ and $NiFe_2O_4$[31]

Substance	Structure	Tetrahedral A sites	Octahedral B sites	Net moment (μB)
$NiFe_2O_4$	Inverse	$Fe^{3+}(5\downarrow)$	$Fe^{3+}(5\uparrow)$, $Ni(2\uparrow)$	2
$CoFe_2O_4$	Inverse	$Fe^{3+}(5\downarrow)$	$Fe^{3+}(5\uparrow)$, $Co(3\uparrow)$	3
$CoFe_2O_4$	Partially inverse	$Fe^{3+}(5\downarrow)\delta$ $Co(3\downarrow)1-\delta$	$Fe^{3+}(5\uparrow)2-\delta$ $Co(3\uparrow)\ \delta$	7-4δ

However, there always exist some discrepancies between the experimental and the calculated values. For example, the experimentally measured moment is $2.3\mu_B$ per molecule of $NiFe_2O_4$, which is slightly larger than the calculated one, 2 μ_B. The discrepancies can be generally ascribed to one or both of the following:

(i) Orbital moments may not be completely quenched, i.e. there are still some contributions from the orbital moment besides the spin moment. It is thought particularly true for $CoFe_2O_4$;

(ii) The moments in *A* site and in *B* site may not be completely inverse, just like the example shown in Table 1.2. The net magnetic moment is dependent on the inversion extent which can be changed by the preparation conditions such as heat treatment.

1.3.2. Superparamagnetism in spinel ferrites

Superparamagnetism is a unique magnetic phenomenon for nanostructured materials. For ferromagnetic nanoparticles, below a critical particle size, they possess single-domain magnetic structure.[32] If the single-domain nanoparticles are small enough, thermal agitation will directly lead to the fluctuation of magnetization direction of nanoparticles, a sort of Brown rotation.[33,34] Therefore, the magnetization behaviors of these small-sized particles are identical to paramagnetism, except their large magnetic susceptibilities and magnetic moment. Because of these similarities and

differences with respect to the paramagnetism, such thermally agitated magnetic behavior is termed superparamagnetism. It is also called several other names, such as apparent paramagnetism, collective paramagnetism, quasiparamagnetism and subdomain behavior.

Néel [33,34] derived the conditions under which an assembly of isotropic single domain particles can reach thermal equilibrium in a given time comparable to the time of an experiment. Considering an assembly of identical non-interacting aligned uniaxial particles that are first fully magnetized along the easy symmetry axis, after the field is removed, the resulting remanence will vanish as $M_r = M_S \exp(-t/\tau)$, where M_S is the saturation magnetization, t is the time after removal of the field, and τ is the relaxation time for the process. The thermal equilibrium condition corresponds to the state with zero remanence (M_r). Based on the exponential dependence of τ on particle volume, there is a fairly well defined particle size at which the transition to stable behavior occurs with the relaxation time comparable to the experimental time for which the measurable magnetic viscosity would be expected. As a rough measure of the size for transition to stable behavior, one can take the size corresponding to $\tau = 10^2$ seconds. This occurs when the energy barrier is equal to approximately 25 kT. For a given particle, the temperature at which this occurs has been called the "blocking temperature", which can be described by the equation of $1/\tau = f_0 \exp(-KV/k\mathrm{T})$, where K is the anisotropy constant and f_0 is a frequency factor in the order of 10^9 sec^{-1}. V is the volume of the particle, k is the Boltzmann constant and T is absolute temperature. For particles with anisotropy of cubic symmetry, the energy barrier between adjacent easy directions will also appear in the exponential. For example, by using the standard definition of the first order cubic anisotropy constant, the barrier is $KV/4$ for $K > 0$ ([100] easy direction) and $KV/12$ for $K < 0$ ([111] easy direction).

The materials of superparamagnetism should meet at least two requirements. First, the magnetization curve must show no hysteresis, since that is not a thermal equilibrium property. Second, except for particle interaction effects, the magnetization curves for an isotropic sample, which taken at different temperatures, must approximately superimpose when plotted against *H/T* after correction for the temperature dependence of the spontaneous magnetization.[35]

1.4 Magnetic anisotropies of cobalt ferrites

Magnetic anisotropy means that the magnetization of magnetic system is not free to rotate but is bound to a certain direction in which it is easy to be magnetized than in other directions. The existence of magnetic anisotropy indicates that the free energy of a magnetic system depends on the orientation of magnetization with respect to the directions characterizing the magnetic system. For magnetic materials, there are various magnetic anisotropies, such as the magnetocrystalline anisotropy, shape anisotropy and the anisotropies induced by residual stress and magneto-annealing. In terms of the research scope of this thesis project, we will review and discuss the magnetocrystalline anisotropies and the induced anisotropies in the following.

1.4.1 Magnetocrystalline anisotropy of cobalt ferrites

The magnetocrystalline anisotropy is also known as the crystal anisotropy, which is an intrinsic property of magnetic materials. It couples the magnetization to certain crystallographic directions and plays an important role in a variety of magnetic

properties of materials, such as the domain structure, magnetization processes, the shape of hysteresis loops, the magnitude of coercive force and permeability.

In a magnetic crystal, there exist a kind of interaction/coupling between two subsystems: the crystal lattice and the magnetic system consisting of interacting moments.[27] The coupling can exist between the neighboring spins (spin-spin coupling), spin and orbit (spin-orbital coupling), spin and lattice (spin-lattice coupling), and orbital and lattice (orbital-lattice coupling).

The spin-spin coupling is very strong and keeps neighboring spins parallel, or antiparallel, to one another. However, the associated exchange energy is isotropic, and depends only on the angle between adjacent spins, not at all on the direction of the spin axis relative to the crystal lattice. Therefore, the spin-spin coupling cannot contribute to the crystal anisotropy. The orbit-lattice coupling is also strong, because the orientations of the orbits are fixed very strongly to the lattice because of the crystal field (electric field) created by the adjoining atoms. It is the strong orbit-lattice coupling that results in the partial or entire quenching of the orbital moment of electrons in crystal materials. There is also coupling between the spin and orbital motion of each electron, but the coupling is weak when compared with the orbital lattice. When an external field tries to reorient the spin of an electron, the orbit of that electron also tends to be reoriented. Since the orbit is strongly coupled to the lattice and therefore resists the attempt to rotate the spin axis, the energy required to rotate the spin system of a domain away from the easy direction, which is called the anisotropy energy, is just the energy required to overcome the spin-orbit coupling. Therefore, the magnetocrystalline anisotropy arises from the spin-orbit coupling which connects the magnetic moments to the atomic lattice through the electron orbits.[27]

Since the applied field must do work against the anisotropy force to turn the magnetization vector away from an easy direction, there must be energy stored in any crystal in which magnetization vector points in a non-easy direction. This is called the crystal anisotropy energy E_a. In a cubic crystal, such as a spinel ferrite, let magnetization vector make angles *a*, *b*, *c* with the crystal axes, and let α_1, α_2, α_3 be the cosines of these angles, then

$$E_a = K_1(\alpha_1^2\alpha_2^2 + \alpha_2^2\alpha_3^2 + \alpha_1^2\alpha_3^2) + K_2(\alpha_1^2\alpha_2^2\alpha_3^2) + \cdots\cdots$$

where K_1, K_2 ,···· are so-called the anisotropy constants for a particular material. The strength of the anisotropy in any particular crystal is measured by the magnitude of the anisotropy constants K_1, K_2, etc. The first term is usually sufficient of express the actual anisotropy energy. Terms beyond K_2 in above equation are rarely invoked. The cubic ferrites containing cobalt have positive values of K_1, while K_1 is negative for all the cubic ferrites that contain no cobalt.

For cobalt ferrite ($CoFe_2O_4$), K_1 at room temperature is $2.7x10^6$erg/cm^3 and increased with decrease of temperature.[27] The large magnetocrystalline anisotropy results from the contribution of Co^{2+} ions. It was found that even a small concentration of Co^{2+} of the order of 1% in magnetite (Fe_3O_4) can make the anisotropy constant K_1 (negative for Fe_3O_4) positive. To explain the origin of the large anisotropy of $CoFe_2O_4$, based on one-ion model, J. C. Slonczeweski[29] proposed that the large magnetocrystalline anisotropy could be ascribed to the incompletely quenched orbital moment of Co^{2+} ions on the octahedral sites (B sites) of spinel lattice. The residual orbital moment of Co^{2+} is constrained by the crystal electric field to lie parallel to the axis of trigonal symmetry. Spin-orbit energy couples the spin to this axis, accounting for the large anisotropy energy of $CoFe_2O_4$. The magnetocrystalline anisotropies of $CoFe_2O_4$ materials are closely related to the distribution of magnetic ions in the sublattices, i.e.

tetrahedral (A) sites and octahedral (B) sites.[29] Therefore, any change in the site occupation of Co^{2+} ions will result in the change of magnetocrystalline anisotropies, and thus the magnetic coercivities. According to Néel's two sublattice model,[31] a change in saturation magnetization can also be expected when the site occupations of ions are changed. It was reported that the coercivity and saturation magnetization of cobalt ferrite materials are strongly dependent on the thermal annealing histories such as annealing temperatures and cooling rates, which is suggested to be correlated with the change of the site occupations of magnetic ions.[14,36,37] However, in order to understand the effects of the annealing histories, a further detailed study is still necessary. In Chapter 3 of this thesis study, a detailed study was presented for the effects of thermal annealing processes on the phase formation and the magnetic properties of $CoFe_2O_4$ powdered materials. Based on the analysis of the phase, microstructures and the site occupation of magnetic ions of $CoFe_2O_4$ materials, we have tried to elucidate the effects of the site occupations on the magnetocrystalline anisotropies and magnetic properties of well crystallized $CoFe_2O_4$ powdered materials.

On the other hand, the change of the chemical composition may also directly change the intrinsic magnetocrystalline anisotropy. For instance, the substitution of Co^{2+} by other ions such as Ni^{2+} ions may greatly affect the intrinsic anisotropy of $CoFe_2O_4$ materials. As mentioned above, the large magnetocrystalline anisotropy of $CoFe_2O_4$ materials arises from the incomplete quenching of orbital momentum of Co^{2+} which results in large spin-orbit coupling. While the orbital momentum of Ni^{2+} ions is almost fully quenched, the Ni^{2+} substitution will definitely affect the spin-orbit coupling and thus the magnetocrystalline energy of the resultant materials. Therefore, it will be of scientific interest to study the effects of Ni^{2+} substitution on the intrinsic anisotropy and the associated magnetic coercivity of the resultant Ni-Co ferrite

materials. In Chapter 5, a systematical study will be present for revealing the effects of Ni^{2+} substitution on the magnetic properties of Ni-Co ferrite materials.

1.4.2 Stress-induced magnetic anisotropy in spinel ferrites

Strain in magnetic materials can change the magnetocrystalline anisotropy and may thereby alter the magnetization behavior of the materials. This effect is the 'inverse' of magnetostriction, the phenomenon that the sample dimensions change if the direction of the magnetization is altered. The magnetostriction is the experimentally observed lattice deformation which accompanies the process of magnetization in a magnetic crystal.[27] The origin of magnetostriction is mainly due to the spin-orbit coupling, which is also responsible for the magnetocrystalline anisotropy as mentioned above. The relation between the spin-orbit coupling and magnetosctriction can be illustrated by Fig.1.3. Fig.1.3 shows a row of atoms in a crystal. The black dots represent atomic nuclei and the arrows show the direction of the net moment per atom, and the oval lines enclose the electrons distributed nonspherically around each nucleus. Fig. 1.3(a) depicts the paramagnetic sate above T_C, the curie temperature. Once the temperature decreases to below T_C, spontaneous magnetization takes place which leads to the rotation of spins and the electron clouds into some particular orientation determined by the crystal anisotropy, as shown in Fig. 1.3(b). In this case, the nuclei would be forced further apart, and the spontaneous magnetostriction would be $\Delta L'/L'$. In case of Fig. 1.3(c), if a strong magnetic field is applied vertically, the spins and the electron clouds would rotate 90^o, and the domain of which these atoms are a part would magnetostrictively strain by an amount of $\Delta L/L$. The value of $\Delta L/L$ measured at magnetic saturation is called the saturation magnetostriction, generally

denoted as λ_S. The experimentally observed magnetostriction λ_S is usually very small, of the order of 10^{-5}. This means that the reorientation of electron clouds takes place only to a small extent. The conclusion is supported by the fact that orbital magnetic moments are almost entirely quenched, i.e. not susceptible to rotation by an applied field, in most materials. [31]

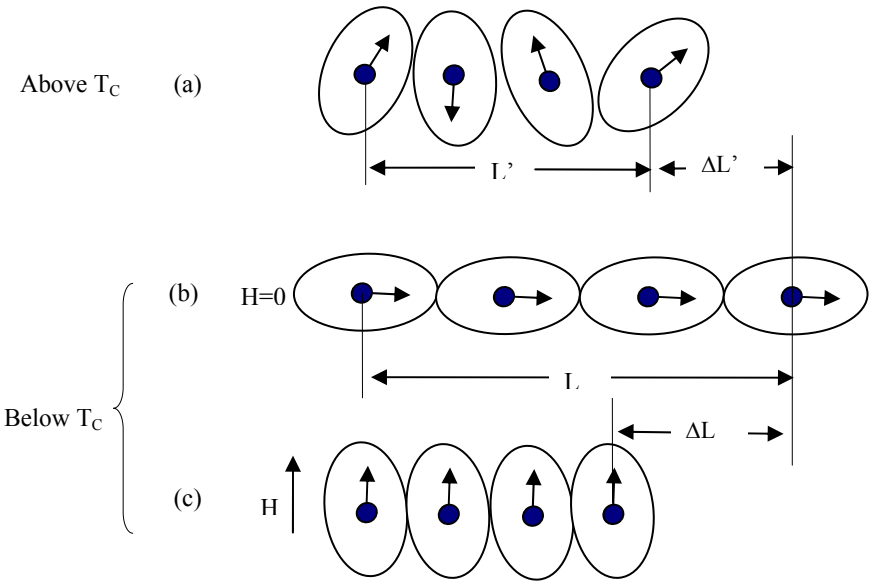

Figure1.3 Mechanism of magnetostriction[31]

Although the magnetostrictive effects are small, it can greatly affects the magnetization behavior of materials when there exist strain in magnetic materials. The effects of stress on the magnetization are thus called the inverse magnetostrictive effects or magnetomechanical effects. The magnetoelastic energy per unit volume (E_{me}) in an elastically isotropic medium associated with isotropic magnetostriction can be written as

$$E_{me} = K_\sigma Sin^2\theta$$

with

$$K_\sigma = \frac{3}{2}\lambda_{si}\sigma = \frac{3}{2}\lambda_{si}E\varepsilon\,.$$

Here K_σ is the stress anisotropy constant, and σ is the stress which is related to the strain, ε, via the elastic modulus E by $\sigma = E\,\varepsilon$.

The magnetostriction constant λ_{si} depends on the orientation and can be positive or negative. The angle θ measures the direction of magnetization relative to the direction of uniform stress. If the strain in a material is non-zero, the magneto-elastic coupling contributes in principle to the effective anisotropy. It means that stress alone can create an easy axis of magnetization. Therefore, when stress/strain exists, stress anisotropy should be considered, along with other anisotropies that may exist. If $\lambda_{si}\,\sigma$ is positive, the axis of stress will be an easy axis for magnetization. If $\lambda_{si}\,\sigma$ is negative, the stress axis will become a hard axis and the plane normal to it is an easy plane for magnetization.

Table 1.3 lists the magnetostriction constants of some spinel ferrites. As seen from it, cobalt ferrites have a very large magnetostriction, considerably higher than those of other ferrites, such as nickel ferrites. [27,38] This could be ascribed to the strong magnetoelastic coupling which arises from the coupling between the energy of orbitally degenerate ground state of Co^{2+} and lattice strain (via crystal field) as well as the magnetic moment (via spin-orbit coupling)[27]

Table 1.3 The magnetostriction constants of some ferrites [27,31]

Materials	**Temperature (K)**	**λ_{100} x 10^{-6}**	**λ_{111} x10^{-6}**	**polycrystalline x10^{-6}**
$Co_{0.8}Fe_{2.2}O_4$	293	-590	120	-
$CoFe_2O_4$	293	-	-	-110
Fe_3O_4	293	-19	81	40
$NiFe_2O_4$	293	-45.9	-21.6	-26
$MnFe_2O_4$	-	-	-	-5
Mg Fe_2O_4	-	-	-	-6
$Ni_{0.8}Fe_{2.2}O_4$	293	-36	-4	-

1.5 Remarks in summary

With reviewing the magnetisms and various magnetic anisotropies in cobalt ferrite materials, it is clear that the magnetic properties of cobalt ferrite ($CoFe_2O_4$) materials depend on various factors. These include the chemical composition, site occupation of magnetic ions and the microstructure features (e.g. grain size/size distribution, defects and residual strain). Understanding the effects of the above-mentioned factors on the magnetic properties will be essential for synthesizing high-quality cobalt ferrite materials and thus for realizing their practical applications. As hard oxide magnetic materials, cobalt ferrites have been recognized as promising candidates for magnetic data recording, for which coercivity enhancement is a crucial issue.

Many research groups in the world are investigating how to improve magnetic coercivity of cobalt ferrite ($CoFe_2O_4$) materials. For $CoFe_2O_4$ thin film materials, high coercivities of up to 12.5 kOe have been achieved in our group by using laser ablation process.[18,26] As mentioned previously, achieving such a high coercivity can be ascribed to the tailoring of microstructure and the building-up of high-level strain inside the thin-film structure. For $CoFe_2O_4$ powdered materials, various processes have been employed to fabricate nanopowders, including chemical precipitation,[39-42] sol-gel,[43,44] micro-emulsion,[45] modified oxidation process,[40] and mechanical alloying.[25,46,47] For these works, the efforts were mainly devoted to controlling the microstructure (such as grain size) and/or doping with different elements. Among these processes, micro-emulsion is quite effective for controlling average grain size and size distribution. However, the maximum coercivity obtained was only 1.44 kOe due to small grain size achievable.[45] By the modified co-precipitation process, Chinnasamy et al ynthesized $CoFe_2O_4$ nanoparticles and achieved a high coericivity

of 4.6 kOe with a size-selection method.[39] However, there was no detailed studies regarding the cation distribution of the synthesized samples. Doping other elements into $CoFe_2O_4$ lattice was another strategy for coercivity enhancement. Several works were reported regarding the doping with rare earth ions such as Gd^{3+}, Tb^{3+} and Dy^{3+}.[13,48,49] Unfortunately, the coercivities achieved in these works were less than 2 kOe. By mechanical alloying, Ding and et al synthesized $CoFe_2O_4/SiO_2$ nanocomposites and a high coercivity of up to 3.5 kOe was achieved in milling-derived SiO_2-10wt%$CoFe_2O_4$ nanocomposites. An increase in Curie temperature of 20^oC was observed in the SiO_2-doped samples in comparison with that of pure Co-ferrite. Such coercivity enhancement was ascribed to doping of SiO_2 into $CoFe_2O_4$ lattice. However, more detailed studies are still necessary. There were several works reported for Ni^{2+} doped cobalt ferrites. By the co-precipitation method, Yamamoto et al synthesized Co-Ni ferrite ($Ni_xCo_{1-x}Fe_2O_4$) fine particles.[50] They presented a detailed study on the effects of Ni concentration on the magnetic properties of $Ni_xCo_{1-x}Fe_2O_4$ powders. With the increase in Ni^{2+} substitution, it was found that the saturation magnetization decreased monotonously, but the coercivity first increased and then decreased. A maximum coercivity of around 3.5 kOe was observed for the $Ni_{0.7}Co_{0.3}Fe_2O_4$ sample.[50] In contrast, both Zhang et al[51,52] and Kitamoto et al[53] reported the different coercivity dependence on Ni^{2+} substitution in Ni-Co ferrite materials. In both works, it was found that both the saturation magnetization and the coercivity monotonously decreased with increasing Ni^{2+} substitution.[51-53] Therefore, these results are contradictory to those reported by Yamamoto et al. In this sense, more detailed and systematic studies are necessary such as chemical composition, cation distribution for understanding the effects of Ni^{2+} doping.

In this thesis project, the major research efforts will be devoted to the exploration of the ways for coercivity enhancement and the investigation of the related coercivity mechanisms in cobalt ferrite powdered materials. Herewith, four major effects on the magnetic coercivity of cobalt ferrite powdered materials will be discussed in terms of above arguments, i.e. the effects of (i) chemical composition, (ii) site occupation of magnetic ions, (iii) grain/particle size and distribution, and (iv) defects and the associated residual strain.

The effects of chemical composition and site occupation of magnetic ions on magnetic coercivity mainly lie in the contribution of Co^{2+} ions to the magnetocrystalline anisotropy of cobalt ferrite materials. As mentioned above, unlike other spinel ferrites, cobalt ferrite possesses large magnetocrystalline anisotropy which can be ascribed to the incompletely quenched orbital moment of Co^{2+} ions at the octahedral sites in spinel lattice.[29] Therefore, the changes in either site occupation of Co^{2+} ions or the composition (e.g. substitution of Co^{2+} by other ions such as Ni^{2+}) will change the intrinsic magnetocrystalline anisotropy. In this sense, to study the effects of chemical composition and site occupation of magnetic ions will be essential for understanding the coercivity mechanisms of cobalt ferrite materials. Thus the discussion of phase and cation distribution will be covered in all chapters in this thesis. In addition, a detailed study will be presented in Chapter 5 for discussing the effects of the Ni^{2+} substitution on the magnetocrystalline anisotropy and the magnetic properties of the resultant Ni-Co ferrites materials.

On the other hand, it has been well established that the magnetic coercivity is strongly correlated with the grain size, and the defects and the related residual strain. The effects of these microstructural features on the coercivity of magnetic materials have been well recognized and widely studied.[54-58] The effects of the grain size are

correlated with the domain structure of magnetic materials, which greatly affects the reversal magnetization behaviors and thus the magnetic coercivity of materials. Large grains with multidomain structures generally have low coercivity. The reason lies in the fact that the reversal magnetization processes are mainly through the domain wall movement which lead to easy demagnetization and the resultant low coercivity. With grain size decreasing, the coercivity increase and reach a maximum value when the grain size is near single-domain size. However, further decrease in grain size leads to the drop of coercivity due to the increasing effects of thermal agitation on the grain magnetization. This eventually results in zero coercivity, i.e. the appearance of superparamagnetism, which has been mentioned in the previous section. Therefore, in order to achieve a high coercivity, the controlling of average grain size will be of great importance. Thus, to study the effects of grain/particle size, different processes will be employed for synthesizing cobalt ferrite materials with different grain/particle sizes in this project. This will be discussed in Chapter 3.

As mentioned above, the residual strain always plays an important role in affecting the coercivity of magnetic materials. On one hand, residual stress alone can induce the uniaxial stress anisotropy, and generate an additional contribution to the magnetic anisotropies of materials. On the other hand, as is well known, the build-up of a high residual strain is always accompanied by the formation of various defects such as dislocations in order to accommodate the high strain energy. As it is well recognized, defects and other magnetic inhomogeneities (such as grain boundaries and inclusions) may act as effective pinning centers for hindering the movement of domain walls during the reverse magnetization processes of magnetic materials.[55,56,59] Therefore, introducing residual strain may bring about two major effects on the coercivity developments; one is related to the stress-induced anisotropy and the other is related to the pinning effects of defects on the reversal magnetization processes of magnetic

materials. Although many research works proposed that stress-induced anisotropy was responsible for the significant increase in coercivities in various magnetic thin-film materials,[18,52,54,56,58-62] the mechanisms behind stress-induced anisotropy haven't been well understood and more detailed investigations are needed. Most importantly, for powdered magnetic materials, there are still no effective ways to introduce high-density defects and high-level internal strain in order to obtain high stress anisotropy. In this thesis project, for the purpose of the coercivity enhancement, mechanical milling will be employed. We will examine whether mechanical milling could generate a highly-strained defective microstructure in cobalt ferrite powdered materials. A detailed investigation of the effects of both residual stress and defects on the magnetic coercivity will be presented in order to understand the coercivity mechanisms. These will be discussed in both Chapter 4 and Chapter 5.

It should be pointed out that two terminologies are frequently used in this thesis, i.e. mechanical milling and mechanochemical synthesis (milling). The mechanical milling refers to the milling process without involving the material transferring and phase changes during processing, while mechanochemical milling has material transferring and phase changes, namely chemical reactions during the milling processes.

1.6 Objectives and scope of the study

In view of above discussions, the main purposes of this thesis can be listed as the followings:

(i) To explore the feasibility of the synthesis of high-coercivity spinel cobalt ferrite ($CoFe_2O_4$) powdered materials by both co-precipitation and mechanochemical processes, and to investigate the effects of the microstructure (e.g. grain size) on the magnetic properties of the resultant powdered materials. (Chapter 3)

(ii) To study the effect of post annealing processes on the site occupation, phases and average grain size of mechanochemically derived $CoFe_2O_4$ powders, and their influences on the magnetocrystalline anisotropy and magnetic properties of $CoFe_2O_4$ powdered materials; (Chapter 3)

(iii) To explore the feasibility of the introduction of high-level strain and high-density defects in $CoFe_2O_4$ powdered materials by mechanical milling, and to study microstructure evolution during the milling processes and its effects on magnetic properties of the milled $CoFe_2O_4$ samples; and to investigate the coercivity mechanisms if a high coercivity could be achieved after mechanical milling; (Chapter 4)

(iv) To explore the feasibility of the Ni^{2+} substitution of Co^{2+} for the formation of $Ni_xCo_{1-x}Fe_2O_4$ powdered materials by mechanochemical process, and to study the effects of the Ni^{2+} substitution on the magnetic properties and magnetocrystalline anisotropy of $Ni_xCo_{1-x}Fe_2O_4$ powdered materials; (Chapter 5)

(v) To examine whether mechanical milling could induce high-level strain and high-density defects in $Ni_xCo_{1-x}Fe_2O_4$ powdered materials, and to study the effects of mechanical milling on magnetic properties of the samples. If a high coercivity could be induced after milling, to investigate the effects of Ni^{2+} substitution on the milling-induced coercivity and the associated mechanisms; (Chapter 5)

(vi) To further examine whether mechanical milling could induce high coercivity in other spinel ferrites, Fe_3O_4 powder will be subjected to milling. (Chapter 5)

1.7 References

[1] T. Yamaguchi and M. Abe, 1992 (unpublished).
[2] D.C. Mattis, *The theory of magentism I*. (Springer-Verlag, Berlin Heidelberg, Germany, 1981).
[3] R. Valenzuela, *Magnetic Ceramics*. (Cambridge University Press, United Kingdom, 1994).
[4] S. Hilpert and A. Wille, Phys. Chem. B **18**, 291 (1932).
[5] T. Takei, J. Electrochem. Ass. Japan **5**, 411 (1937).
[6] A. Goldman, *Modern Ferrite Technology*. (Van Nostrand Reinhold, New York, 1990).
[7] G.F. Dionne, D.E. Oates, D.H. Temme, and J.A. Weiss, IEEE Trans. Microwave Theor. Tech. **44**, 1361 (1996).
[8] H. Watanabe, S. Iida, and M. Sugimoto, *Ferrites, Proceeding Of International Conference in Ferrites,*. (Centre for Academic Publications, Japan,, 1980).
[9] A.L. Tronconi, A.C. Oliveira, E.C.D. Lima, and P.C. Morais, Journal of Magnetism and Magnetic Materials **272-76**, 2335 (2004).
[10] B. M. Berkovsky, V. F. Medvedev, and M. S. Krakov, *Magnetic Fluids: Enginering Applications*. (Oxford University Press, New York, 1933).
[11] M. Bonini, A. Wiedenmann, and P. Baglioni, Journal of Physical Chemistry B **108**, 14901 (2004).
[12] Q.A. Pankhurst and R.J. Pollard, Journal of Physics-Condensed Matter **5** 8487 (1993).
[13] F. X. Cheng, J. T. Jia, Z. G. Xu, B. Zhou, C. S. Liao, C. H. Yan, L. Y. Chen, and H. B. Zhao, J. Appl. Phys. **86**, 2727 (1999).
[14] J. Ding, T. Reynold, W.F. Miao, P.G. McCormick, and R. Street, Appl. Phys. Lett. **65**, 7074 (1994).
[15] J. Ding, Y. J. Chen, Y. Shi, and S. Wang, Appl. Phys. Lett. **77** 3621 (2000).
[16] L. Bouet, P. N. Tailhades, and A. Rousset, J. Magn. Magn. Mater. **153**, 389 (1996).
[17] P. Rice and J. Moreland, IEEE Transactions on Magnetics **27**, 3452 (1991).
[18] Y. C. Wang, J. Ding, J. B. Yi, B. H. Liu, T. Yu, and Z. X. Shen, Appl. Phys. Lett. **84**, 2596 (2004).
[19] Y. Kitamoto, S. Kantake, F. Shirasaki, M. Abe, and M. Naoe, J. Appl. Phys. **85** 4708 (1999).
[20] Y. Suzuki, R. B. Van Dover, E. M. Gyorgy, J. M. Philips, V. Korenivski, D. J. Werder, C. H. Chen, R. J. Cava, J. J. Krajewski, W. F. Peck, and K.B. Do, Appl. Phys. Lett. **68**, 714 (1996).
[21] K. Butter, P. H. H. Bomans, P.M. Frederik, G.J. Vroege, and A. Phlips, Nature Mater., **2**, 88 (2003).
[22] R. Langer, Science **249**, 1527 (1990).

[23] B. Viswanathan and V. R. K. Murthy, *Ferrite Materials Science and Technology*. (SPRINGER-VERLAG, Narosa Publishing House, 1990).
[24] K. H. J. Buschow, *Ferromagnetic Materials,*. (Elsevier, New York, 1988), p.1.
[25] J. Ding, P. G. McCormick, and R. Street, Solid State Commun **95**, 102 (1995).
[26] J.H. Yin, J. Ding, B.H. Liu, X.S. Miao, and J.S. Chen, Appl. Phys. Lett. **88**, 162502 (2006).
[27] D.J. Craik and J. Derek, *Magnetic Oxides*. (Wiley, London, New York 1975), p.327.
[28] E. Prince, Phys. Rev. **102**, 674 (1956).
[29] J. C. Slonczeweski, Phys. Rev. **110**, 1141 (1958).
[30] W.G. Wyckoff, *Crystal Structures,*. (Willey-Intersceince, New York, 1965).
[31] B.D. Cullity, *Introduction to magnetism and magnetic materials*. (Addison-Wesley Publishing Company, Notre Dame, Holland, 1973).
[32] J. Frenkel and J. Dorfman, Nature Mater., **126**, 274 (1930).
[33] L. Néel, "Compt. Rend. Acad. Sci," **228**, 664 (1949).
[34] L. Néel, Ann. géophys **5**, 99 (1949).
[35] E. R. Jette and F. Foote, J. Chem. Phys. **1** 29 (1933).
[36] C.S. Kim, S.W. Lee, S.I. Park, J.Y. Park, and Y.J. Oh, J. Appl. Phys. **79**, 5428 (1996).
[37] S.J. Kim, S.W. Lee, S.Y. An, and C.S. Kim, J. Magn. Magn. Mater. **210**, 215 (2000).
[38] B.M. Bozorth and J.G. Walker, Phys. Rev. **88**, 1209 (1952).
[39] C. N. Chinnasamy, B. Jeyadevan, K. Shinoda, K. Tohji, D. J. Djayaprawira, M. Takahashi, R. Justin J oseyphus, and A. Narayanasamy, Appl. Phys. Lett. **83**, 2862 (2003).
[40] C.N. Chinnasamy, M. Senoue, B. Jeyadevan, Oscar Perales-Perez, K. Shinoda, and J. K. Tohji, Journal of Colloid and Interface Science **263**, 80 (2003).
[41] V. Kumar, A. Rana, M.S. Yadav, and R.P. Pant, Journal of Magnetism and Magnetic Materials **320**, 1729 (2008).
[42] H. Yamamoto, IEEE Trans. Magn. **38** 3488 (2002).
[43] B.G. Toksha, S. E. Shirsath, S.M. Patange, and K.M. Jadhav, Solid State Communications **147**, 479 (2008).
[44] S. H. Xiao, H. J. Xu, J. Hu, L. Y. Li, and X. J. Li, Physica E **40** 3064 (2008).
[45] V. Pillai and D. O. Shal, J. Magn. Magn. Mater. **163**, 243 (1996).
[46] J. Ding, H. Gong, R. Melaka, S. Wang, Y. Shi, Y.J. Chen, and N.X. Phuc, Journal of Magnetism and Magnetic Materials **230**, 1382} (2001).
[47] S.R. Mekala and J. Ding, Journal of Alloys and Compounds **296**, 152 (2000).
[48] B. A. Calhoun and M. J. Freiser, Journal of Applied Physics **34**, 1140 (1999).
[49] M. L. Kahn and Z. J. Zhang, Appl. Phys. Lett **78**, 3651 (2001).
[50] H. Yamamoto and Y. Nissato, IEEE TRANSACTIONS ON MAGNETICS **38**, 3488 (2002).
[51] F. Zhang, Y. Kitamoto, M. Abe, and M. Naoe, J. Appl. Phys. **87**, 6881 (2000).
[52] H.W. Zhang, C.B. Rong, J. Zhang, S.Y. Zhang, and B.G. Shen, Phys. Rev. B, **66**, 184436 (2002).
[53] Y. Kitamoto, F. Zhang, F. Shirasaki, M. Abe, and M. Naoe, IEEE Trans. Magn. **35**, 2694 (1999).
[54] D. Givord, Q. Liu, and M.F. Rossignol, *Science and Technology of Nanostructured Magnetic Materials*. (Plenum Press, New York, 1991).
[55] H. Kronmüller, Physica Stat. Sol. (b) **44**, 385 (1987).

[56] H. Kronmüller, K. D. Durst, and G. Martinek, J. Magn. Magn. Mater. **69**, 69 (1987).
[57] E.F. Wolfarth, Journal of Physcis F **14**, L155 (1984).
[58] D. Givord, P. Tenaud, and T. Viadieu, IEEE Trans. Magn. **24** 1921 (1988).
[59] K.D. Dust and H. Kronmuller, J. Magn. Magn Mater. **68**, 63 (1987).
[60] A. Lisfi, J. C. Lodder, E. G. Keim, and C. M. Williams, Appl. Phys. Lett. **82**, 76 (2003).
[61] A. Lisfi and C. M. Williams, J. Appl. Phys. **93**, 8143 (2003).
[62] B.G. Demczyk and J.O. Artman, J. Phys. D, Appl. Phys. **24**, 1627 (1991).

CHAPTER 2

Characterization Techniques

2.1 X-ray diffraction (XRD)

2.1.1 Bragg's law and phase analysis

With x-ray interactions with a crystal consisting of atoms arranged periodically in three dimensions, the scattering of x-rays occurs in all directions. In case of the coherent scattering, the scattered x-ray waves have the same frequency and definite phase difference, and thus interfere with one another constructively or destructively. The diffraction is generated when a large number of scattered rays mutually reinforce one another. The specific condition for the generation of diffraction can be described by the well-know Bragg's law, i.e. [1,2]

$$2d \sin\theta = n\lambda$$

where θ : angle between the incident X-ray and the diffraction plane,

d : interplane (diffraction plane) distance,

λ : wavelength of the incident X-ray, and

n : an integer corresponding to the order of diffraction plane.

Given the fixed wavelength (λ) of the x-ray wave from a source, the diffraction occurred at a certain diffraction angle (θ) corresponds to a particular d spacing of the material. By indexing several sets of diffraction peaks in the XRD spectra, the phase identification can be possible in terms of the unique sets of d spacing for a particular material.

2.1.2 The line broadening and the analysis of average grain size and residual strain

Generally, diffraction line broadening has three contributions from instrumental effect, crystallite size and microstrain.[1,2] Therefore, the total experimental line broadening (B_{exp}) can be expressed as

$$B_{exp}=B_{ins}+B_{size}+B_{strain,}$$

where B_{exp} is the experimentally measured line broadening, i.e. full width at half maximum of the diffraction peaks (FWHM);

B_{ins} is FWHM due to the instrumental broadening;

B_{size} is FWHM due to the crystallite (grain) size broadening and

B_{strain} is FWHM due to the strain-induced broadening.

A. The instrument broadening

There is always extraneous broadening due to the causes such as the slit widths, imperfect focusing of x-ray beam, unresolved $K\alpha_1$ and $K\alpha_2$ peaks and the wavelength widths of $K\alpha_1$ and $K\alpha_2$ waves. All these can contribute to the so-called "instrument broadening".[1] To correct the instrument broadening, it is necessary to run a standard stress-free sample whose grain size should be large enough to eliminate the effects of crystallite broadening. Under the same scanning conditions, the line broadening obtained for the standard sample should be the same as that existed in the diffractions of other real samples.

B. Grain-size broadening

The first treatment of grain size broadening was done by Scherrer.[1,2] Assuming there

is no instrumental broadening and the crystals are free of strains, the grain size-induced broadening can be expressed by the well-known Scherrer equation,

$$B(2\theta) = \frac{0.94\lambda}{Lcos\theta} \qquad (2\text{-}1)$$

where $B(2\theta)$ is FWHM due to the grain size broadening;

θ is the diffraction angle;

λ is the wavelength of the x-ray and

L is the average crystal dimension perpendicular to the diffraction planes

Therefore, based on the Scherrer equation, Eq. (2-1), the average grain size of polycrystalline samples can be estimated if the samples are free of strain and the instrumental broadening is corrected.

The experimental difficulties involved in the grain size measurement from the line broadening increases with the size of crystals as measured. With good instruments and experimental techniques, the upper limit of the measurable grain size can approach around 200nm.

C. Strain broadening

The effect of strain, both uniform and non-uniform, on the x-ray diffraction can be illustrated in Fig.2.1. For an unstrained grain, the diffraction from the transverse diffraction planes will give rise to a sharp and symmetric diffraction peak as shown in Fig.2.1 (a). If the grain undergoes a uniform tensile strain at the right angle to the diffraction planes, their spacing d_1 is larger than $d_{0,}$ and thus the diffraction peak will shift to a low angle as shown in Fig.2.1 (b). This is the basis for the measurement of the macrostress by x-ray diffraction method. (Macrostress refers to the stress that does

not vary from one grain to another but keep quite uniform over a large distance). If the grain is bent and the strain inside it will be nonuniform, i.e., the top side of the grain will undergo tensile strain with a large *d* spacing while the bottom side will have compression strain with a smaller *d* spacing, as shown in Fig.2.1 (c). This strain state is so-called microstrain which means that it may vary from one grain to another or from one part of the grain to another part. Therefore, these different strained regions will give rise to the diffraction with different Bragg's angles, each slightly displaced from other.

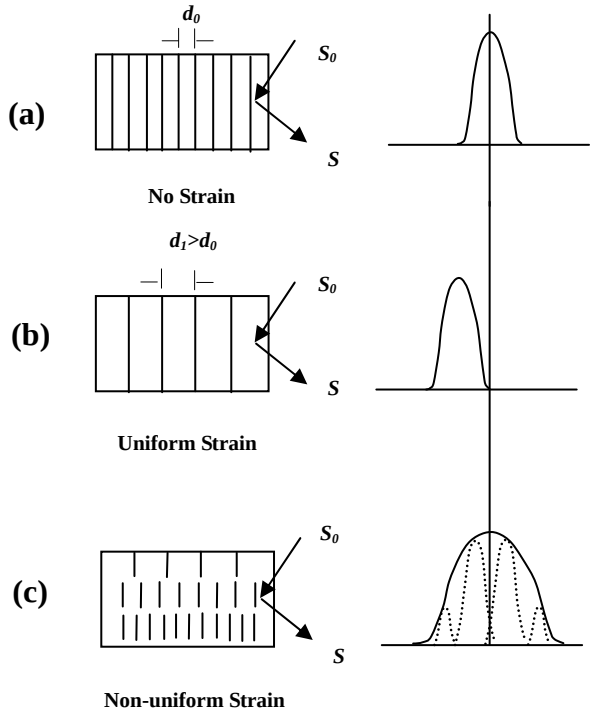

Figure 2.1 The effect of uniform and non-uniform strains (left side of the figure) on the diffraction peak position and width (right side of the figure). (a) shows the unstrained samples, (b) shows uniform strain, and (c) shows non-uniform strain within the volume sampled by the x-ray beam.[2]

Thus the resultant diffraction peak consists of various sharp diffraction peaks from the strained planes, i.e. the broadening of the diffraction peak appears as shown in Fig.2.1 (c). Differentiating Bragg's law leads to the relation between the broadening and the

nonuniform strain:

$$B(2\theta) = -2\frac{\Delta d}{d}\tan\theta \qquad (2\text{-}2)$$

where $B(2\theta)$ is FWHM due to the strain broadening;

θ is the diffraction angle;

$\Delta d/d$ is the nonunoform strain

D. The separation of grain-size broadening and strain-broadening

The separation of grain-size broadening and strain broadening can be done by using the Williamson-Hall plot.[2] If the broadening of diffraction peaks could be due to both the size and strain effects, the overall broadening after eliminating the instrumental broadening can be expressed by the combination of Eq.(2-1) and Eq.(2-2), i.e.,

$$B(2\theta) = \frac{0.94\lambda}{Lcos\theta} - 2\frac{\Delta d}{d}\tan\theta \text{ , and thus}$$

$$B\cos\theta = \frac{0.94\lambda}{L} - 2\frac{\Delta d}{d}\sin\theta \qquad (2\text{-}3)$$

Based on Eq.(2-3), the identification of the contribution of broadening from size and strain effects can be done by plotting $B\cos\theta$ as a function of $\sin\theta$. The plot of $B\cos\theta$~ $\sin\theta$ is the famous Williamson-Hall plot. If there is no microstrain inside, $B\cos\theta$ will show no dependence on $\sin\theta$, and thus a flat and linear plot will appear. If strain shows an important contribution to the broadening of diffraction peak, $B\cos\theta$ will be a linear function of $\sin\theta$, and the slope of the plot will be $\Delta d/d$ from which the average strain can be obtained.

E. Calculation of lattice parameters based on the extrapolating function

The process for measuring the lattice parameters by X-ray diffraction is indirect as the lattice parameters need to be derived from the measured parameters such as Bragg θ of the diffraction planes. For cubic materials such as spinel cobalt ferrite, the lattice parameter (a) is proportional to the spacing (d) of any particular set of (hkl) Bragg plane, i.e.

$$a = d\sqrt{h^2 + l^2 + k^2}\,. \qquad (2\text{-}4)$$

By measuring the Bragg angle θ and using the Bragg law $2d\sin\theta = \lambda$ to determine d, the lattice parameter a can be calculated based on Eq. (2-4). Therefore, the precision of a depends on d. When a diffractometer is used to measure d-spacings, the largest systematic error in d is the displacement errors.[2] The displacement error refers to the specimen displacement from the diffractometer axis. It causes an error in d given by

$$\frac{\Delta d}{d} = \frac{D\cos^2\theta}{R\sin\theta}, \qquad (2\text{-}5)$$

where D is the specimen displacement parallel to the diffraction-plane normal and R is the diffraction radius.[2] Since cosθ approaches zero as θ approaches 90^o, $\Delta d/d$ and $\Delta a/a$, the fractional errors will also approaches zero asθ approaches 90^o. Therefore, in order to get accurate value of lattice parameter a, it is necessary to extrapolate the lattice parameters against $\frac{\cos^2\theta}{\sin\theta}$ at θ =90^o. $\frac{\cos^2\theta}{\sin\theta}$ is so-called extrapolation function.

In this thesis work, for average grain size and microstrain analysis, the instrument broadening was removed from the XRD line broadening. To determine the instrument

broadening, a single-crystal quartz sample was used. The estimated instrument broadening is 0.05^{o}.

2.2 Vibrating Sample Magnetometer

The vibrating sample magnetometer (VSM) is an important instrument which is widely used for various magnetic measurements. The working principle of VSM is based on the magnetic induction measurements, involving observation of the voltage induced in a detection coil by a flux change when the applied magnetic field or sample position is changed. According to Faraday's law of electromagnetic induction, the voltage induced in an electrical circuit is proportional to the rate of change of magnetic flux linking the circuit [3], i.e.

$$V = -N_0 (\frac{d\Phi}{dt}), \qquad (2\text{-}6)$$

where Φ is the magnetic flux passing through a coil of N_0 turns and $d\Phi/dt$ is the rate of flux change. Since the magnetic induction is the flux density B, i.e.,

$$B = \frac{\Phi}{A} \qquad (2\text{-}7)$$

where A is the cross-sectional area of the coil, the law of electromagnetic induction (Equation 2-6) can be written as,

$$V = -N_0 A(\frac{dB}{dt}). \qquad (2\text{-}8)$$

Accordingly, the change of the magnetic induction can be obtained by measuring the electric voltage induced.

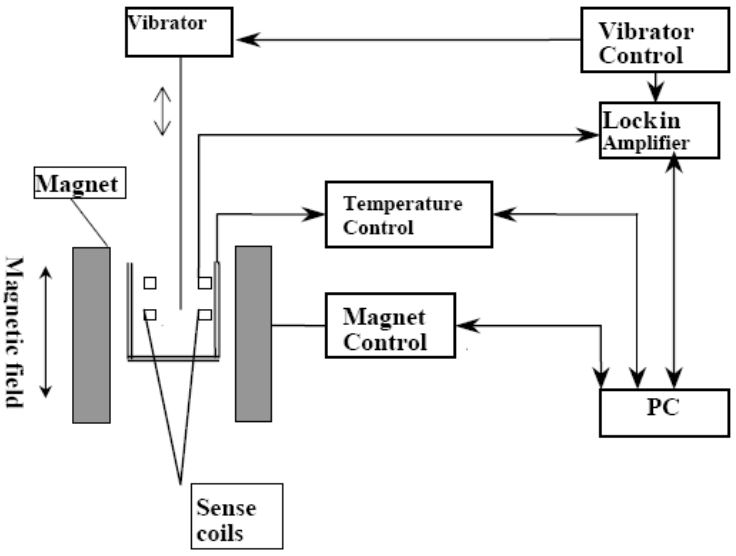

Figure 2.2 The schematic diagram of a typical VSM [4]

A schematic diagram of a typical VSM is shown in Fig.2.2. The sample is attached to the end of a long plastic rod in a superconductive solenoid type electromagnet that can produce a magnetic field of up to 9 T. A set of detection coils, which measures the magnetic moment, is symmetrically distributed about the sample with the axis of the detection coils parallel to the applied magnetic field. In order for the detection coils to measure a magnetic moment, the magnetized sample is vibrated up and down in small oscillations to cause a time-varying flux that is detected by the detection coils. This time-varying flux induces an e.m.f. in the coils according to the Faraday's law, and the magnitude of the e.m.f. is proportional to the total moment of the sample. An M-H hysteresis loop is obtained by slowly sweeping the applied field from a maximum positive field, through zero, to a maximum negative field and back again.

In this project, two types of VSMs, one from Oxford Maglab, another from Lakeshore, were used for various magnetic studies, including the measurements of magnetic hysteresis loops, minor loops, DCD (DC demagnetization) curves and the magnetic

viscosities as well as the magneto-annealing studies. All the powder samples were pressed into small pellets of 5 mm in diameter and ~2 mm.

A. Measurement of hysteresis loops

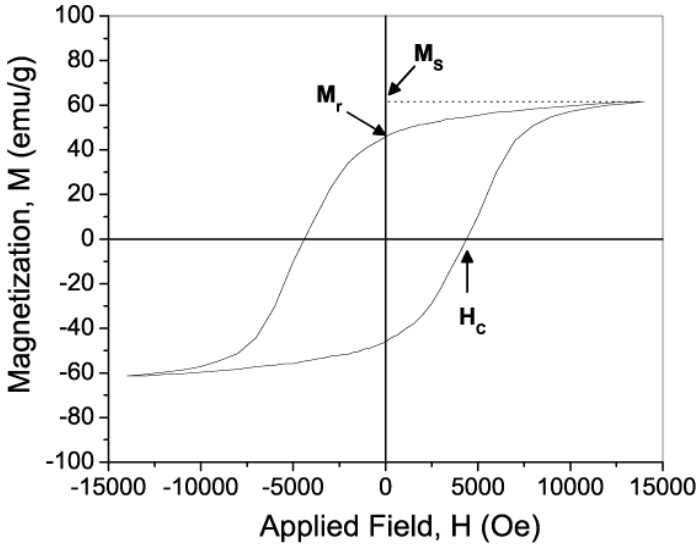

Figure 2.3 A typical hysteresis loop

A hysteresis loop (M-H) can be obtained by slowly sweeping the applied field from a maximum positive field, through zero, to a maximum negative field, and then back again to the maximum positive field. A typical hysteresis loop is shown in Fig.2.3. From the hysteresis loop, we can determine the saturation magnetization M_S, remnant magnetization M_r, squareness (M_r/M_S) and coericivity H_C.

B. Measurement of minor loops

The minor loops consist of a family of hysteresis loops which are measured at the gradually increased maximum applied fields. Fig.2.4 (a) and (b) show respectively the method for measuring minor loops and the typical minor loops obtained experimentally. To measure minor loops, the sample should be firstly at

demagnetization state and then a small field (typically 100 Oe) is applied under which a hysteresis loop is recorded. Then the applied field is continuously increased and the correspondingly the hysteresis loops are recorded until the magnetization saturation is achieved. The family of the loops as obtained is so-called minor loop. Basically, from the family of the loops, we can derive the field-dependent coercivity, field-dependent initial magnetization and the field-dependent magnetic remanence. Therefore, the minor loops can provide useful information for studying the magnetization and demagnetization behaviors of magnetic materials.

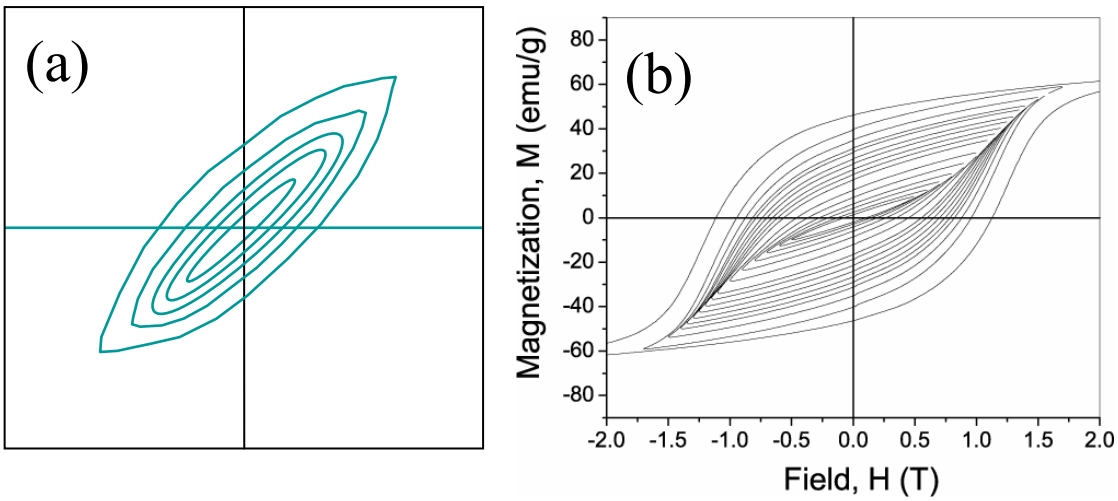

Figure 2.4 (a) The illustration of measuring minor loops; (b) the typical hysteresis loops

C. Measurement of the DC demagnetization remanence curves and irreversible susceptibility [5-8]

The measurements of DC demagnetisation remanence were made by saturating a sample in a positive field, and thereafter measuring the value of the reduced remanence ($M_d(H)$) after the application of progressively larger negative (reverse) fields. Thus the DC demagnetization remanence curves can be obtained by plotting

out the $M_d(H)$ as a function of the reverse fields (H). Based on the DC demagnetization curves, the field-dependent irreversible magnetic susceptibility χ_{irre} can be obtained by differentiating the $M_d(H)$-H curves, i.e. $dM_d(H)/dH$

The irreversible magnetic susceptibility χ_{irre} is an important parameter that characterizes the reversal magnetization processes of the magnetic materials. The detailed discussion on the role of χ_{irre} will be mentioned in Chapter 4 where the coercivity mechanism of $CoFe_2O_4$ materials will be discussed on the basis of a phenomenological model.

2.3 Mössbauer spectroscopy

Gamma ray (γ-ray) emitted from radioactive nuclei decaying from excited states can excite nuclei of the same isotope in ground state by resonant absorption. However, such kind of resonant absorption can be greatly reduced due to the recoil of the free nuclei which leads to the loss of energy. Therefore, the as obtained signal is weak with strong background which greatly limits the application of such technique. In 1957, Mössbauer discovered that emission and absorption of γ-rays could occur without nuclear recoil in a solid where nuclei are fixed in the lattice. The Mössbauer effect thus refers to the recoilless resonant absorption without energy loss and thermal broadening. [9,10]

The unique feature of the Mössbauer effect is the production of the monochromatic electromagnetic radiation with a very narrowly defined energy spectrum. It can be used to resolve minute energy variation of interactions between the nuclei and the

extra-nuclear electrons. Therefore, Mössbauer effect has its unique application in chemical analysis. When γ-rays from a source that has a substantial recoil-free fraction pass through an absorber, the transmission of γ-rays will decrease due to the resonant absorption and the subsequent re-emission. The decrease in transmission is affected by the difference in relative values of γ–ray energy ($E\gamma$). The effective Eγ value can be altered by moving the source and the absorber relatively to each other with a velocity by using externally applied Doppler effects. If the effective γ_E values are exactly matched at a certain Doppler velocity, resonance will be at a maximum and the count-rate a minimum. At any other higher or lower velocities, the resonance will decrease until it is zero at velocities well away from that defines the maximum resonance. [11]

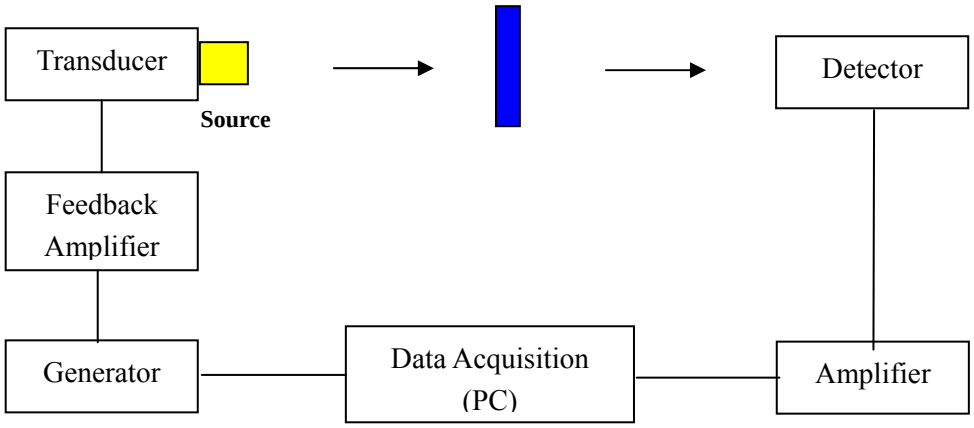

Figure 2.5 The schematic diagram of a typical Mössbauer spectrometer

Fig 2.5 shows the basic setup of a typical Mössbauer system [11] An electromechanical transducer is oscillate the Mössbauer source to generate a particular relative velocity between the source and absorber (specimen). At such a particular Doppler velocity, the γ–ray energy from the source can match precisely the nuclear energy gap and thus the resonance absorption can be at a maximum. A detector can then measure the

γ-rays transmitted from the absorber. The microprocessor system with the amplifiers and a single-channel analyzer accumulates the counts corresponding to the velocity of the source with respect to the absorber. Therefore, a Mössbauer spectrum is a plot of transmission versus a series of Doppler velocity between the source and absorber (i.e. versus the effective γ-ray energy).

In this work, a FAST Mössbauer system (FAST ComTec GmbH, Grnwadlder Weg28 A, 82041 Oberhaching, Germany) was used. The powders were mixed with vacuum grease and fixed on transparent slits. The calibration was performed using a foil of α-Fe at room temperature. The measured spectra were analyzed using RECOIL software. Some constraints were used in the fitting procedures.

2.4 Transmission Electron Microscopy (TEM)

Transmission electron microscopy (TEM) is one of most effective tools for material characterization. A TEM utilizes both the wave and particle natures (as-theorized by Louis-Victor de Broglie) of the electrons for the purposes of various imaging and diffraction analysis of materials. TEM analysis can provide various information regarding morphological, phase and crystallographic information of materials. The configuration of a modern TEM is complicated. Basically, a TEM system mainly includes an electron source (electron gun), the illumination system (condenser lenses and condenser mini-lenses) and the imaging system (objective lens, intermediate lenses and projector lenses). The main imaging and diffraction techniques in TEM analysis can be summarized as the following:[12]

(a) Bright field imaging:

A bright field image is formed using the center electron beam transmitted through the specimen. Regions of the specimen that are thicker or with larger atomic number or generating strong diffractions will scatter electrons more strongly and will appear darker in the image. Therefore, the contrast in bright-field images is mainly so-called the mass-thickness contrast and the diffraction contrast. It is suitable for the analysis of all specimens (amorphous or crystalline, biological or metallic), provided the specimen is thin enough.

(b) Dark field imaging:

A dark field image is formed by selecting scattered electron beam of any form with the field-limiting aperture inserted into the back focal plane of the objective lens. To obtain a dark field imaging with better resolution, the primary electron beam is tilted so that the chosen diffracted beam travels along the optical axis and pass through the centered aperture. The contrast in dark-field imaging is mainly the diffraction contrast. This imaging technique can provide useful crystallographic information of the specimen. (For example, the defects in crystals due to local distortion around the defect which changes the scattering conditions around the defects.) For polycrystalline materials, due to the difference in the crystallographic orientation between the neighboring grains, the electron scattering conditions will be different between the neighboring grains. In other words, the satisfaction with the Bragg conditions for the neighboring grains is different, which leads to the difference in the intensity of the electron scattering. Therefore, the neighboring grains will appear different contrast under dark-field imaging. In this sense, dark field imaging technique can be used for

analyzing grain size and size distribution.

In this thesis work, dark-field imaging technique has been widely used to estimate the average grain size and size distribution. Generally, 200 grains will be counted and the average grain size is obtained by averaging out all the measured grain size.

(c) High-resolution imaging:

High-resolution TEM (HRTEM) imaging is also known as phase contrast imaging as the images are formed due to differences in phase of electron waves scattered through a thin specimen. Therefore, the contrast formation in HRTEM imaging is due to the Bragg scattering of the electron waves which introduces the phase difference between the scattered and transmitted electron waves. The successes of many structural studies have established that HRTEM has a valuable role in determining atomic configurations in complex materials, especially at structural irregularities or defects.

(d) Selected-area diffraction:

When a electron beam passes through a specimen, the transmitted electron beam and the scattered electron beams can be focused on the back focal plane of objective lens. By inserting a field-limiting aperture into the image plane of the objective lens, a certain selected area of the specimen is covered by the aperture and thus only the diffraction patterns from the selected area will be recorded. This allows the diffraction analysis of the selected micro-region of a crystalline structure.

(e) Nanobeam diffraction:

The nanobeam diffraction is also called as convergent-beam diffraction. Through changing the excitation strength of the condenser lens system and selecting the condenser lens aperture size, a convergent electron beam with small convergent angle

can be formed for the illumination of micro-area of a specimen. Therefore, a diffraction pattern can be obtained from the small illuminated area. Such diffraction technique can extract the crystallographic information from the nanoszied area of a specimen and thus is very useful for the phase and microstructure analysis of micro or nanosized regions which can not be realized by the conventional selected area diffraction analysis. In this thesis project, a JEOL JEM 3010 TEM will be used for the phase, microstructure analysis by various imaging and diffraction techniques.

2.5 References

[1] B. E. Warren, *X-ray diffraction* (Addison-Wesley Publishing Company, Massachusetts, 1968).

[2] B. D. Cullity and S. R. Stock, *Elements of x-ray diffraction* (Prentice Hall, NJ, 2002).

[3] D. Jiles, *Introduction to magnetism and magnetic materials* (Chapman and Hall, London, UK, 1994).

[4] *The operation manual of vibration sample magnetometer,* (Oxford Instrument, England, 1997).

[5] K. Kanga, J. S. Jiang, and S. D. Bader, J. Appl. Phys. **98**, 113906 (2005).

[6] S. Uren MW, K. O'Grady, and R. W. Chantrell, IEEE Transactions on Magnetics **24,** 1808 (1998).

[7] A. Lyberatos and R. W. Chantrell, J. Phys.: Condens. Matter **9,** 2623 (1997).

[8] D. C. Crew, S. H. Farrant, P. G. McCormick, and R. Street, Journal of Magnetism and Magnetic Materials **163,** 299 (1996).

[9] L. H. Brown, E. D. Grave, and R. E. Vandenberghe, *Mossbauer Spectroscopy Applied to Magnetism and Materials Science* (Plenum Press, New York, USA, 1993).

[10] T. E. Granshaw, *Mössbauer spectroscopy and its application,* (Cambridge University Press, New York, USA, 1985).

[11] N. N. Greenwood and T. C. Gibb, *Mössbauer Spectroscopy* (Chapman & Hall, London, UK, 1971).

[12] David B. Williams and C.B. Carter, *Transmission electron microscopy: a textbook for materials science* (Plenum Press, New York and London, 2000).

CHAPTER 3

Synthesis of Cobalt Ferrite Powdered Materials

3.1 Background

As important hard magnetic materials, cobalt ferrite ($CoFe_2O_4$) powdered materials have a wide range of applications. For some practical applications such as data storage, it is essential that $CoFe_2O_4$ materials should possess high coercivities and reasonable magnetization. For a random assembly of magnetic particles, the coercivity depends crucially on particle size and size distribution. This has been verified both theoretically and experimentally.[1-4] The size effects on coercivity are associated with the physics of magnetic domain structure and the reversal magnetization processes. For any magnetic material there exists a single-domain critical size, d_{sd}. There also exists a characteristic size of the particle, d_{sp}, below which the material becomes superparamagnetic, i.e. no hysteresis, zero coercivity and zero remanence. Therefore, the highest coercivity usually appears in a particle assembly with the particle size (d) falling in the range of $d_{sp} < d < d_{sd}$. For $CoFe_2O_4$ materials, the critical single-domain size was found to be around 40-70nm.[5-7] This was also verified by our work on $CoFe_2O_4$ thin-film materials. In recent years, our group has devoted great efforts to the coercivity enhancement in $CoFe_2O_4$ materials, and high coercivities up to 12.5 kOe were achieved in $CoFe_2O_4$ thin-film materials.[8,9] Such high coercivities were found to be closely related to the nanocrystalline structure of the thin films with average grain size of around the single domain size. [8,9] Therefore, in order to get high-coercivity $CoFe_2O_4$ powdered materials, it is important to get a nanocrystalline structure with average grain size close to the single-domain size.

For an assembly of the $CoFe_2O_4$ nanograins, the agglomeration of the nanograins to form large particles is inevitable. The level of the agglomeration may suggest two major types of nanostructured $CoFe_2O_4$ powdered materials. One consists of the relatively well separated nanosized $CoFe_2O_4$ particles with each particle having

single-crystalline structure, and the other is assembly large-sized (in micrometer/submicrometer size range) $CoFe_2O_4$ particles/agglomerates which consist of nanosized grains. The magnetic properties of these two types of $CoFe_2O_4$ particulate systems could be different. Therefore, in order to study the size effects on coercivity in these two particulate systems, two different synthesis routines will be employed in this work in order to synthesize $CoFe_2O_4$ nanocrystalline powders, i.e. co-precipitation and mechanochemical processes.

As a classical aqueous solution routine, co-precipitation possesses the advantage of easy experimental setup and has been widely used for synthesizing various magnetic nanoparticles including $CoFe_2O_4$ nanoparticles.[7,10-12] However, the $CoFe_2O_4$ nanoparticles prepared by the conventional co-precipitation process at room temperature are usually very small with a coercivity usually less than 1kOe.[11,12] The low coercivity could be attributed to the poor crystallinity of particles and small particle/grain size.[7] In contrast to the conventional room-temperature co-precipitation process, the modified co-precipitation process is performed at boiling temperature of aqueous solutions, namely at around 100^oC. It has been reported that, at an elevated temperatures, large-sized nanoparticles with high crystallinity can be obtained by such modified co-precipitation process.[6,7,20] Therefore, the modified co-precipitation process was employed to synthesis well-crystallized $CoFe_2O_4$ nanoparticles in this study.

As is well known, mechanochemical process is an unique technique with easy experimental setup and has been widely employed for the mass synthesis of various powdered materials.[21-26] The solid-state reaction process induced by mechanical milling represents an important class of solid state reactions. On the one hand, mechanical milling-derived materials could be refined to the nanometer size

range;[21,23] on the other hand, high-energy mechanical milling could always modify the reaction conditions by mechanical activation effects. Thus solid-state chemical reactions can be induced even for the systems with positive free energies.[27,28] In this work, mechanochemical process was chosen for the synthesis of the $CoFe_2O_4$ powders. By using mechanochemical process, we wish to explore the possibility of synthesizing nanocrystalline $CoFe_2O_4$ powders with a relatively high coercivity and productivity by using the commercially available α-Fe_2O_3 and Co raw powdered materials. The post annealing of the mechanochemically derived $CoFe_2O_4$ powders will also be performed in order to form well-crystallized nanostructures. In order to study the effects of annealing on cation distribution, the post annealing with slow cooling and quenching processes have been conducted.

3.2 Purposes of study

The objectives of the research work in this chapter are given as the followings:

A. Synthesis of $CoFe_2O_4$ nanoparticles by the modified co-precipitation process

1. To explore the feasibility of synthesizing the well-crystallized $CoFe_2O_4$ nanoparticles with high coercivities by the modified co-precipitation process;
2. To investigate the effects of the processing parameters on the phase and microstructure of the resultant $CoFe_2O_4$ nanoparticles;
3. Based on the detailed analysis of phase, microstructure and cation distribution of $CoFe_2O_4$ nanoparticles;
4. To investigate the effects of the grain size on magnetic properties of the samples, especially the coercivity;
5. To optimize the processing parameters in order to control the grain size and achieve high magnetic coercivity of the resultant $CoFe_2O_4$ nanoparticles.

B. Synthesis of nanocrystalline $CoFe_2O_4$ powders by the mechanochemical process

1. To explore the feasibility of mechanochemically synthesizing nanocrystalline $CoFe_2O_4$ powdered materials with a relatively high coercivity and high productivity by using the commercially available Co and α-Fe_2O_3 precursors;
2. To investigate the phase evolution during the mechanochemical process and its effects on the magnetic properties of as-synthesized materials;
3. To study the effects of the average grain size, site occupation on the magnetic properties of the resultant $CoFe_2O_4$ powdered materials.

3.3 Synthesis of $CoFe_2O_4$ nanoparticles by modified co-precipitation process

3.3.1 Experimental procedures

Two aqueous solutions were first prepared. One is 1M NaOH by dissolving 40g NaOH (Fluka, 99%) in deionized water to form 1000 ml solution. The other is the aqueous solution containing Co^{2+} and Fe^{3+} by dissolving $Co(NO_3)_2$ $6H_2O$ (Fluka, 99%) and $Fe(NO_3)_2$ $9H_2O$ (Fluka, 99%) in deionized water with the molar ratio of Co^{2+} to Fe^{3+} equal to 1:2. Typically, 0.291g $Co(NO_3)_2$ $6H_2O$ and 0.80774 g $Fe(NO_3)_3$ $9H_2O$ were dissolved in 10ml deionized water to form the 0.3M solution. The resultant Co^{2+}/Fe^{3+} solution was added into a boiling 100 ml 1 M NaOH solution under vigorous stirring. During this stage, the ferrite formation was witnessed by the progressive color conversion of precipitates from the brownish initially into black finally. After the dropping of Co^{2+}/Fe^{3+} solution was finished, the suspension solution was further boiled for 2 hours in order to permit the dehydration and atomic

rearrangement involved in the conversion of the intermediate hydroxide phase into the spinel phase. [6,7,20]

In order to achieve high coercivity, it is necessary to obtain $CoFe_2O_4$ nanoparticles with the size near the critical single-domain size (40~70nm),[5-7] as mentioned above. For co-precipitation process, it is well known that the particle size is closely related to the relative interdependence between the nucleation and growth stages, which is strongly affected by the solution chemistry and the precipitation conditions.[20] Under this premise, the effects of [Me]/[OH] ratio, the molar ratio of metal ions (Me refer to Co^{2+} and Fe^{3+}) to OH^- ions in the solution, and the feeding rate of metal ions were studied.

3.3.2 Results and Discussion

3.3.2.1 Effects of [Me]/[OH] ratio, the molar ratio of metal ions (Co^{2+}+Fe^{3+}) to OH^-

A. Magnetic properties

Fig.3.1 (a) and (b) show the hysteresis loops of the powders synthesized by the co-precipitation process at 100°C with different [Me]/[OH] ratio. The feeding rate was fixed at 0.0017mol/min for each experiment. With the high [Me]/[OH] ratio of 0.375, the powder showed paramagnetic-like magnetization behavior with a very low magnetization (9.3 emu/g) and zero coercivity at room temperature, as seen in Fig.3.1 (a) and (b). With decreasing [Me]/[OH] ratio, both the magnetization (M_S) and coercivity (H_C) increased, as indicated in Fig.3.2. After the [Me]/[OH] ratio reached around 0.045, both magnetization and coercivity remained nearly unchanged even with the further decrease in [Me]/[OH] ratios. The maximum coercivity H_C was found in the range of 500~600Oe and the maximum magnetization M_S was around 50 emu/g.

In order to understand the effects of [Me]/[OH] ratio on the magnetic properties of as-synthesized powders, detailed phase and microstructure studies were conducted, i.e. X-ray diffraction (XRD), Mössbauer and transmission electron microscopy (TEM) analysis.

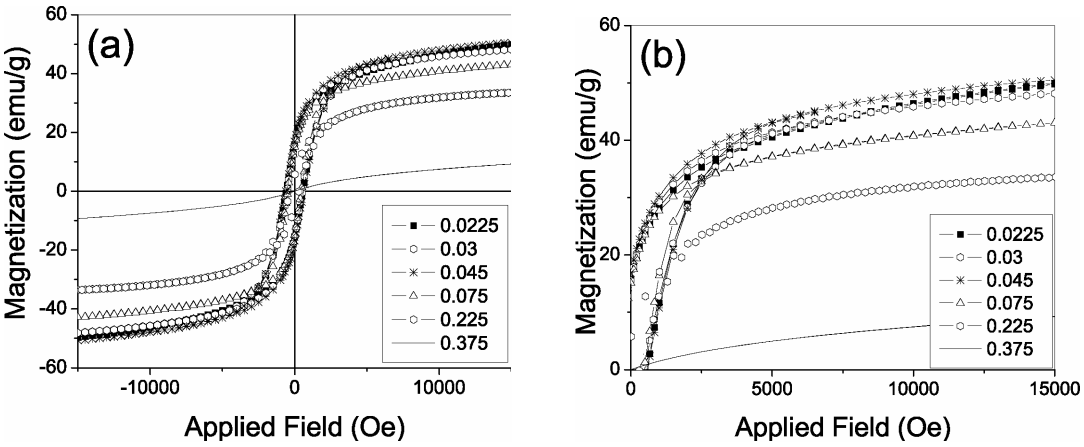

Figure 3.1 The hysteresis loops of $CoFe_2O_4$ powders synthesized by the co-precipitation at 100°C with different [Me]/[OH] ratios ((a) the overall loops and (b) the loops in the second quadrant) (Synthesis was conducted at 100°C and feeding rate was fixed at 0.0017mol/min for each experiment)

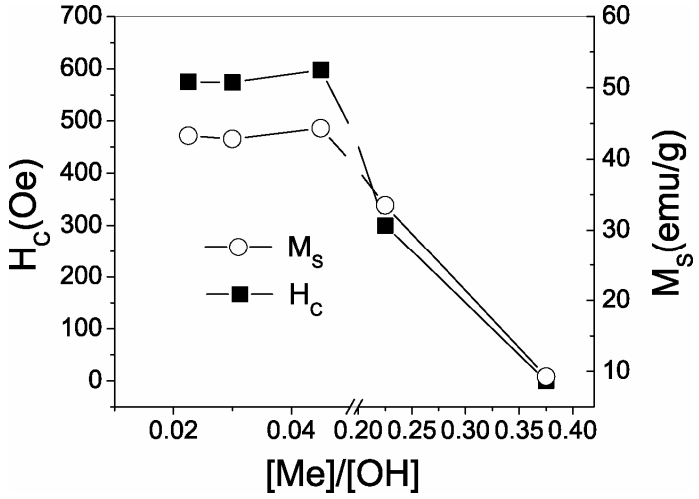

Figure 3.2 The effects of [Me]/[OH] ratio on the magnetic properties (H_C-coercivity; M_S-magnetization at 15kOe) of $CoFe_2O_4$ powders synthesized by the co-precipitation at 100°C (Synthesis was conducted at 100°C and feeding rate was fixed at 0.0017mol/min for each experiment)

B. XRD analysis

Fig.3.3 shows the XRD spectra of the $CoFe_2O_4$ powders as-synthesized at different [Me]/[OH] ratios. As seem from Fig.3.3 (a), when [Me]/[OH] ratio is 0.375 (the highest ratio in this work), the as-obtained powder was amorphous-like as no apparent diffraction peaks could be identified. With [Me]/[OH] ratio decreased to 0.225 and below, the characteristic diffraction peaks of $CoFe_2O_4$ spinel phase can be well resolved, as shown in Fig.3.3 (b)~(f). It indicates that the formation of $CoFe_2O_4$ crystalline phase is favorable at lower [Me]/[OH] ratios. Based on the Scherrer formula, the average grain size was estimated from the (311) diffraction peak and plotted in Fig. 3.4.

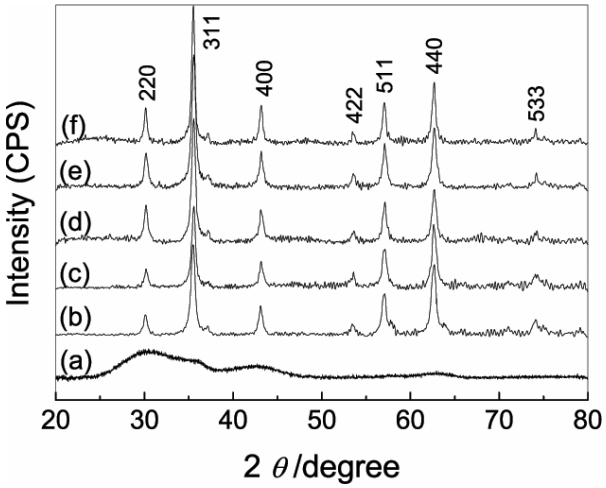

Figure 3.3 The XRD patterns of $CoFe_2O_4$ powders synthesized by the co-precipitation at 100°C with different [Me]/[OH] ratios of (a) 0.375; (b) 0.225; (c) 0.075; (d) 0.045; (e) 0.03; (f) 0.0225 (the feeding rate was fixed at 0.0017mol/min for each experiment)

For the sample synthesized with the [Me]/[OH] ratio of 0.375, it was impossible to deduce the average grain size based on the XRD analysis because no appreciable diffraction peaks could be resolved. As shown in Fig.3.4, the average grain size of the $CoFe_2O_4$ powder increased with decreasing [Me]/[OH] ratios. However, when [Me]/[OH] ratio was lower than 0.045, the further decrease in [Me]/[OH] ratio did not lead to an apparent increase in average grain size as indicated by Fig.3.4. The average

grain size remained nearly unchanged (18~19 nm) when [Me]/[OH] ratio decreased from 0.045 to 0.0225.

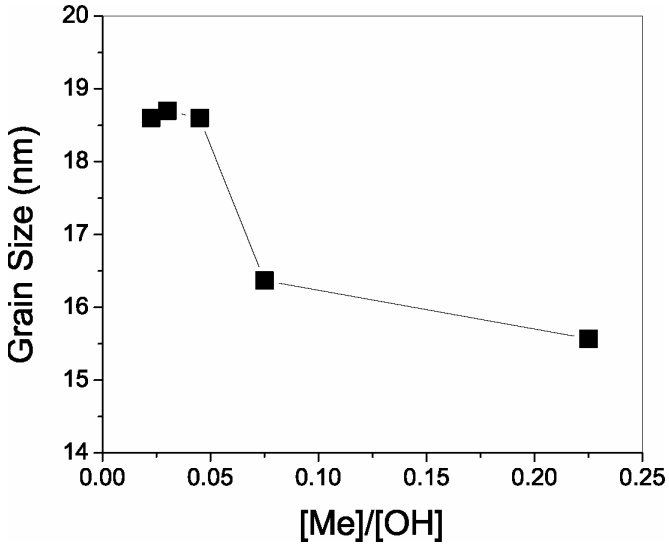

Figure 3.4 The average grain size of $CoFe_2O_4$ powders synthesized by the co-precipitation at 100°C with different [Me]/[OH] ratios (estimated from XRD analysis) (feeding rate was fixed at 0.0017mol/min for each experiment)

C. Mössbauer analysis

To investigate the phase and the site occupation of magnetic ions of the resultant powders, three typical samples were selected for the Mössbauer analysis, i.e. samples synthesized with [Me]/[OH] ratios of 0.375 (high), 0.225 (medium) and 0.045 (low).

Figure 3.5 shows the room-temperature (300K) Mössbauer spectra of these three samples. The fitted parameters are listed in Table 3.1. As shown in Figure 3.5 (a), only a doublet was observed for the sample synthesized with a [Me]/[OH] ratio of 0.375. It indicates the paramagnetic and/or superparamagnetic nature of the sample at the room temperature. For the samples synthesized with lower [Me]/[OH] ratios of 0.225 and 0.045, the room-temperature magnetic splitting appeared, as shown in Figure 3.5 (b) and (c). For both samples, the sextets were overlapped with a doublet, suggesting the presence of paramagnetism and/or superparamagnetism in these two

samples. In addition, the weight percentage of the doublet decreased with decreasing [Me]/[OH] ratios, indicating the decrease in the percentage of the paramagnetic and/or superparamagnetic phases.

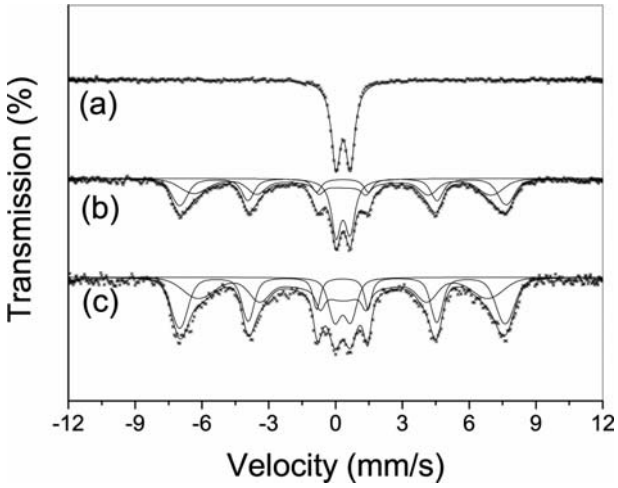

Figure 3.5 The room-temperature Mössbauer spectra of the $CoFe_2O_4$ samples prepared by co-precipitation at 100°C with [Me]/[OH] ratios of (a) 0.375, (b) 0.225 and (c) 0.045. (the feeding rate was fixed at 0.0017mol/min)

Table 3.1 The room-temperature Mössbauer parameters of the $CoFe_2O_4$ samples prepared by co-precipitation at 100°C with different [Me]/[OH] ratios (δ-isomer shift; Δ -quadrupole splitting; P-weight percentage of subspectrum; H-hyperfine field)

[Me]/ [OH]	Paramagnetic Fe^{3+}			Ferrimagnetic Fe^{3+} - A site				Ferrimagnetic Fe^{3+} - B site			
	δ (mm/s)	Δ (mm/s)	P (%)	δ (mm/s)	Δ (mm/s)	H (T)	P (%)	δ (mm/s)	Δ (mm/s)	H (T)	P (%)
0.375	0.3397	0.651	100	-	-	-	-	-	-	-	-
0.225	0.3366	0.63	23.61	0.3009	0.0089	45.46	35.08	0.365	0.041	33.18	41.31
0..045	0.3183	0.711	13.13	0.3060	-0.0007	45.35	40.92	0.341	-0.010	30.62	45.95

In order to elucidate the nature of phases and site occupation of magnetic ions in these three samples, Mössbauer analysis was performed at 80K. The spectra recorded at 80K are shown in Figure 3.6 and the fitted parameters are listed in Table 3.2. As seen from Figure 3.6 (a), for the sample synthesized with [Me]/[OH]=0.375, no doublet but only sextets were observed at 80K. Therefore, the doublet in the room-temperature

spectrum can be ascribed to the superparamagnetic relaxation due to the rather small grain size. The sextets were well fitted with two sub-spectra with effective hyperfine fields of H=49.44T and H=37.01 T, corresponding to Fe^{3+} ions in A (tetrahedral) and B (octahedral) sites respectively, as shown in Table 3.2. The broadened sub-spectra and the reduced hyperfine field of B sites can be ascribed to the finite size effects of nanoparticles, such as surface disorder.[29-32] The isomer shifts (δ) of A and B sites were 0.382 mm/s and 0.437 mm/s respectively, well consistent with those of the bulk $CoFe_2O_4$ materials.[33]

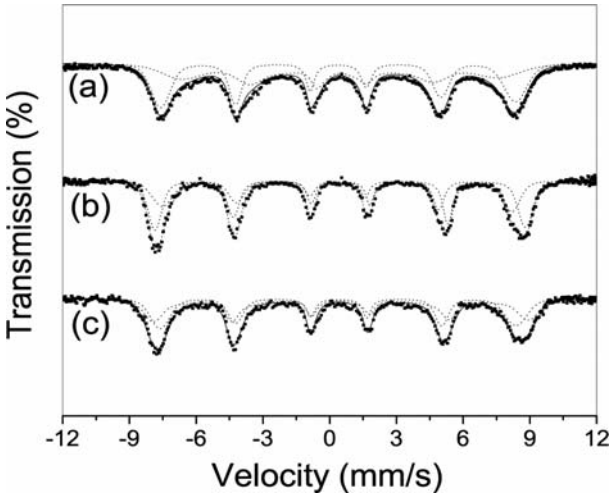

Figure 3.6 The 80K Mössbauer spectra of the $CoFe_2O_4$ samples prepared by co-precipitation at 100°C with [Me]/[OH] ratios of (a) 0.375, (b) 0.225 and (c) 0.045. (Synthesis was conducted at 100°C and the feeding rate was fixed at 0.0017mol/min)

Table 3.2 The 80K Mössbauer parameters of the $CoFe_2O_4$ samples prepared by co-precipitation at 100°C with different [Me]/[OH] ratios (δ-isomer shift; Δ -quadrupole splitting; P-weight percentage of subspectrum; H-hyperfine field; α_A/α_B- absorption area ratio)

[Me]/ [OH]	**A site**				**B site**				**α_A/α_B**
	δ (mm/s)	*Δ (mm/s)*	*H (T)*	*P (%)*	*δ (mm/s)*	*Δ (mm/s)*	*H (T)*	*P (%)*	
0.375	0.382	-0.003	49.441	35.05	0.437	-0.003	37.012	64.95	0.539
0.225	0.384	-0.009	49.695	48.24	0.482	-0.008	48.634	51.76	0.932
0.045	0.390	-0.001	49.61	48.40	0.450	0.001	47.972	51.60	0.938

All these results further confirmed that the sample synthesized with [Me]/[OH]=0.375 had the spinel $CoFe_2O_4$ phase. For the samples synthesized with lower [Me]/[OH] ratios (0.225 and 0.045), the as-fitted Mössbauer parameters (isomer shift and hyperfine field) were quite close to those of the bulk $CoFe_2O_4$ materials.[33] The disappearance of the doublets at 80K also suggested that the doublets at room-temperature were due to the presence of superparamagnetic $CoFe_2O_4$ small grains. In this sense, the decrease in the weight percentages of the doublets with decreasing [Me]/[OH] ratios at room temperature may indicate less amount of superparamagnetic small grains at lower [Me]/[OH] ratios.

Based on the Mössbauer analysis, α_A/α_B, the absorption area ratio of A sites to B sites was determined for these three samples, as shown in Table 3.2. Assuming the recoilless fractions of A and B sites are same, the α_A/α_B ratio is proportional to the ratio of Fe^{3+} ions in A sites to those in B sites. Therefore, from these α_A/α_B ratios, the cation distribution of the magnetic ions can be derived for these samples. For the sample synthesized with [Me]/[OH]=0.375, the corresponding formula can be expressed as $(Co_{0.2987}Fe_{0.7013})_A\{Co_{0.7013}Fe_{1.2987}\}_BO_4$. For the sample synthesized with [Me]/[OH]=0.225 and 0.045, the inversed structures like $(Fe)_A\{CoFe\}_BO_4$ were obtained. Obviously, the $CoFe_2O_4$ sample with small grain size has a partially inversed spinel structure, while the samples with relatively large grain size possess the inversed structure.

D. TEM analysis

In order to study the morphologies of as-synthesized nanoparticles, three $CoFe_2O_4$ samples were selected for the detailed TEM analysis, i.e. the samples synthesized at the different [Me]/[OH] ratios (0.375 (high), 0.225 (medium) and 0.045 (low)). These three samples are the same as those for Mössbauer analysis.

Fig.3.7 (a) and (b) show respectively the bright-field and dark-field TEM images of the $CoFe_2O_4$ nanoparticles synthesized at [Me]/[OH]=0.375. It is clear that the sample possessed very small particle/grain size, which was evidenced by the diffusive diffraction rings in the selected-area electron diffraction inserted in Fig. 3.7(a). This is consistent with the XRD analysis (Fig. 3.3(a)), which showed no apparent diffraction peaks. The phase was further checked by nanobeam electron diffraction. As seen from Fig. 3.7 (c), all the diffraction spots and diffraction rings can be assigned to the spinel $CoFe_2O_4$ phase. The result is consistent with that of Mössbauer analysis. The $CoFe_2O_4$ phase was also confirmed by high-resolution TEM analysis. As shown in Fig. 3.7 (d), one nanograin was clearly identified as $CoFe_2O_4$ phase with <111> zone-axis. In addition, the high-resolution TEM analysis revealed that the sample consisted of cluster-level-sized nanoparticles, and the majority of the nanoparticles were smaller than 2nm. Such small particle/grain size can well explain the superparamagnetic behavior of the sample at room-temperature as shown in Fig.3.1.

With the reduction of [Me]/[OH] ratio to 0.225, the sample possessed apparently a larger particle size than the sample synthesized at [Me]/[OH]=0.375, as evidenced by both bright-field (Fig. 3.8 (a)) and dark-field (Fig. 3.8 (b)) TEM images. The selected-area electron diffraction in Fig.3.8 (c) indicated the formation of well-crystallized $CoFe_2O_4$ spinel phase. Based on the dark-field TEM analysis, the average gain size of this sample was estimated to be 13nm and shown in Fig.3.8 (d), which was close to that estimated from the XRD analysis.

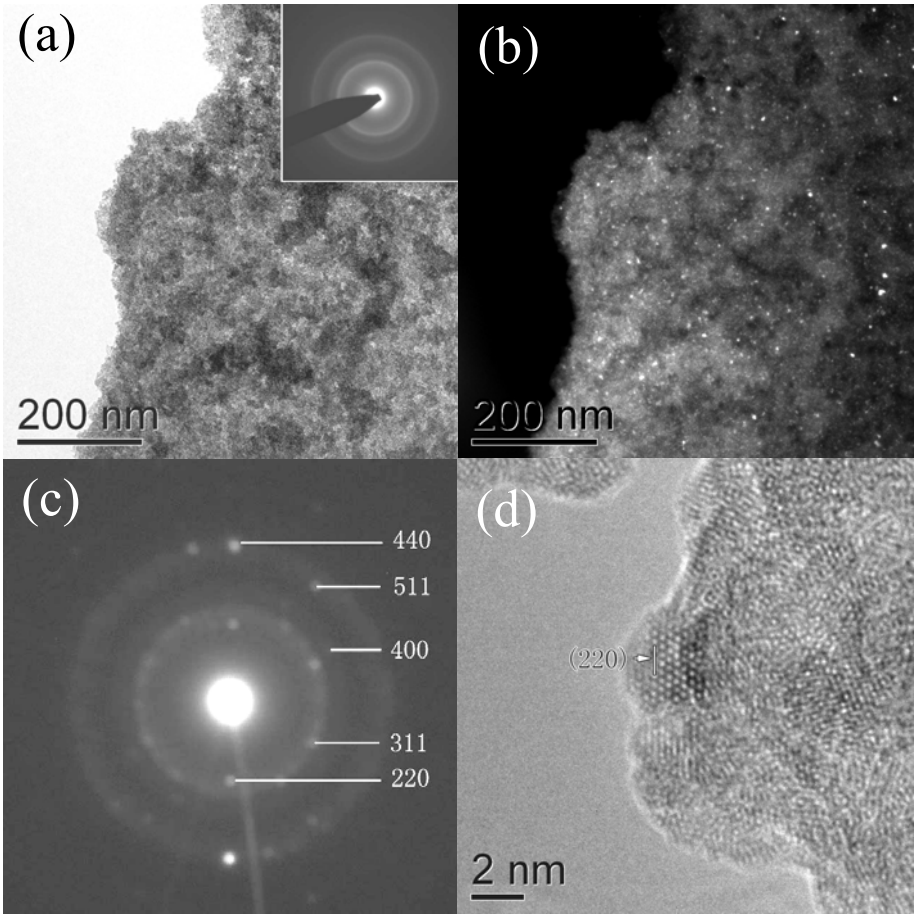

Figure 3.7 (a) Bright-field TEM image, (b) dark-field TEM image and (c) nanobeam diffraction pattern as well as (d) high-resolution TEM image of the sample prepared by co-precipitation at 100°C with [Me]/[OH] ratio of 0.375 (feeding rate was fixed at 0.0017mol/min for each experiment)

For the samples synthesized at [Me]/[OH]=0.045, besides the small nanoparticles, many $CoFe_2O_4$ nanoparticles larger than 30nm were observed under TEM, as shown in Fig.3.9 (a) and (b). The formation of these large-sized nanoparticles directly led to the increase in average grain size, consistent with the results of XRD analysis shown in Fig.3.4. The as-synthesized $CoFe_2O_4$ nanoparticles had a broad grain size distribution, as shown in Fig.3.9 (d) which was derived from the dark-field TEM analysis. Therefore, the sample had a higher magnetization and coercivity, when compared with those samples synthesized at higher [Me]/[OH] ratios.

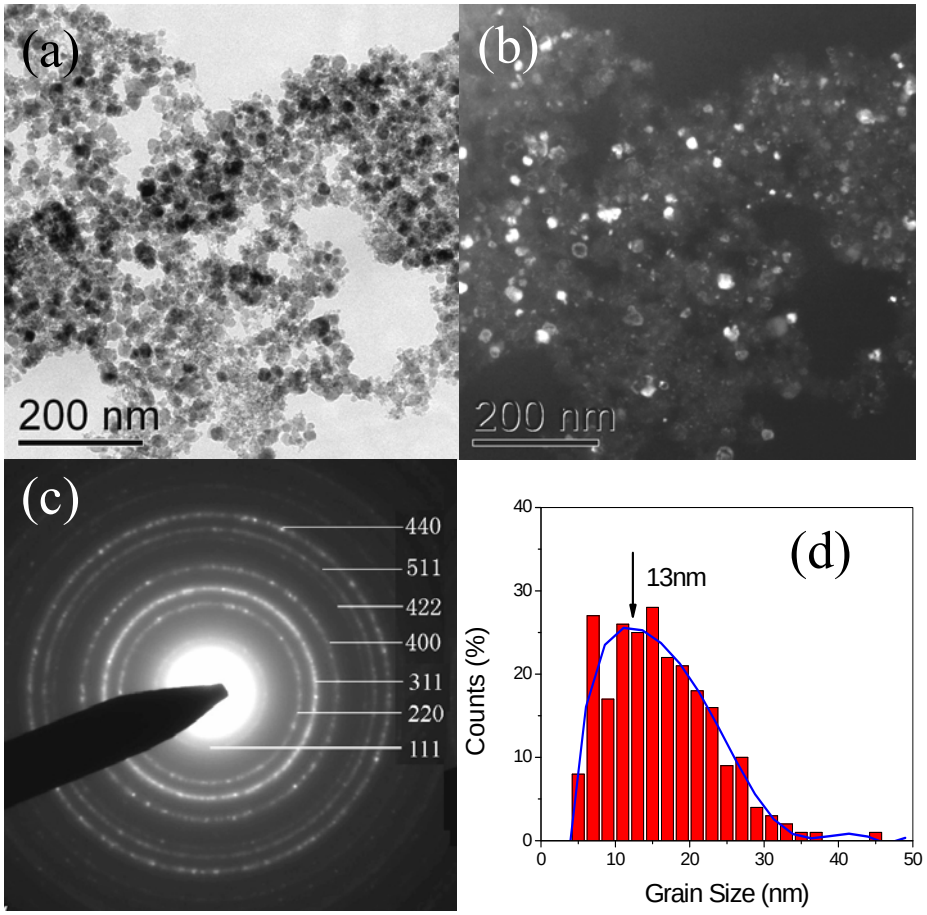

Figure3.8 (a) Bright-field TEM image, (b) dark-field TEM image, (c) selected-area electron diffraction, and (d) grain size distribution (estimated from dark-field TEM analysis) of $CoFe_2O_4$ powders prepared by co-precipitation at 100°C with [Me]/[OH] ratio of 0.225 (the feeding rate was fixed at 0.0017mol/min)

In summary, above experimental results clearly indicate that [Me]/[OH] ratio plays an important role in the particle/grain size and thus in magnetic properties of $CoFe_2O_4$ nanoparticles. A low [Me]/[OH] ratio was favorable for the formation of large-sized $CoFe_2O_4$ nanoparticles. Different [Me]/[OH] ratios resulted in different average gain size and the site occupation of magnetic ions. The very low magnetization and zero coercivity of the sample obtained with the highest [Me]/[OH] ratio (0.375) should be ascribed to its superparamagnetic behavior at the room temperature due to the small grain size. With decrease in [Me]/[OH] ratio, the average grain size of the $CoFe_2O_4$ samples increased, which could account for the increase in magnetization at the room temperature. It is well known, magnetic coercivity is strongly dependent on the

microstructure. Thus the effect of both average grain size and cation distribution should be considered. According to the Mössbauer analysis as mentioned above, the $CoFe_2O_4$ samples synthesized with [Me]/[OH] ratio equal to 0.225 and 0.045 had similar cation distribution,. Therefore, grain size effects should account for the difference in coercivity of these two samples, as shown in Figure 3.2.

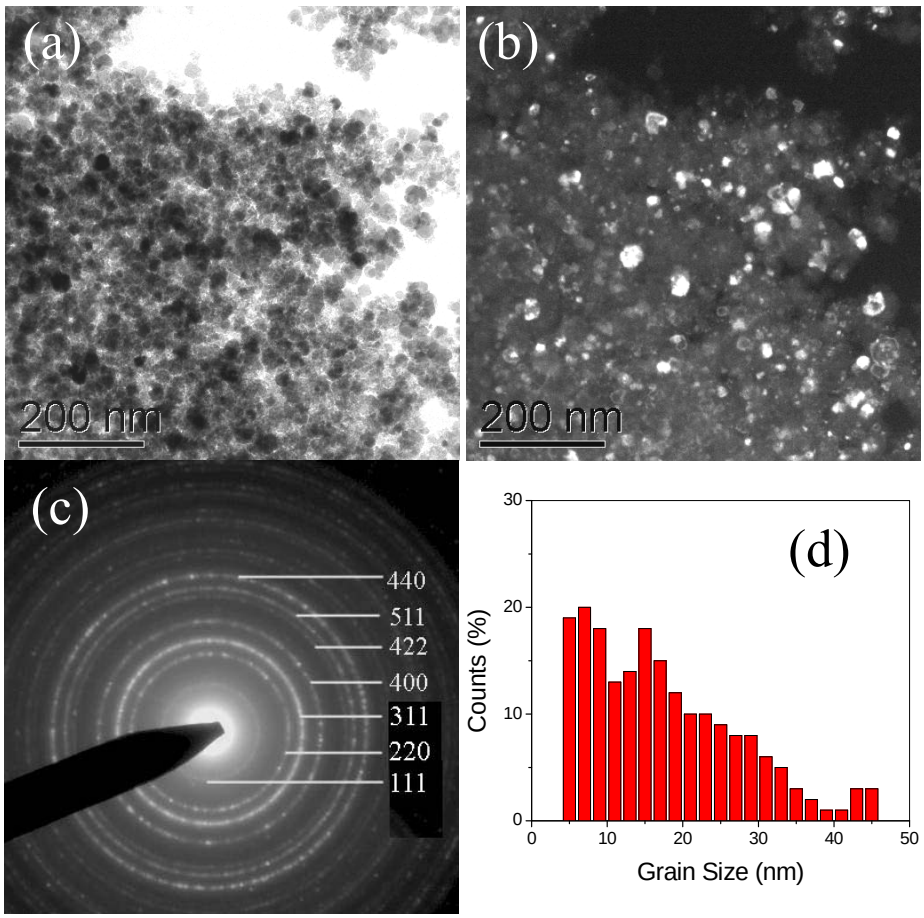

Figure 3.9 (a) Bright-field TEM image, (b) dark-field TEM image, (c) selected-area electron diffraction as well as (d) grain size distribution (estimated from dark-field TEM analysis) of $CoFe_2O_4$ powders prepared by co-precipitation at 100°C with [Me]/[OH] ratio of 0.045 (Synthesis was conducted at 100°C and the feeding rate was fixed at 0.0017mol/min)

3.3.2.2 The effects of the feeding rate of metal ions

A. Magnetic properties

To study the effect of the feeding rate of metal ions, the final [Me]/[OH] ratio was 0.045 for all co-precipitation experiments. The feeding rate was adjusted by either fast injection (around. 0.18 mol/min) or dropwise adding of metal ion solution into 1M NaOH solution at 100°C. Fig.3.10 shows the dependence of coercivity (H_C) and saturation magnetization (M_S) of the samples on the feeding rate of metal ions. In case of the fast injection (around. 0.18 mol/min), the obtained sample had a low M_S (around 38 emu/g) and low H_C (around 300 Oe). With decreasing feeding rate, both Ms and H_C increased. A maximum coercivity of 1510 Oe was obtained with the feeding rate of 1.875×10^{-4} mol/min. The further decrease in feeding rate didn't lead to apparent changes in both coercivity and the saturation magnetization as shown in Fig. 3.10. Fig.3.11 shows the room-temperature hysteresis loops of the samples synthesized with different feeding rates of metal ions.

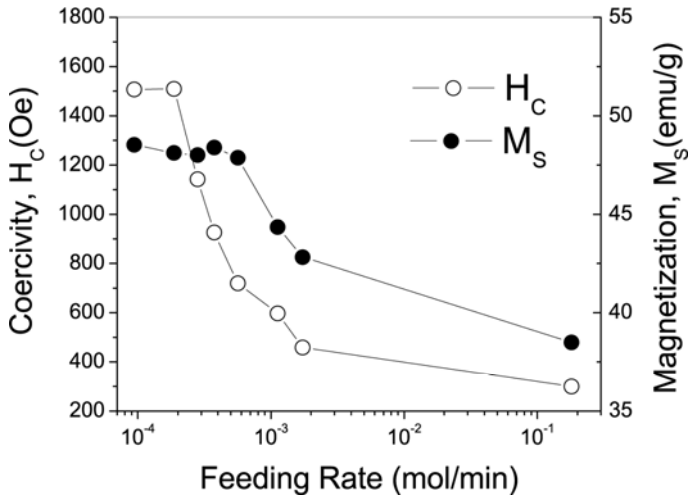

Figure 3.10 The effects of feeding rates of metal ions on the magnetic properties of $CoFe_2O_4$ powders synthesized by the co-precipitation at 100°C (Synthesis was conducted at 100°C and the final [Me]/[OH] ratio was 0.045)

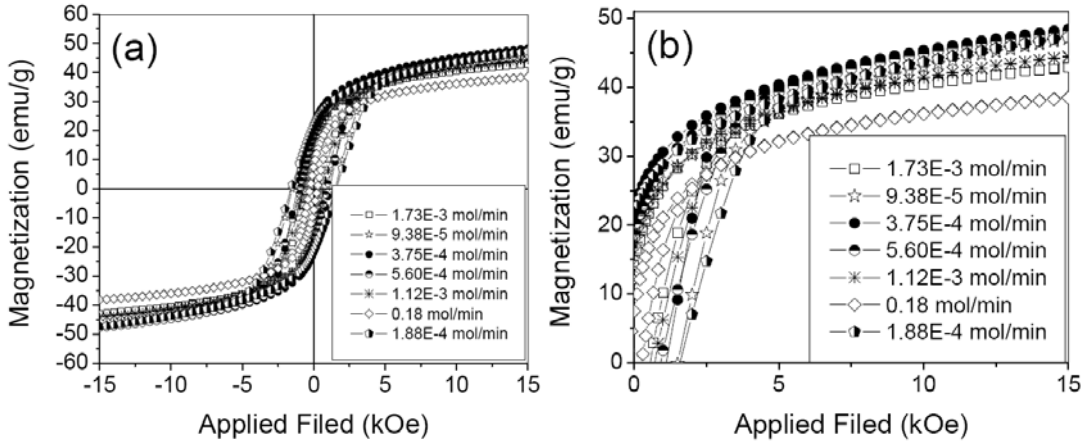

Figure 3.11 The hystersis loops of $CoFe_2O_4$ powders synthesized by the co-precipitation at 100°C with different feeding rates of metal ions (the final [Me]/[OH] ratio was 0.045)((a) the overall loops and (b) the loops in the second quadrant of (a))

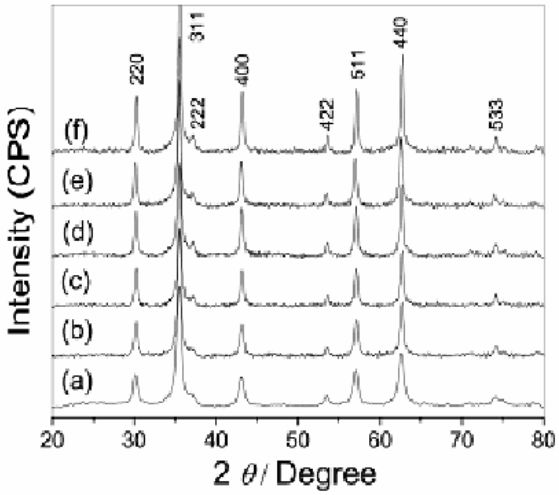

Figure 3.12 The XRD spectra of $CoFe_2O_4$ powders synthesized by the co-precipitation at 100°C with the feeding rates of ((a) fast injection(0.18 mol/min); (b) 1.73 $x10^{-3}$ mol/min; (c) 5.62$x10^{-4}$ mol/min; (d) 2.81$x10^{-4}$ mol/min; (e) 1.88$x10^{-4}$ mol/min; (f) 9.38$x10^{-5}$ mol/min) (the final [Me]/[OH] ratio was 0.045)

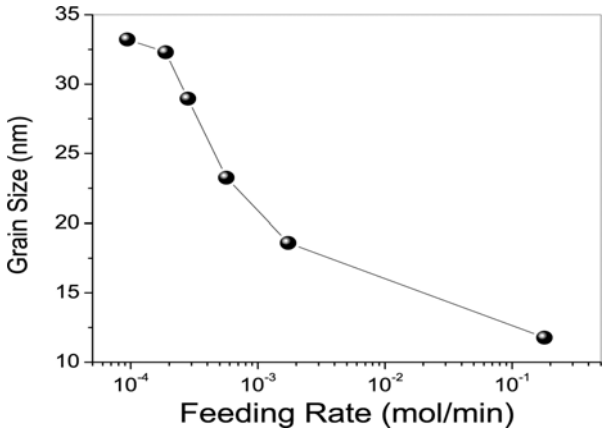

Figure 3.13 The effects of feeding rates on the average grain size (estimated from XRD analysis) of $CoFe_2O_4$ powders synthesized by the co-precipitation at 100°C (Synthesis was conducted at 100°C and the [Me]/[OH] ratio was 0.045)

B. XRD analysis

Fig.3.12 shows the XRD spectra of samples synthesized with different feeding rates. All the samples were of the spinel structure and no other phases could be detected. Broad diffraction peaks appeared for the samples synthesized with fast feeding rates (e.g. fast injection, Fig.3.12 (a)), suggesting the small grain size. Based on the Scherrer equation, the average grain size was estimated by analyzing the strongest diffraction peak (i.e. (311) peak). The variation of the average grain size with feeding rate was shown in Fig.3.13. Clearly, the average grain size increased with the decrease in the feeding rate, same as the trend of coercivity with the feeding rate in Fig.3.10. It may indicate that the increase in coercivity could be related to the increase in grain size.

C. Mössbauer analysis

Three samples were selected for Mössbauer analysis. i.e. (i) the sample synthesized with the fastest feeding rate (0.18 mol/min); (ii) the sample synthesized with a medium feeding rate (0.0017mol/min) and (iii) the sample synthesized with a low feeding rate (9.38×10^{-5} mol/min).

The room-temperature (300K) Mössbauer spectra are shown in Figure 3.14 and the fitting results are listed in Table 3.3. Clearly, the sextets were overlapped with doublet for all three samples at room temperature. The appearance of the doublet indicated the presence of some paramagnetic and/or superparamagnetic component(s) in the three samples. In addition, with decreasing feeding rate, the weight ratio of the doublet decreased. It implied that the percentage of paramagnetism and/or superparamagnetism decreased with the decrease in the feeding rate.

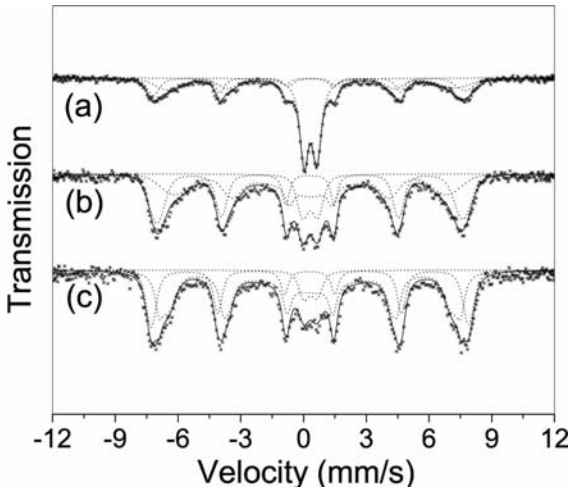

Figure 3.14 Room-temperature Mössbauer spectra of the $CoFe_2O_4$ samples prepared by co-precipitation at 100°C with different feeding rate of metal ions: (a) fast injection, (b) 0.0017mol/min and (c) $9.38x10^{-5}$ mol/min (the [Me]/[OH] ratio was 0.045)

Table 3.3 Room-temperature Mössbauer parameters of the $CoFe_2O_4$ samples prepared by co-precipitation at 100°C with different feeding rate (δ-isomer shift; Δ -quadrupole splitting; P-percentage; H-hyperfine field)

Feeding Rate	Paramagnetic Fe^{3+}			Ferrimagnetic Fe^{3+} - A site				Ferrimagnetic Fe^{3+} - B site			
	δ (mm/s)	Δ (mm/s)	P (%)	δ (mm/s)	Δ (mm/s)	H (T)	P (%)	δ (mm/s)	Δ (mm/s)	H (T)	P (%)
Fast Injection 0.18mol/min	0.334	0.603	43.80	0.291	-0.025	46.209	24.61	0.368	0.014	42.553	31.59
0.0017 mol/min	0.318	0.711	13.13	0.306	-0.001	45.348	40.92	0.341	-0.010	30.617	45.95
$9.38x10^{-5}$ mol/min	0.334	0.619	7.39	0.299	0.005	47.037	41.47	0.328	0.003	33.886	51.14

In order to clarify the phase and site occupation of magnetic ions in these three samples, Mössbauer analysis was conducted at 80K. The 80K spectra were shown in Figure 3.15 and the fitted results were list in Table 3.4. As seen form Figure 3.15, no doublet but only sextets were observed at 80K for all three samples. It indicates that the doublets in the room-temperature spectra can be ascribed to the superparamagnetic relaxation of some small grains in the samples. In this sense, the smaller weight ratio of the doublets at room temperature indicates less superparamagnetic small grains with smaller feeding rate. The results are consistent with those of the XRD analysis,

as mentioned above. All the sextets can be well fitted with two sub-spectra with the hyperfine fields corresponding to Fe^{3+} ions in A (tetrahedral) and B (octahedral) sites, as shown in Table 3.4. The Mössbauer parameters indicate that all three samples are of the $CoFe_2O_4$ spinel phase. The relatively small hyperfine field of B sites can be ascribed to the finite size effects, such as surface disorder, [29-32] as mentioned previously.

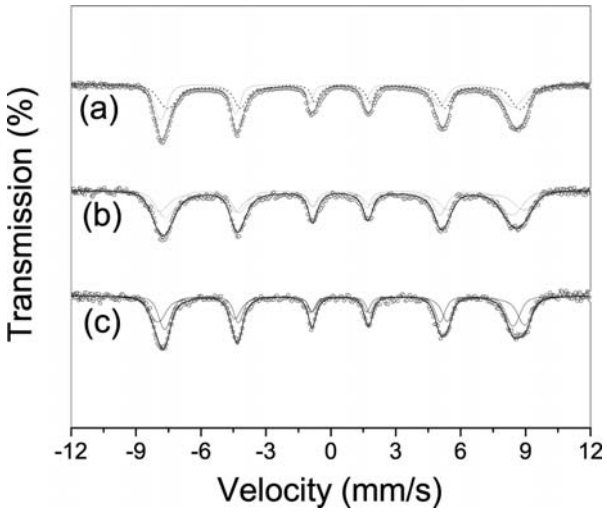

Figure 3.15 The 80K Mössbauer spectra of the $CoFe_2O_4$ samples prepared by co-precipitation at 100°C with different feeding rate of metal ions: (a) fast injection, (b) 0.0017mol/min and (c) $9.38x10^{-5}$ mol/min (Synthesis was conducted at 100°C and the final [Me]/[OH] ratio was 0.045)

Based on the Mössbauer analysis, α_A/α_B, the absorption area ratio of A site to B site was determined for these three samples, as shown in Table 3.4. Assuming the recoilless fractions of A and B sites are same, the α_A/α_B ratio is proportional to the ratio of Fe^{3+} in A site to that in B site. Therefore, from these α_A/α_B ratios, the cation distribution of the magnetic ions can be derived for these samples. For the samples synthesized with the feeding rate of 0.375, 0.0017 mol/min and $9.38x10^{-5}$, the corresponding formula can be expressed as $(Co_{0.085}Fe_{0.915})_A\{Co_{0..915}Fe_{1.085}\}_BO_4$, $(Co_{0.032}Fe_{0.968})_A\{Co_{0.968}Fe_{1.032}\}_BO_4$ and $(Co_{0.038}Fe_{0.962})_A\{Co_{0.962}Fe_{1.038}\}_BO_4$ respectively. Obviously, the $CoFe_2O_4$ samples synthesized with different feeding rate had similar cation distribution, i.e. almost fully inversed structure.

Table 3.4 The 80K Mössbauer parameters of the $CoFe_2O_4$ samples prepared by co-precipitation at 100°C with different feeding rates and the [Me]/[OH] ratio of 0.045 (δ-isomer shift; Δ -quadrupole splitting; P-percentage; H-hyperfine field)

Feeding Rate	A site				B site				α_A/α_B
	δ (mm/s)	Δ (mm/s)	H (T)	P (%)	δ (mm/s)	Δ (mm/s)	H (T)	P (%)	
Fast injection 0.18 mol/min	0.369	-0.002	50.513	45.78	0.483	0.003	47.132	54.22	0.844
0.0017 mol/min	0.390	-0.001	49.61	48.40	0.450	0.001	47.972	51.60	0.938
$9.38x10^{-5}$ mol/min	0.379	-0.005	49.90	48.10	0.489	0.008	51.92	51.90	0.927

D. TEM analysis

For TEM analysis, three samples were chosen, same as those for the Mössbauer analysis. They are: (i) the sample synthesized with fast injection of metal ions (0.18 mol/min); (ii) the sample synthesized with a medium feeding rate (0.0017mol/min) and (iii) the sample synthesized with low feeding rate ($9.38x10^{-5}$ mol/min). Fig3.16 (a) and (b) show the bright-field and dark-field TEM images of the sample synthesized with fast injection of the metal ions. The selected-area electron diffraction analysis (Fig.3.16 (c)) revealed the polycrystalline spinel structure of the sample. The dark-field TEM analysis indicated that almost all the nanoparticles were single crystalline. The average particle (or grain size) was around 9 nm, close to 11 nm as estimated from the XRD analysis (Fig. 3.13). In the sample synthesized with a medium feeding rate (0.00173mol/min), there were many nanoparticles larger than 30 nm as shown in Figure 3.9. Hence, the sample possessed a larger average grain size when compared with the sample synthesized with a fast injection of metal ions.

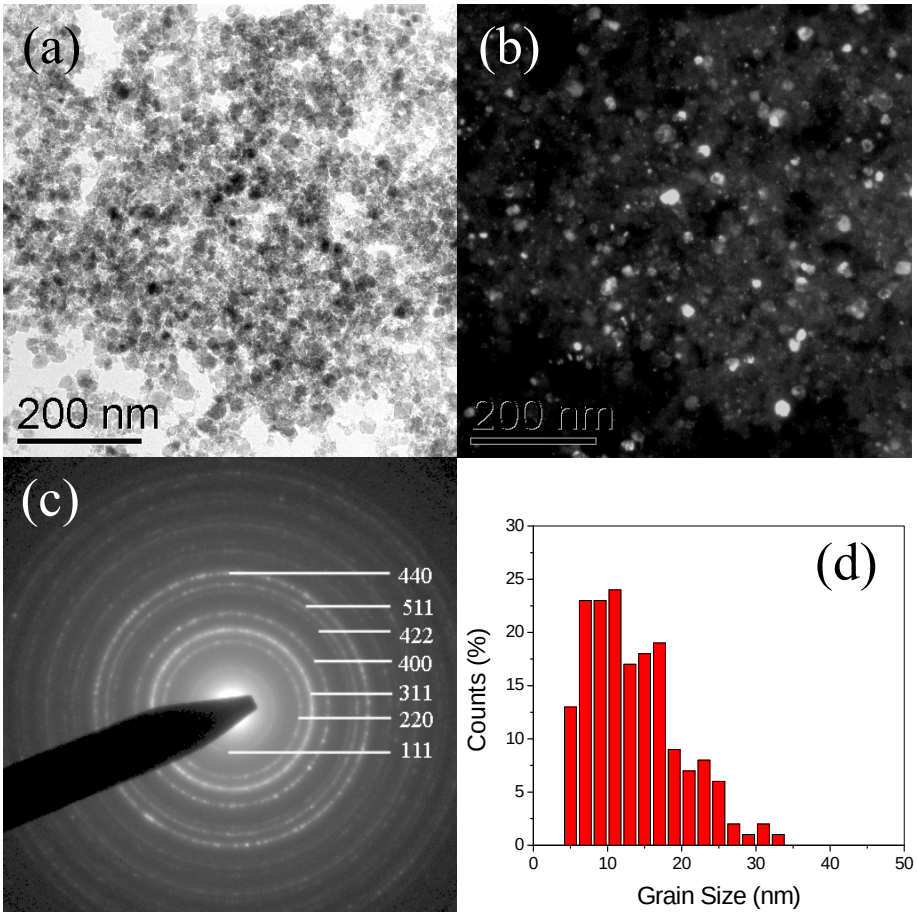

Figure 3.16 (a) Bright-field TEM image, (b) dark-field TEM image, (c) selected-area electron diffraction as well as (d) grain size distribution (estimated from dark-field TEM analysis) of $CoFe_2O_4$ powders prepared by co-precipitation at 100°C with the fast injection process (The final [Me]/[OH] ratio was 0.045)

With the further decrease in the feeding rate to 9.38 x 10^{-5} mol/min, the as-synthesized $CoFe_2O_4$ nanoparticles were apparently larger, as seen from Fig.3.17 (a)~(d). Both dark-field and bright-field TEM analysis revealed that the majority of nanoparticles were in the range of 30~40nm.The spotty diffraction rings in the selected-area electron diffraction (Fig.3.17 (c).) also suggested the presence of large-sized grains.

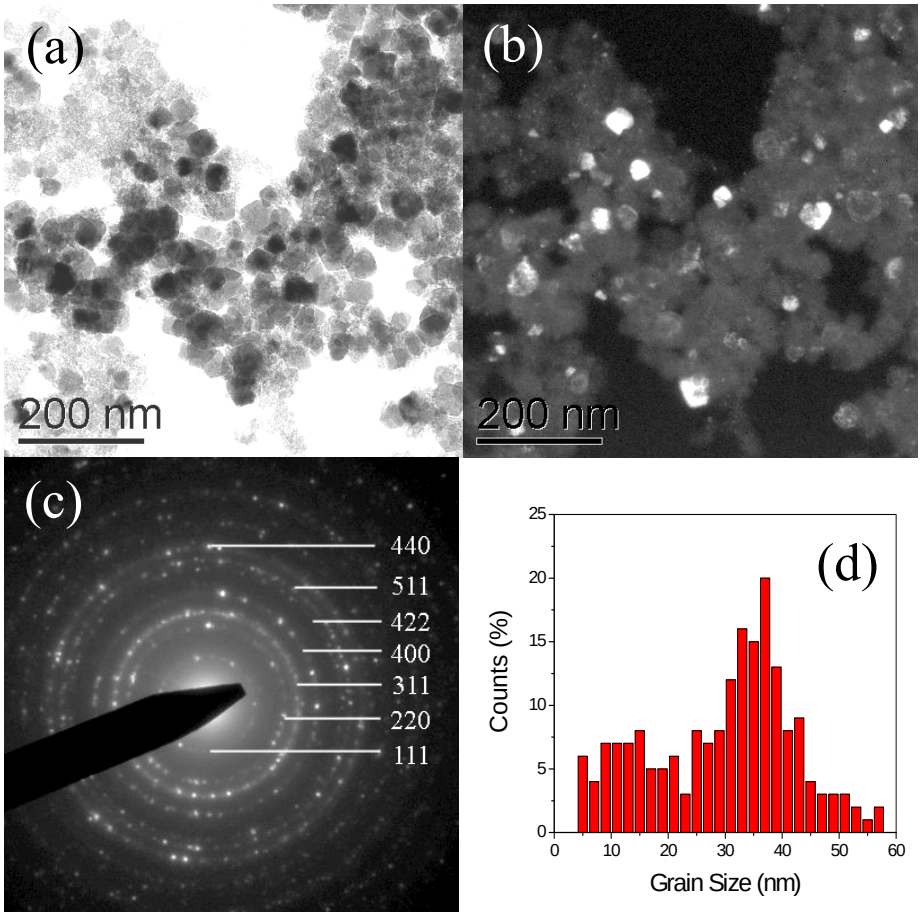

Figure 3.17 (a) Bright-field TEM image, (b) dark-field TEM image, (c) selected-area electron diffraction as well as (d) grain size distribution (estimated from dark-field TEM analysis) of $CoFe_2O_4$ powders prepared by co-precipitation at 100°C with the feeding rate of $9.38x10^{-5}$ mol/min (Synthesis was conducted at 100°C and the final [Me]/[OH] ratio was 0.045)

3.3.2.3 Size selection

As shown in Fig.3.10, coercivity increased with decreasing feeding rate, indicating that small nanoparticles are not favorable for high coercivity. Therefore, in order to further increase coercivity, it is necessary to eliminate the small nanoparticles in the samples. Thus a size-selection method was used by centrifuging the aqueous suspension solution at a low centrifuging speed of 200rpm. The hysteresis loops of the samples before and after the simple size selection were shown in Fig. 3.18. As shown in Fig.3.18, the coercivity and saturation magnetization were increased to 2.1 kOe and 62.3 emu/g respectively after the size selection. TEM analysis (Fig. 3.19) suggested that the amount of the small particles was reduced after the size selection. The

majority of nanoparticles were in the size range of 40~50nm, which was near the critical single-domain size of $CoFe_2O_4$ materials. Therefore, the sample had large magnetic coercivity of 2.1 kOe. The increase in magnetization could be also ascribed to the decrease in the number of these small particles which may appear superparamagnetic at room temperature.

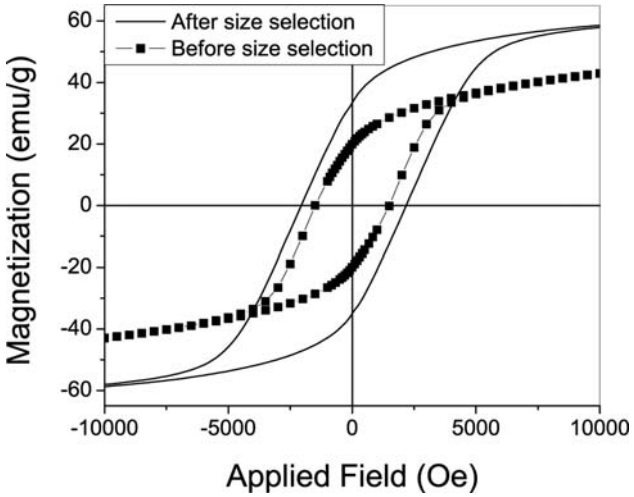

Figure 3.18 the hysteresis loops of $CoFe_2O_4$ powders prepared by co-precipitation at 100°C with the feeding rate of $9.38x10^{-5}$ mol/min and [Me]/[OH]=0.045 before and after size selection

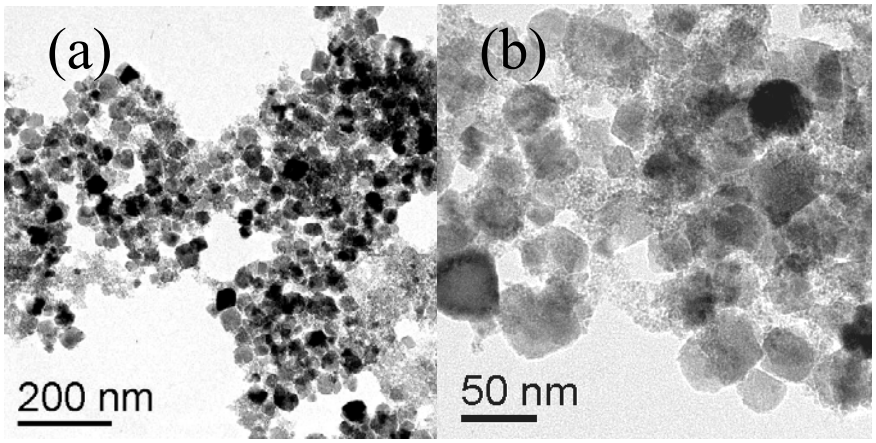

Figure 3.19 TEM images of $CoFe_2O_4$ powders prepared by co-precipitation at 100°C with the feeding rate of $9.38x10^{-5}$ mol/min and [Me]/[OH]=0.045 after size selection ((a)-(b) Bright-field TEM images)

Based on above experimental results, it is clear that the average particle (or grain) size of $CoFe_2O_4$ samples were strongly dependent on the feeding rate of metal ions. The slow feeding rates were apparently favorable for the formation of large $CoFe_2O_4$ grains. Mössbauer analysis revealed no much difference in cation distributions. In this

sense, the larger coercivity of the sample with lower feeding rate should be ascribed to the effects of particle (or grain) size on coercivity. The particle (or grain) size effects were also clearly evidenced by the apparent coercivity enhancement after the size selection with centrifuging. With adjusting the feeding rates, we have tried to control the average gain size and size distribution of $CoFe_2O_4$ nanopaticles. $CoFe_2O_4$ nanosized powders with a high coercivity of up to 2 kOe have been successfully synthesized by the modified co-precipitation process with an average particle size of ~40nm, which is close to the single-domain particle size.

3.4 Synthesis of $CoFe_2O_4$ by mechanochemical processes

3.4.1 Experimental procedures

The starting raw materials were α-Fe_2O_3 (>99% purity, Fluka) and Co (>99% purity, Fluka) powders. The molar ratio of Co to α-Fe_2O_3 was equal to 1:1. The mixture of α-Fe_2O_3 and Co powders was loaded together with stainless-steel grinding balls (15 mm in diameter) into a cylindrical hardened stainless steel vial. The ball to powder weight ratio was 12:1. The mechanochemical reaction between α-Fe_2O_3 and Co was realized by milling the mixture using a Spex 8000 high-energy miller. The milled powders were collected after milling for 3, 6, 15 and 30 hours. The mechanochemical reaction induced during milling can be written as

$$Co + Fe_2O_3 \xrightarrow{\frac{1}{2}O_2} CoFe_2O_4$$

3.4.2 Results and Discussions

3.4.2.1 Synthesis of nanocrystalline $CoFe_2O_4$ powders with the mechanochemical process

Fig.3.20 shows the XRD spectra of the Co/α-Fe_2O_3 samples as-milled for different periods of time. As seen from Fig. 20 (a), all the diffractions from the sample before milling can be assigned to hcp-Co and α-Fe_2O_3 phase. No other phases could be detected. After milling for 3 hours, apparent broadening of diffraction peaks for both phases appeared, as shown in Fig.3.20 (b). Further milling up to 6 hours led to the formation of spinel $CoFe_2O_4$ phase, as evidenced by the (220) and (400) diffractions in Fig.3.20 (c). After milling for 15 hours, the formation of appreciable amount of $CoFe_2O_4$ took place which was accompanied by the dismissing of the diffractions from both Co and α-Fe_2O_3 phases, as shown in Fig.3.20 (d). Further milling up to 30 hours resulted in the further diminishing of the diffractions from both Co and α-Fe_2O_3 phases, as shown in Fig.3.20 (e). The results indicated that spinel $CoFe_2O_4$ phase could be directly obtained by the mechanochemical process through the mechanical milling of Co and α-Fe_2O_3 phases.

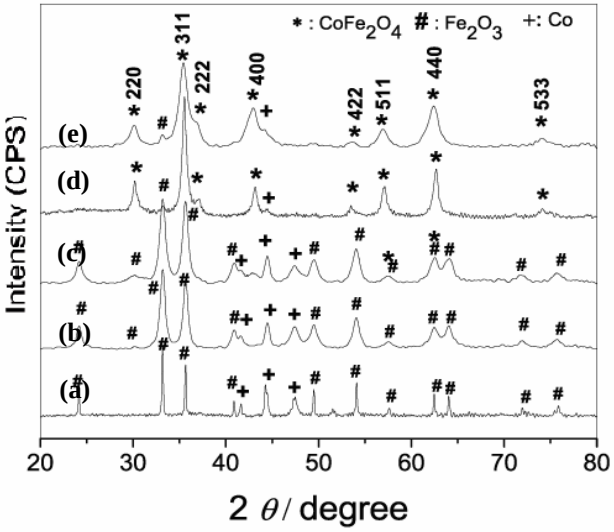

Figure.3.20 XRD spectra of Co/α-Fe_2O_3 samples as-milled for different periods of time: (a) before milling; (b) as-milled for 3 hours; (c) as-milled for 6 hours; (d) as-milled for 15 hours; (e) as-milled for 30 hours

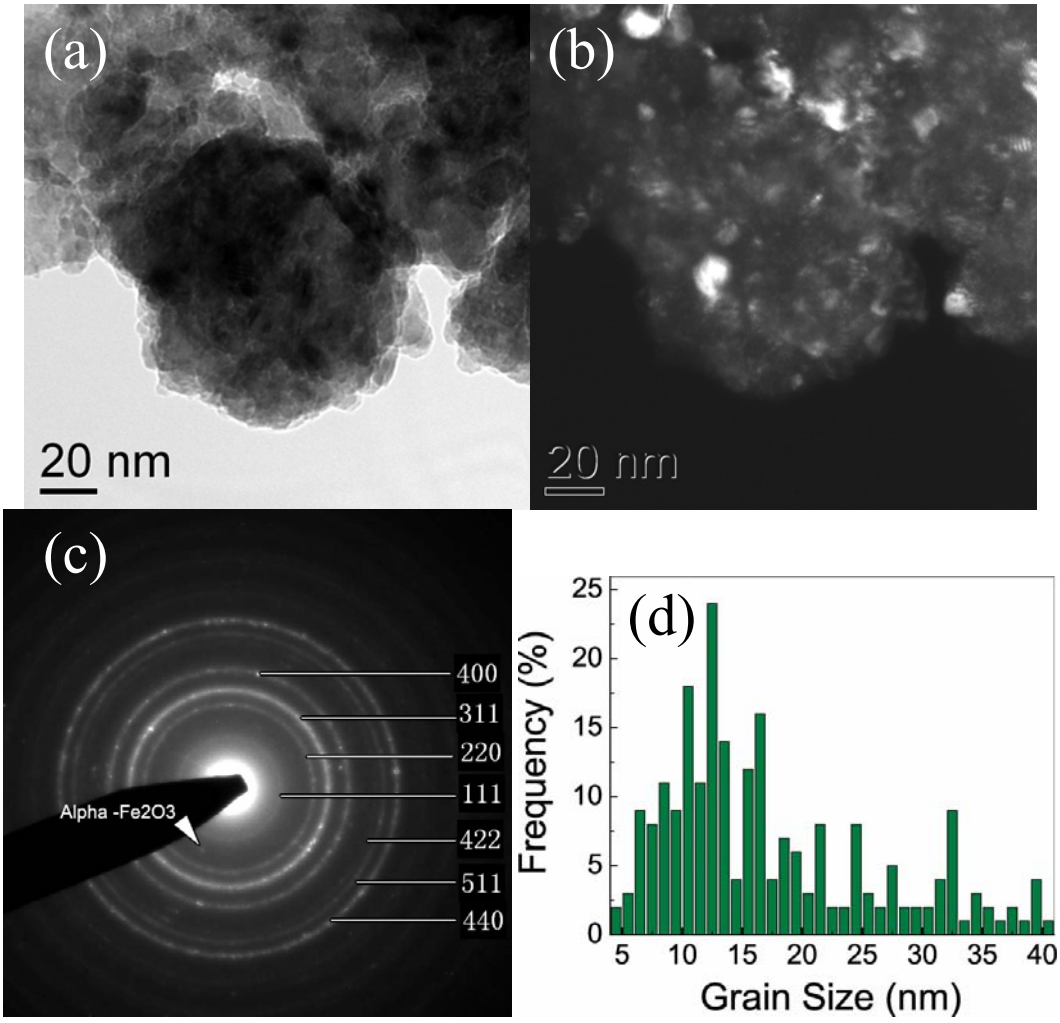

Figure.3.21 (a) bright-field, (b) dark-field TEM images, (c) selected-area electron diffraction and (d) the grain size distribution (based on dark-field TEM analysis) of nanocrystalline $CoFe_2O_4$ powders by mechanochemical milling for 30 hours

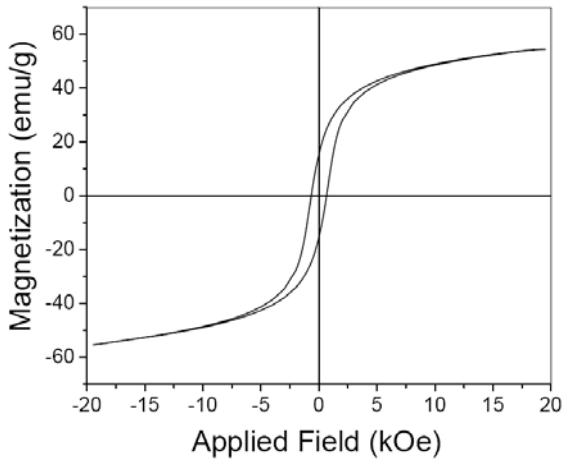

Figure.3.22 The hysteresis loop of the nanocrystalline $CoFe_2O_4$ powders by mechanochemical milling for 30 hours

For the sample milled for 30 hours, TEM analysis showed a lot of submicrometer-sized particles, as shown in Fig.3.21 (a). Dark-field TEM analysis in Fig.3.21 (b)

indicated that that such large particles consisted of nanosized grains with average grain size of around 10nm. The TEM results confirmed the nanocrystalline microstructure of the samples, consistent with the XRD analysis. The selected-area electron diffraction in Fig.3.21 (c) revealed the formation of polycrystalline $CoFe_2O_4$ phase, and the strong diffraction rings can be well assigned to $CoFe_2O_4$ phase. Based on dark-field TEM analysis, the average grain size and size distribution were shown in Fig.3.21 (d). The average grain size was around 10nm.

Fig.3.22 shows the hysteresis loop of the nanocrystalline $CoFe_2O_4$ powders by mechanochemical milling for 30 hours. The magnetization of the sample was not saturated at 20kOe and was around 55emu/g, smaller than the theoretical value of 80 emu/g. The coercivity of the sample was also very low, around 670 Oe. Such low coercivity and magnetization could be ascribed to the nanocrystalline structure of the sample. As revealed by XRD and TEM analysis, the average grain size of the sample is only around 10nm, which is much less than the single-domain size (40~70nm) of the $CoFe_2O_4$ materials.[5-7]. This may account for the small coercivity of the sample. The low saturation could be ascribed to the finite size effects such as surface spin canting/disordering.[34]

3.4.2.2 The post annealing of as-milled $CoFe_2O_4$ samples

A. Magnetic properties of $CoFe_2O_4$ samples annealed with quenching and slow-cooling processes

Figure 3.23 shows the variation of the magnetic properties (saturation magnetization M_S and coercivity H_C) of $CoFe_2O_4$ samples with the annealing temperatures after slow cooling or quenching processes. As seen in Figure3.23 (a) and (b), with increasing annealing temperature, the coercivity (H_C) continuously decreased while the

saturation magnetization (M_S) continuously increased. For the samples annealed with the slow cooling process, there were no significant changes in coercivity when the annealing temperatures increased from 400°C to 1000°C. In addition, at a same temperature, the coercivity H_C of the quenched samples was apparently lower than that of slowly-cooled samples. In contrast, the saturation magnetization M_S of the quenched samples was apparently higher than that of the slowly cooled samples after annealed at the same temperatures, as shown in Figure 3.23 (b). Figure 3.24 shows the hysteresis loops of the samples obtained with the slow-cooling and quenching processes after annealing at 1000°C for 2 hours. Compared with the slowly cooled samples, the quenched sample possessed a lower coercivity H_C (200 Oe) and higher M_S (93 emu/g). The results indicate that the annealing process can greatly affect the magnetic properties of cobalt ferrite materials.

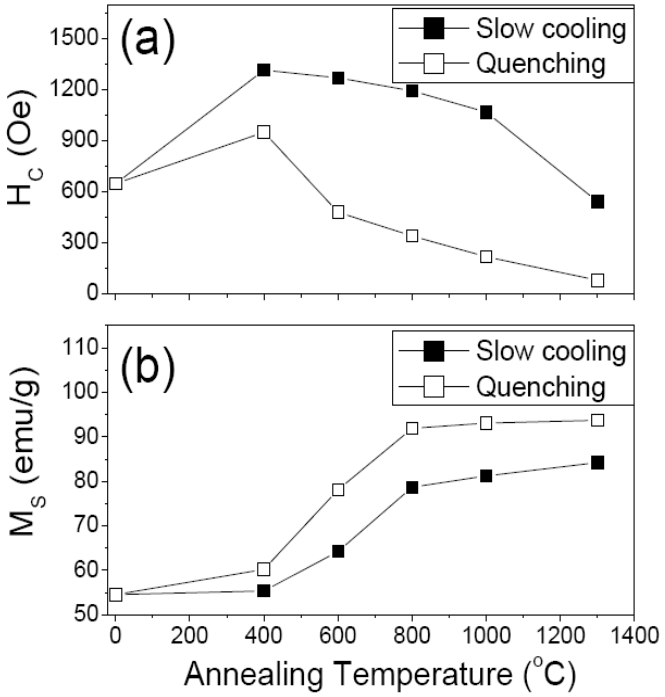

Figure 3.23 The room-temperature magnetic properties (saturation magnetization M_S and coercivity H_C) of $CoFe_2O_4$ samples after annealing at different temperatures for 2 hour with the slow-cooling and quenching processes

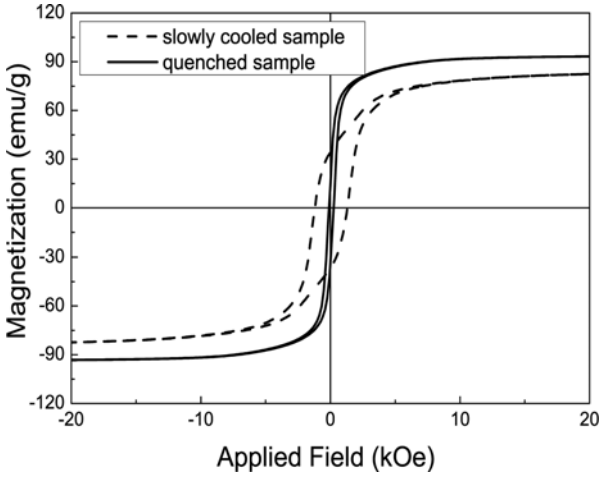

Figure 3.24 The room-temperature hysteresis loops of $CoFe_2O_4$ samples obtained with the quenching (—) and slow cooling (---) processes after annealing at 1000°C for 2hours

.

B. XRD and TEM analysis

Figure 3.25 and Fig. 3.26 show respectively the typical XRD spectra of the $CoFe_2O_4$ samples annealed at different temperatures with the slow cooling and quenching processes. Clearly, the samples annealed at the temperatures of 600°C and above were of single spinel phase. Based on the Scherrer equation, the temperature dependent average grain sizes were estimated and shown in Figure 3.27. As shown by Figure 3.27, the slowly cooled and quenched samples had comparable average grain size when annealed at a same temperature. With increasing annealing temperature, the average grain size of samples continuously increased. This may account for the continuous increase in M_S and the decrease in H_C as shown in Fig. 3.23. In addition, Williamson-Hall plots indicated that no appreciable microstrain can be detected in the samples annealed at 1000oC with both slow-cooling and quenching processes.

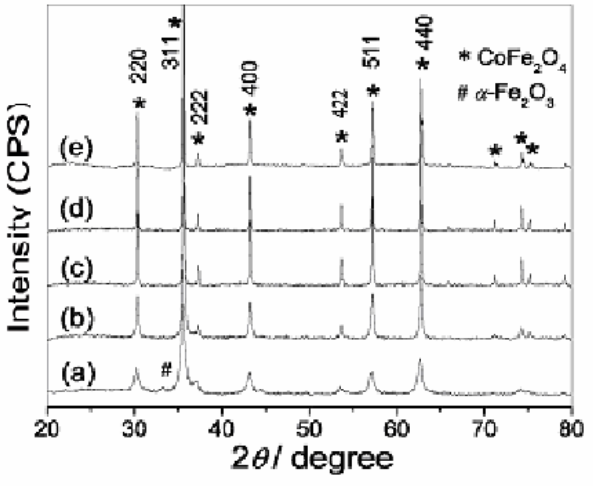

Figure 3.25 The XRD spectra of the $CoFe_2O_4$ samples annealed at different temperatures with a slow cooling process: (a) 400°C; (b) 600°C; (c) 800°C; (d) 1000°C; (e) 1300°C

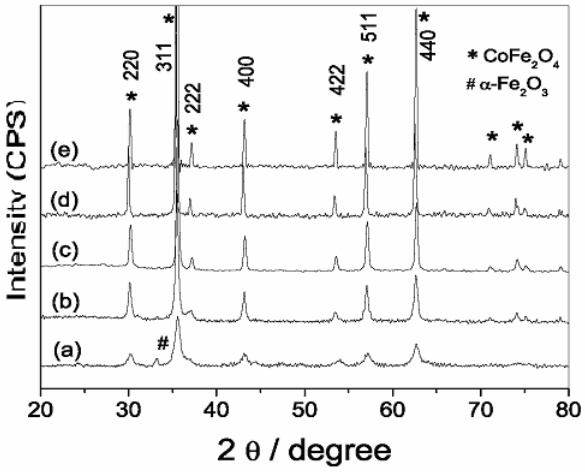

Figure 3.26 The XRD spectra of the $CoFe_2O_4$ samples annealed at different temperatures with quenching process: (a) 400°C; (b) 600°C; (c) 800°C; (d) 1000°C; (e) 1300°C

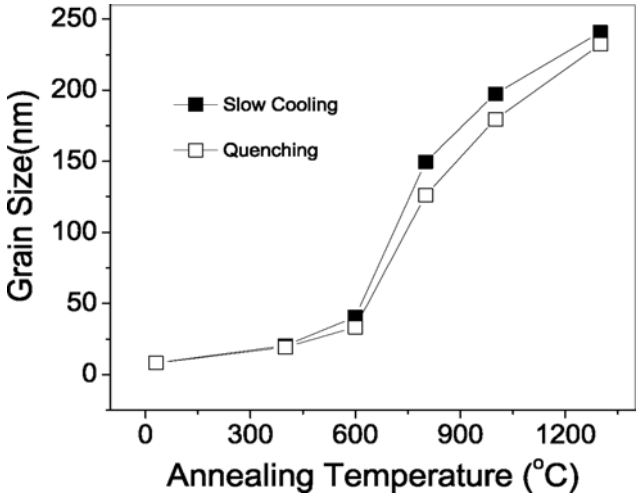

Figure 3.27 The temperature dependent average grain size (estimated from XRD analysis) of the $CoFe_2O_4$ samples annealed at different temperatures with slow cooling and quenching processes

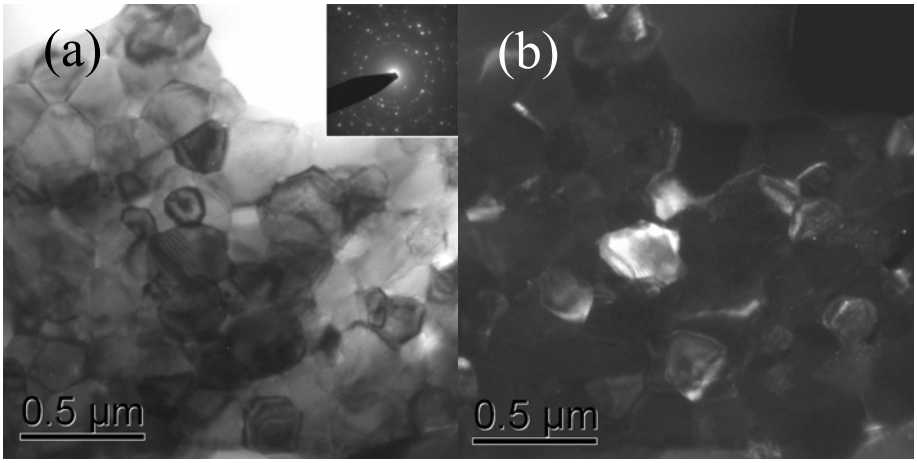

Figure 3.28 (a) Bright-field and (b) dark-field TEM images of $CoFe_2O_4$ sample annealed at 1000°C with the slow-cooling process

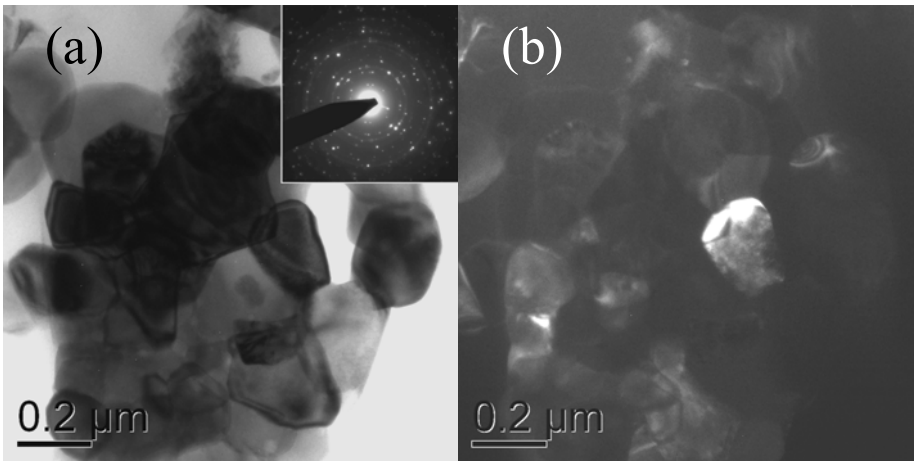

Figure 3.29 (a) Bright-field and (b) dark-field TEM images of $CoFe_2O_4$ sample annealed at 1000°C with the quenching process

In order to examine the average grain size estimated from XRD analysis, two samples were selected for TEM analysis, namely, the samples annealed at 1000°C with slow-cooling and quenching processes. Fig.3.28 (a) and (b) show respectively the bright-field and dark-field TEM images of the sample slowly cooled from 1000°C. Apparently, the sample possessed polycrystalline structure. The close packing of the grains in the large particles suggested that severe grain growth and sintering occurred during the annealing at 1000°C. Based on the dark-field TEM analysis, the average grain size was around 200nm, consistent with XRD analysis. For the sample quenched from 1000°C, similar microstructure was observed as shown in Fig.3.29 (a) and (b).

The average grain size of the quenched sample was also comparable to that of the slowly-cooled sample, consistent with the results of the XRD analysis as discussed above. Above results indicate that different annealing histories did not lead to the appreciable changes in both phase and the average grain size after annealing at 1000°C for 2 hours. Therefore, the effects of both the chemical composition and grain size may not be that major reason that results in the difference in the magnetic properties of quenched and slowly-cooled samples.

C. Mössbauer analysis

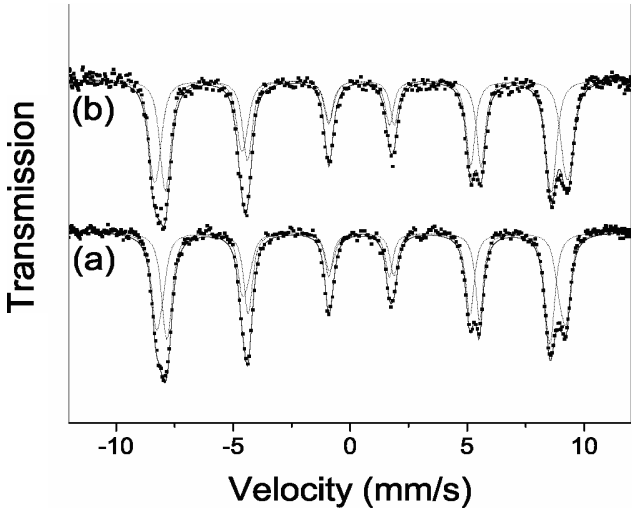

Figure 3.30 Mössbauer spectra of $CoFe_2O_4$ annealed at (a) 600°C and (b) 1000°C for 2 hours with slow cooling process

Table 3.5 Mössbauer parameters (at 80K) of $CoFe_2O_4$ samples annealed at 600°C and 1000°C with the slow cooling processes. (δ- Isomer shift; Δ- Quadrupole splitting, *P*-percentage; α_A/α_B –absorption area ratio of A site to B site)

Samples	A site				B site				α_A/α_B
	δ (mm/s)	Δ (mm/s)	H (T)	P (%)	δ (mm/s)	Δ (mm/s)	H (T)	P (%)	
Slowly cooled from 600°C	0.366	-0.013	50.71	48.97	0.483	-0.021	53.72	51.02	0.96
Slowly cooled from 1000°C	0.372	-0.023	51.01	47.88	0.484	-0.010	54.55	52.12	0.92

Fig. 3.30 (a) and (b) show respectively Mössbauer spectra (recorded at 80K) of the samples annealed at 600°C and 1000°C with the slow cooling processes. The as-fitted Mössbauer parameters were listed in Table 3.5. The characteristic Mössbauer parameters in Table 3.5 indicated that both samples were of the single spinel $CoFe_2O_4$ phase.[35,36] The sextet with the smaller isomer shift (δ) can be assigned to Fe^{3+} in the tetrahedral sites (A sites) and the sextets with the larger δ can be ascribed to Fe^{3+} in the octahedral site (B sites) of $CoFe_2O_4$.[35,36] The relatively smaller isomer shift of A sites could be due to the larger covalence of A site.[35,36] In addition, as seen from Table 3.5, the samples annealed at 600°C and 1000°C had similar cation distribution. The result indicated that cation distribution was not the major reason that accounted for the different coercivity of these two samples. The continuous decrease in coercivity with annealing temperature in Fig.3.23 (a) should be ascribed to the effect of average grain size as shown in Fig. 3.27.

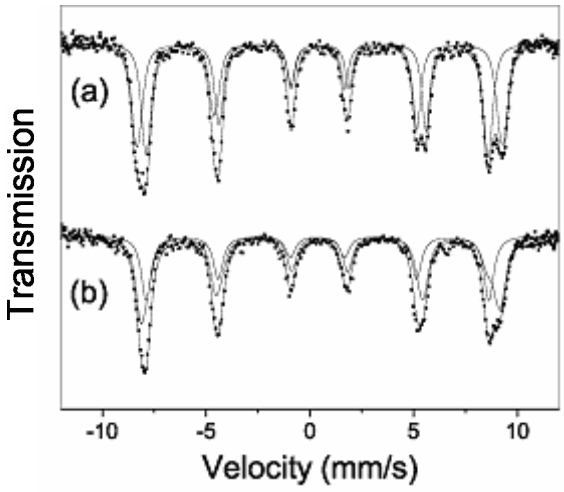

Figure 3.31 Mössbauer spectra of $CoFe_2O_4$ annealed at 1000°C for 2hours with (a) slow cooling process and (b) the quenching process

Fig.3.31 (a) and (b) show the Mössbauer spectra (recorded at 80K) of the samples annealed at 1000°C with the quenching and slow cooling processes respectively. The as-fitted Mössbauer parameters were listed in Table 3.6. For both quenched and slowly-cooled samples, the characteristic Mössbauer parameters indicated the single

spinel $CoFe_2O_4$ phase.[35,36] Based on the Mössbauer analysis, α_A/α_B, the absorption area ratio of A site to B site was determined for both 1000°C-quenched and slowly-cooled samples, as shown in Table 3.6. Assuming the recoilless fractions of A and B sites are same, the α_A/α_B ratio is proportional to the ratio of Fe^{3+} in A site to that in B site. Therefore, from these α_A/α_B ratios, the cation distribution of the quenched and slowly-cooled samples can be derived, which were listed in the Table 3.7. For the samples quenched and slowly cooled from 1000°C, the corresponding formula can be expressed as $(Co_{0.2473}Fe_{0.7527})_A\{Co_{0.7527}Fe_{1.2473}\}_BO_4$ and $(Co_{0.0424}Fe_{0.9516})_A\{Co_{0.9516}Fe_{1.0424}\}_BO_4$ respectively. Therefore, the cation distribution of the quenched sample was apparently different from that of the slowly-cooled sample. The sample obtained with the slow cooling process possesses a more inversed structure, i.e. the absorption-area ratio is close to 1. Therefore, such an inversed structure is expected to be thermodynamically stable at room temperature.

Table 3.6 Mössbauer parameters (at 80K) of $CoFe_2O_4$ samples annealed at 1000°C with the quenching and slow cooling processes. (δ- isomer shift; Δ- quadrupole splitting, *P*-percentage; α_A/α_B –absorption area ratio of A site to B site)

Samples	**A site**				**B site**				**α_A/α_B**
	δ (mm/s)	*Δ (mm/s)*	*H (T)*	*P (%)*	*δ (mm/s)*	*Δ (mm/s)*	*H (T)*	*P (%)*	
Quenched from 1000°C	0.351	-0.021	50.86	37.64	0.475	-0.003	53.82	62.36	0.604
Slowly cooled from 1000°C	0.372	-0.023	51.01	47.88	0.484	-0.010	54.55	52.12	0.918

Table 3.7 The absorption area ratio α_A/α_B (at 80K) and the deduced magnetic data of $CoFe_2O_4$ samples as annealed at 1000°C with quenching and slow-cooling processes. (δ-isomer shift; Δ- quadrupole splitting, *P*-percentage; α_A/α_B –absorption area ratio of A site to B site)

Samples	**α_A/α_B**	**Formula**	**Theoretic moment**	**Experimental moment**
Quenched from 1000°C	0.6035	$(Co_{0.2473}Fe_{0.7527})\{Co_{0.7527}Fe_{1.2473}\}O_4$	$3.9892\mu_B$ (98.23 emu/g)	$3.7807\mu_B$ (93.1 emu/g)
Slowly cooled from 1000°C	0.918	$(Co_{0.0424}Fe_{0.9516})\{Co_{0.9516}Fe_{1.0424}\}O_4$	$3.1816\ \mu_B$ (79.35 emu/g)	$3.2987\mu_B$ (81.23 emu/g)

In light of the Néel's two-sublattice model of ferrimagnetism, the magnetic moments per unit chemical formula are the net moment difference between A site and B site.[37] Assuming that each Fe^{3+} and Co^{2+} ions have the moments of 5 μ_B and 3 μ_B respectively,[37] the calculated magnetic moment of the 1000°C-quenched and slowly-cooled samples are 3.9892 μ_B and 3.1816 μ_B per chemical formula respectively, as shown in Table 3.7. These values are consistent with those reported.[38] For both samples, the calculated magnetic moments are also in reasonable agreement with the experimental values as indicated in Table 3.7.

In order to further examine the effects of cation distribution on the magnetization of quenched samples, we compared the Mössbauer spectra of the samples quenched from different temperatures. Fig.3.32 and Table 3.8 show respectively the Mössbauer spectra and the fitted parameters of the samples quenched from 600°C, 1000°C and 1300°C. As seen from Table 3.8, the higher the temperature from which the sample was quenched, the smaller is the α_A/α_B ratios of the sample. This directly resulted in the increase of the saturation magnetization M_S of the samples with the decrease in α_A/α_B ratios, as shown in Table 3.9. Based on the chemical formula derived from α_A/α_B ratios, the estimated M_S values were closed to the experimental ones for all three samples.

Therefore, based on results mentioned above, it is clear that the quenching process has led to apparent changes in the cation distribution in the $CoFe_2O_4$ spinel structure when compared with the slow-cooling process. The different cation distribution could account for the difference in the saturation magnetization of samples with different annealing histories.

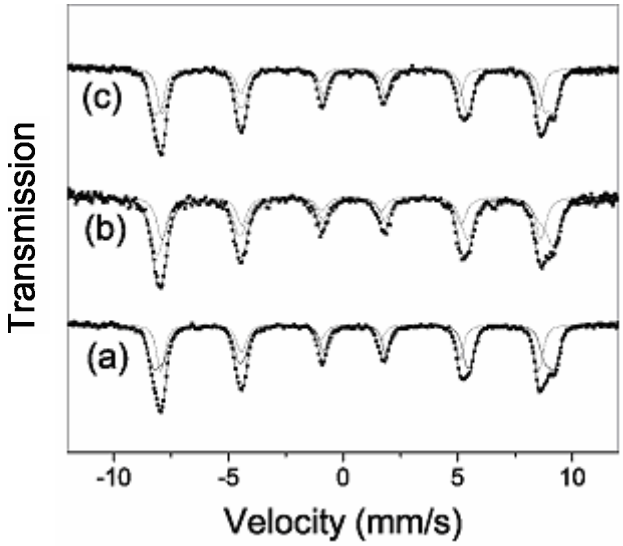

Figure 3.32Mössbauer spectra of $CoFe_2O_4$ annealed with the quenching process: (a) quenched after annealing at 600°C; (b) quenched after annealing at 1000°C; (c) quenched after annealing at 1300°C

Table 3.8 Mössbauer parameters (at 80K) of $CoFe_2O_4$ samples annealed at different temperatures with quenching process. (δ- Isomer shift; Δ- Quadrupole splitting, *P*-percentage; α_A/α_B –absorption area ratio of A site to B site)

Samples	**A site**				**B site**				α_A/α_B
	δ *(mm/s)*	Δ *(mm/s)*	*H (kOe)*	*P (%)*	δ *(mm/s)*	Δ *(mm/s)*	*H (kOe)*	*P (%)*	
Quenched from 600°C	0.364	-0.012	50.89	40.23	0.489	-0.011	53.11	59.77	0.673
Quenched from 1000°C	0.351	-0.021	50.86	37.64	0.475	-0.003	53.82	62.36	0.6035
Quenched from 1300°C	0.348	-0.014	50.67	35.74	0.484	-0.011	52.90	64.26	0.5562

Table 3.9 The absorption area ratio α_A/α_B (at 80K) and the deduced magnetic data of $CoFe_2O_4$ samples as annealed different temperatures with quenching processes. (δ- Isomer shift; Δ- Quadrupole splitting, *P*-percentage; α_A/α_B –absorption area ratio of A site to B site)

Samples	α_A/α_B	**Formula**	**Theoretic moment**	**Experimental moment**
Quenched from 600°C	0.673	$(Co_{0.1954}Fe_{0.8046})\{Co_{0.8046}Fe_{1.1954}\}O_4$	$3.7816\mu_B$ (93.12 emu/g)	$3.6142\mu_B$ (89.00 emu/g)
Quenched from 1000°C	0.6035	$(Co_{0.2473}Fe_{0.7527})\{Co_{0.7527}Fe_{1.2473}\}O_4$	$3.9892\mu_B$ (98.23 emu/g)	$3.7807\mu_B$ (93.1 emu/g)
Quenched from 1300°C	0.5562	$(Co_{0.2852}Fe_{0.7148})\{Co_{0.7148}Fe_{1.2852}\}O_4$	$4.1408\mu_B$ (101.96 emu/g)	$3.8051\mu_B$ (93.7 emu/g)

D. Coercivity and magnetocrystalline-anisotropy analysis

Above experimental results clearly indicated that the annealing processes greatly affected the magnetic coercivities of $CoFe_2O_4$ powdered samples. Mössbauer analysis suggested different cation distributions in the slowly-cooled and quenched samples. It is well known that the magnetocrystalline anisotropy of cobalt ferrite is mainly attributed to the presence of Co^{2+} ions in B sites.[39] According to one-ion crystalline-field model, the large magnetic anisotropy of Co^{2+} arises from its incompletely quenched angular moment which is constrained to lie parallel to an axis of trigonal symmetry of B (octahedral) site.[38] Therefore, the spin-orbit coupling leads to the strong interactions between the spins of Co^{2+} ions and the crystal field, which thus generates a large anisotropy energy.[38] Therefore, it is expected that any change in the site occupation of Co^{2+} will readily result in the change in the magnetocrytalline anisotropy, thus the magnetic coercivity of cobalt ferrite materials.

In order to investigate the effects of the cation distribution on the magnetic anisotropy of cobalt ferrite, a numerical analysis based on the law of the approach to saturation[40,41] was used for estimating the magnetocrystalline anisotropies of the samples quenched and the slowly cooled from 1000°C. At a field larger than the coercive force of magnetic materials, the theoretic calculation of the magnetization curve leads to the so-called the law of the approach to saturation, which can be expressed as the formula as Equation 3.1 [40,41]

$$M(H) = M_S(1 + \frac{A}{H} + \frac{B}{H^2}), \qquad (3.1)$$

where M(H) is the magnetization at an applied field of H and M_S is the saturation magnetization. A/H term is related to magnetic inhomogeneities and theoretically should vanish at high fields. B/H^2 term is closely related to magnetic anisotropy of

materials.[40,41] For cubic structured materials, if ignoring A/H term and K_2, the law of approach to saturation can be expressed as[40,41]

$$M(H) = M_S(1 - \frac{0.07619K_1^2}{H^2M_S^2}) \qquad (3.2)$$

Therefore, based on Equation 3.2, the second anisotropy constant K_1 can be derived by fitting M(H)-H curves at a certain field range within which A/H can be ignored. It was found that in a median field range between 10kOe and 20 kOe, the A/H term can be ignored which can be evidenced by a good linearity between M(H) and$1/H^2$ as shown in Fig.3.33 (a) and Fig.3.34 (a). Therefore, a good fitting of the M(H)-H curve by Equation (3-2) can be achieved for both quenched and slowly-cooled samples, as shown in Fig.3.33 (b) and Fig.3.34 (b) respectively. Based on the fitting of the magnetization curves of the samples at this filed range, the estimated magnetocrystalline anisotropy constants K_1 are listed in the Table 3.10. As seen from Table 3.10, the slowly cooled sample possesses larger magnetocrystalline anisotropy constant than that of the quenched sample. As discussed above, both samples have similar average grain size as estimated from both XRD and TEM analysis, and thus the effect of the grain size should not be the dominant reason for the difference in coercivities of two samples. Mössbauer and magnetocrystalline anisotropy analysis suggest that the slowly cooled sample possesses a more inversed spinel structure with more Co^{2+} occupying the octahedral sites. Therefore, based on the one-ion model,[39] the large difference in the magnetocrystalline anisotropy constants may well explain the large difference in magnetic coercivity H_C of the slowly cooled and quenched samples.

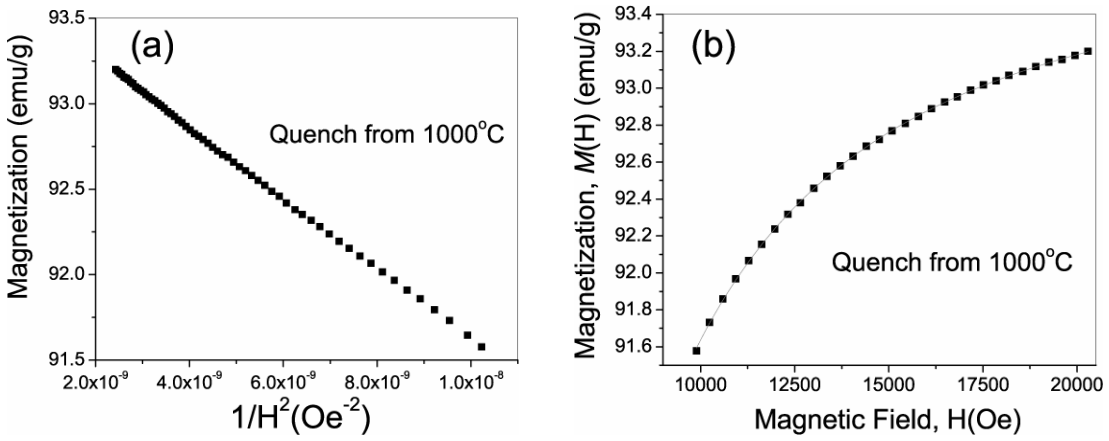

Figure 3.33 (a) M(H)~1/H^2 curve and (b) the experimental magnetization M(H) curve (scatters) and the fitting curve (solid line) using the law of the approach to saturation (Eq.(3-2)) for the sample annealed at 1000°C with quenching process

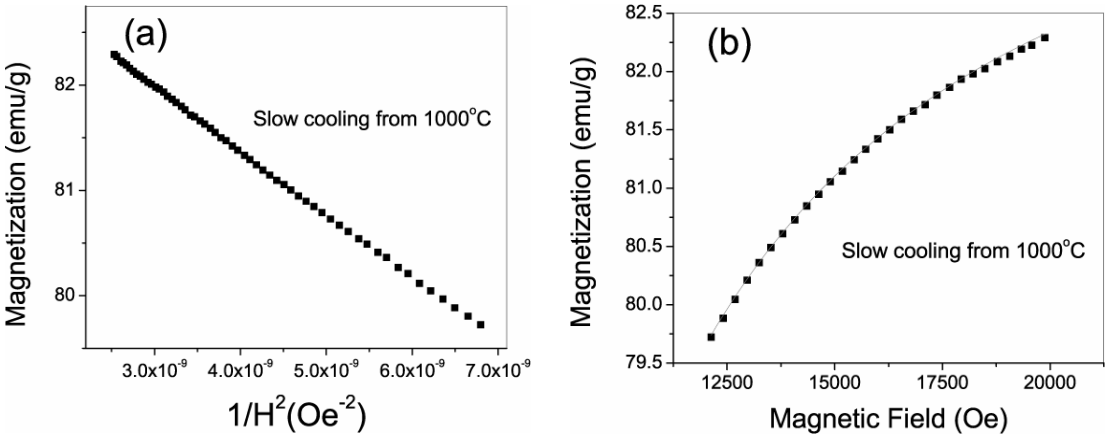

Figure 3.34 (a) M(H)~1/H^2 curve and (b) the experimental magnetization M(H) curve (scatters) and the fitting curve (solid line) using the law of the approach to saturation (M(H)=) for the sample annealed at 1000°C with slow cooling process

Table 3.10 the magnetic coercivity and the magnetocrystalline anisotropy constant K_1 estimated by fitting the law of approach to saturation for the samples annealed at 1000°C for 2 hours with slow cooling and quenching processes

Samples	**Formula**	**Coercivity (Oe)**	**Anisotropy Constant, K_1 (J/m^3)**
Slowly-cooled from 1000°C	$(Co_{0.1954}Fe_{0.8046})\{Co_{0.8046}Fe_{1.1954}\}O_4$	970	3.20×10^5
Quenched from 1000°C	$(Co_{0.2473}Fe_{0.7527})\{Co_{0.7527}Fe_{1.2473}\}O_4$	195	2.66×10^5

3.5 Conclusions

A modified co-precipitation process has been successfully employed for synthesizing $CoFe_2O_4$ nanoparticles. The results indicated that the morphology (particle size and size distribution) of the as-obtained nanoparticles was strongly dependent on both the ratio of metal ions to OH^- and the feeding rate of metal ions. Higher coercivity (up to 1500 Oe) was achieved for the sample obtained with a slow feeding. With removing the small particles, a high coercivity of up to 2.1 kOe was achieved for the sample prepared with the slow feeding rate.

Mechanochemical process was proven to be a unique process for synthesizing $CoFe_2O_4$ powdered materials with a higher productivity when compared with the co-precipitation process. Both XRD and Mössbauer analysis indicated that the solid-state reactions between Fe_2O_3 and Co phases for the formation of $CoFe_2O_4$ can be induced by mechanical milling for a relatively short time (around 6 hours). Single-phased $CoFe_2O_4$ powdered materials with relatively high coercivities of up to 1.3kOe were obtained by the post-annealing. Different post-annealing processes resulted in different magnetic properties of the resultant $CoFe_2O_4$ powdered materials.. The difference in the cation distribution well accorded with the difference in the saturation magnetization and magnetic coercivity as well as the magnetocrystalline anisotropy of the samples. The results indicate that the average particle/grain size and cation distribution play crucial roles in the magnetic coercivity of the resultant $CoFe_2O_4$ powdered materials.

3.6 Reference

[1] E. P. Wohlfarth, *Magnetism*, Vol. III, 351 (Academic Press, New York, 1963).
[2] Q. A. Pankhurst and R. J. Pollard, J. Phys.:Condens. Matter. **5,** 8487 (1993).
[3] J. W. F. Brown, *Micromagnetics* (Wiley-Interscience, New York, 1963).
[4] C. P. Bean and J. D. Livingston, J. Appl. Phys. **30** (1959).
[5] A. E. Berkowitz and W. J. Schuele, J. Appl. Phys. **30,** 134S (1959).
[6] C. N. Chinnasamy, B. Jeyadevan, O. Perales-Perez, K. Shinoda, K. Tohji, and A. Kasuya, IEEE Trans. Magn. **38,** 2640 (2002).
[7] C. N. Chinnasamy, B. Jeyadevan, K. Shinoda, K. Tohji, D. J. Djayaprawira, M. Takahashi, R. J. J. oseyphus, and A. Narayanasamy, Applied Physics Letter **83,** 2862 (2003).
[8] Y. C. Wang, J. Ding, J. B. Yi, B. H. Liu, T. Yu, and Z. X. Shen, Apply. Phys. Lett. **84,** 2596 (2004).
[9] J. H. Yin, J. Ding, B. H. Liu, X. S. Miao, and J. S. Chen, Appl. Phys. Lett. **88,** 162502 (2006).
[10] T. Sato, T. Iijima, M. Seki, and N. Inagaki, J. Magn. Magn. Mater. **65,** 252 (1987).
[11] V. Pillai and D. O. Shal, J. Magn. Magn. Mater. **163,** 243 (1996).
[12] Y. Shi, J. Ding, and H. Yin, J. Alloys & Compd. **308,** 290 (2000).
[13] J. G. Lee, H. M. Lee, C. S. Kim, and Y. J. Oh, J. Magn. Magn. Mater. **177,** 900 (1998).
[14] K. J. Dvies, S. Wells, R. V. Upadhyly, S. W. Charles, K. O. Grady, M. Elhilo, T. Meaz, and S. Morup, J. Magn. Magn. Mater. **149,** 14 (1995).
[15] L. J. Cote, A. S. Teja, A. P. Wilkinson, and Z. J. Zhang, Fluid Phase Equilibria **210,** 307 (2003).
[16] M. Bonini, A. Wiedenmann, and P. Baglioni, Physica A **339,** 86 (2004).
[17] J. Ding, P. G. Mccormik, and R. Street, Solid State Commun **95,** 31 (1995).
[18] Q. Song and J. Zhang, J. Amer. Chem. Soc. **126,** 6164 (2004).
[19] T. Hyeon, Y. Chung, J. Park, S. S. Lee, Y. W. Kim, and B. H. Park, J. Phys. Chem. B **106,** 6831 (2002).
[20] Z. X. Tang, K. J. Klabunde, and G. C. Hadjipanayis, J. Colloid and Inter. Sci. **146,** 38 (1991).
[21] J. Ding, W. F. Miao, P. G. McCormick, and R. Street, Appl. Phys. Lett. **67,** 3804 (1995).
[22] E. Gaffet, F. d. r. Bernard, J. C. Niepce, F. d. r. Charlot, C. Gras, G. r. L. Cae¨r, J. L. Guichard, P. Delcroix, A. Mocellin, and O. Tillement, J. Mater. Chem. **9,** 305 (1999).
[23] P. G. McCormick, T. Tsuzuki, J. S. Robinson, and J. Ding, Adv. Mater. **13,** 1008 (2001).
[24] M. Muroi, R. Street, and P. G. McCormick, J. Appl. Phys. **87,** 3424 (2000).
[25] X. Y. Qin, J. S. Lee, and J. G. Kim, J. Appl. Phys. **86,** 2146 (1999).
[26] A. R. Yavari, Mater. Trans. JIM **36,** 228 (1995).
[27] G. B. Schaffer and P. G. McCormick, Apply. Phys. Lett. **55,** 45 (1989).
[28] V. V. Boldyreva, N. Z. Lyakhov, Y. T. Pavlyukhin, E. V. Boldreva, E. Yu Ivanov, and E. G. Avvakumov, Sov. Sci. Rev. B. Chem. **14,** 105 (1990).
[29] F. Bødker, S. Mørup, and S. Linderoth, Phys. Rev. Lett. **72,** 282 (1994).
[30] G. F. Goya, H. R. Rechenberg, and J. Z. Jiang, J. Appl. Phys. **84,** 1101 (1998).
[31] J. Z. Jiang, G. F. Goya, and H. R. Rechenberg, J. Phys.: Condens. Matter **11,** 4063 (1999).

[32] C. J. Serna, F. Bødker, S. Mørup, M. P. Morales, F. Sandiumeng, and S. Veintemillas-Verdaguer, Solid State Commun. **118,** 437 (2001).
[33] R. Mark, D. Guire, C. Robert, O. Handley, and G. Kalonji, J. Appl. Phys. **65,** 3167 (1989).
[34] J. M. Coey, Phys. Rev. Lett. **27,** 1140 (1971).
[35] N. N. Greenwood and T. C. Gibb, *Mossbauer Spectroscopy* (Champman and Hall Ltd, London, 1971).
[36] C. S. Kim, S. W. Lee, S. I. Park, J. Y. Park, and Y. J. Oh, J. Appl. Phys. **79,** 5428 (1996).
[37] B. D. Cullity, *Introduction to Magnetic Materials* (Addison Wesley Publishing Company, University of Notre Dame, 1972).
[38] J. C. Slonczeweski, Phys. Rev. **110,** 1341 (1958).
[39] R. F. Penoyer and L. R. Bickford, Jr. Phys. Rev. **108,** 271 (1957).
[40] R. Grössinger, Phys. Stat. Sol. A **66,** 665 (1981).
[41] J. Willian Fuller Brown, Phys. Rev. **58,** 736 (1940).

CHAPTER 4

Mechanical Milling of Cobalt Ferrite Powdered Materials

4.1 Background

As mentioned previously, magnetic coercivity is microstructure sensitive and shows its dependence on not only the grain size but also the residual strain. In our previous work, large residual strain has been recognized as one of the major contributions to the high coercivities (up to 12.5 kOe) in $CoFe_2O_4$ thin-film materials.[1,2] Therefore, building-up high-level strain could be another effective way to achieve high coercivity in $CoFe_2O_4$ powdered materials. As is well known, the build-up of a high residual strain is always accompanied by the formation of various defects such as dislocations in order to accommodate the high strain energy. Therefore, introducing a high residual strain may bring about two major effects on the coercivity developments; one is related to the stress-induced anisotropy and the other is related to the pinning effects of defects on the reversal magnetization processes of magnetic materials. Many works have reported the importance of microstructure for the coercivity enhancement.[3-9] However, the relationship between microstructure (such as residual strain) and coercivity has not been well understood for cobalt ferrite materials. In addition, so far there has been no attempt to deliberately introduce a high level of strain and a high-density of defects into oxide magnetic materials such as cobalt ferrites for the purpose of the coercivity enhancement.

As it is well recognized, mechanical milling is a high-energy deformation process, which can introduce a high density of defects and build up large residual strain inside materials. Therefore, it will be of interest to study whether mechanical milling can be employed as an effective tool to introduce the strained and defective microstructure inside the $CoFe_2O_4$ materials. In this work, we will study the effects of residual strain on the coercivity of $CoFe_2O_4$ materials and explore the possibility of the coercivity enhancement

in $CoFe_2O_4$ materials by the mechanical milling process. Based on the XRD and TEM analysis, we will study the microstructural evolution of $CoFe_2O_4$ materials during mechanical milling. The detailed phase, microstructural and magnetic studies will be presented in order to understand the effects of the microstructural evolution on the magnetic properties of the milled samples.

4.2 Purposes of study

Based on above arguments, the purposes of this study can be summarized as:

1. To explore the feasibility and possibility of mechanical milling as an effective way to introduce a high level of strain and a high density of defects in $CoFe_2O_4$ powdered materials;

2. To explore the feasibility and possibility of coercivity enhancement in $CoFe_2O_4$ powdered materials by the mechanical milling process;

3. To study the microstructure evolution during the mechanical milling its effect on the magnetic properties (coercivity and saturation magnetization) of $CoFe_2O_4$ powders;

4. To investigate the effects of the initial grain size of $CoFe_2O_4$ powders on the microstructure evolution during the mechanical milling;

5. To investigate the mechanisms behind the milling-induced high coercivity based on the detailed magnetic studies.

4.3 Experimental procedures

$CoFe_2O_4$ precursor powders were prepared by the co-precipitation process. After thorough washing, the as-obtained precursors were annealed at different temperatures to obtain the well crystallized spinel phase ($CoFe_2O_4$). In order to investigate the effect of initial grain size on the microstructure evolution, two $CoFe_2O_4$ powders were used as the starting materials for mechanical milling, namely powders annealed at 1000°C (denoted as Powder A) and annealed 1300°C (denoted as Powder B). Mechanical milling was conduced in a Spex-8000 high-energy miller with a 12:1 weight ratio of ball to powder. Three powders were mechanically milled and sampled for different periods of time up to 36 hrs. The phase, grain size and residual strain of milled samples were analyzed by X-ray diffraction. The microstructure of the milled samples was examined using transmission electron microscopy (TEM, JEOL JEM 3010). A VSM was used for magnetic measurements, including magnetic viscosity, minor loops and DC demagnetization curves. ^{57}Fe Mössbauer spectroscopy was used for the analysis of the site occupation of the magnetic ions in the $CoFe_2O_4$ spinel lattice before and after mechanical milling.

4.4 Experimental results

4.4.1 Starting materials

Table 4.1 shows the coercivity (H_C) and magnetization (M_S) of samples after annealing at different temperatures. While M_S continuously increased with the annealing temperature,

H_C increased initially and reached the maximum of 1.28 kOe. A further increase of annealing temperature resulted in the decrease of H_C. The variation of H_C with annealing temperature can be ascribed to the grain size effects [11,12] The results were consistent with those published previously,[4] which reported that $CoFe_2O_4$ powdered materials usually possess relatively low coercivities in the range of 1~2 kOe. Fig.4.1 shows the hysteresis loops of Power A and Powder B. The saturation magnetization (M_s) was 81 and 83 emu/g for Powder A and Powder B respectively. The low M_s value of the sample annealed at low temperatures such as 300°C could be attributed to the finite-size effects such as surface spin disordering/cantering, as often found in nanosized materials.[13] The Ms values of 81 and 83 emu/g for Powder B and

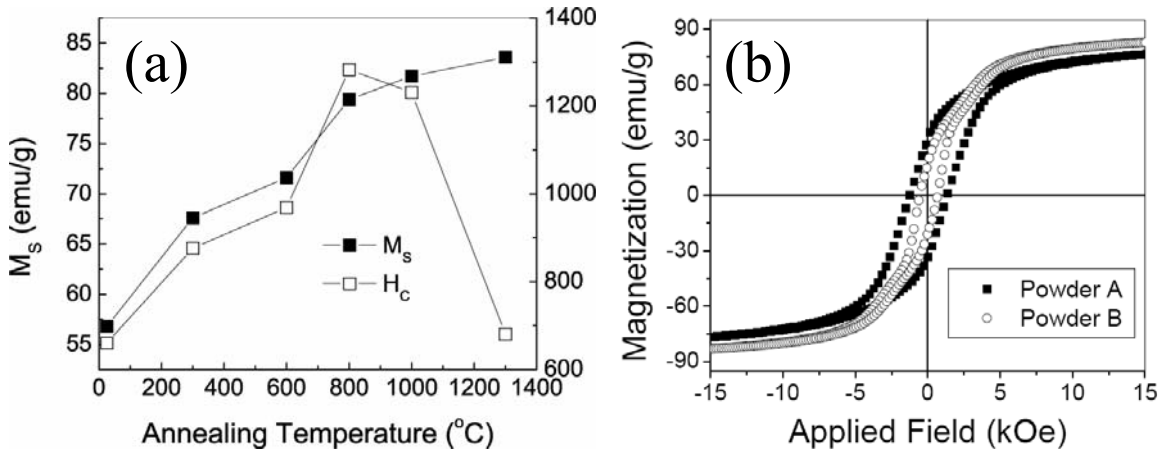

Figure 4.1 (a) Coercivity (H_C) and saturation magnetization (M_S) of $CoFe_2O_4$ samples after annealing; (b) The hysteresis loops of Powder A and Powder B before mechanical milling

Powder C are close to the theoretical value (80 emu/g) for bulk $CoFe_2O_4$.[14] The coercivity was 1.2 kOe and 0.6 kOe for Powder A and Powder B respectively.

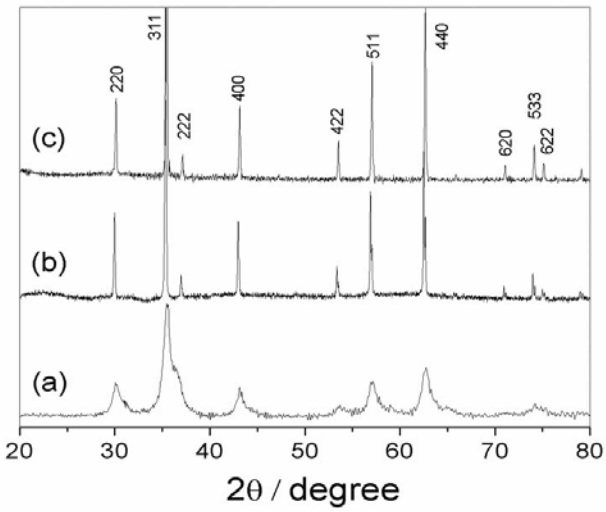

Figure 4.2 XRD spectra of samples before mechanical milling: (a) annealed at 300°C; (b) annealed at 1000°C (Powder A); (c) annealed at 1300°C (Powder B)

Fig.4.2 shows XRD spectra of three $CoFe_2O_4$ samples annealed at 300°C, 1000°C and 1300°C. As seen from Fig.4.2, all three samples were of crystallized spinel phase. For the sample annealed at 300 °C, broadening of the diffraction peaks was apparent, which could be due to the small grain size of the $CoFe_2O_4$ nanoparticles. Based on the 311 diffraction peak broadening and the Scherrer equation, the estimated average grain sizes were 12nm, 230nm and 350nm for the samples annealed at 300°C, 1000°C (Powder A) and 1300°C (Powder B), respectively.

For the sample annealed at 300°C, TEM analysis indicated that the particle size remained in the nanosize range with relatively uniform size distribution, as indicated by the bright-field TEM image shown in Fig. 4.3(a). The selected-area electron diffraction pattern in Fig. 4.3 (a) indicates the polycrystalline structure. For powders A and B, large-sized particles in the sub-micrometer or micrometer size range were observed under TEM. The typical microstructure of these large-sized particles is shown in the bright-field TEM images in Fig. 4.3 (b) and (d). These large-sized particles were hard agglomerations of

sub-micrometer sized grains, indicating severe grain growth and sintering when the samples were annealed at 1000°C and 1300°C.

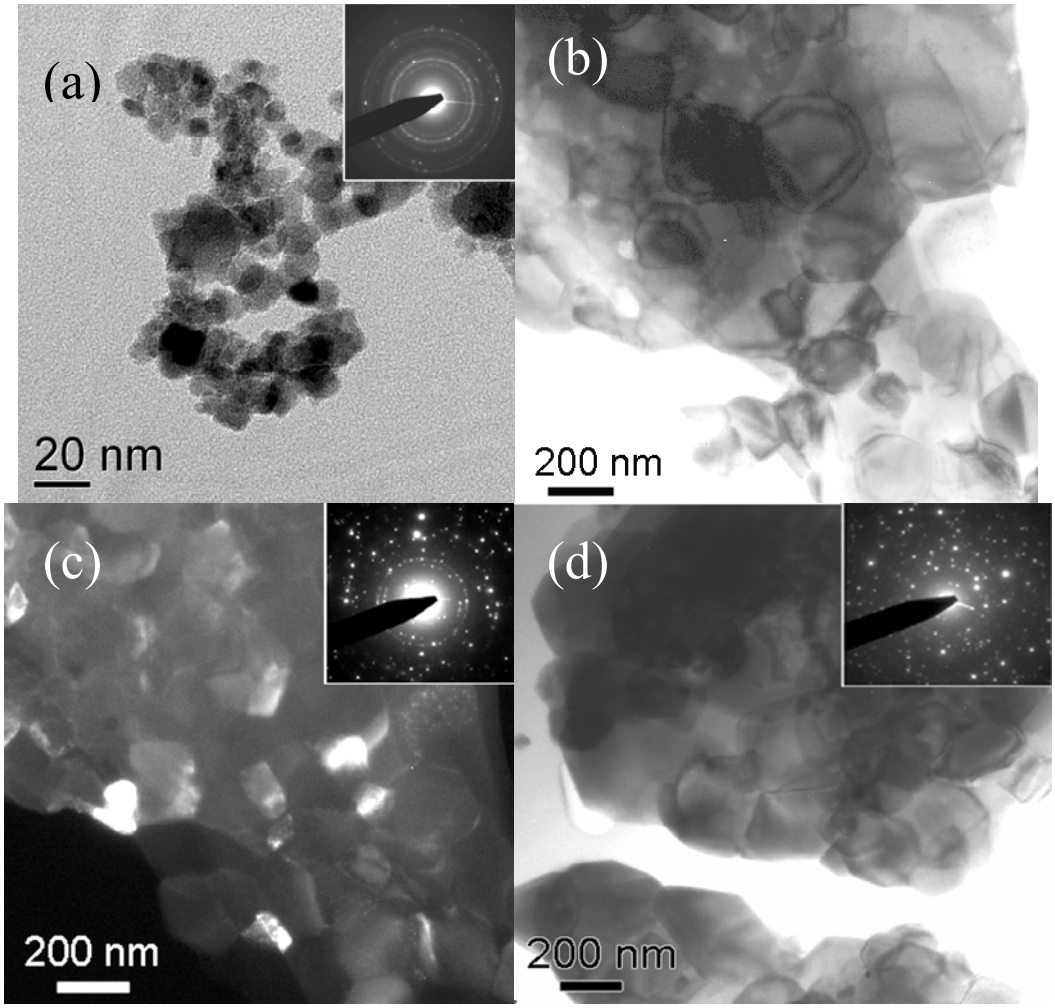

Figure 4.3 TEM images and electron diffraction patterns (inserted) of samples before mechanical milling: (a) the sample annealed at 300°C; (b)-(c) Powder A annealed at 1000°C; (d) Powder B annealed at 1300°C

The spotty diffraction rings in the selected-area electron diffraction patterns in Fig. 4.3 (c) and (d) also suggested the large-grained microstructure of these two samples. Dark-field TEM analysis (as shown in Fig. 4.3 (c) for powder A) was used to estimate the grain size and size distribution of three samples. The estimated average grain sizes were around 12nm, 240nm and 340nm for the sample annealed at 300°C, Powder A and Powder B respectively, consistent with the results of XRD analysis. The sample annealed at 300°C

possessed a relatively uniform grain size distribution, while powder A and B had rather broad grain size distributions.

4.4.2 Milled $CoFe_2O_4$ samples

4.4.2.1 Effects of milling time on magnetic properties

Fig. 4.4 shows the room-temperature saturation magnetization M_s and coercivity H_c of the three $CoFe_2O_4$ powders after mechanical milling for different periods of time. As shown in Fig. 4.4 (a) and (b), Powder A and Powder B had the similar trend of the change in M_S and H_C. For both samples, the saturation magnetization M_S continuously decreased initially and then gradually reached the final value after a prolonged milling (from 80-85 emu/g initially to 40-45 emu/g after milling over 20 hours). The coercivity H_C of both samples increased fast initially and reached the maximum values after a short milling time (5.1 kOe after milling for 1.5 hours for and 4.6 kOe after milling for 2 hours for Powder B).

Further milling led to the decease in H_c, which finally reached the values of around 1 kOe after a prolonged milling for the both samples. It is noteworthy that a maximum H_C up to 5.1 kOe was obtained for Powder A after milling for 90min, as indicated by the hysteresis loop shown in Fig.4.4 (c). This value is the highest H_C as reported in literature for cobalt ferrite powdered materials.

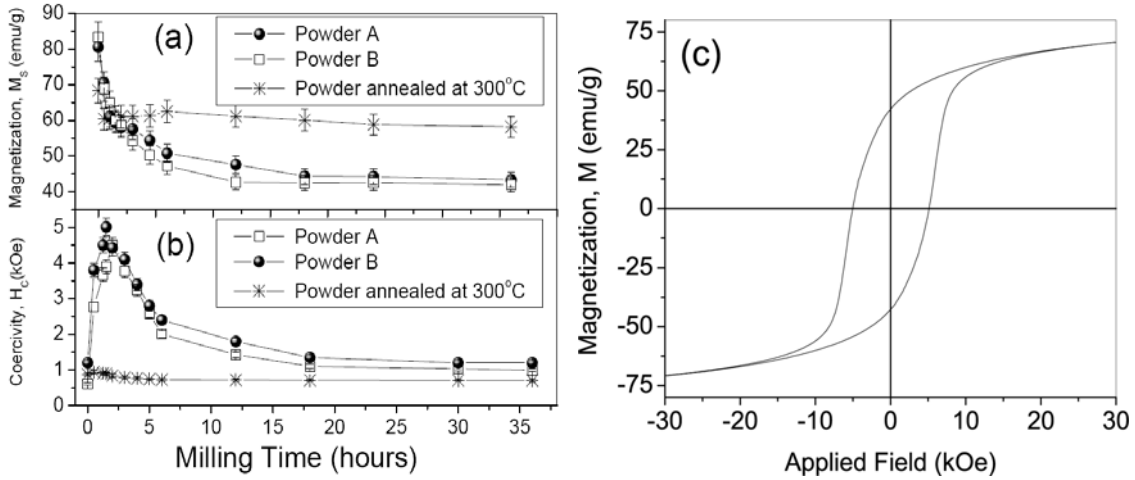

Figure 4.4 (a) Milling-time dependent coercivity (H_C) and (b) saturation magnetization (M_S) of the $CoFe_2O_4$ powders (Powder A, B and the sample annealed at 300°C); (c) the hysteresis loop of Powder A milled for 1.5 hours

4.4.2.2 XRD analysis

Fig. 4.5 shows the XRD spectra of Powder A before milling and after milling for different periods of time. As seen in Fig. 4.5, with the progress of mechanical milling, the broadening of diffraction lines was observed. Except $CoFe_2O_4$ phase, no other phase was detected. As it is well known, the broadening of the diffraction may be due to the size broadening and/or strain broadening. The separation of the size broadening from the strain broadening can be realized by using the Williamson-Hall plots.[10]

Fig.4.6 shows the Williamson-Hall plots of Powder A milled for different periods of time. Based on the mechanism and the procedures as mentioned in Chapter 2, the average grain size and the residual strain of the milled samples were derived. The derived residual strain and the average grain size are shown in Fig.4.7 (a) and (b) respectively. As seen Fig. 4.7 (a), the change in residual strain was quite similar to that of H_C with milling time as shown in Fig. 4.4 (b). It indicates that the highest H_C corresponds to the largest residual strain (around 1.03%) which appeared after milling for 1.5 hours. The results

suggest that the high coercivity is closely related to the large residual strain induced by mechanical milling. For Powder A before and after milling, XRD spectra showed similar patterns to Fig. 4.5. The milling-induced high-level residual strain was also detected in the milled Powder B as indicated in Fig. 4.7 (b). The change of residual strain also agreed with the change in H_C with milling time, as found in Powder A after mechanical milling.

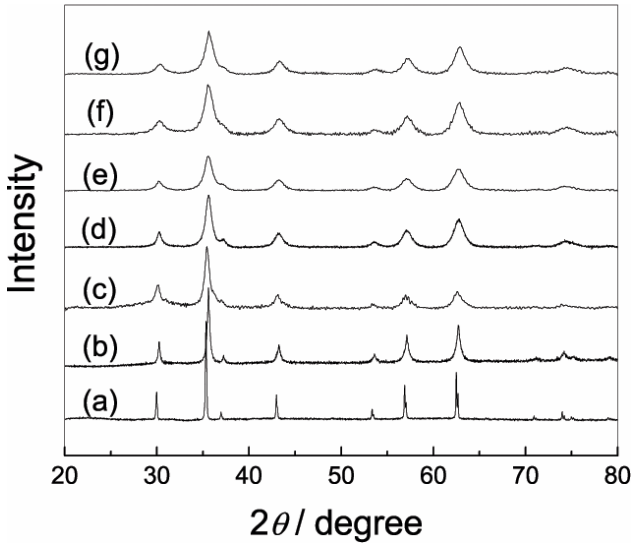

Figure 4.5 XRD spectra of Powder A before milling and after milling for different time: (a) annealed at 1000°C before milling; (b) milled for 30mins; (c) milled for 90mins; (d) milled for 3hours; (e) milled for 6 hours; (f) milled for 12 hours; (g) milled for 18 hours

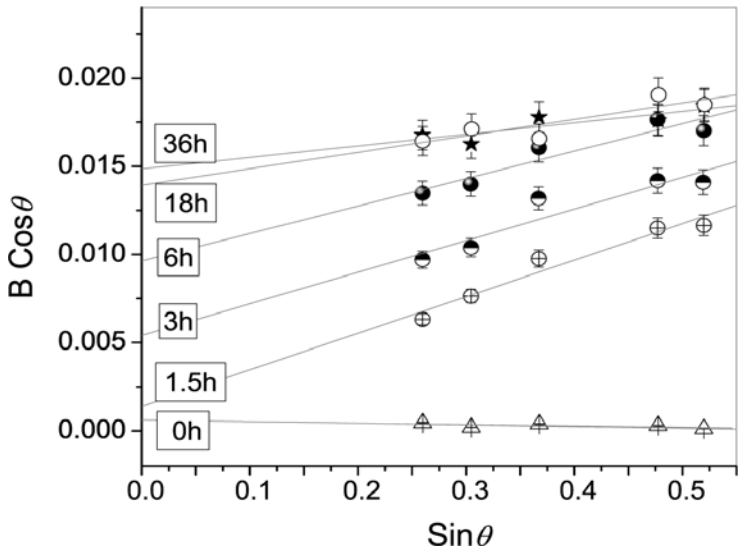

Figure 4.6 Williamson-Hall Plots of Powder A mechanically milled for different periods of time

On the other hand, the mechanical milling resulted in an apparent grain refinement for both Powder A and Powder B as indicated in Fig. 4.7 (a) and (b). The milled Powder A with the highest coercivity (5.1 kOe) had an average grain size of 110nm, while milled Powder B with the highest coercivity (4.6 kOe) had an average grain size of 174 nm. As discussed previously (Table 4.1), relatively low coercivities (0.9~1.3 kOe) were found in the annealed $CoFe_2O_4$ powders, when the grain size was in the range of 12-340 nm. The milling-induced high coercivities (around 5 kOe) were much higher than those in annealed samples with similar grain sizes (<1.3 kOe). These results indicated that the gain size effects do not play a major role in the high coercivity.[11]

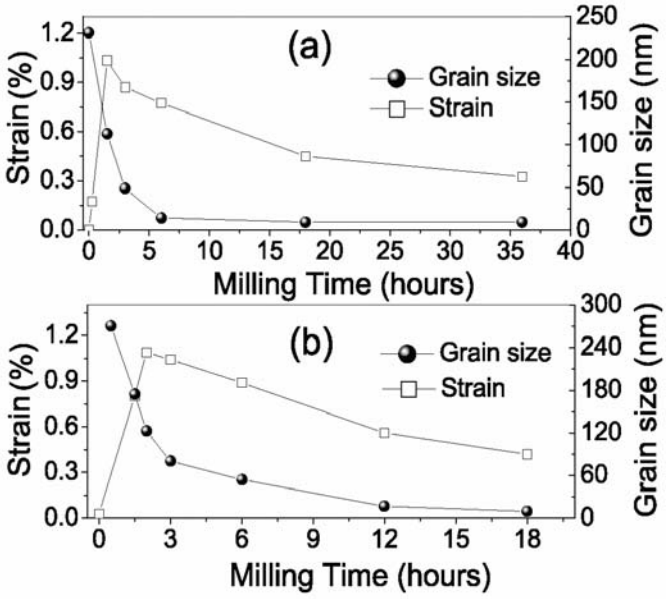

Figure 4.7 The variation of strain and average grain size of (a) Powder A and (b) Powder B with mechanical milling time

It is noted that the prolonged milling did not result in the continuous decrease of average grain size for both Power A and B. As indicated by Fig.4.7 (a) and (b), the final minimum average grain size after milling was around 10nm for both samples. In order to further examine the effects of mechanical milling on the grain refinement and the coercivity enhancement in nanosized $CoFe_2O_4$ powders, the sample annealed at 300^{o}C before

milling with the average grain size of 12nm was selected for further milling. Hereafter, the sample was named as Powder C. The time-dependent changes in magnetization M_S and coercivity H_C of Powder C were shown in Fig.4.4 (a) and (b). Compared to Powder A and B, Powder C showed relatively smaller reduction in magnetization (from approximately 68 emu/g to 57 emu/g), and its coercivity H_c remained nearly unchanged with the mechanical milling for up to 36 hours. Fig.4.8 shows XRD spectra of Powder C before milling and after milling for 18 hours and 36 hours. Detailed analysis indicates that mechanical milling did not lead to an apparent change in the spectra (peak shift and line broadening), and also no other phases were detected. Strain analysis based on Williamson-Hall plots[10] revealed no strain in samples before and after mechanical milling. In addition, the average grain size remained almost unchanged after milling for 36 hours. Therefore, above results indicated that the initial grain size of raw materials may play an important role in affecting the milling processes and thus magnetic properties of the milled samples.

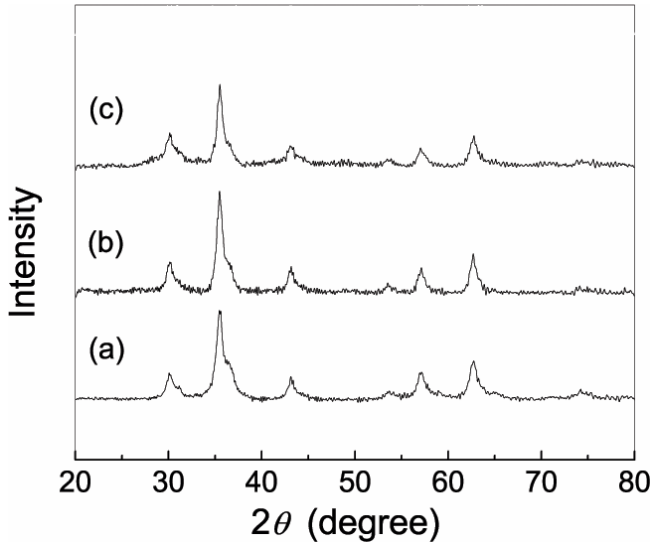

Figure 4.8 XRD spectra of Powder C before milling and after milling for different time: (a) annealed at 300°C before milling; (b) milled for 18 hours; (c) milled for 36hours

4.4.2.3 TEM analysis

4.4.2.3.1 Powder A and Powder B after milling

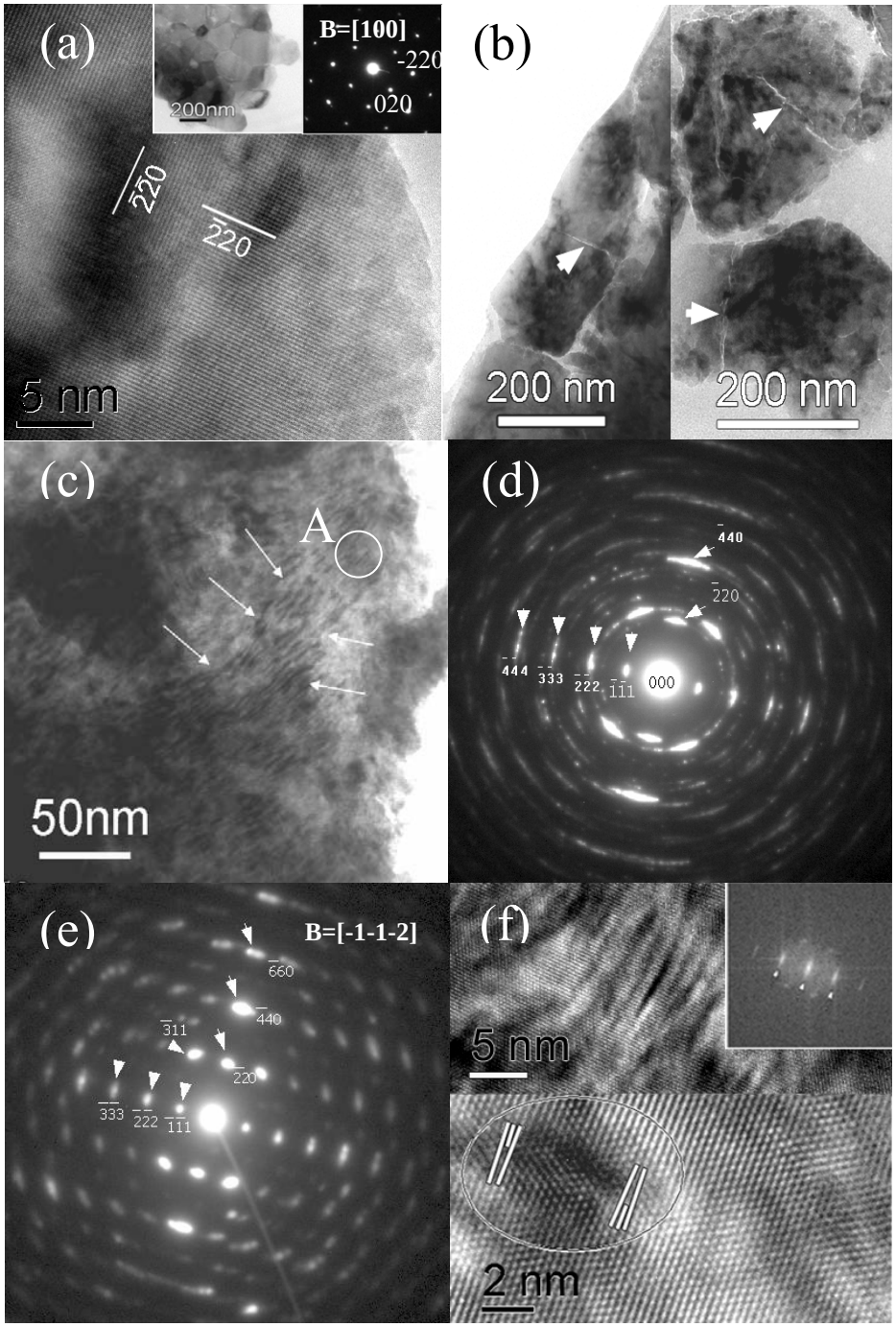

Figure 4.9 (a) high-resolution TEM image of Powder A before mechanical milling (inserted are bright-field TEM image and nanobeam electron diffraction pattern); (b)~(c) bright-field TEM images of Powder A as-milled for 1.5 hours; (d) the selected-area electron diffraction (taken from the large particles in Fig.4.10 (c)); (e) the nanobeam diffraction (taken from the area A in Fig.4.10(c)); (f) high-resolution TEM images of Powder A as-milled for 1.5 hours.

Before mechanical milling, Powder A possessed a well-crystallized structure with few defects as shown in the high-resolution TEM (HRTEM) image (Fig. 4.9(a)). As seen from Fig.4.3 (b), the uniform contrast inside each grain and along grain boundaries in TEM images may indicate a low strain level in the sample, as shown by bright-field TEM image (Fig. 4.3 (b)) and dark-filed TEM image (Fig. 4.3 (c)).

After mechanical milling for 1.5 hours, in Powder A, micro-cracks were observed as shown in Fig. 4.9(b) (indicated by arrows). These micro-cracks usually ran along the original grain boundaries, suggesting that the fracture processes have been induced by the short-time high-energy mechanical milling. In addition, many defects were seen inside each grain in both dark-field and bright-field due to their strain fields. The bright-field TEM image in Fig. 4.9(c) indicates the formation of distorted bands as indicated by arrows. These bands are so-called shear bands as often observed in the mechanically-milled materials.[15-17] The formation of subgrains inside particles or the "parent" grains took place, as verified by the selected-area electron diffraction in Fig. 4.9(d) (taken from the large particle in Fig. 4.9(c)), revealing a textured polycrystalline structure of the large particle. The nanobeam diffraction in Fig. 4.9(e) (taken from the circled area "A" in Fig. Fig. 4.9(c)) indicates that the textured grains are present with a similar orientation with respect to each other. Fig. 4.9(f) shows HRTEM images of the shear bands, revealing the strong distortion of these shear bands. The diffractogram from these irregular shear bands indicates double diffractions along a preferred orientation, which suggests that these shear bands are actually moiré fringes. The distortion of the moiré fringes could be ascribed to the existence of defects such as dislocations inside. Within these shear bands, many dislocations were observed. The associated strong strain contrast indicates a high level of strain in this sample. These results indicate that a highly strained defective

structure was formed in Powder A after mechanical milling for the relatively short time of 1.5 hours. Further mechanical milling up to 6 hours readily led to the formation of many nanosized subgrains inside the parent grains, which can be clearly evidenced by both bright-field and dark-filed TEM images shown in Fig. 4.10 (a) and (b). The selected-area electron diffraction pattern (inserted in Fig. 4.10 (a)) indicates the polycrystalline structure and the loss of the texture relationships among these grains. Further evidence of the formation of nanosized grains was provided by the high-resolution TEM image shown in Fig. 4.10 (c). As seen from it, several nanocrystals were formed with well distinguished grain boundaries. Some regions between the grain boundaries had a disordered or amorphous-like structure.

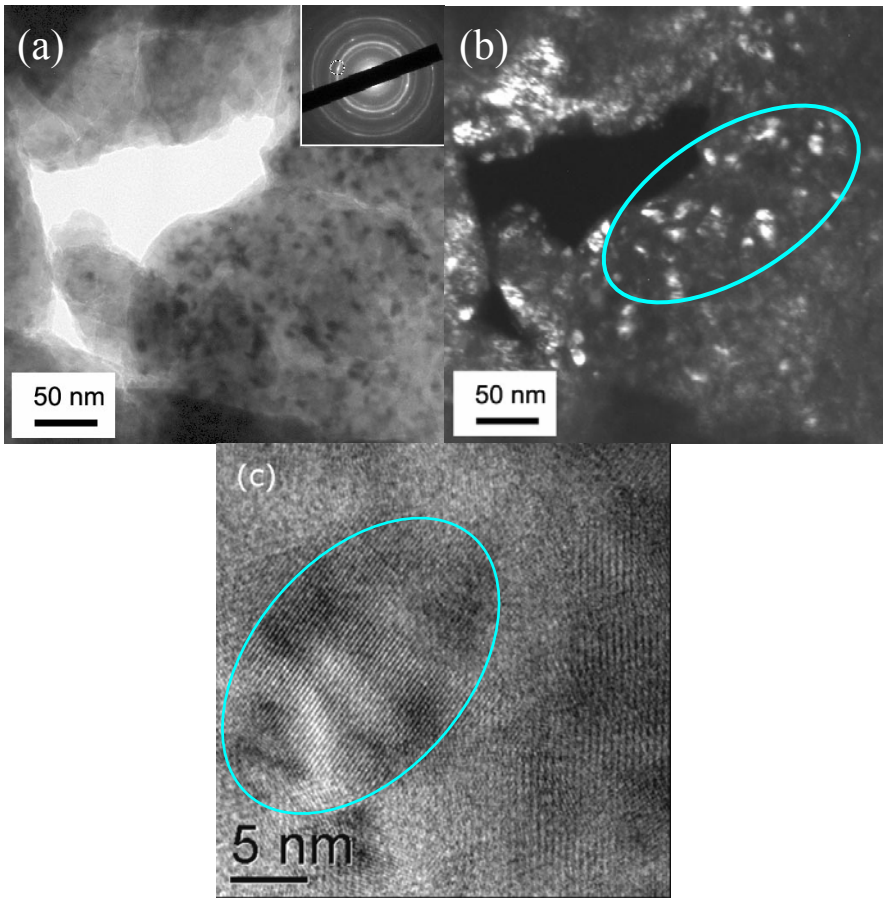

Figure 4.10 (a) Bright-field, (b) dark-field and (c) high-resolution TEM images of Powder A as-milled for 6 hours (inserted in (a) is the selected-area electron diffraction pattern)

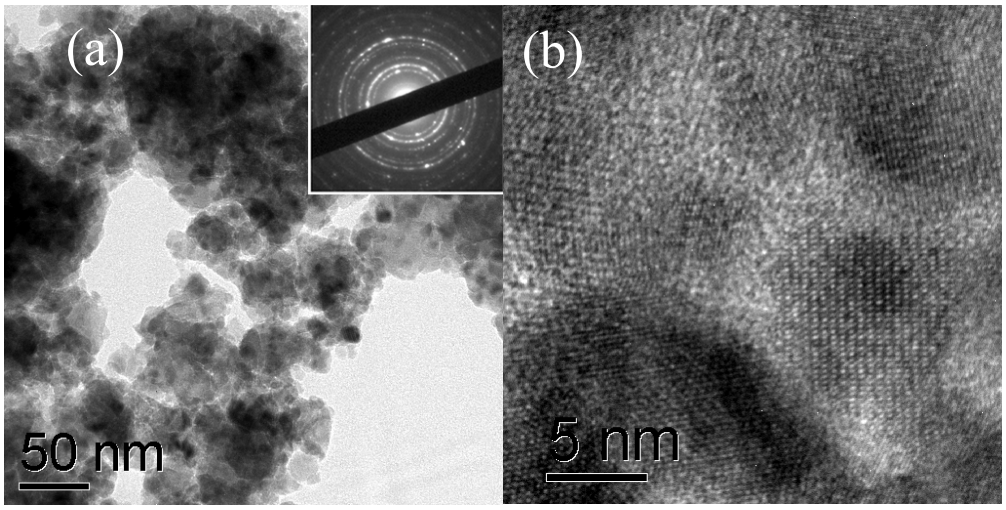

Figure 4.11 (a) Bright-field and (b) high-resolution TEM images with electron diffraction of Powder A milled for 36 hours

Prolonged mechanical milling up to 36 hours resulted in significant grain refinement as indicated by the bright-field TEM image shown in Fig. 4.11(a). The inset selected-area electron diffraction pattern also suggests the polycrystalline structure of the milled sample. High-resolution images in Fig. 4.11(b) suggested the formation of nanosized grains with an amorphous phase at the grain boundaries.

For Powder B, similar microstructures as for Powder A were observed under TEM after milling for 2 hours, 6 hours and 36 hours. It indicates that Powder A and Powder B underwent similar microstructure evolution during mechanical milling.

4.4.2.3.2 Powder C after milling

Fig. 4.12 (a) and (b) show respectively the bright-field and dark-field TEM images of Powder C after milling for 36 hours. Compared with the sample before mechanical milling, no apparent changes in morphologies were observed after milling for 36 hours. Dark-field TEM analysis (in Fig. 4.12 (b)) showed that no apparent change in average grain size was induced after mechanical milling for up to 36 hours. All these results

imply that prolonged mechanical milling did not induce appreciable microstructural changes in Powder C.

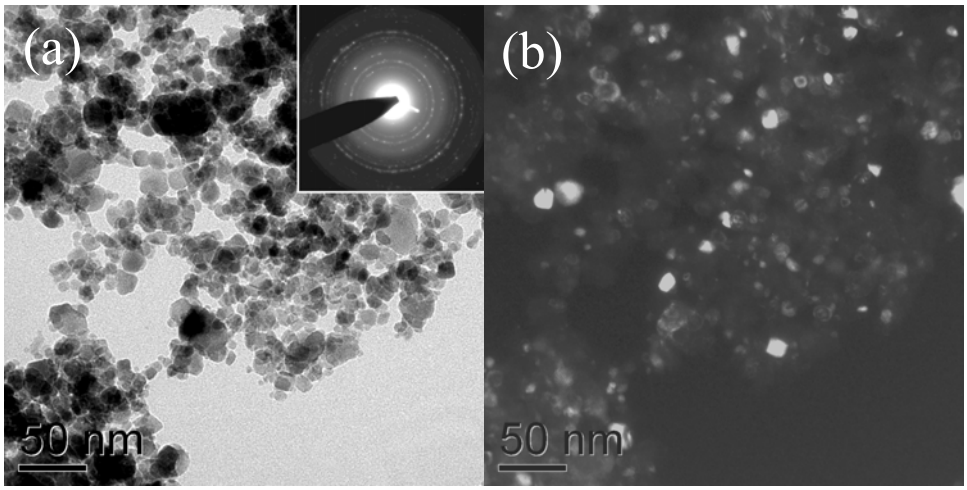

Figure 4.12 (a) Bright-field and (b) dark-field TEM images of Powder C as-milled for 36hrs (Inserted: the selected-area electron diffraction pattern)

4.5 Discussion

4.5.1 The milling-induced microstructure evolution and its effects on magnetic properties

4.5.1.1 Milled Powder A and Powder B

For large-grain $CoFe_2O_4$ samples such as Powder A and Powder B, apparent microstructural changes were induced by mechanical milling. Based on XRD and TEM analysis as mentioned above, we suggest that the microstructure evolution of large-grain $CoFe_2O_4$ powders can be illustrated by Fig.4.13, namely, (i) the initial stage with the formation of textured subgrains accompanied by the introduction of high-level strain and high-density defects; (ii) the intermediate stage with the formation of subgrains with the loss of texture and the decrease in both microstrain and defect density; (iii) the final stage with the formation of the final nanostructure.

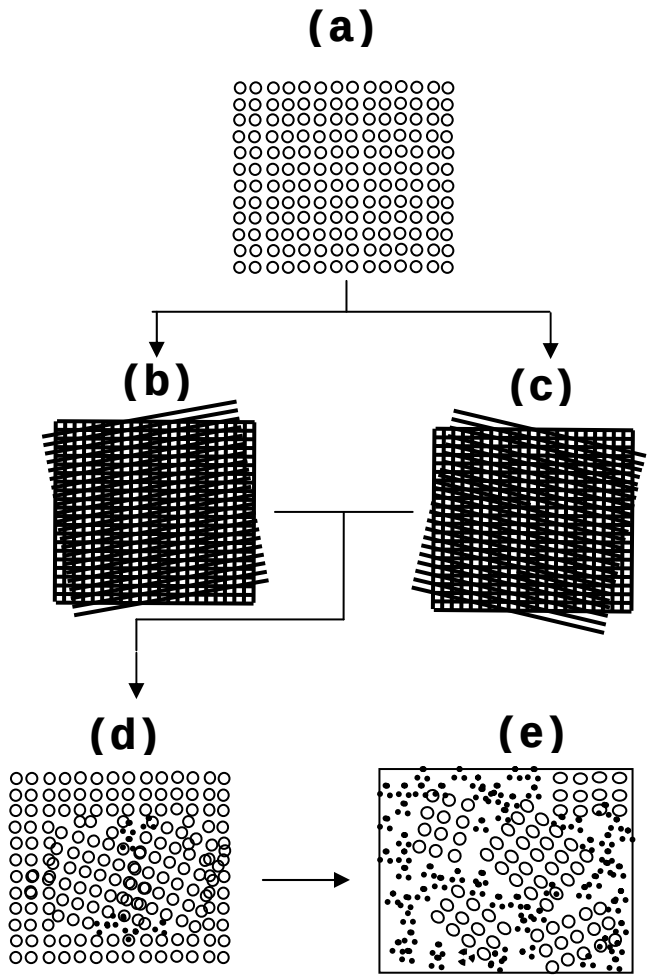

Figure 4.13 The schematic illustration of the proposed microstructure evolution of $CoFe_2O_4$ powders with large grain size during mechanical milling: (a) before milling; (b) and (c) the initial stage of milling; (d) the intermediate stage of milling; (e) the final nanocrystalline microstructure after the prolonged milling

A. The initial milling stage

At the initial stage of milling, typically with a milling time of several hours, the high-energy milling induced a highly-strained defective microstructure accompanied by the formation of subgrains inside the parent grains. The defective micorstructure was evidenced by the formation of distorted shear bands within which bountiful dislocations were observed. It was reported that the development of shear bands was responsible for the formation of subgrains during by mechanical milling with the accumulation of dislocations.[15-17] Therefore, the development of distorted shear bands signals not only

the formation of subgrains but also the accumulation of defects. The strong lattice distortion and strain contrast associated with distorted shear bands may suggest the high-level strain inside the sample. In addition, TEM analysis revealed textured structures among subgrains, implying the milling-induced gliding or rotation between subgrains or between subgrains and parent grains at this initial milling stage. Therefore, in areas with fewer defects, the slight misorientation between the subgrains led to the formation of more regular moiré fringes as illustrated in Fig.4.13 (b); while where there were many defects, distorted moiré fringes appeared as illustrated in Fig. 4.13 (c).

At this initial milling stage, both magnetization (M_S) and coercivity (H_C) of the milled samples underwent appreciable changes. A rapid decrease in the M_S was observed, which could be ascribed to the structural disordering and/or the partial amorphization at the grain boundaries. A rapid decrease in M_S with a short milling time was also observed in mechanically milled $SmCo_5$.[20] The milling-induced high coercivity at this milling stage could be related to the formation of a defective structure with a high level of strain and a high density of defects as mentioned above, which will be discussed in details later.

B. The intermediate milling stage

During this stage, further grain refinement occurred due to the accumulation of milling-induced defects, as for the samples milled for 6 hours. The increased structure disordering/amorphorization near grain boundaries were observed, which may lead to the strain release as indicated by XRD analysis. In addition, the loss of the texture and the formation of high-angle grain boundaries indicate that the subgrains were highly misoriented, which was verified by high-resolution TEM and electron diffraction. The structure formed at this stage can be illustrated by Fig.4.13 (d).

The decrease in Ms at this milling stage could be ascribed to the structural disordering and the formation of appreciable amounts of nanograins. The decrease in Hc could be due to the release of residual strain and the decrease in the defect density as well as the formation of nanograins that may appear superparamagnetic at room temperature.

C. The final milling stage

Prolonged mechanical milling led to the continuous grain refinement and finally reached an equilibrium microstructure, namely the formation of randomly oriented nanograins with amorphous-like phases in the region of grain boundaries, as illustrated by Fig. 4.13(e). The achievement of such a final nanostructure could be due to the balance between the milling-induced strain energy and the high surface energy of $CoFe_2O_4$ nanograins.[15] Hence further milling will not lead to further microstructural changes. In this study, the sample milled for 36 hours was close to the final milling stage, as indicated by high-resolution TEM analysis. Given the finite-size effects of nanocrystalline materials and the low magnetization and magnetic anisotropy of disordered materials,[11] the low values of M_s and H_c of the samples milled for 36 hours can be reasonable.

4.5.1.2 Milled Powder C

For Powder C with a nanocrystalline structure, as mentioned above, both structural and magnetic analysis suggested that mechanical milling did not induce significant changes in either microstructural or magnetic properties. It is recognized that, in very small crystals, the formation and the movement of the dislocations require very high strain energy, which hinders the deformation of nanograins.[15,18,19] This may well explain why Powder C did not show apparent structural changes even after prolonged milling for up to 36 hours. The decrease in Ms with milling might be due to the small amount of large

particles in the starting powders before mechanical milling. Since no compositional and microstructural changes were induced by mechanical milling, it is expected that the coercivity H_C of Powder C did not show apparent changes with milling.

4.5.2 The mechanism of milling-induced high coercivity

For large grain-sized $CoFe_2O_4$ materials such as Powder A, a high coercivity of up to 5.1 kOe has been induced by a short-time mechanical milling. Both XRD and TEM analysis revealed that such high coercivity may be related to the milling-induced defective microstructure with high-level strain and a high-density of defects. It is possible that the residual strain and defects may change either magnetic anisotropies or the reversal magnetization behaviours of the milled $CoFe_2O_4$ samples.

4.5.2.1 Magnetic anisotropy

Using the law of approach to saturation,[21,22] we estimated the magnetic anisotropy of the milled Powder A. As mentioned previously, if K_2 is ignored, the law of approach to saturation in case of the cubic anisotropy can be expressed by Eq. (4-1), i.e.

$$M(H) = M_S(1 - \frac{0.07619K_1^2}{H^2M_S^2}), \qquad (4\text{-}1)$$

where M(H) is the magnetization at an applied field of H and M_S is the saturation magnetization. The K_1 can be estimated by fitting M(H)-H curves at a certain field range. The estimated K_1 (more accurately, the effective anisotropy constant in this case) is shown in Fig. 4.14. Clearly, the change of K_1 was consistent with that of H_C as shown in Fig. 4.4(b), i.e., the highest H_C corresponded to the highest anisotropy constant. It indicates that the sample milled for 1.5 hours possessed an enhanced magnetic anisotropy, around 5.8 x10^5 J/m^3 which is approximately 50% higher than that of the sample before

milling. The enhanced magnetic anisotropy may have two possible contributions: (i) the change in the site occupation of magnetic ions due to mechanical milling; (ii) the stress anisotropy due to the milling-induced high-level strain.

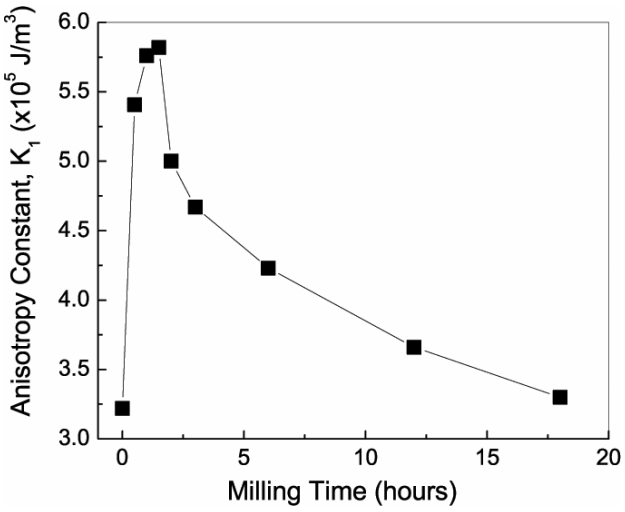

Figure 4.14 The variation of the magnetic anisotropy constant of Powder A with mechanical milling time

It has been recognized that the high magnetocrystalline anisotropy of $CoFe_2O_4$ arises from the incompletely quenched orbital momentum of Co^{2+} at the octahedral sites in the spinel lattice. Therefore, the change in cation distribution may lead to the change in the magnetocrystalline anisotropy and thus magnetic coercivity. Milling-induced cation redistribution has been reported in ferrite materials, such as $ZnFe_2O_4$ [23] and $MgFe_2O_4$.[24] In order to examine whether cation redistribution could be induced in $CoFe_2O_4$ samples after milling for a short time, Mössbauer analysis was conducted at 80K. Fig.4.15 shows the Mössbauer spectra at 80K of Powder A before milling and after milling for 1.5 hours. The fitting results are listed in Table 4.2. As seen from Fig.4.15 and Table 4.2, mechanical milling for 1.5 hour did not induce significant cation redistribution in Powder A. After milling for 1.5 hours, the fitting results showed that the absorption area ratio of A-site to B-site subspectra (α_A/α_B) was changed from 0.918 to 0.835, indicating that a

small amount of Co^{2+} ions have migrated from B sites to A sites. As the magnetocrystalline anisotropy of $CoFe_2O_4$ arises mainly from the contribution of Co^{2+} on the B sites, the milling-induced migration of Co^{2+} from B to A sites may decrease the magnetocrystalline anisotropy in $CoFe_2O_4$, as reported previously.[25,26] Therefore, the milling-induced enhancement in the magnetic anisotropy in Fig. 4.14 might be mainly resulted from other mechanisms, such as the stress anisotropy.

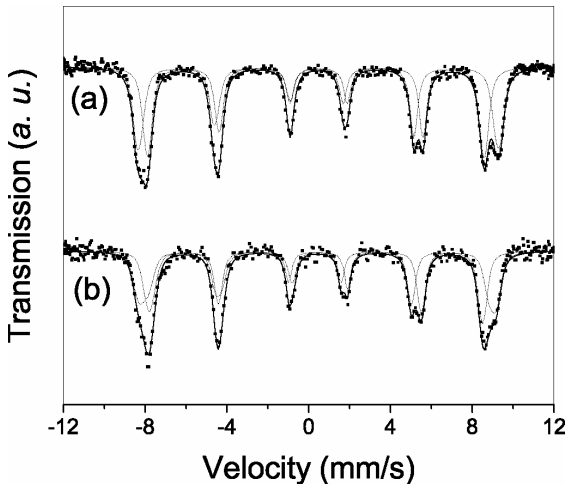

Figure 4.15 Mössbauer spectra (at 80K) of Powder A (a) before milling; (b) after milling for 1.5 hours

Table 4.2 The Mössbauer parameters (at 80K) of Powder A before and after milling for 1.5 hours and 18 hours (δ-isomer shift; Δ -quadrupole splitting; P-percentage; H-hyperfine field; α_A/α_B-absorption area ratio)

Sample	A site				B site				α_A/α_B
	δ (mm/s)	Δ (mm/s)	H (T)	P (%)	δ (mm/s)	Δ (mm/s)	H (T)	P (%)	
Before milling	0.372	-0.023	51.01	47.88	0.484	-0.010	54.55	52.12	0.918
Milled for 1.5 hours	0.329	0.026	50.55	45.53	0.498	-0.048	53.09	54.47	0.835

In terms of magnetoelastic theory, the residual strain may induce additional uniaxial magnetic anisotropy, i.e. stress anisotropy K_S. In case of isotropic magnetostriction, stress anisotropy is given by

$$K_S = \frac{3}{2}\lambda\sigma, \qquad (4\text{-}2)$$

where λ is the magnetostriction constant and σ is the stress which is proportional to strain via Young's modulus Y. For polycrystalline $CoFe_2O_4$ materials, the average magnetostriction constants λ is $-1.1\text{x}10^{-4}$ and Young's modulus Y is $142\text{x}10^9$ Pa (i.e. $1.42\text{x}10^{11}$ N/m^2).[14,27] Therefore, the estimated stress anisotropy K_S of Powder A milled for 1.5 hours (with a strain of ~1.03% estimated from XRD) is calculated to be 2.4 x 10^5 J/m^3. Given the magnetocrystalline anisotropy K_1 of $3.8\text{x}10^5$ J/m^3 of Powder A before milling, the effective anisotropy K_{eff} of the sample after milling could be $K_{eff} = \sqrt{K_1^2 + K_s^2}$,[28] i.e. 4.5 x$10^5$ J/m^3. This value is in the same order as that estimated by the law of approach to saturation in Fig.4.14. Based on the above discussion, the enhanced magnetic anisotropy observed in Powder A milled for 1.5 hours could be mainly attributed to the stress anisotropy. It is interesting to note that the coercivity increased from 1.23 kOe (before the milling) to 5.1 kOe after milling for 1.5 h for Powder A (corresponding to an increase rate of 360%), while the increase of anisotropy was approximately 50% (from 3.8 to 5.8 x10^3 J/m^3). Therefore, besides the stress anisotropy, other factors may also have an important contribution to the large increase of coercivity. As it is well known, the defects and strained areas may play as pinning centres to enhance the coercivity.[9,29-35] In order to examine the pinning-controlled mechanism, we choose the milled Powder A with the highest coercivity for the detailed investigation.

4.5.2.2 The initial magnetization and the field-dependent coercivity and remanence of milled Powder A

The examination of the initial magnetization behaviours of hard magnetic materials can provide useful information on magnetic hardening mechanisms. Generally, in case of the domain-wall pinning mechanism, the domain wall movement is hindered by some magnetic inhomogeneities such as dislocations, and thus low initial magnetic susceptibilities are expected. While in case of nucleation controlled mechanism, large initial susceptibilities are expected since the domain walls can easily move inside grains.[9]

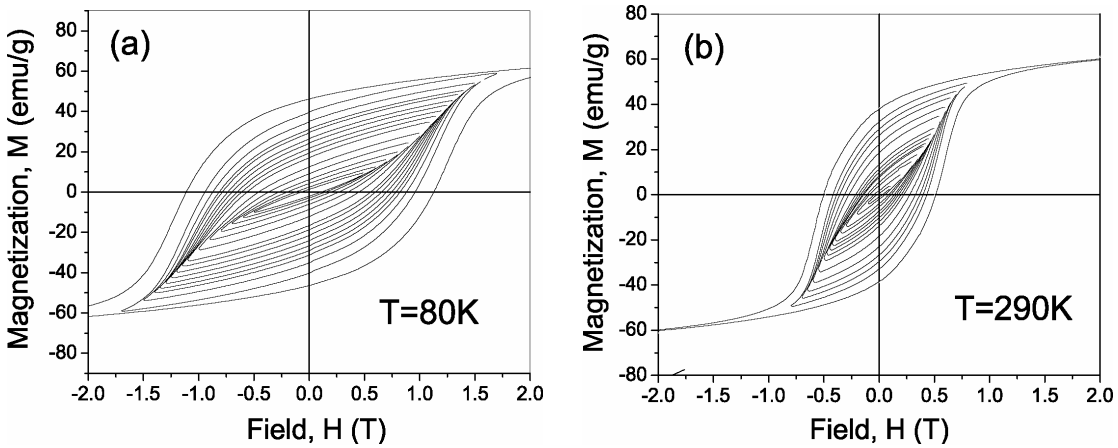

Figure 4.16 (a) The initial magnetization curves of Powder A as-milled for 1.5 hours measured at (a) 80K and (b) 290K

Fig.4.16 (a) and (b) show respectively the minor loops (80K and 290K) of Powder A as-milled for 1.5 hours. Based on the minor loops, the field-dependent initial magnetization $M_i(H)$ was derived and plotted in Fig.4.17 (a) at both 80K and 290K. Apparently, at both temperatures, the initial magnetization increased slowly at low applied field, and increased fast when the applied field reached a level comparable to the intrinsic coercive field, $H_{C,max}$. Similar behaviours were observed for the demagnetization processes of the sample, as indicated by the field dependent remanence $M_r(H)$ and coercivity $H_C(H)$ in Fig. 4.33 (b) and (c) respectively. This type of magnetization and demagnetization behaviours

can be generally described as the indications of domain-wall pinning mechanism.[29-35] In addition, there was no much difference in the field dependence of M_i (initial magnetization), H_C and M_r curves at 290K and 80K, suggesting the similar magnetic hardening mechanisms at both temperatures.

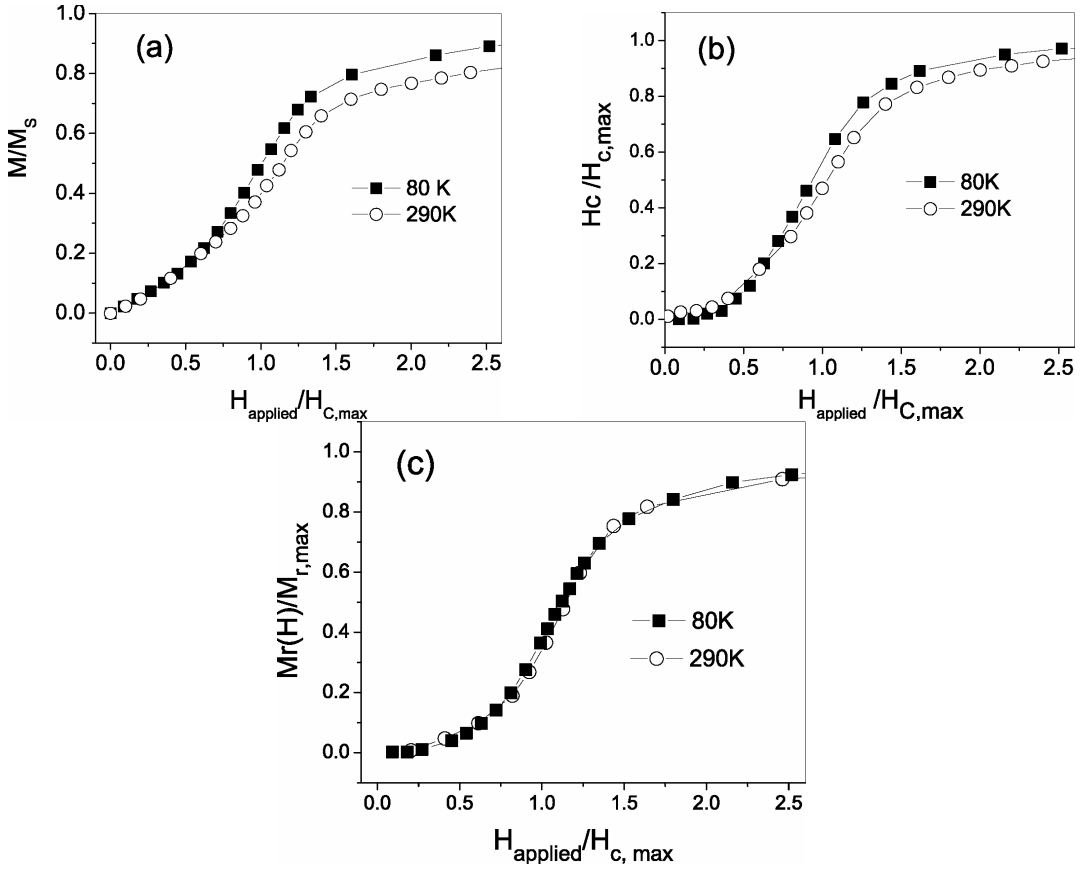

Figure 4.17 The normalized field dependence of (a) initial magnetization ($M_i(H)$), (b) coercivity $H_C(H)$ and (c) remanence ($M_r(H)$) of Powder A as-milled for 1.5 hours at 80K and 290 K ($H_{applied}$-applied field, $H_{c,max}$- the saturation coercivity measured at 60kOe, $M_{r,max}$-the saturation remanence)

4.5.2.3 The examination of temperature dependent coercivity

According to the micromagnetic model, the temperature dependent coercivity $H_C(T)$ can be expressed as[31-33,36,37]

$$H_C(T) = \alpha_k \alpha_\varphi H_N(T) - N_{eff} M_S(T), \qquad (4\text{-}3)$$

where H_N, M_S and N_{eff} are nucleation field, saturation magnetization and demagnetization factor respectively. α_φ and α_k are micromagnetic parameters which describe respectively the misalignment of grains and the anisotropy inhomogeneity range. Because of the cubic anisotropy and the random distribution of easy axis of milled $CoFe_2O_4$ samples, the nucleation field H_N can be expressed as

$$H_N(T) = a\frac{K_1}{\mu_0 M_S},$$

where *a* is an unknown constant, and thus Eq.(4-3) can be rewritten as

$$H_C(T) = a\frac{K_1(T)}{\mu_0 M_S(T)}\alpha_k\alpha_\varphi - N_{eff}M_S(T) \qquad (4\text{-}4)$$

In the case of the pinning controlled reversal magnetization, the temperature dependent coercivity $H_C(T)$, i.e. Eq. (4-4) can be expressed as [31-33,36,37]

$$H_C = b\frac{K_1}{3\sqrt{3}\mu_0 M_S}\frac{\pi r_0}{\delta_B} - N_{eff}M_s \qquad \text{if } r_0 < \delta_B \qquad (4\text{-}5)$$

and

$$H_C = b\frac{K_1}{\mu_0 M_S}\frac{2\delta_B}{3\pi r_0} - N_{eff}M_s, \qquad \text{if } r_0 > \delta_B, \qquad (4\text{-}6)$$

where r_0 and δ_B refer to the size of pinning site and the domain wall width respectively, and *b* is a constant.

As is known, domain wall width δ_B is proportional to $T_C^{1/2}/K_1^{1/2}$, where T_C and K_1 refer to Curie temperature and secondary magnetic anisotropy constant respectively.[11] Therefore, δ_B can be expressed as $\delta_B = c\frac{T_C^{1/2}}{K_1^{1/2}}$, where *c* is a constant. Considering the

temperature dependence of both K_1 and M_S, substitution of $\delta_B = c\frac{T_C^{1/2}}{K_1^{1/2}}$ into Eq.(4-5) and Eq.(4-6) leads to,

$$\frac{H_C(T)}{M_S(T)} = \frac{\pi K_1^{3/2}(T)}{3\sqrt{3}\mu_0 T_C^{1/2} M_s^2(T)}\frac{br_0}{c} - N_{eff}, \qquad \text{if } r_0 < \delta_B, \qquad (4\text{-}7)$$

and

$$\frac{H_C(T)}{M_S(T)} = \frac{2T_C^{1/2}K_1^{1/2}(T)}{3\pi\mu_0 M_s^2(T)}\frac{bc}{r_0} - N_{eff}, \quad \text{if } r_0 > \delta_B, \qquad (4\text{-}8)$$

The $H_C(T)$ and $M_S(T)$ can be experimentally obtained (Fig.4.18 (a)), and temperature dependent $K_1(T)$ can be derived by using the law of approach to saturation as mentioned above. For the milled Powder A with the highest coercivity of 5.1 kOe, the estimated temperature dependent magnetic anisotropy $K_1(T)$ is plotted out in Fig. 4.18 (b). According to the $K_1(T)$ function reported,[38] fitting the experimental data in Fig.4.18 (b) led to

$$K_1(T) = 1.29\times10^6 \times \exp(-1.0\times10^{-5}T^2) \qquad J/m^3, \qquad (4\text{-}9)$$

which is close to the $K_1(T)$ function as reported.[38]

Fig.4.19 (a) and (b) show two plots for testing these two pinning models as described by Eq.(4-7) and Eq.(4-8) respectively. It follows from a good linear relation between $\frac{H_C(T)}{M_S(T)}$ and $\frac{\pi K_1^{3/2}(T)}{3\sqrt{3}\mu_0 T_C^{1/2} M_s^2(T)}$ as shown in Fig.4.19 (a) that the coercivity is controlled by the magnetic inhomogeneities with the size smaller than the domain wall width, namely $r_0 < \delta_B$. This could be reasonable and consistent with the results of our TEM analysis by which high-density dislocations were observed in this sample. It is possible

that these low-dimensional defects act as the effective pinning centers for the hindrance of domain wall movement. Fitting the data in Fig.4.19 (a) gave rise to N_{eff} of around 0.8235, which is reasonable. However, due to the unknown constants *b* and *c*, the estimation of r_0 is impossible.

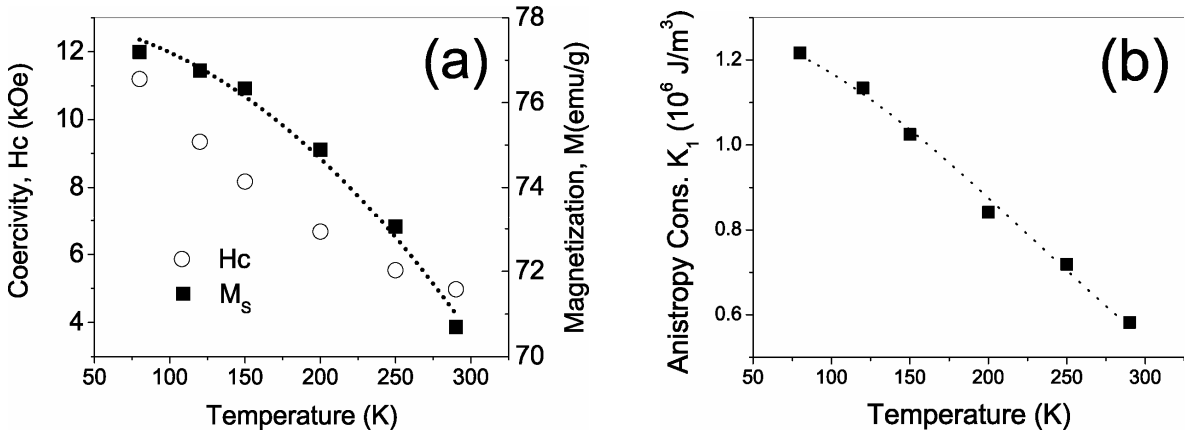

Figure 4.18 (a) The temperature dependent magnetic anisotropy, and (b) coercivity (H_C) as well saturation magnetization (M_S) of Powder A as-milled for 1.5 hours (Scatters: experimentally obtained data; lines: fitting curves);

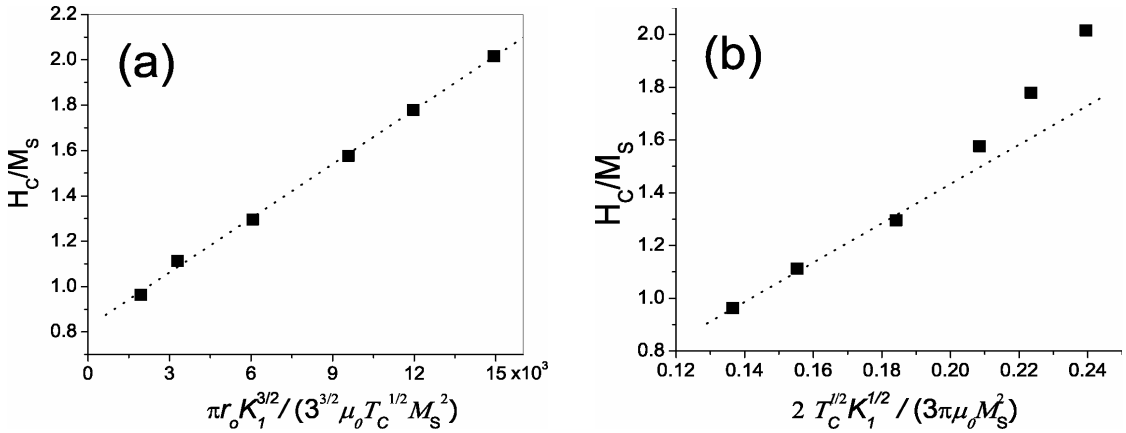

Figure 4.19 (a) Test of pinning-controlled coercivity mechanism with $r_0<\delta_B$; (b) test of pinning-controlled coercivity mechanism with $r_0>\delta_B$ for the Powder A as-milled for 1.5 hours

4.5.2.4 The magnetic viscosity and the examination of coercivity mechanism

4.5.2.4.1 Fundamentals of magnetic viscosity and the reversal magnetization processes

Magnetic viscosity, i.e., the time dependence of the magnetization under a constant external field H, arises from the thermal activation of the reversal magnetization over energy barriers. The time-dependent magnetization M(t) has the contributions from both reversible magnetization ($M_{rev}(t)$) and irreversible magnetization ($M_{irre}(t)$), and thus is given in general as [39-43]

$$M(t) = M_{irre}(t) + M_{rev}(t) \qquad (4\text{-}10)$$

where $M_{irre}(t)$ is defined as the remanent component obtained by the instantaneous removal of the field H at time t . Variations of $M_{rev}(t)$ with time are relatively small and arise for example from a magnetization-dependent demagnetizing field. So usually only $M_{irr}(t)$ is considered for the thermally activated reversal magnetization processes. [39-43] For most magnetic materials, the time-dependent irreversible magnetization obeys the logarithmic time dependent behaviors,[35,42,44,45] i.e.,

$$M_{irr}(t) = M_0 + S\ln(t), \qquad (4\text{-}11)$$

where S is the so-called magnetic viscosity and M_0 is the initial magnetization. Such a logarithmic dependence of the magnetization is often observed in permanent magnets and spin glass systems.[46] To measure the time-dependent magnetization, the sample was first saturated at a positive field (i.e. 60kOe in this study), and then magnetic field was fast changed to a negative field at which the time-dependent magnetization curve was measured. From the logarithmic dependence of the magnetization, the viscosity $S=-dM/d\ln t$ can be derived. S has a sharp maximum for applied magnetic fields in the vicinity of coercivity and it is much weaker when the applied field is very different from coercivity. In addition, it was observed that S is proportional to the irreversible susceptibility χ^{irre} as described by the Eq. (4-12) as

$$S_v = S / \chi^{irr} , \qquad (4\text{-}12)$$

where S_v is constant at a given temperature and has a dimension of magnetic field. It has been shown that S_v can be expressed as [46,47]

$$S_v = kT / (\partial E / \partial H)_T , \qquad (4\text{-}13)$$

where E is an activation energy which determines the observed magnetization relaxation, and kT refers to Boltzmann's energy. Therefore, the substitution of Eq. (4-13) into Eq. (4-12) leads to

$$S = \frac{kT}{(\partial E / \partial H)_T} \chi^{irre} \qquad (4\text{-}14)$$

The field-dependent activation energy $(\partial E / \partial H)_T$ is associated with the activation volume v_a by Eq. (4-15) as

$$(\partial E / \partial H)_T = M_S v_a \qquad (4\text{-}15)$$

where M_S is saturation magnetization. Thus, the activation volume v_a can be expressed as

$$v_a = \frac{kT \chi^{irre}}{M_S S} \qquad (4\text{-}16)$$

where kT, M_S, χ^{irre} and S refer to Boltzmann's energy, saturation magnetization, irreversible magnetic susceptibility and magnetic viscosities.[35,42,44,45].

The concept of the thermal activation volume is very important for understanding the reversal magnetization processes and coercivity mechanisms of hard magnetic materials. As is well known, the reversal magnetization processes correspond to a series of critical processes, such as the nucleation, domain wall expansion and pinning-depinning, each one occurring within a local critical volume under an effective critical field. The critical volume can be identified with the activation volume (v_a) which appears to be an important parameter for determining the coercive field of magnetic materials.[35,44,45] For

most magnetic materials, beside the external applied field, thermal activation can induce irreversible magnetization reversal over energy barriers. Thus, the thermal activation volume v_a associated with magnetic relaxation processes can provide useful information on coercivity mechanisms of hard magnetic materials.[9,35,42,44,45]

4.5.2.4.2 Examination of the coercivity mechanisms

To further confirm the pinning-controlled coercivity mechanism, we examined the reversal magnetization of Powder A as milled for 1.5 hours based on a phenomenological model. Based on the work of Barbier[48] and Wohlfarth,[45] Liu and Luo[30] proposed the relationship between the temperature-dependent $H_C(T)$ and the thermal activation volume $v_a(T)$ as

$$\lg H_C(T) = \lg v_a^{-1}(T) + b(T), \qquad (4\text{-}17)$$

where $b(T)$ is a function of temperature which characterizes the mechanisms of the magnetization reversal processes.

The temperature-dependent $b(T)$ can be obtained through the measurement of $H_C(T)$ and $v_a(T)$. While $H_C(T)$ can be directly measured experimentally, $v_a(T)$ has to be deduced based on Eq. (4-16). Thus, in order to deduce $v_a(T)$, we need to obtain the temperature-dependent magnetic viscosity S and the irreversible susceptibility χ^{irre}. The magnetic viscosity S can be derived from the time-dependent magnetization $M(t)$ at different field strength and different temperatures, based on Eq. (4-11). The χ^{irre} can be obtained by the derivative of the field-dependent DC demagnetization remanence ($M_d(H)$~H) curves at different temperatures, as mentioned in Chapter 2.[49,50]

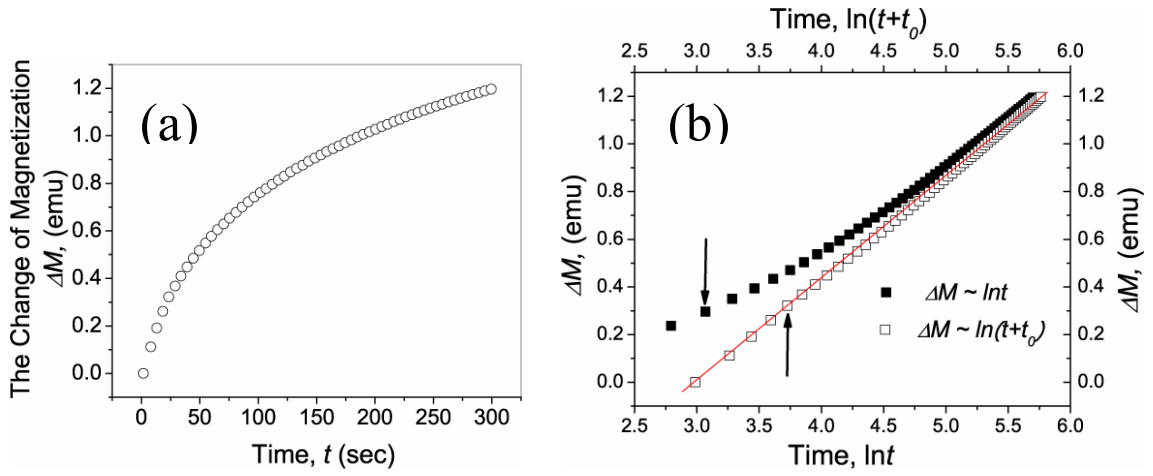

Figure 4.20 The time-dependent magnetization curves at 290 K with an applied field of 4 kOe: (a) t-dependence; (b) ln$t$ and ln$(t+t_0)$ dependence (ΔM is the change of the magnetization)

The time dependent magnetization $M(t)$ under different applied magnetic fields was measured at different temperatures, 80K, 120K, 150K, 200K, 250K and 290K. Fig. 4.20(a) shows a typical time-dependent change of magnetization ($\Delta M(t)$~t) curve measured at 290K with an applied field of 4 kOe. Clearly, the change of magnetization showed nonlinear time dependence. Thus the curve was fitted with Equation (4-11). However, the nonlinear logarithmic dependence was observed, as shown by the ΔM~ln$t$ curve in Fig. 4.20(b). Such nonlinear logarithmic dependence has been reported by Street et al.,[41,42,51] and a modified equation was proposed for fitting the non-linear magnetization curves, i.e.

$$M_{irr}(t) = M_0 + S\ln(t + t_0), \qquad (4\text{-}18)$$

where t_0 is a constant. With the modified function, a linear logarithmic time dependence was found as shown by the ΔM~ln$(t+t_0)$ curve in Fig. 4.20(b) with fitted t_0 value of 15. By following the similar procedures, the time-dependent magnetization curves at different temperatures and under different applied fields were measured and fitted.

Fig. 4.21 (a) and (b) showed the typical logarithmic time-dependent magnetization curves

that were measured at 80K and 290K respectively. The field-dependent $M_d(H)$ curves were obtained by measuring the DC demagnetization curves at the different temperatures. Fig. 4.21(c) and (d) show respectively the field-dependent $M_d(H)$ curves measured at 80K and 290K respectively. Therefore, the field-dependent viscosity S and the irreversible susceptibility χ^{irre} in the temperature range of 80K-290K were obtained. Fig.4.22 (a) and (b) show the typical field-dependent S and χ^{irre} curves at 80K and 290K respectively.

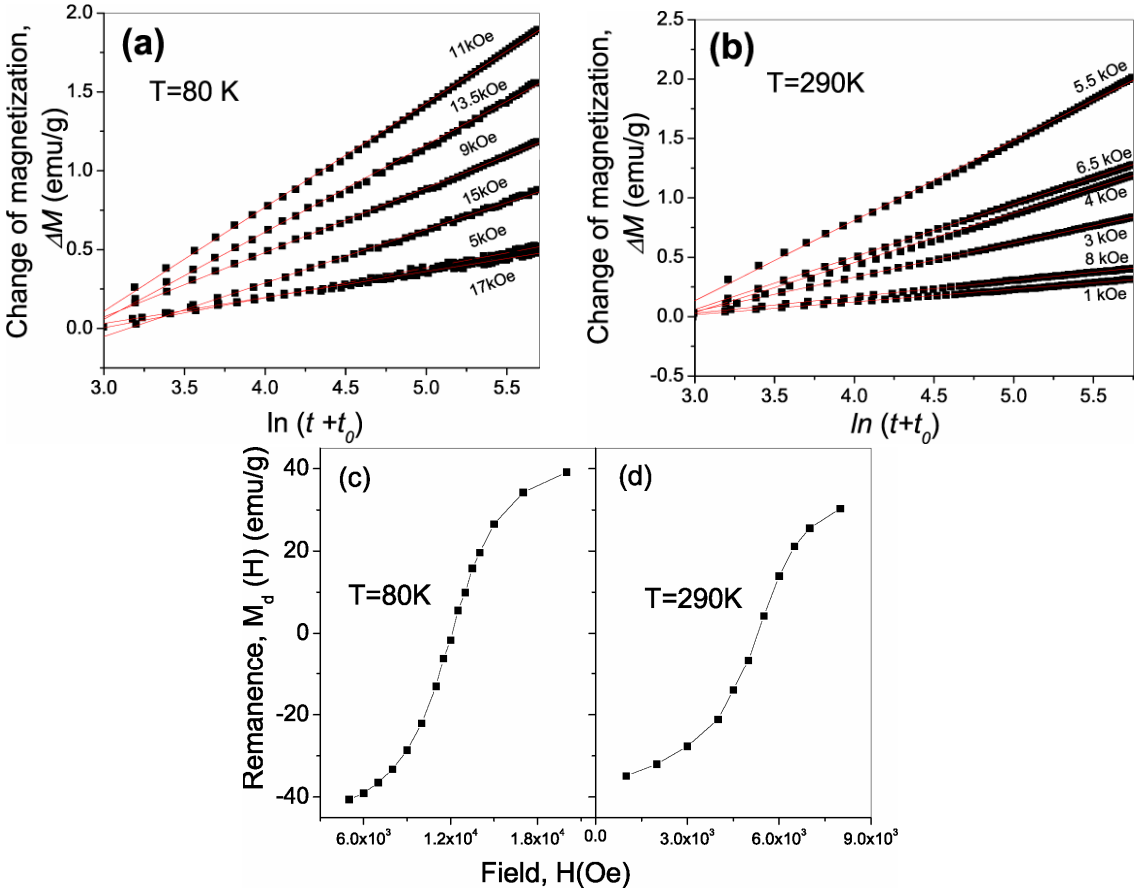

Figure 4.21 The time-dependent magnetization curves at (a) 80K and (b) 290K, and field-dependent remanence $M_d(H)$ at (c) 80K and (d) 290K for the Powder A as-milled for 1.5 hours

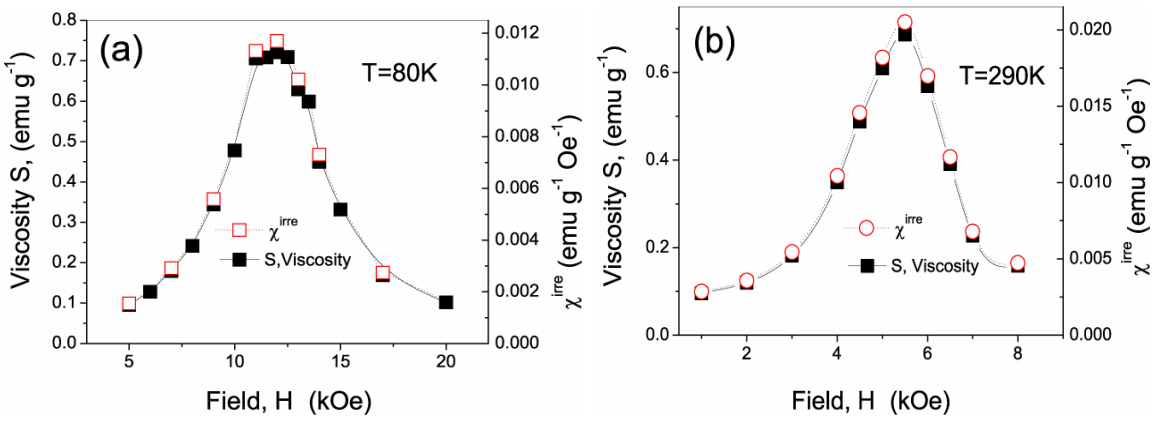

Figure 4.22 The field-dependent magnetic viscosity (S) and irreversible susceptibility (χ^{irre}) at (a) 80K and (b) 290K for the Powder A as-milled for 1.5 hours

Based on the Eq.(4-16), the temperature-dependent thermal activation volume v_a(T) is calculated and plotted out in Fig.4.23. Apparently, the activation volume decreased with temperature, implying the decrease in the size of the active regions that were responsible for the thermal activated magnetization reversal processes. At room temperature, the thermal activation volume v_a is around 3100 nm^3, which is comparable to the volume of a small spherical grain of 9nm in diameter, apparently smaller than the average grain size, 110nm as estimated by XRD analysis as mentioned above. In terms of physics of the pinning controlled reverse magnetization, the thermal activation volume v_a could be the volume of material which is covered by a single jump between pinning centers of a domain wall after thermal activation[45] or the volume associated with the magnetization change between the maximum and minimum energy positions of a domain wall or the maximum and minimum magnetization orientations in a single-domain,[35] or the volume related to pinning sites.[42] Whichever is true, the small activation volume v_a in this study may suggest that domain walls can not propagate freely through the inner part of the grains, and were probably pinned by the pinning sites inside the grains. According to the high resolution TEM analysis as mentioned above, mechanical milling for 1.5 hours has induced highly defective structure in $CoFe_2O_4$ materials with a high-level of strain and a

high-density of dislocation-typed defects. These dislocations inside grains could be active pinning centers that are responsible for the hindrance of domain wall movement.

With temperature decreasing, the activation volume v_a drops continuously, which could be understood in terms of the temperature dependence of the pinning force of pinning centers. As pointed out by Chen and Gaunt,[52] the pinning force f of a pinning site is linearly proportional to $K_1^{3/2}/A^{1/2}$, namely $f = aK_1^{3/2}/A^{1/2}$, where a, K_1 and A are a constant, the anisotropy constant and exchange constant respectively. Since A is proportional to the Curie temperature T_C[11], the pinning force can be written as

$$f = a K_1^{3/2} / T_C^{1/2} \quad , \qquad (4\text{-}19)$$

where a is a constant. Because T_C is a constant and K_1 increases with temperature decreasing, it is expected that the pinning force increases with temperature decreasing. Therefore, some pinning sites that are weak at room temperature can be "activated" at low temperatures due to their increased pinning force. This leads to either the increase in the density of active pinning sites or the decrease in the size of pinning sites with averaging out the size of all pinning sites. Therefore, the thermal activation volume v_a will decrease with temperature decreasing as shown in Fig. 4.22. Based on the experimentally obtained values of $H_C(T)$ and $v_a(T)$, the temperature dependent $b(T)$ was derived and is shown by scatters in Fig. 4.22.

As given in Ref.[30], for the strong pinning model, $b(T)$ can be expressed as

$$b(T) = \lg\{\frac{75kT}{4M_S}[(\frac{4f\delta_B}{75kT})^{2/3} - 1]\}, \qquad (4\text{-}20)$$

where k, T, M_S, f and δ are Boltzmann's constant; absolute temperature, spontaneous magnetization, the maximum pinning force from a single pin and domain wall width respectiviely.

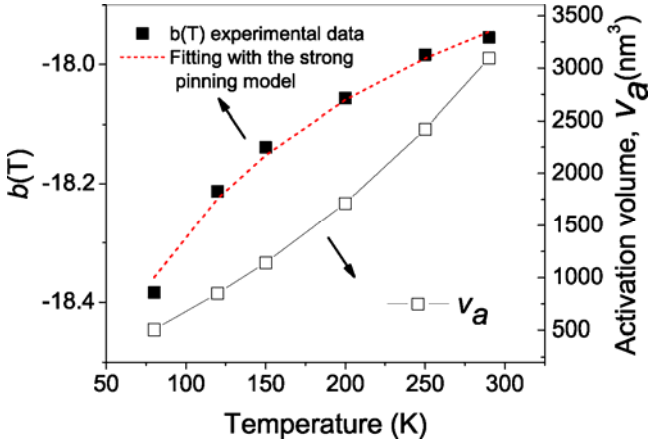

Figure 4.23 Temperature dependence of activation volume, v_a (denoted by scatters: □), and the experimentally obtained b(T) (denoted by scatters: ■) of Powder A as milled for 1.5 hours (the dotted curve was the b(T) curve fitted with the strong pinning model)

Apparently, Eq.(4-20) is a complex function. Fortunately, it was reported that $(\frac{4f\delta}{75kT})^{2/3} \gg 1$,[30,53] thus Eq.(4-20) can be rewritten as

$$b(T) \approx \lg[\frac{75kT}{4M_S}(\frac{4f\delta_B}{75kT})^{2/3}] \qquad (4\text{-}21)$$

Substitution of Eq.(4-19) and $\delta_B = c\frac{T_C^{1/2}}{K_1^{1/2}}$ into Eq.(4-21) leads to

$$b(T) \approx \lg[a^{2/3}\frac{(75kT)^{1/3}K_1(T)^{2/3}}{4M_S(T)}]$$
$$= \lg(c\frac{(T^{1/3}K_1^{2/3}(T)}{M_S(T)}), \qquad (4\text{-}22)$$

where *c* is a constant. If the coercivity mechanism of Powder A as-milled for 1.5 hours can be described by the strong pinning model, then the experimentally obtained *b*(T) can be well fitted by the function shown in Eq.(4-22).

The temperature dependence of M_S was shown in Fig. 4.18 (a) and the as-fitted function of M_S(T) was

$$M_S(T) = 78.02\text{-}8.0\times10^{-5}\ T^2\ \text{(emu/g)}, \qquad (4\text{-}23)$$

which follows the similar function as reported for $CoFe_2O_4$ materials.[54] With converting all the units into SI units and the combination of Equation (4-9) and (4-23), the temperature dependence of *b*(T) was fitted with Eq.(4-22). The as-fitted curve was shown in Fig. 4.23. As seen from Fig. 4.23, a good fitting was achieved, which suggests that the strong pinning model can well describe the coercivity mechanism in the Powder A as milled for 1.5 hours. This is consistent with the analysis based on both the micromagentic model and the field-dependent magnetization and demagnetization behaviors.

4.6 Conclusions

Mechanical milling was demonstrated to be an effective way for introducing a high level of strain and a high density of defects in $CoFe_2O_4$ powdered materials. A high coercivity of up to 5.1 kOe was induced by milling large-grained $CoFe_2O_4$ powders for a relatively short time of 1.5 hours. The initial grain/particle size was found to play an important role in affecting the microstructural evolution and the magnetic properties of $CoFe_2O_4$ powders during mechanical milling. The magnetic properties of milled $CoFe_2O_4$ powders showed different milling-time dependent behaviors for different precursors. Analysis based on XRD and TEM revealed the detailed microstructural evolution of $CoFe_2O_4$

powders during the mechanical milling. The results indicate that the milling-induced high coercivity was closely related to the high density of defects and high level of strain induced by milling. The enhanced in magnetic anisotropy was observed in large-grained samples after milling, which could be mainly due to the milling-induced stress anisotropy. In order to understand the coercivity mechanism behind the milling-induced high coercivity, we have presented detailed magnetic studies which revealed that the pinning controlled coercivity mechanism is responsible for the milling induced high coercivity. The pinning centers could be dislocation-type defects, highly strained areas and grain boundaries with the formation of subgrains during mechanical milling.

4.7 Reference

[1] J. H. Yin, J. Ding, B. H. Liu, X. S. Miao, and J. S. Chen, Appl. Phys. Lett. **88,** 162502 (2006).
[2] Y. C. Wang, J. Ding, J. B. Yi, B. H. Liu, T. Yu, and Z. X. Shen, Appl. Phys. Lett. **84,** 2596 (2004).
[3] B. G. Demczyk and J. O. Artman, J. Phys. D: Appl. Phys. **24,** 1627 (1991).
[4] J. Ding, T. Reynold, W. F. Miao, P. G. McCormick, and R. Street, Appl. Phys. Lett. **65,** 7074 (1994).
[5] A. Lisfi, J. C. Lodder, E. G. Keim, and C. M. Williams, Appl. Phys. Lett. **82,** 76 (2003).
[6] A. Lisfi and C. M. Williams, J. Appl. Phys. **93,** 8143 (2003).
[7] S. Nakagawa, Y. Kitamoto, and M. Naoe, IEEE Trans. Magn. **26,** 106 (1990).
[8] S. Nakagawa and M. Naoe, J. Magn. Magn. Mater. **120,** 345 (1993).
[9] H. W. Zhang, C. B. Rong, J. Zhang, S. Y. Zhang, and B. G. Shen, Phys. Rev. B, **66,** 184436 (2002).
[10] B. D. Cullity and S. R. Stock, *Elements of X-ray diffraction* (3rd edition, Prentice Hall, 2002).
[11] B. D. Cullity, *Introduction to magnetic materials* (Reading, Mass, Addison-Wesley Pub. Co., Holland, 1972).
[12] E. F. Kneller and F. E. Lubo, J. Appl. Phys **34,** 656 (1963).
[13] J. M. Coey, Phys. Rev. Lett **27,** 1140 (1971).
[14] D. J. Craik, *Magnetic oxides* (Wiley London , New York,, 1975).
[15] E. Hellstern, H. J. Fecht, C. Garland, and W. L. Johnson, Mater. Soc. Symp. Proc. **32,** 137 (1989).
[16] J. Y. Huang, Y. K. Wu, and H. Q. Ye, Acta. Mater. **44,** 1211 (1996).
[17] P. G. McCormick, W. F. Miao, P. A. I. Smith, J. Ding, and R. Street, J. Appl. Phys. **83,** 6256 (1998).
[18] J. Karch, R. Birringer, and H. Gleiter, Nature **330,** 556 (1987).
[19] P. E. Donovan and W. M. Stobbs, Acta. Metall. **31,** 1 (1983).
[20] D. L. leslie-pelecky and R. L. Schalek, Phys. Rev. B **59,** 457 (1999).
[21] R. Grössinger, **66,** 665 (1981).
[22] J. Willian Fuller Brown, Phys. Rev. **58,** 736 (1940).
[23] V. Sepelák, U. Steinike, D. C. Uecker, S. Wibmann, and K. D. Becker, J. Solid State Chem. **135,** 52 (1998).
[24] V. Sepelák, D. Baabe, F. J. Litterst, and K. D. Becker, J. Appl. Phys. **88,** 5884 (2000).
[25] J. C. Slonczeweski, Phys. Rev. **110,** 1341 (1958).
[26] R. F. Penoyer and L. R. Bickford, Phys. Rev. **108,** 271 (1957).
[27] M. D. Sturge, E. M. Gyorgy, R. C. LeCraw, and J. P. Remeika, Phys. Rev. **180,** 413 (1969).
[28] T. D. Shen, R. B. Schwarz, and J. D. Thompson, Phys. Rev. B **72,** 14431 (2005).
[29] U. S. Ram, D. Ng, and P. Gaunt, J. Magn. Magn. Mater. **50,** 193 (1985).
[30] J. F. Liu and H. L. Luo, J. Magn. Magn. Mater. **94,** 43 (1991).
[31] H. Kronmüller, Phys. Stat. Sol. (b) **144,** 385 (1987).
[32] X. C. Kou, H. Kronmüller, D. Givord, and M. F. Rossignol, Phys. Rev. B **50,** 3849 (1994;).

[33] D. Givord, Q. Lu, and M. F. Rossignol, *Sci. and Tech. Nanostruc. Mater.* (Plenum Press, New Yok, 1991).
[34] P. Gaunt and C. K. Mylvaganam, Philos. Mag. B **44,** 569 (1981).
[35] P. Gaunt, J. App. Phys. **59,** 4129 (1986).
[36] H. Kronmüller, K. D. Dust, and G. Martineck, J. Magn, Magn. Mater. **69,** 69 (1987).
[37] H. Kronmüller, K. D. Dust, and M. Sagawa, J. Magn, Magn. Mater. **74,** 291 (1988).
[38] H. Shenker, Phys. Rev. **107,** 1246 (1957).
[39] A. Lyberatos and R. W. Chantrell, J. Phys.: Condens. Matter **9,** 2623 (1997).
[40] J. Ding, R. Street, and H. Nishio, J. Magn. Magn. Mater. **164,** 385 (1996).
[41] R. Street and S. D. Brown, J. Appl. Phys. **76,** 6386 (1994).
[42] R. Street, R. K. Day, and J. B. Dunlop, J. Magn. Magn. Mater. **69,** 106 (1987).
[43] L. Wang, J. Ding, Y. Li, Y. P. Feng, and X. Z. Wang, J. Magn. Magn. Mater. **206,** 127 (1999).
[44] D. Givord, M. Rossignol, and V. M. T. S. Barthem, J. Magn. Magn. Mater. **258-259,** 1 (2003).
[45] E. F. Wohlfarth, J . Phys. F. **14,** L155 (1984).
[46] D. Givord, A. Lienard, P. Tenaud, and T. Viadieu, J. Magn. Magn. Mater. **67,** L281 (1987).
[47] P. Gaunt, Philos. Mag. **34,** 775 (1976).
[48] J. C. Barbier, Ann. de Phys. **9,** 84 (1954).
[49] K. Kanga, L. H. Lewis, J. S. Jiang, and S. D. Bader, J. App. Phys. **98,** 113906 (2005).
[50] S. Uren, M. Walker, K. O'Grady, and R. W. Chantrell, IEEE TRANSACTIONS ON MAGNETICS **24,** 1808 (1998).
[51] R. Street, L. Folks, and S. Hirosawa, in *Sixth Symposium on Magn. Anisotropy and Coercivity in Rare Earth-Transition Metal Alloys*, Pittsburgh, 1990.
[52] X. H. Chen and P. Gaunt, J. Appl. Phys. **67,** 2540 (1990).
[53] G. C. Hadjipanayis and A. Kim, J. Appl. Phys. **63,** 3310 (1988).
[54] R. Pauthenet, Ann. Phys. **7,** 710 (1952).

CHAPTER 5

The Synthesis and Magnetic Properties of Nickel-Cobalt Ferrites ($Ni_xCo_{1-x}Fe_2O_4$)

5.1 Background

In the previous studies, the influence of various factors on the magnetic properties of cobalt ferrite ($CoFe_2O_4$) powdered materials were studied. These include the effects of cation distribution, average grain size /size distribution, the milling-induced residual strain and defects on the magnetic coercivity of $CoFe_2O_4$ samples. High coercivities up to 5 kOe have been achieved in the powdered $CoFe_2O_4$ samples. As mentioned in Chapter 1 and Chapter 3, the magnetic hardness of $CoFe_2O_4$ materials stems from the large magnetocrystalline anisotropy due to the unquenched angular momentum of Co^{2+} ions. In other words, Co^{2+} ions play key roles in the intrinsic magnetic hardness of $CoFe_2O_4$ materials. If Co^{2+} ions are substituted by those ions with quenched angular momentum, such as Ni^{2+}, it is expected that the contribution of Co^{2+} ions to the intrinsic magnetocrystalline anisotropy will be decreased. The associated magnetic properties such as coercivity will be changed. On the other hand, in terms of magnetoelastic theory, stress anisotropy arises from the magnetostriction due to the spin-orbit coupling.[1] It is well recognized that the orbital momentum of Co^{2+} in $CoFe_2O_4$ is incompletely quenched, and thus $CoFe_2O_4$ possesses strong spin-orbit coupling and large magnetostriction. For polycrystalline $CoFe_2O_4$ materials, the magnetostriction constant (λ) was reported to be -110 x 10^{-6}.[2] Such a large magnetostriction is very unique among the cubic spinel ferrites. In contrast, the orbital momentum of Ni^{2+} in nickel ferrite ($NiFe_2O_4$) is almost fully quenched. Therefore, $NiFe_2O_4$ has a weak spin-orbit coupling and a small magnetostriction. The reported magnetostriction constant (λ) of polycrystalline $NiFe_2O_4$ materials is around -26 x 10^{-6},[2] about five times smaller than that of $CoFe_2O_4$. In this scenario, it could be expected that Ni^{2+} substitution in $CoFe_2O_4$ will lead to the changes in the magnetostriction behaviors of the resultant $Ni_xCo_{1-x}Fe_2O_4$ materials. Thus milling-induced stress anisotropy will be changed with Ni^{2+} substitution. Therefore, it will be

of interest to systematically examine the milling-induced stress anisotropy and the coercivity in the $Ni_xCo_{1-x}Fe_2O_4$ materials with Ni^{2+} substitution.

Therefore, Ni^{2+} substitution of Co^{2+} in $CoFe_2O_4$ materials could result in the changes in both intrinsic magnetocrystalline anisotropy and stress anisotropy in the resultant $Ni_xCo_{1-x}Fe_2O_4$ materials. It is thus interesting to systematically investigate the magnetization behaviors of the $Ni_xCo_{1-x}Fe_2O_4$ materials with different levels of Ni^{2+} substitution. In addition, as it is well known, nickel ferrite ($NiFe_2O_4$) is a type of soft materials with a very low magnetocrystalline anisotropy ($-6.5x10^3$ J/m^3).[3] If a large magnetic anisotropy can be induced in $NiFe_2O_4$ powders after mechanical milling, the induced anisotropy could be of purely magnetoelastic nature, i.e. stress anisotropy. In this case, it is possible to separate the stress anisotropy from the intrinsic magnetocrystalline anisotropy. Therefore, $NiFe_2O_4$ is an ideal material for studying the milling-induced anisotropy when considering its soft nature.

There are some studies on Ni^{2+} substitution for Co^{2+} in $CoFe_2O_4$ materials. Kim and et al. studied the effects of Ni^{2+} substitution on the atomic migration in nickel substituted cobalt ferrites (Ni-Co ferrite, $Ni_xCo_{1-x}Fe_2O_4$) powdered materials.[4] It was found that, with the increase in Ni^{2+} substitution, the temperature dependent migration of Fe^{3+} from A (tetrahedral) to B (octahedral) sites was enervated. But the work did not present the results regarding the effects of Ni^{2+} substitution on the magnetic properties of Ni-Co ferrites.[4] By the co-precipitation method, Yamamoto et al synthesized Co-Ni ferrite ($Ni_xCo_{1-x}Fe_2O_4$) fine particles.[5] They presented a detailed study on the effects of Ni concentration on the magnetic properties of $Ni_xCo_{1-x}Fe_2O_4$ powders. With the increase in Ni^{2+} substitution, it was found that the saturation magnetization decreased monotonously, but the coercivity first increased and then decreased. A maximum coercivity of around 3.5 kOe was observed for the $Ni_{0.7}Co_{0.3}Fe_2O_4$ sample.

[5] In contrast, both Zhang et al[6] and Kitamoto et al[7] reported a different coercivity dependence on Ni^{2+} substitution in Ni-Co ferrite thin film materials. In both works, it was found that both the saturation magnetization and the coercivity monotonously decreased with increasing Ni^{2+} substitution.[6,7] Therefore, the results as reported are contradictive regarding the coercivity dependence of Ni^{2+} substitution. Such contradictive results could be possible if we consider the complex dependence of the coercivity on the microstructure, phase and site occupation of magnetic ions in $Ni_xCo_{1-x}Fe_2O_4$ ferrite materials. Unfortunately, the works mentioned above did not give detailed studies. Therefore, in order to understand the effects of the Ni^{2+} substitution on the magnetic properties, a systematic study is necessary to reveal the details regarding the microstructure, phase and site occupation of the synthesized $Ni_xCo_{1-x}Fe_2O_4$ ferrite materials.

Although the co-precipitation process has been successfully employed to synthesize the $Ni_xCo_{1-x}Fe_2O_4$ ferrite powdered materials, [5] the processing parameters were not easy to be controlled in order to get single-phase spinel ferrite. As pointed out by H. Yamamoto et al, α-FeOOH phase was formed when the molar ratio of Ni^{2+}/Co^{2+} was high. [5] This could be due to the fact that the formation of Ni ferrite was slower than that of Co ferrite and an excess of Fe^{3+} was preferably reacted to form α-FeOOH phase.[5] Therefore, in terms of experimental setup and phase control, the co-precipitation process may not be preferable for synthesizing single-phased $Ni_xCo_{1-x}Fe_2O_4$ ferrite powdered materials. In contrast, the mechanochemical process was a unique technique with easy experimental setup for synthesizing various spinel ferrite materials, such as $CoFe_2O_4$ materials, as discussed in Chapter 3. The advantages of the mechanochemical process have also been highlighted in Chapter 3. In this work, the mechanochemical process has been selected for synthesizing $Ni_xCo_{1-x}Fe_2O_4$ ferrite materials. Further mechanical milling of the $Ni_xCo_{1-x}Fe_2O_4$ ferrite materials will also

be studied in order to understand the effects of mechanical milling on the magnetic properties of the substituted cobalt ferrites.

On the other hand, as discussed in Chapter 4, relatively large lattice expansion was detected in the milled $CoFe_2O_4$ samples. The largest lattice expansion was around 0.14% in the sample milled for 1.5 hours. However, no additional reflections were observed in both x-ray diffraction and electron diffraction analysis for this sample. It means that such a level of lattice expansion could not induce phase change and the sample remained its cubic symmetry. Also in literatures, there is no report regarding the phase changes in $CoFe_2O_4$ materials under any circumstance. In contrast, magnetite (Fe_3O_4) is an interesting and unique material which has demonstrated the phase change under thermal and mechanical treatments. The phase change related to thermal effects is the famous Verwey transition which occurs at a critical temperature (T_V) near 125K. The origin of the Verwey transition has been ascribed to the charge disordering and ordering above and below T_V.[8-11] Within this model, the charge ordering will produce a structural phase transition from the cubic to an orthorhombic phase.[8-11] It was also reported that the Verwey transition temperature (T_V) was strongly dependent on pressure.[9] As it is well known, mechanical milling is a high-energy deformation process. The fast collision between powder and the milling balls can produce unusually high temperature and pressure. It was reported that, the microscopic temperature and the pressure generated during mechanical milling can be up to 1000^oC[12-14] and 6 GPa[8,14,15] respectively. Therefore, in this work, Fe_3O_4 will be subjected to the high-energy mechanical milling in order to examine whether high-energy mechanical milling could induce the phase transformation.

5.2 Purposes of study

In terms of above arguments, the purposes for this study can be summarized as the followings:

(i) To explore the feasibility of synthesizing single-phase $Ni_xCo_{1-x}Fe_2O_4$ (x=0.1~1) powdered materials by mechanochemical process.

(ii) To present a systematic study on the effects of the Ni^{2+} substitution on the magnetic properties of mechanochemically synthesized $Ni_xCo_{1-x}Fe_2O_4$ powdered materials. The major efforts will be devoted to studies on the magnetocrystalline anisotropy associated with phase and site occupation of $Ni_xCo_{1-x}Fe_2O_4$ materials. With these studies, we expect to better understand the key roles played by Co^{2+} ions in the coercivity of cobalt ferrite materials.

(iii) To examine whether mechanical milling can still induce a high coercivity in $NiFe_2O_4$ materials. If it is true, to systematically investigate the microstructure evolution during milling and its effects on the magnetic properties of $NiFe_2O_4$ materials, and to study the correlations between milling-induced coercivity and stress anisotropy/pinning effects of defects

(iv) To study the effects of mechanical milling on the magnetic properties of $Ni_xCo_{1-x}Fe_2O_4$ materials with different levels of Ni^{2+} substitution.

(v) To investigate the microstructure evolution and its effects on the magnetic properties of $Ni_xCo_{1-x}Fe_2O_4$ materials, and to study the correlations between milling-induced magnetic coercivity and stress anisotropy/pinning effects of defects.

(vi) To mechanically mill magnetite (Fe_3O_4) samples and to examine whether mechanical milling could induce phase transformation.

5.3 Synthesis of Ni-Co Ferrites ($Ni_xCo_{1-x}Fe_2O_4$, x=0.1~1) by Mechanochemical Process

5.3.1 Experiments

For synthesizing $Ni_xCo_{1-x}Fe_2O_4$ (x=0.1, 0.3, 0.5, 0.7, 0.9 and 1) samples, metal Co, Ni and α-Fe_2O_3 powders were used as the raw materials. With the proper molar ratios, the raw powders were mixed and ground in a mortar before the mechanical milling. The mechanochemical synthesis of $Ni_xCo_{1-x}Fe_2O_4$ samples was performed using a Spex-8000 high-energy miller with a ball to powder ratio of 12:1. For all samples, the milling time was 24 hours. The milled powders were then annealed at different temperatures (400~1200^oC) for 2 hours followed by slow cooling process (1^oC/min).[16]

The phases, grain size and residual strain of all $Ni_xCo_{1-x}Fe_2O_4$ samples were analyzed by X-ray diffraction (Bruker XRD with CuKα radiation). The lattice parameters for each $Ni_xCo_{1-x}Fe_2O_4$ sample were deduced by using the extrapolation function method.[17] The separation of the line broadenings due to the grain-size effect and the strain effect of XRD diffraction peaks was based on the Williamson-Hall plots.[18] The microstructure of the milled samples was examined using a transmission electron microscopy (TEM, JEOL JEM 3010) operated at 300kV. A VSM (Vibration Sample Magnetometer, lakeshore 4500) was used for the room-temperature magnetic analysis and the Curie temperature measurements. For Curie temperature measurements, the temperature-dependent magnetization was recorded with a small applied field of 200 Oe. ^{57}Fe (^{57}Co in a Rh matrix) Mössbauer spectroscopy (FAST ComTec, Germany) was used for the analysis of the site occupation of the magnetic ions in the $Ni_xCo_{1-x}Fe_2O_4$ spinel lattice. A spectrum of metallic bcc-Fe was used for the calibration. Low temperature Mössbauer measurements were conducted in a liquid nitrogen cryostat.

Spectra were analyzed with a analytical program (Recoil). The area ratio of tetrahedral (A site) to octahedral (B site) subspectra was used for the determination of cation distribution.

5.3.2 Results and Discussion

5.3.2.1 X-ray diffraction (XRD) analysis

The XRD analysis indicated that the mechanical milling of Co, Ni and α-Fe_2O_3 powders for 24 hours directly led to the $Ni_xCo_{1-x}Fe_2O_4$ spinel phase, just as for the mechanochemical synthesis of $CoFe_2O_4$ samples as discussed in Chapter 3. Besides the spinel phase, there were some residual α-Fe_2O_3, Co and/or Ni phases after milling for 24 hours, as evidenced by some weak diffraction peaks in Fig. 5.1 (a). The appearance of the weak diffraction from α-Fe_2O_3, Co and/or Ni phases implied that the formation of spinel phase was not fully completed after the mechanochemical milling for 24 hours. In order to obtain pure spinel phase, the milled samples were annealed in air at different temperatures with a slow cooling process (1^oC/min). With a subsequent thermal annealing at 400^oC, the diffraction from the residual α-Fe_2O_3, Co and/or Ni phases became apparently weaker, as shown by Figure 5.1 (b). After annealing at the temperatures higher than 600^oC, all the diffraction peaks can be assigned to the spinel phase, suggesting the complete formation of the spinel phase, as shown by Figure 5.1 (c)~(f).

Based on the Scherrer equation, the average grain size of the annealed $Ni_{0.5}Co_{0.5}Fe_2O_4$ samples was estimated from the strongest 311 diffraction. Figure 5.2 shows the dependence of average grain size of the $Ni_{0.5}Co_{0.5}Fe_2O_4$ samples on the annealing temperature. Clearly, average grain size increased with the increase of annealing temperature. The results were similar to those of the mechanochemically synthesized

$CoFe_2O_4$ samples after annealing, as discussed in Chapter 3.

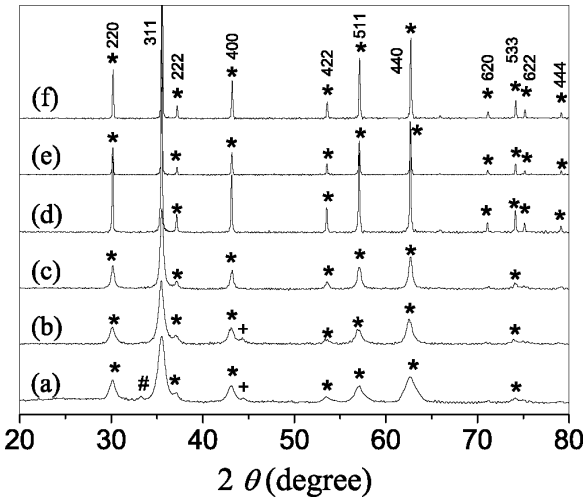

Figure 5.1 The XRD spectra of the mechanochemically synthesized $Ni_{0.5}Co_{0.5}Fe_2O_4$ samples before and after annealing (a): the sample milled for 24 hours; (b) after annealing at 400°C; (c) after annealing at 600°C; (d) after annealing at 800°C; (e) after annealing at 1000°C; (f) after annealing at 1200°C) (*: spinel phase; #: α-Fe_2O_3; +: Co and/or Ni)

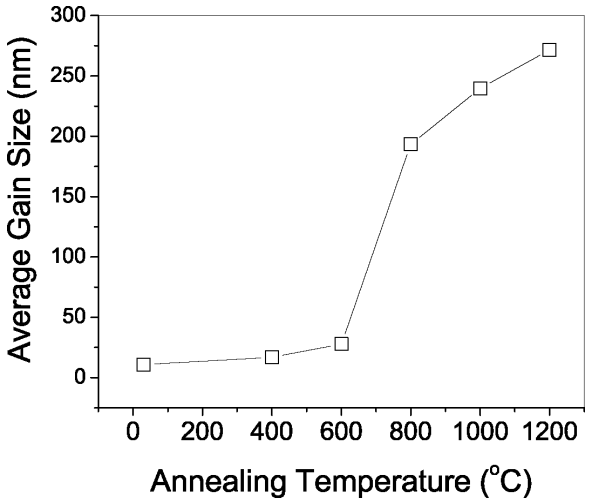

Figure 5.2 The dependence of average grain size of the $Ni_{0.5}Co_{0.5}Fe_2O_4$ samples on the annealing temperature

For other mechanochemically synthesized $Ni_xCo_{1-x}Fe_2O_4$ (x=0.1, 0.3, 0.7, 0.9 and 1) samples, the XRD analysis indicated that the thermal annealing led to the similar phase evolution and the increase in average grain size, as for the $Ni_{0.5}Co_{0.5}Fe_2O_4$ samples. The average grain size of the $Ni_xCo_{1-x}Fe_2O_4$ samples annealed at the same temperature was also comparable.

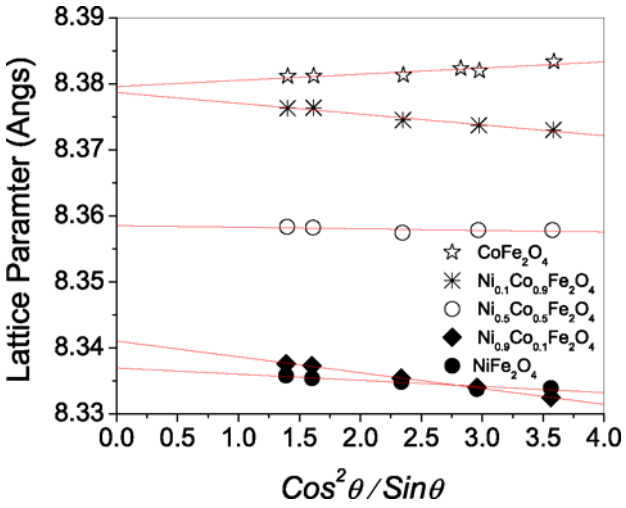

Figure 5.3 The plots of the lattice parameters as a function of the displacement extrapolation factor ($cos^2\theta/sin\theta$) for the $Ni_xCo_{1-x}Fe_2O_4$ samples annealed at 1000°C

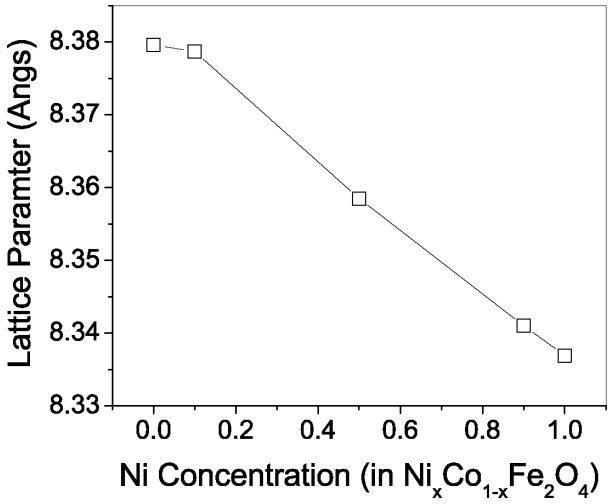

Figure 5.4 The dependence of the lattice parameters on Ni concentration for the $Ni_xCo_{1-x}Fe_2O_4$ samples annealed at 1000°C

In order to investigate the Ni^{2+} substitution on the lattice parameters of the $Ni_xCo_{1-x}Fe_2O_4$ samples, the samples annealed at 1000°C were selected for a detailed study as these samples are of single spinel phase and well crystallized. Based on the extrapolating method as mentioned in Chapter 2, the lattice parameters (a) for each $Ni_xCo_{1-x}Fe_2O_4$ sample were deduced by plotting $a(\theta)$ against the displacement extrapolation factor ($cos^2\theta/sin\theta$) and extrapolating to θ=90°.[17] The plots of the lattice parameters as a function of the displacement extrapolation factor are shown in Figure 5.3. Based on the lineal fitting results, the deduced the lattice parameters for each composition were shown in Figure 5.4. As seen from Figure 5.3 and 5.4, with

increasing Ni concentration (x), the lattice parameters continuously decreased. This can be understood in view of the fact that the Ni^{2+} ion (radius of 0.69 Å) is smaller than Co^{2+} ion (radius of 0.78 Å).[4] The lattice parameters of $CoFe_2O_4$ (8.380 Å) and $NiFe_2O_4$ (8.337 Å) obtained in this study are well consistent with those reported.[4,19]

5.3.2.2 Curie temperature analysis

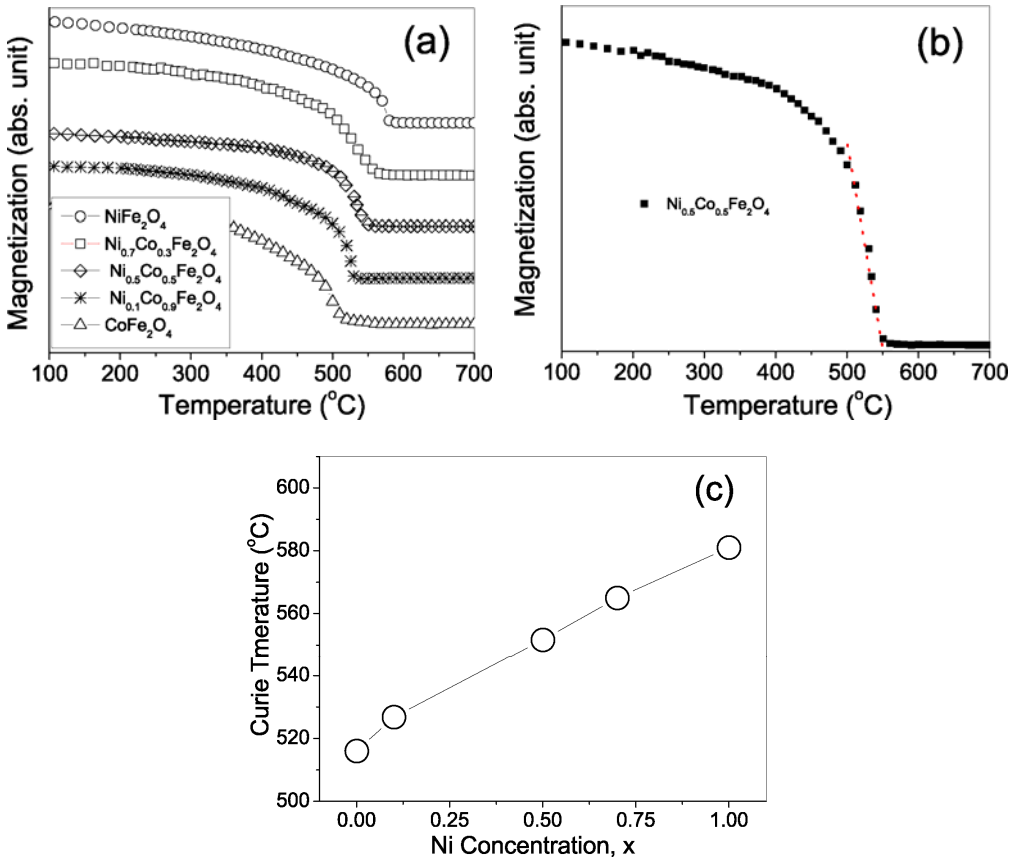

Figure 5.5 (a) temperature dependent magnetization (*M*~*T*) curves; and (b) the illustration for the measurement of the Curie temperature of the $Ni_{0.5}Co_{0.5}Fe_2O_4$ sample; (c) Ni concentration dependent Curie temperature of the $Ni_xCo_{1-x}Fe_2O_4$ samples annealed at 1000°C

The temperature dependent magnetization (*M*~*T*) curves of $Ni_xCo_{1-x}Fe_2O_4$ (x=0, 0.1, 0.3, 0.5, 0.7, 1) samples were recorded with an applied field of 200 Oe, as shown in Figure 5.5(a). As seen from Figure 5.5(a), it is clear that each sample underwent a single and sharp ferrimagnetic to paramagnetic transition at a certain temperature. With increasing Ni concentration, the transition temperature, i.e. Curie temperature

(T_C) increased apparently. The Curie temperature was estimated by lineally extrapolating the main part of the *M~T* curve near the transition temperature.[20-22] Figure 5.5 (b) illustrates the T_C estimation by using the *M~T* curve of $Ni_{0.5}Co_{0.5}Fe_2O_4$ sample as an example, as indicated by the red dot line. Figure 5.5 (c) more clearly indicated the continuous increase of T_C with increasing Ni^{2+} substitution. The as-measured Curie temperatures of $CoFe_2O_4$ and $NiFe_2O_4$ were 789K (516^{o}C) and 854K (581^{o}C) respectively, which well agreed with those reported.[19]

5.3.2.3 Mössbauer analysis

In order to study the cation distribution, four $Ni_xCo_{1-x}Fe_2O_4$ (x=0, 0.5, 0.7 and 1) samples annealed at 1000^{o}C were selected for the Mössbauer analysis at 80K. Fig.5.6 show the 80K Mössbauer spectra of the four samples annealed at 1000^{o}C. The as-fitted Mössbauer parameters are listed in Table 5.1. As seen from Fig.5.6 and Table 5.1, for all the samples, their spectra were well fitted with two sub-spectra with the weight ratio of A site to B site quite close to 1. The results indicated that the $Ni_xCo_{1-x}Fe_2O_4$ samples had almost fully inversed spinel structure with the cation distribution as $(Fe^{3+})_{A\text{-site}}[Ni^{2+}{}_xCo^{2+}{}_{1-x}Fe^{3+}]_{B\text{-site}}O_4$, i.e. almost all Ni^{2+} and Co^{2+} occupying B sites.

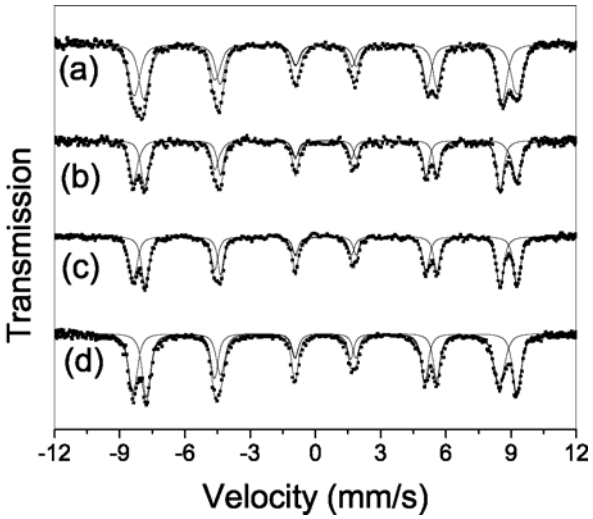

Figure 5.6 The 80K Mössbauer spectra of $Ni_xCo_{1-x}Fe_2O_4$ samples annealed at 1000°C: (a) $CoFe_2O_4$; (b) $Ni_{0.5}Co_{0.5}Fe_2O_4$: (c) $Ni_{0.7}Co_{0.3}Fe_2O_4$; (d) $NiFe_2O_4$

Table 5.1 Mössbauer parameters (at 80K) of $Ni_xCo_{1-x}Fe_2O_4$ samples annealed at 1000°C with the slow cooling processes. (δ- Isomer shift; Δ- Quadrupole splitting, *P*-percentage; α_A/α_B – absorption area ratio of A site to B site)

Samples	A site				B site				α_A/α_B
	δ (mm/s)	Δ (mm/s)	*H* (kOe)	*P* (%)	δ (mm/s)	Δ (mm/s)	*H* (kOe)	*P* (%)	
$CoFe_2O_4$	0.372	-0.023	51.01	47.88	0.484	-0.010	54.55	52.12	0.918
$Ni_{0.5}Co_{0.5}Fe_2O_4$	0.344	-0.017	50.67	49.98	0.467	-0.029	54.52	50.02	0.999
$Ni_{0.7}Co_{0.3}Fe_2O_4$	0.349	-0.015	50.60	49.09	0.460	0.015	54.75	50.91	0.964
$NiFe_2O_4$	0.337	0.002	50.31	49.20	0.453	-0.014	54.73	50.80	0.968

5.3.2.4 Magnetic properties of the mechanochemically synthesized $Ni_xCo_{1-x}Fe_2O_4$ samples

Figure 5.7 (a) and (b) show the dependence of the room-temperature saturation magnetization (M_S) and coercivity (H_C) on the Ni^{2+} substitution for $Ni_xCo_{1-x}Fe_2O_4$ samples annealed at different temperatures. Apparently, for the samples annealed at the same temperature, both M_S and H_C continuously decreased with increasing Ni^{2+} substitution. The results are consistent with those reported by Zhang et al[6] and

Kitamoto et al[7] In order to understand the changes in M_S and H_C with Ni^{2+} substitution, we choose the $Ni_xCo_{1-x}Fe_2O_4$ samples annealed at 1000°C for a detailed analysis.

According to the Mössbauer analysis mentioned above, the $Ni_xCo_{1-x}Fe_2O_4$ samples annealed at 1000°C have the inversed spinel structure with almost all Ni^{2+} and Co^{2+} occupying B sites. Based on the Néel ferrimagnetism, the net magnetic moments of the $Ni_xCo_{1-x}Fe_2O_4$ samples are total moments of both Ni^{2+} and Co^{2+} ions in B sites. Considering that Ni^{2+} has a smaller magnetic moment of ($2\mu_B$ per Ni^{2+}) than Co^{2+} ($3\mu_B$ per Co^{2+}), it is expected that the increase in Ni^{2+} substitution will lead to the decrease in M_S. As it is well known, magnetic coercivity is not an intrinsic property, which is dependent on not only intrinsic magnetocrystalline anisotropy but also the microstructure features. Therefore, in order to understand why H_C decrease with increasing Ni^{2+} substitution, it is necessary to consider the effects of both microstructure features and magnetic anisotropy. The XRD analysis indicated no appreciable microstrain in the $Ni_xCo_{1-x}Fe_2O_4$ samples annealed at 1000°C. All the samples possessed the comparable average grain size, around 230nm. This was further confirmed by the TEM analysis.

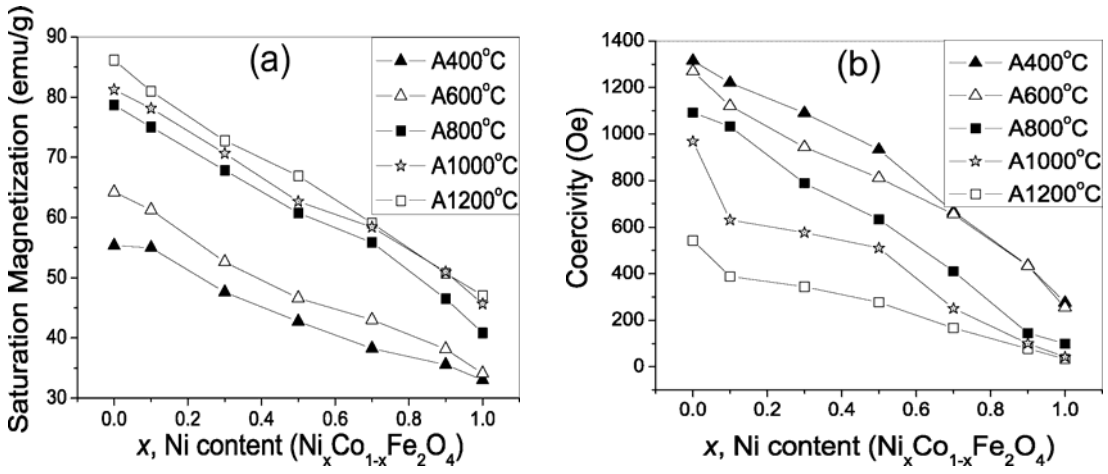

Figure 5.7 The dependence of the room-temperature saturation magnetization (a) and coercivity (b) on the Ni^{2+} substitution for $Ni_xCo_{1-x}Fe_2O_4$ samples annealed at different temperatures

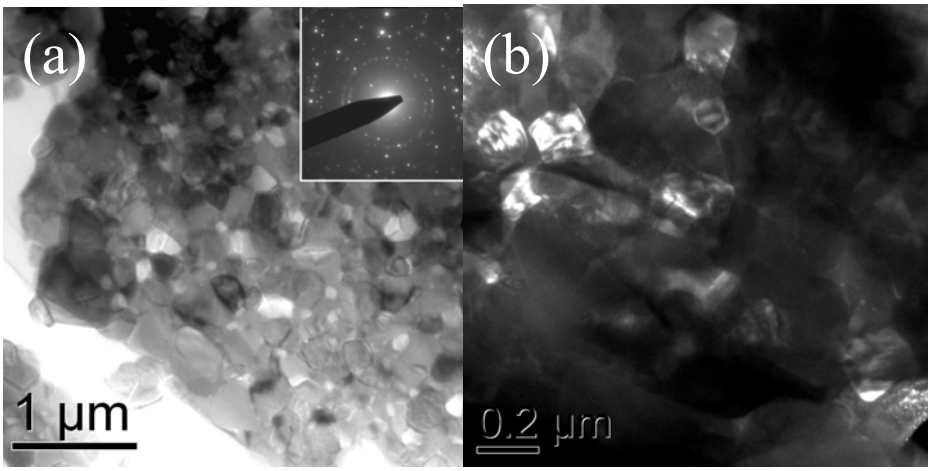

Figure 5.8 (a) Bright-field and (b) dark-field TEM images of $Ni_{0.5}Co_{0.5}Fe_2O_4$ sample after annealing at 1000°C

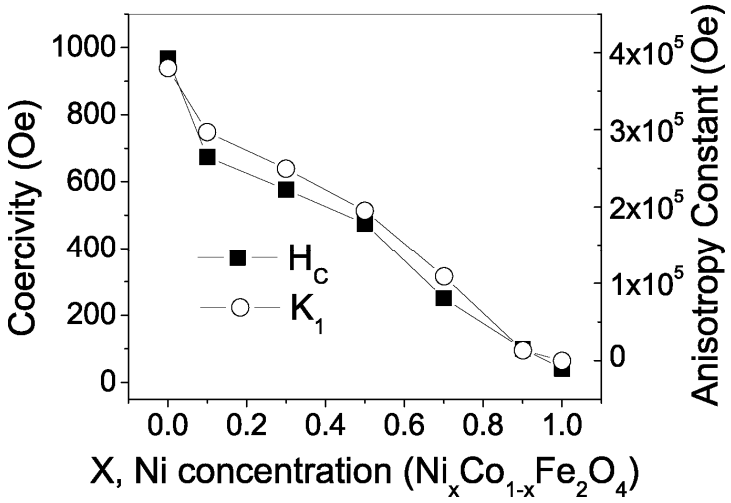

Figure 5.9 The dependence of coercivity (H_C) and magnetocrystalline anisotropy (K_1) of $Ni_xCo_{1-x}Fe_2O_4$ samples after thermal annealing at 1000°C

Figure 5.8 (a) and (b) show respectively the typical bright-field and dark-field TEM images of $Ni_{0.5}Co_{0.5}Fe_2O_4$ sample after annealing at 1000°C. Under the TEM, large particles in micrometer size range were observed. Figure 5.8 (a) shows one typical large particle, which consisted of submicrometer/nanometer sized grains. The ploycrystalline structure of the particles was evidenced by both the selected-area electron diffraction (inserted in Figure 5.8 (a)) and the dark-field TEM image (Figure 5.8(b)). Therefore, based on the XRD and TEM analysis, the $Ni_xCo_{1-x}Fe_2O_4$ samples annealed at 1000°C possessed the similar microstructure features, i.e. polycrystalline structure with the comparable average grain size and a low strain level. In this case,

the effects of the microstructure should not be the major reasons that account for the H_C decrease with increasing Ni^{2+} substitution.

Based on the law of approach to saturation as described in Chapter 2, the magnetocrystalline anisotropy (K_1) of the $Ni_xCo_{1-x}Fe_2O_4$ samples annealed at 1000°C was estimated. Figure 5.9 shows the K_1 and coercivity (H_C) dependence on the Ni^{2+} substitution for the $Ni_xCo_{1-x}Fe_2O_4$ samples annealed at 1000°C. It is clear that Ni^{2+} substitution readily led to the continuous decrease in K_1, following the similar tendency as that of H_C change. In terms of the similar microstructure features of $Ni_xCo_{1-x}Fe_2O_4$ samples as indicated by TEM and XRD analysis, the decrease in H_C should be ascribed to the decrease in K_1 with Ni^{2+} substitution. The results confirmed that Co^{2+} plays a key role in the magnetocrystalline anisotropy of $Ni_xCo_{1-x}Fe_2O_4$, for which the magnetic coercivity is strongly depended on the Co^{2+} concentration.

5.4 Mechanical milling of $NiFe_2O_4$ materials

5.4.1 Experiments

Mechanical milling was conduced in a Spex-8000 high-energy miller with a 12:1 weight ratio of ball to powder. The phases, the grain size and residual strain of milled samples were analyzed by X-ray diffraction (XRD, Bruker with Cu$K\alpha$ radiation). The diffraction patterns were collected using θ-2θ scanning with the step size of 0.02°. The separation of the line broadenings due to the grain-size effect and the strain effect of XRD diffraction peaks was based on the Williamson-Hall plot.[23] The microstructure of the milled samples was examined using different transmission electron microscopy (TEM) imaging and diffraction techniques with a JEOL JEM 3010 TEM operated at 300kV. A VSM (Vibration Sample Magnetometer, Oxford) was used for magnetic

measurements. ^{57}Fe Mössbauer spectroscopy (FAST ComTec, Germany) was used for the analysis of the site occupation of the magnetic ions in the spinel lattice before and after mechanical milling. Mössbauer spectra were analyzed with a computer program (Recoil). The area ratio of tetrahedral (A site) to octahedral (B site) subspectra was used for determination of the cation distribution.

5.4.2 Milling-time dependent magnetic properties of $NiFe_2O_4$ samples

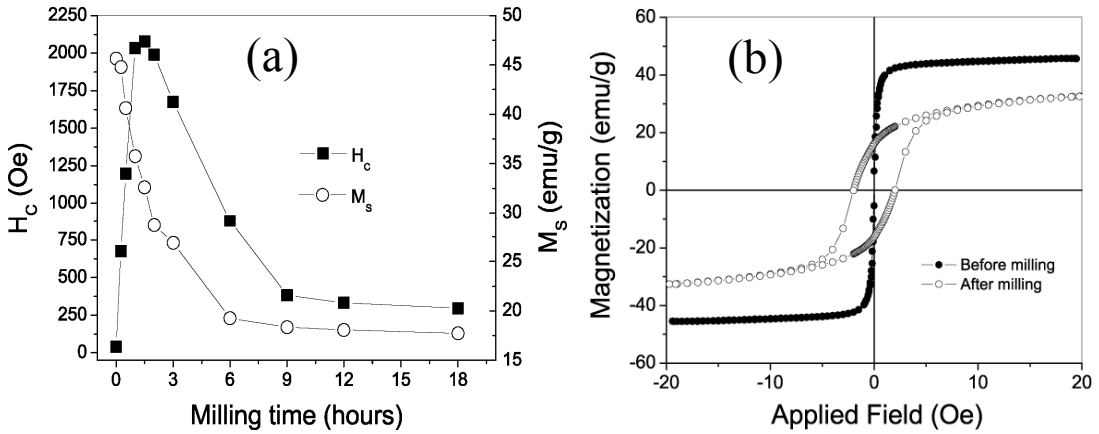

Figure 5.10 (a) Milling-time dependent coercivity (H_C) and saturation magnetization (M_S) of $NiFe_2O_4$ samples, and (b) the hysteresis loops of the $NiFe_2O_4$ samples before milling and after milling for 90 mins

Fig. 5.10(a) shows the room-temperature magnetic coercivity (H_C) and saturation magnetization (M_S) of the $NiFe_2O_4$ sample after milling for different periods of time. The saturation magnetization M_s continuously decreased initially and then gradually reached the final value after a prolonged. The coercivity H_c of all samples increased fast initially and reached the maximum values after a short milling time. Further milling led to the decease in H_c, which finally reached certain values after a prolonged milling. Such trends of the change in H_C and M_S are quite similar to those of the milled $CoFe_2O_4$, as discussed in Chapter 4. Figure 5.10 (b) shows the hysteresis loops of the $NiFe_2O_4$ samples before milling and after milling for 90 mins (with the maximum milling-induced coercivity). The comparison between two loops clearly indicated a large coercivity enhancement after mechanical milling. The maximum

coercivity achieved in $NiFe_2O_4$ after milling was 2.1 kOe. The results are quite interesting in terms of the soft nature of $NiFe_2O_4$, which can be verified by its very small coercivity of 42 Oe before mechanical milling. Although the maximum coercivities achieved in $NiFe_2O_4$ samples were smaller than that of the milled $CoFe_2O_4$ powdered materials (5.1 kOe), the large coercivity enhancement indicated the significant hardening of $NiFe_2O_4$ materials by mechanical milling.

In order to understand the effects of mechanical milling on the magnetic properties, detailed phase and microstructure analysis was conducted.

5.4.3 XRD analysis

Figure 5.11 shows the XRD spectra of the $NiFe_2O_4$ samples before milling and after milling for different periods of time. As seen from Fig. 5.11(a), the $NiFe_2O_4$ sample before mechanical milling was well crystallized, as evidenced by the sharp diffraction peaks. With the progress of the mechanical milling, the broadening of the diffraction peaks appeared, as shown in Fig. 5.12 (b) ~ (g).

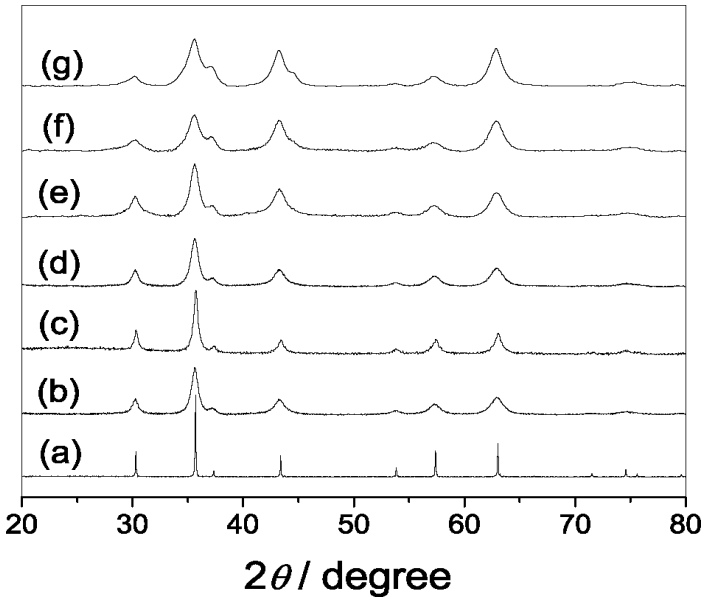

Figure 5.11 The XRD spectra of $NiFe_2O_4$ samples after milling for different periods of time: (a) before milling; (b) milled for 0.5 hour; (c) milled for 1.5 hour; (d) milled for 3 hours; (e) milled for 6 hours; (f) milled for 12 hours; (g) milled for 18 hours

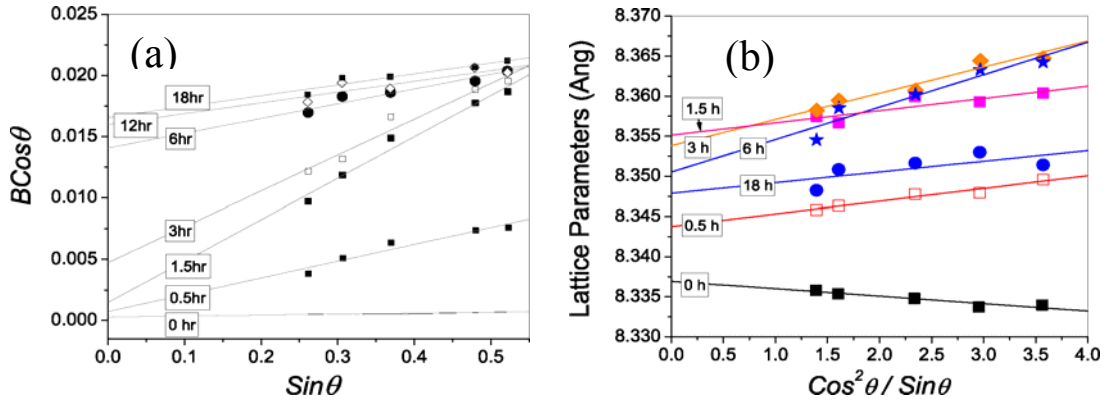

Figure 5.12(a) Williamson-Hall Plots and (b) the plots of the lattice parameters as a function of the displacement extrapolation factor ($cos^2\theta/sin\theta$) for $NiFe_2O_4$ samples after milling for different periods of time

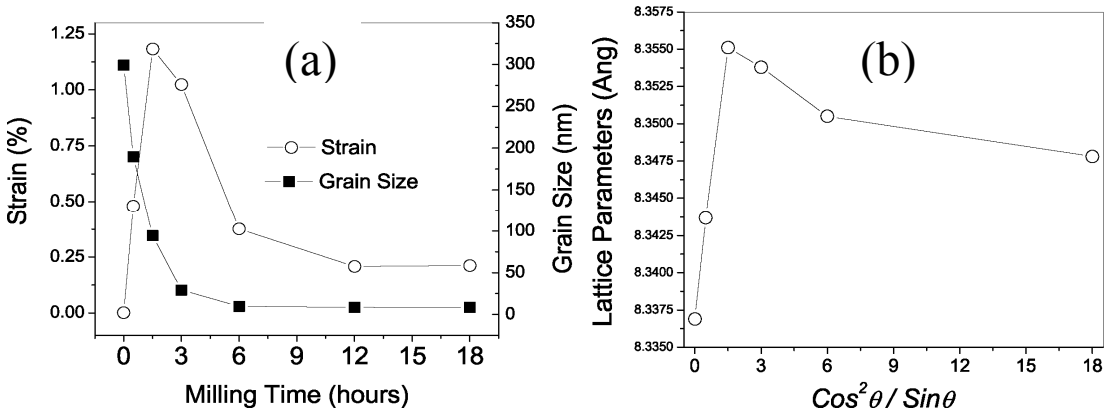

Figure 5.13 The variation of (a) strain and average grain size, and (b) lattice parameters of $NiFe_2O_4$ samples with mechanical milling time

XED analysis indicated that there was no other phase but only spinel phase in the milled samples. Fig.5.12 (a) shows the Williamson-Hall plots of the $NiFe_2O_4$ samples milled for different periods of time. Based on the Williamson-Hall plots, the average grain size and the residual strain of the milling samples were derived and shown in Fig.5.13 (a). Fig. 5.13 (a) clearly indicated a large residual strain in $NiFe_2O_4$ samples after a short-time milling for 1.5 hours. Further milling resulted in the continuous decrease of the strain. After the prolonged milling over 6 hours, the residual strain gradually stabilized at certain small values. The development of the residual strain followed the similar trend as that of H_C with milling time as shown in Fig. 5.10(a). The highest Hc corresponded to the largest residual strain. The results suggest that the high coercivity is closely related to the large residual strain induced by mechanical

milling. It was also noted that the milling-induced maximum residual strain in $NiFe_2O_4$ samples was around 1.18 %, in the same order as that (~1.03%) in milled $CoFe_2O_4$. In addition, it was also found that the lattice parameters of the $NiFe_2O_4$ samples changed after mechanical milling. Based on the extrapolating method as mentioned in Chapter 2, the lattice parameters for each milled $NiFe_2O_4$ sample were deduced by plotting lattice parameters against the displacement extrapolation factor ($cos^2\theta/sin\theta$) and extrapolating to θ=90°.[23] The plots were shown in Fig. 5.12(b). Based on the lineal fitting results, the deduced the lattice parameters for each composition were shown in Fig. 5.13(b), which indicated lattice expansion after a short time milling. The largest lattice expansion (0.22%) occurred in the sample with the highest milling-induced coercivity and residual strain. The results were similar to those observed in the milled $CoFe_2O_4$ samples as discussed in Chapter 4. Based on the results of XRD analysis, it can be concluded that a short-time milling induced a large residual strain accompanied with large lattice expansion, which should be closely related to the milling-induced high coercivity.

5.4.4 TEM analysis

In order to understand the effects of mechanical milling on the phase and microstructures of $NiFe_2O_4$ powdered materials, the detailed TEM analysis was conducted. Three milled samples were chosen, namely (i) the sample milled for 1.5 hours with the highest milling-induced coercivity, (ii) the sample milled for 6 hours and (iii) the sample milled for 18 hours.

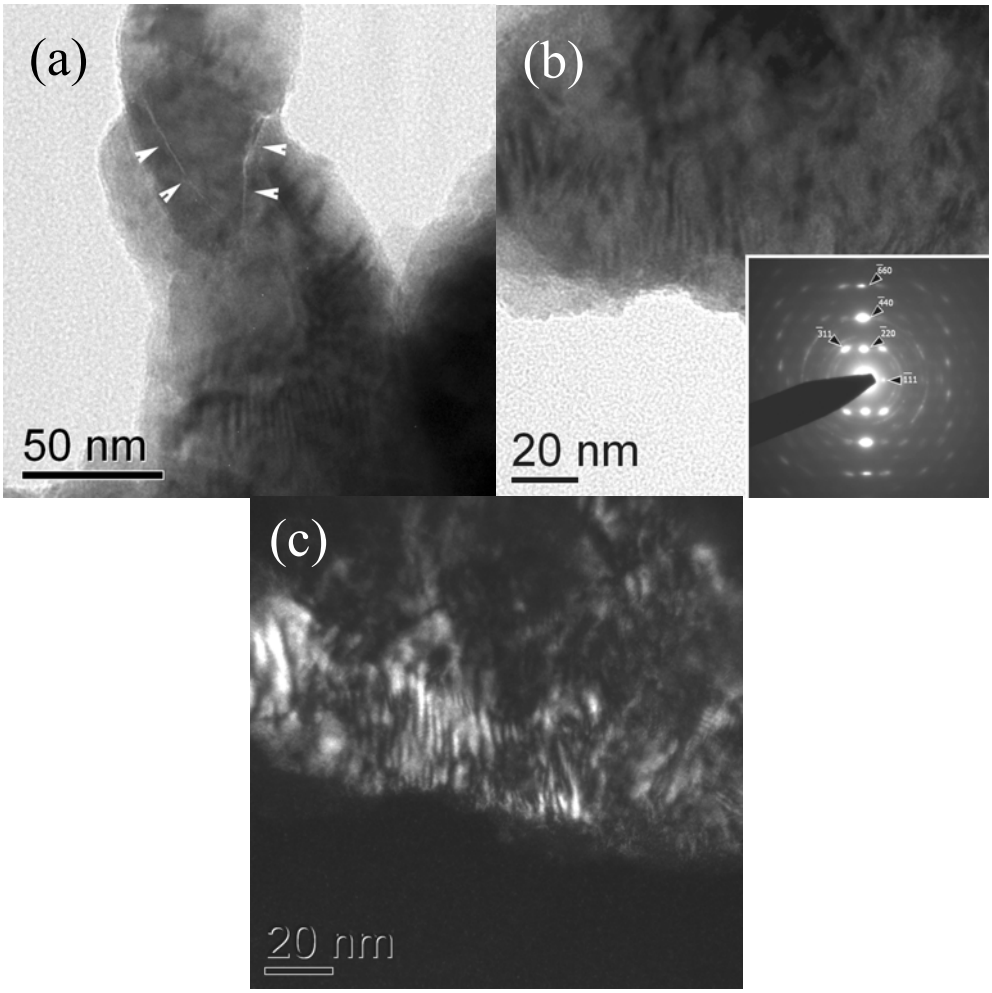

Figure 5.14 (a) and (b) Bright-field TEM images (inserted: selected-area electron diffraction); (c) dark-field TEM images of $NiFe_2O_4$ milled for 1.5 hours

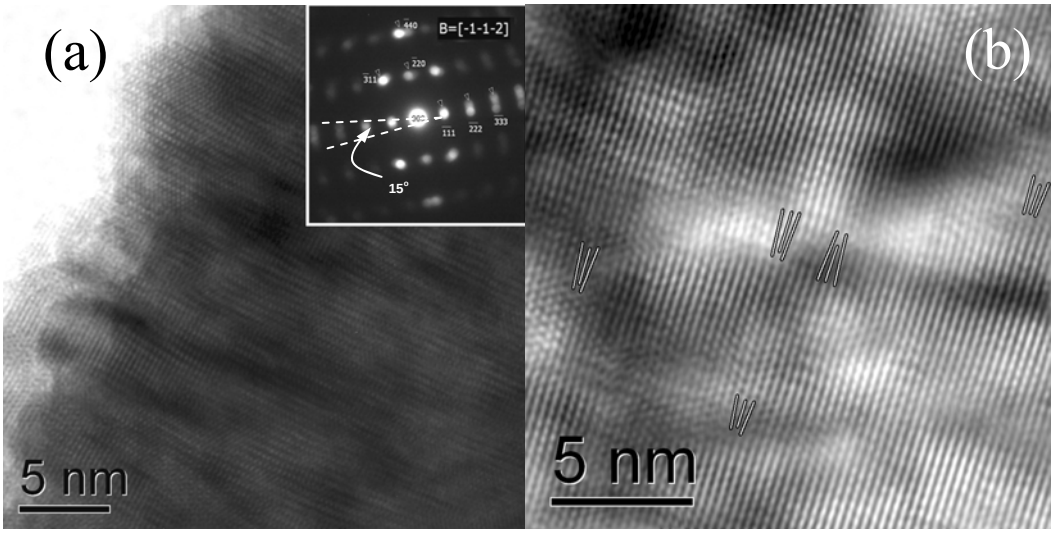

Figure 5.15 (a) and (b) High-resolution TEM images of $NiFe_2O_4$ milled for 1.5 hours (inserted in (a): nanobeam diffraction pattern)

Before mechanical milling, TEM analysis indicated that the $NiFe_2O_4$ sample was well crystallized with a low level of residual strain, which was consistent with the XRD

analysis as shown in Fig. 5.12(a) and Fig. 5.13(a). After the mechanical milling for a short time (typically around 1~2 hours), microcracks were frequently observed under TEM. Fig.5.14 (a) shows a typical bright field TEM image of the $NiFe_2O_4$ sample milled for 1.5 hours and the microcracks in the particles were indicated by the arrows. The formation of these microcracks indicates the fracture process induced by the high-energy milling. In addition, inside each grain/particle, complex contrast was formed as observed under both dark-field and bright-field TEM analysis. Fig. 5.14(b) and (c) show respectively the bright-field and dark-field images of a large particle in the $NiFe_2O_4$ sample milled for 1.5 hours. As seen from Fig. 5.14(b), bountiful irregular bands with complex contrast variation were formed in the particle. These bands were so-called as shear bands as constantly observed in the mechanical milled samples,[16,24,25] just like those observed in the milled $CoFe_2O_4$ samples as discussed in Chapter 4. The complex contrast variation and the strong distortion along these shear bands indicated a high level of strain in the sample. The electron diffraction taken from the particle in Fig. 5.14(b) showed a polycrystalline structure of the particle. In addition, the arc-like diffraction spots indicated that the grains inside the particle were textured with texture axis along <112> direction, as indexed. The dark-field image in Fig. 5.14(c) showed more clearly the features of the shear bands. The distortion and irregular features with the complex contrast variation implied a significant variation in the diffraction conditions along these shear bands. This once again confirmed the strong structure deformation with large residual strain induced by the milling. Fig. 5.15(a) showed a high-resolution TEM image. As seen from it, along the shear bands, the strong lattice distortion with complex contrast variation was observed. The nanobeam diffraction taken from the area showed clearly a textured and polycrystalline structure. The misorientation among the textured grains was around 15^o, as indicated in the inserted pattern in Fig. 5.15(a). The high resolution

TEM analysis further revealed high-density dislocations in the shear bands. Fig. 5.15(b) showed a typical high-resolution TEM image in which dislocation-like defects were observed, as indicated in the figure. Above experimental results indicated that the highly-strained and defective microstructure was formed in the $NiFe_2O_4$ sample after mechanical milling for 1.5 hours.

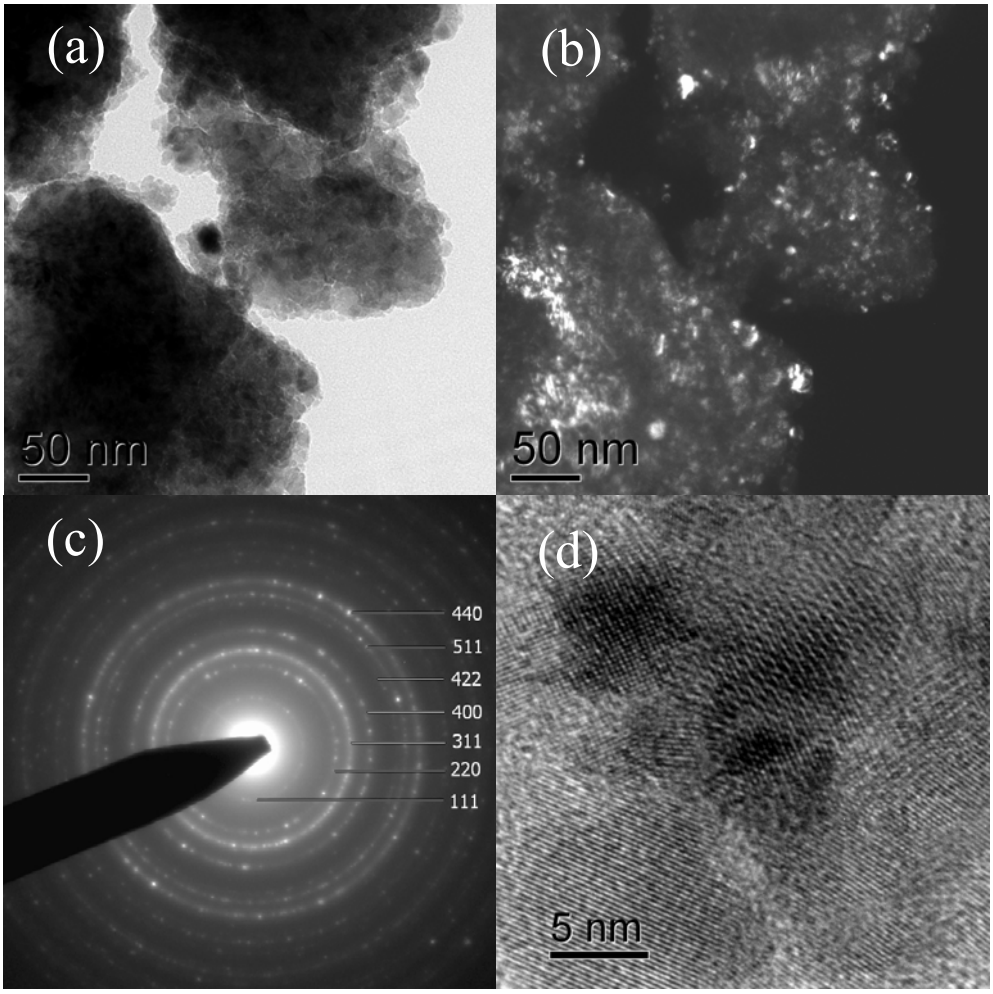

Figure 5.16 (a) Bright-field TEM image, (b) dark-field TEM image, (c) selected-area electron diffraction and (d) high-resolution TEM image of $NiFe_2O_4$ milled for 6 hours

Further milling up to 6 hours led to the formation of many nanosized subgrains inside the parent grains/particles. Fig. 5.16(a) and (b) show respectively the bright-field and dark-field TEM of the $NiFe_2O_4$ sample after milling for 6 hours. The formation of nanosized subgrains was clearly evidenced by the diffraction contrast from the nanograins in the dark-field imaging. Fig. 5.16(c) showed the selected-area electron diffraction pattern, which indicated the polycrystalline structure. Unlike the sample

milled for 1.5 hours, the sample milled for 6 hours did not show any texture relationship among the grains, as indicated by Fig. 5.16(c). The formation of subgrains was also evidenced by the high-resolution TEM analysis. As shown in Fig. 5.16(d), the nanosized subgrains with different orientations can be well distinguished, and the structural disordering can be also observed at the grain boundaries.

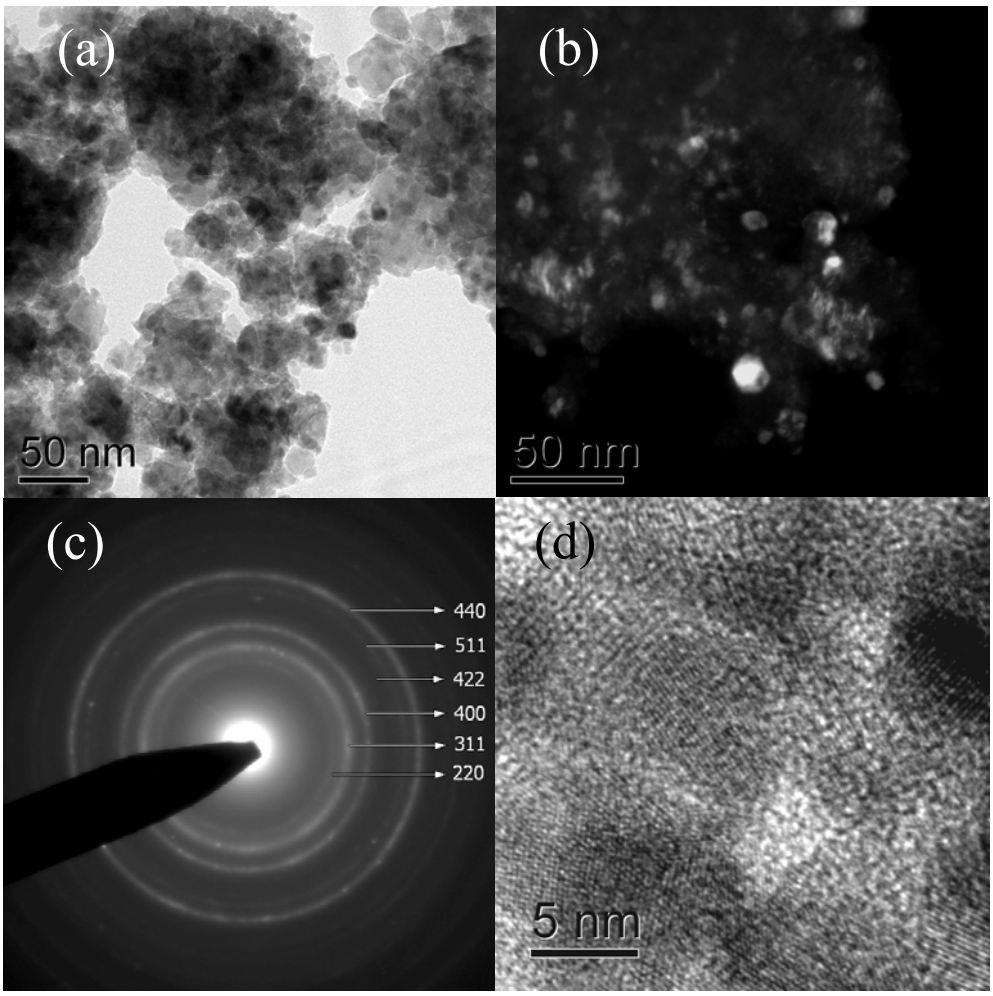

Figure 5.17 (a) Bright-field TEM image, (b) dark-field TEM image, (c) selected-area electron diffraction and (d) high-resolution TEM image of $NiFe_2O_4$ milled for 18 hours

After the milling for 18 hours, TEM analysis indicated the significant grain refinement. Fig. 5.17(a) was typical bright-field TEM image of the $NiFe_2O_4$ sample after milling for 18 hours. Beside the micrometer-sized particles, many nanosized particles can be observed. It implied an appreciable grain refinement after the prolonged milling. In addition, the formation of nanostructure was well verified by both the dark-field TEM analysis (Fig. 5.17(b)) and the selected-area electron

diffraction analysis (Fig. 5.17 (c)). According to the dark-field analysis, the as-formed nanosized subgrains showed a broad size distribution, in the range of 5~50nm. The high-resolution TEM analysis clearly indicated a polycrystalline nanostructure. As shown in Fig. 5.17(d), the nanoszied grains with random orientations were observed with the amorphous-like grain boundaries.

5.4.5 Mössbauer analysis

Figure 5.18 (a)~(c) show Mössbauer spectra (recorded at 80K) of the $NiFe_2O_4$ samples before and after milling for 1.5 and 6 hours. The fitting results of the spectra are listed in Table 5.2. As seen from Fig. 5.18, the spectra at 80K consisted of sextets for all samples. Comparing with the spectra before milling, the spectra of the milled samples became apparently broadened. For the samples milled for a long time of 18 hours, the spectrum was greatly broadened for which the fitting became very difficult and uncertain. Therefore, the spectra of the samples milled for such a long time was not shown. The broadening of the spectra could be ascribed to the finite size effects, such as surface disorder.[26-29] According to the fitting results, no other phase but only the spinel phase was identified. However, appreciable changes in the absorption area ratio (α_A/α_B) of A site to B site were observed after mechanical milling, even for a short-time milling of 1.5 hours. As seen from Table 5.2, the area ratio α_A/α_B decrease from the value of around 1 to 0.603 after milling for 1~2 hours. Further milling resulted in the continuous decrease in α_A/α_B. The results revealed that mechanical milling induced apparent cation redistribution in $NiFe_2O_4$ materials. Before milling, $NiFe_2O_4$ sample had the inversed spinel structure with Fe^{3+} ions evenly distributed in two sublattices, i.e. A sites and B sites. After mechanical milling, the decrease in α_A/α_B indicated that certain amount of Fe^{3+} ion migrated from A sites to B sites in the spinel lattice.

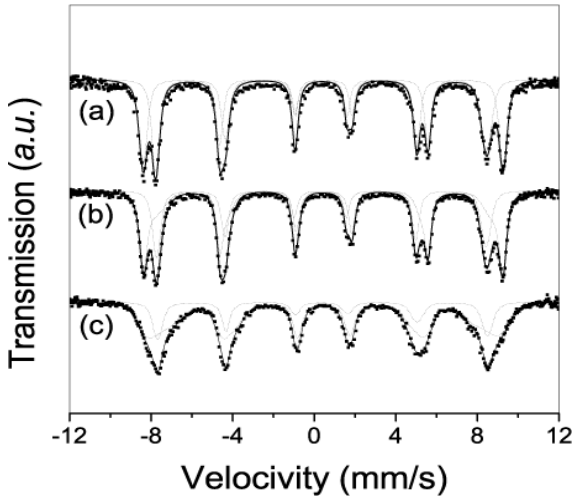

Figure 5.18 The 80K Mössbauer spectra of $NiFe_2O_4$ samples (a) before milling, (b) after milling for 1.5 hour and (c) after milling for 6 hours

Table 5.2 Mössbauer parameters (at 80K) of $NiFe_2O_4$ samples before milling and after milling (δ- Isomer shift; Δ- Quadrupole splitting, *P*-percentage; α_A/α_B –area ratio of A site to B site)

Samples	A site				B site				α_A/α_B
	δ (mm/s)	Δ (mm/s)	*H* (kOe)	*P* (%)	δ (mm/s)	Δ (mm/s)	*H* (kOe)	*P* (%)	
Before milling	0.337	0.0017	50.31	49.98	0.45334	-0.014	54.73	50.02	0.999
Milled for 1.5 hr	0.326	0.023	50.11	36.51	0.470	-0.018	51.327	63.49	0.575
Milled for 6 hr	0.338	0.0024	50.18	26.34	0.441	-0.020	49.41	73.66	0.358

In light of the Néel's two-sublattice model of ferrimagnetism,[30] the magnetic moments per unit chemical formula are the net moment difference between A site and B site. Considering the fact that Fe^{3+} has a large magnetic moment (5 μ_B) than those of both Co^{2+} (3 μ_B) and Ni^{2+} (2μ_B) ions, the decrease in α_A/α_B corresponded to the increase in the total magnetic moments of $NiFe_2O_4$ samples. Therefore, the magnetization of $NiFe_2O_4$ samples should continuously increase with milling time. However, this was not the case according to the experiments results. As shown in Fig. 5.10(a), with increasing milling time, the saturation magnetization of milled samples continuously decreased and then stabilized at a certain value. The reason for this could be ascribed to the fast decrease of magnetization with the structure disordering

and amorphization as well as the grain refinement induced by the high-energy mechanical milling.

5.4.6 The milling-induced microstructure evolution and its effects on the magnetic properties of $NiFe_2O_4$ samples

Based on the above XRD and TEM analysis, the milling-induced microstructure evolution of $NiFe_2O_4$ samples was more or less similar to that of the $CoFe_2O_4$ sample as discussed in Chapter 4. Generally, the microstructure evolutions followed up with three major stages in terms of the structural changes, i.e. (i) the initial stage with the formation of highly strained and defective microstructure; (ii) the intermediate stage with the formation of subgrains and the release of residual strain; (iii) the final stage with the significant grain refinement and the formation of nanostructures.

At the initial milling stage with a short milling time, XRD and TEM analysis revealed that mechanical milling induced a high level of strain and a high density of defects. At this stage, both magnetization (M_S) and coercivity (H_C) of the milled samples underwent appreciable changes. A rapid decrease in the Ms was observed, which could be ascribed to the structural disordering and/or the partial amorphization at the grain boundaries， as indicated by TEM analysis. In the mean time, the highest coercivities appeared at this milling stage. The milling-induced high coercivity could be related to the formation of a defective structure with high-level strain and high-density defects.

At the intermediate stage with the typical milling time of 6 hours, the formation of the appreciable amount of subgrains inside the parent grains was observed under TEM. The release of residual strain also occurred as indicated by the XRD analysis. The

decrease in M_S at this milling stage could be ascribed to the structural disordering and the formation of appreciable amounts of nanograins. The decrease in H_C could be due to the release of residual strain and the decrease in the defect density as well as the formation of nanograins that may be superparamagnetic at room temperature.

At the final milling stage with a long time milling, the final stationary microstructure was formed, i.e. the nanostructures. This could be due to the balance between the milling-induced strain energy and the high surface energy of nanograins.[24] The low magnetization and coercivity at this final stage could be due to the finite-size effects of nanocrystalline materials and the low magnetization and magnetic anisotropy of disordered materials.

5.4.7 The mechanism of the milling-induced high coercivities of $NiFe_2O_4$ samples

5.4.7.1 Magnetic anisotropy

By using the law of approach to saturation, the magnetic anisotropies of $NiFe_2O_4$ samples milled for different periods of time were estimated, as shown in Fig. 5.19. The trend of change in anisotropy constants is similar to that of the milling-time dependent coercivity and residual strain as shown in Fig. 5.10 and Fig. 5.13 respectively. The milling-induced highest coercivities corresponded to the highest magnetic anisotropies. The results once again confirmed that the milling-induced high coercivities were closely related to the milling-induced residual strain and the associated stress anisotropies. As indicated by Fig. 5.19, after mechanical milling for 1.5 hours, the large increase in anisotropy were observed, from -6.5×10^3 J/m^3 to 1.01×10^5 J/m^3. Such a large anisotropy enhancement indicated a significant hardening

of $NiFe_2O_4$ materials by mechanical milling. For $CoFe_2O_4$ materials, due to the contributions from Co^{2+}, the site occupation of Co^{2+} ions may greatly affect the magnetocrystalline anisotropy, as discussed in Chapter 4. For $NiFe_2O_4$ materials, the Mössbauer analysis really revealed apparent cation redistribution after mechanical milling. However, to the best of our knowledge, there is no report that cation redistribution in $NiFe_2O_4$ could affect the magnetic anisotropy. Therefore, the large milling induced anisotropy enhancement in $NiFe_2O_4$ could be due to other effects such as the stress anisotropy and the pinning effects of the milling-induced defects. As shown in Fig.5.13, the hardening was really accompanied with the large milling-induced residual strain, it is thus necessary to study the stress anisotropy in order to understand the hardening mechanisms in the $NiFe_2O_4$ samples.

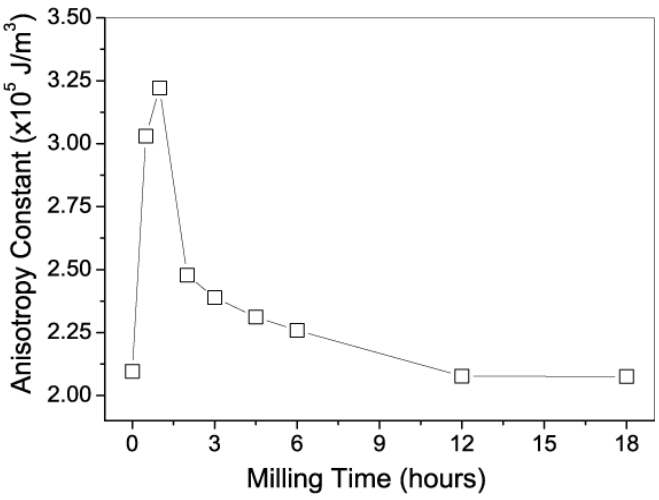

Figure 5.19 Milling-time dependent magnetic anisotropy constants of the milled $NiFe_2O_4$ samples at room temperature

As mentioned above, the stress anisotropy K_S can be expressed as $K_s = \frac{3}{2}\lambda \bullet \sigma$,[31]

where λ is magnetostriction constant and σ is stress which is proportional to strain ε via the Yong's modulus Y. As shown in Fig.5.13, mechanical milling for 1.5 hour induced a maximum strain ε of 1.18 % in $NiFe_2O_4$ materials. Given the Yong's modulus Y of 1.6×10^{11} Pa and the magnetostriction constant λ of -26×10^{-6} for polycrystalline $NiFe_2O_4$ materials,[2] the stress anisotropy K_S was estimated as 7.36 x

10^4 J/m^3. Therefore, the effective anisotropy K_{eff} was calculated as 7.66 x 10^4 J/m^3 based on $K_{eff} = \sqrt{K_1^2 + K_s^2}$ by considering the contribution from both the intrinsic magnetocrystalline anisotropy and the stress anisotropy. The K_{eff} value was comparable to that estimated from the law of approach to saturation (1.01x10^5 J/m^3). With comparing the intrinsic magnetocrystalline anisotropy with the stress anisotropy, it is clear that the intrinsic magnetocrystalline anisotropy had a negligible contribution to the effective anisotropy of the milled $NiFe_2O_4$ sample. The milling-induced large anisotropy mainly arose from the large stress anisotropy. In this sense, the anisotropy in the milled $NiFe_2O_4$ sample is nearly pure magnetoelastic. The results further verified that the mechanical hardening of the soft $NiFe_2O_4$ was closely related to the milling-induced stress anisotropy with the magnetostriction effects.

On the other hand, as TEM analysis revealed the formation of a high density of defects in $NiFe_2O_4$ samples at the initial milling stage, it is thus necessary to examine whether the pinning effects contributed to the milling-induced high coercivities in these samples. The $NiFe_2O_4$ sample milled for 1.5 hours was chosen for a detailed study.

5.4.7.2 The initial magnetization and the field-dependent coercivity of the milled $NiFe_2O_4$ sample

To study the initial magnetization behaviours of the $NiFe_2O_4$ sample milled for 1.5 hours, the minor loops were collected at three temperatures, i.e. 290K, 80K and 4 K, as shown in Fig. 5.20 (a), (b) and (c) respectively. Based on these minor loops, the field-dependent magnetization was plotted out in Fig.5.21 (a) ~ (c). As seen from Fig.5.21, the development of the magnetization (M(H)) with increasing the applied

field followed the similar trend of change. At three temperatures, the magnetization M(H) increased slowly at low applied field, and then increased fast when the applied field reached a level comparable to the maximum coercive field, i.e. $H_{applied}=H_{C,max}$.

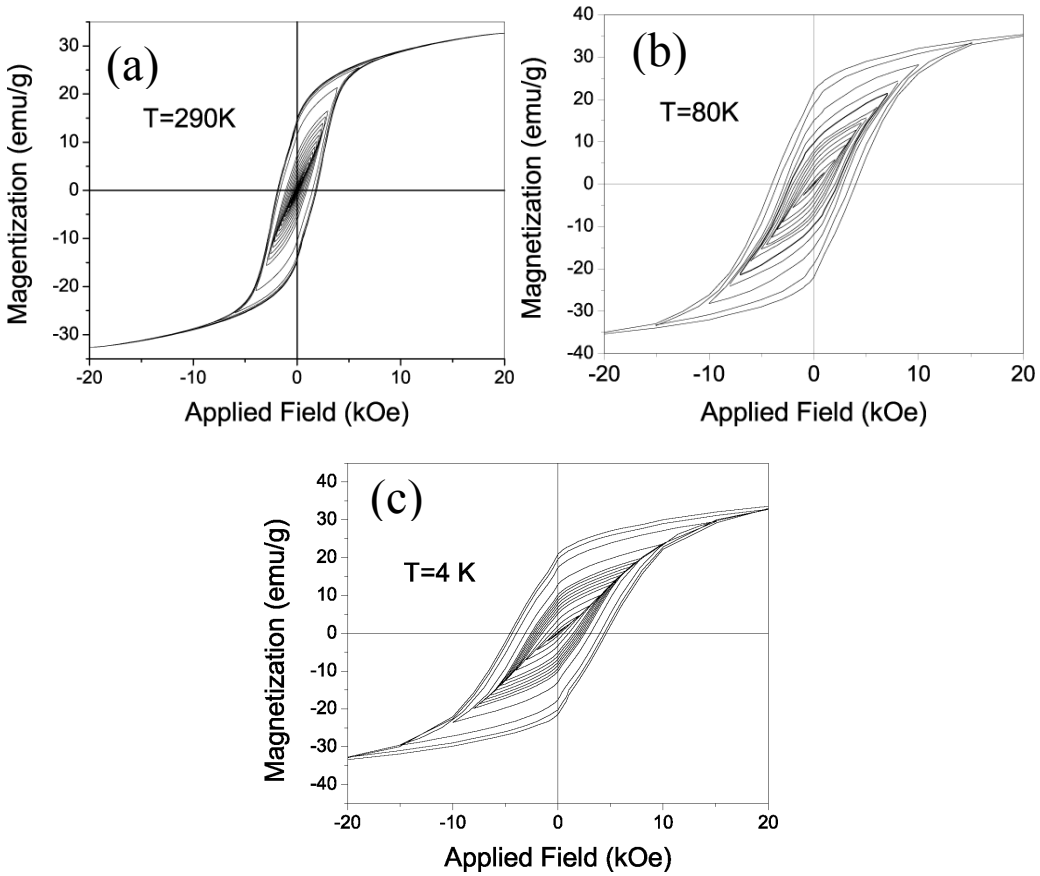

Fig.5.20 The minor loops of the $NiFe_2O_4$ sample milled for 1.5 hours measured at (a) 290K; (b) 80K and (c) 4K

Similar behaviors were also observed for the demagnetization processes of the sample, as indicated the field dependent coercivity Hc(H) at three temperatures, as shown in Fig.5.21 (a)~(c). Such kinds of magnetization and demagnetization behaviours generally indicated the domain-wall pinning controlled hardening mechanism. Therefore, at temperatures from room temperature to a very low temperature of 4K, the milled $NiFe_2O_4$ sample showed the similar magnetic hardening mechanism, i.e. domain wall pinning controlled mechanism.

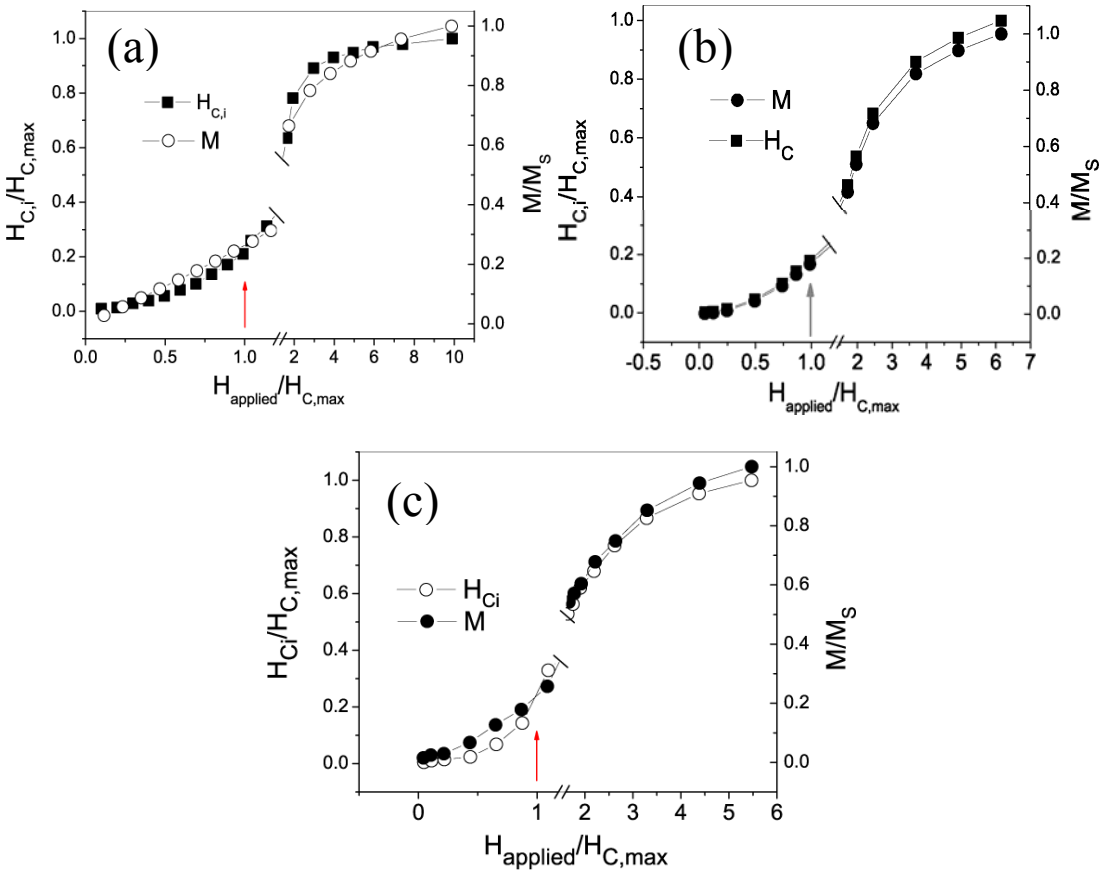

Fig.5.21 The field-dependent coercivity (H_{Ci}) and magnetization (M) of the $NiFe_2O_4$ sample milled for 1.5 hours measured at (a) 290K; (b) 80K and (c) 4K ($H_{applied}$-applied field, $H_{c,max}$-the saturation coercivity, M_S-the saturation magnetization)

5.4.7.3 The examination of coercivity mechanism based on the micromagnetic model

In order to further confirm the domain wall pinning mechanism, a detailed magnetic study was performed based on the micromagnetic model for the $NiFe_2O_4$ sample milled for 1.5 hours. According to the micromagnetic model, the temperature dependent coercivity $H_C(T)$ can be expressed as[32-36]

$$H_C(T) = \alpha_k \alpha_\varphi H_N(T) - N_{eff} M_S(T), \qquad (5\text{-}1)$$

where H_N, M_S and N_{eff} are nucleation field, saturation magnetization and demagnetization factor respectively. α_φ and α_k are micromagnetic parameters which describe respectively the misalignment of grains and the anisotropy inhomogeneity

range. Based on the derivation described in Chapter 4, in case of the pinning-controlled reversal magnetization, Equation (5-1) can be expressed as

$$\frac{H_C(T)}{M_S(T)} = \frac{\pi K_1^{3/2}(T)}{3\sqrt{3}\mu_0 T_C^{1/2} M_s^2(T)} \frac{br_0}{c} - N_{eff}, \quad \text{if } r_0 < \delta_B, \tag{5-2}$$

and

$$\frac{H_C(T)}{M_S(T)} = \frac{2T_C^{1/2} K_1^{1/2}(T)}{3\pi\mu_0 M_s^2(T)} \frac{bc}{r_0} - N_{eff}, \quad \text{if } r_0 > \delta_B, \tag{5-3}$$

where $M_S(T)$, $H_C(T)$, $K_1(T)$ are temperature dependent saturation magnetization, coercivity and anisotropy constant respectively. T_C, r_0 and δ_B refer to Curie temperature, the average size of pinning sites and the domain wall width respectively. b and c are constants. To get the temperature dependent $M_S(T)$ and $H_C(T)$ of the sample, the hysteresis loops were collected at different temperatures.

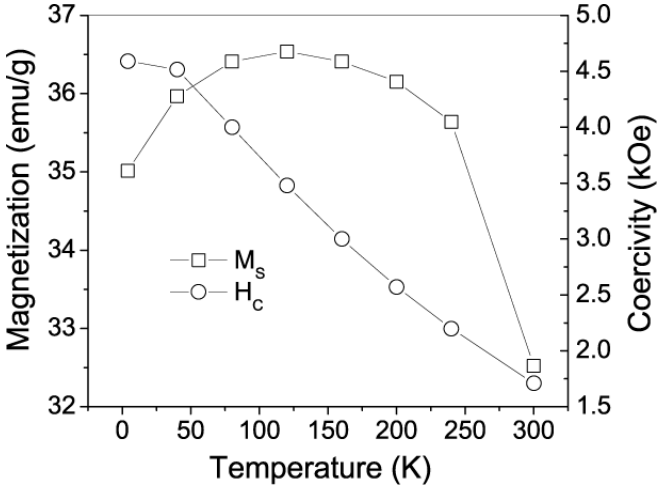

Fig.5.22 The temperature dependent coercivity (H_C) and saturation magnetization (M_S) of the $NiFe_2O_4$ sample milled for 1.5 hours

Fig.5.22 showed $M_S(T)$ and $H_C(T)$ obtained at the different temperatures. In addition, based on the law of approach to saturation, the temperature dependent anisotropy $K_1(T)$ was also derived and shown in Fig.5.23. To test two pinning models as described by Equation (5-2) and (5-3), the experimental values of $M_S(T)$, $H_C(T)$ and $K_1(T)$ were substituted into these two equations respectively. Two plots for testing

these two pinning models were shown in Fig. 5.24(a) and (b) respectively. Apparently, a good linear relationship was found between $\frac{H_C(T)}{M_S(T)}$ and $\frac{\pi K_1^{3/2}(T)}{3\sqrt{3}\mu_0 T_C^{1/2} M_S^2(T)}$ as evidenced by the plot shown in Fig.5.24 (a). Therefore, the pinning model I with $r_0 < \delta_B$ is proper one for describing the pinning effects of defects in the milled $NiFe_2O_4$, namely, the coercivity is controlled by the magnetic inhomogeneities with the size smaller than the domain wall width. This could be reasonable and well consistent with the results of the TEM analysis by which dislocations were observed in this sample. It is possible that these low-dimensional defects act as the effective pinning centres for the hindrance of domain wall movement. Fitting the data in Fig. 5.24(a) gave rise to N_{eff} of around 0.6606, which is reasonable. However, due to the unknown constants b and c, the estimation of the average size of the pinning sites r_0 is impossible.

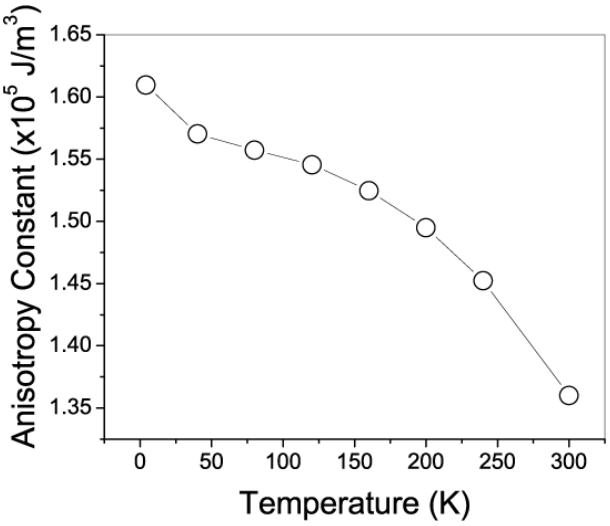

Fig.5.23 The temperature dependent of anisotropy constant of the $NiFe_2O_4$ sample milled for 1.5 hours

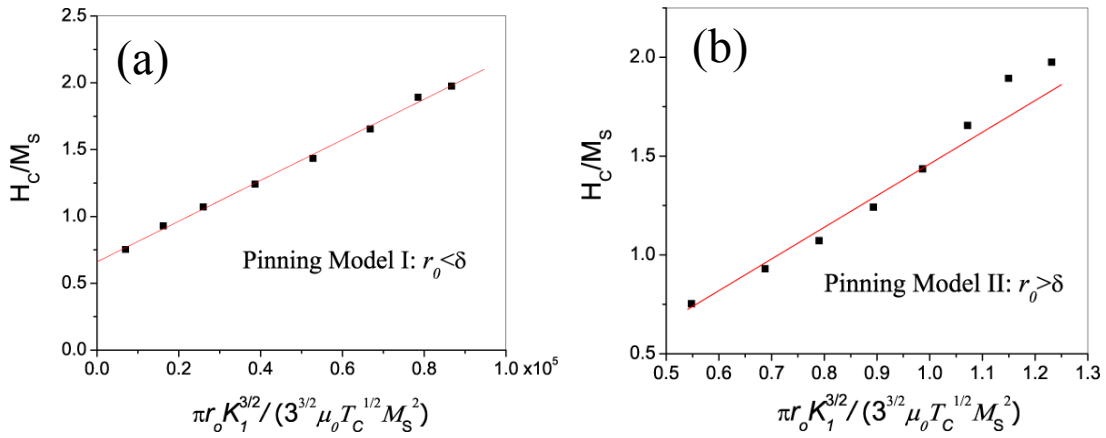

Fig.5.24 (a) Test of the pinning-controlled coercivity mechanism with $r_0<\delta_B$; (b) test of pinning-controlled coercivity mechanism with $r_0>\delta_B$ for the $NiFe_2O_4$ sample milled for 1.5 hours

5.5 Mechanical milling of $Ni_xCo_{1-x}Fe_2O_4$

Further to the mechanical milling of $CoFe_2O_4$ and $NiFe_2O_4$ powdered materials, it will be interesting to study the effects of mechanical milling on the magnetic properties of the Ni^{2+} substituted cobalt ferrites ($Ni_xCo_{1-x}Fe_2O_4$). In this work, three $Ni_xCo_{1-x}Fe_2O_4$ samples were chosen for mechanical milling, i.e. $Ni_{0.1}Co_{0.9}Fe_2O_4$, $Ni_{0.5}Co_{0.5}Fe_2O_4$ and $Ni_{0.7}Co_{0.3}Fe_2O_4$.

5.5.1 Milling-time dependent magnetic properties of $Ni_xCo_{1-x}Fe_2O_4$ samples

Figure 5.25(a)~(c) show the room-temperature magnetic coercivity (H_C) and saturation magnetization (M_S) of three $Ni_xCo_{1-x}Fe_2O_4$ (x=0.1, 0.5 and 0.7) samples after milling for different periods of time. Both M_S and H_C of the three samples showed the similar trends of the change with milling time. The trends of the change in H_C and M_S are quite similar to those of the milled $CoFe_2O_4$ and $NiFe_2O_4$. For all three

samples, the large increase in H_C was observed after milling for a short time, typically around 1~2 hours, as seen from Fig.5.25.

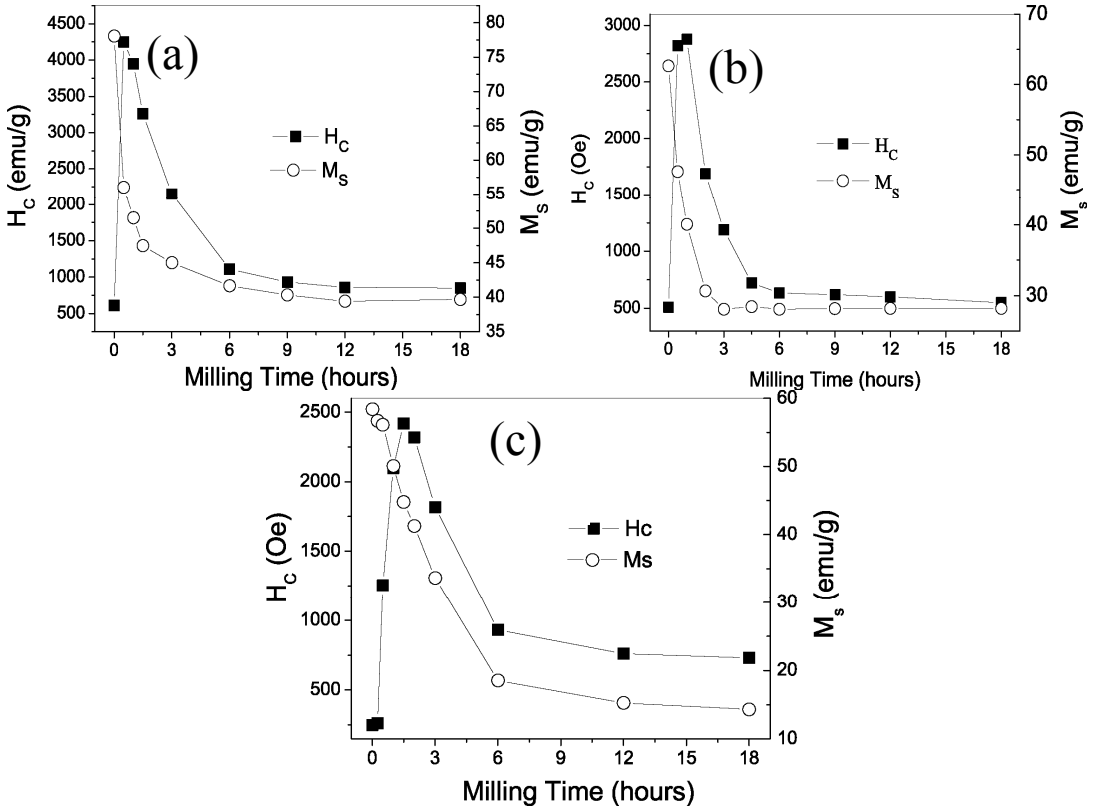

Figure 5.25 Milling-time dependent coercivity (H_C) and saturation magnetization (M_S) of (a) $Ni_{0.1}Co_{0.9}Fe_2O_4$, (b) $Ni_{0.5}Co_{0.5}Fe_2O_4$ samples, (c) $Ni_{0.7}Co_{0.3}Fe_2O_4$

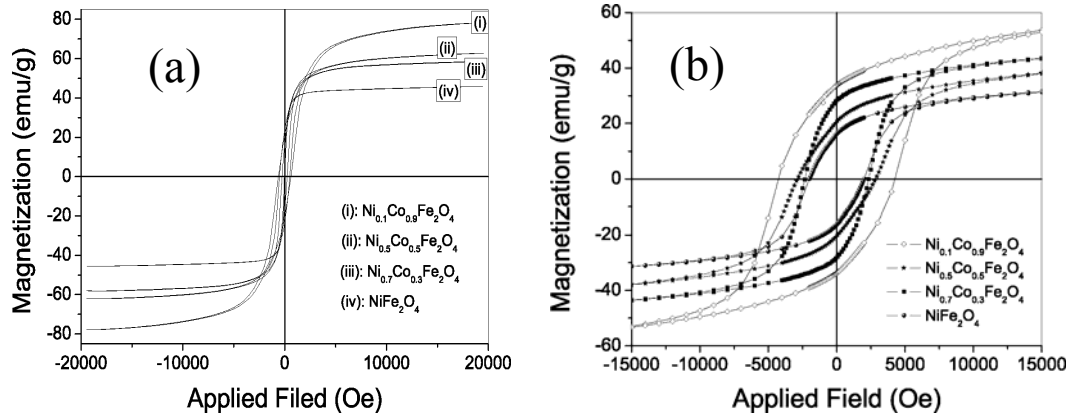

Figure 5.26 The hysteresis loops of the $Ni_xCo_{1-x}Fe_2O_4$ (x=0.1, 0.5 and 0.7) samples (a) before milling, and (b) after milling with the maximum coercivity

Figure 5.26(a) and (b) show respectively the hysteresis loops of the $Ni_xCo_{1-x}Fe_2O_4$ (x=0.1, 0.5 and 0.7) samples before milling and after milling with the maximum milling-induced coercivities. The comparison between Fig. 5.26(a) and (b) clearly

indicated the large coercivity enhancement after mechanical milling. The maximum coercivities achieved with milling were 4.3 kOe, 2.8 kOe and 2.4 kOe for $Ni_{0.1}Co_{0.9}Fe_2O_4$, $Ni_{0.5}Co_{0.5}Fe_2O_4$ and $Ni_{0.7}Co_{0.3}Fe_2O_4$ respectively. It is interesting to note that the maximum milling-induced coercivities decreased with increasing Ni^{2+} substitution.

In order to understand the effects of mechanical milling on the magnetic properties of the $Ni_xCo_{1-x}Fe_2O_4$ samples, $Ni_{0.5}Co_{0.5}Fe_2O_4$ sample was chosen for the detailed phase and microstructure analysis.

5.5.2 XRD analysis

Figure 5.27 shows the XRD spectra of the $Ni_{0.5}Co_{0.5}Fe_2O_4$ samples milled for different periods of time. Before mechanical milling, the $Ni_{0.5}Co_{0.5}Fe_2O_4$ sample was well crystallized, as evidenced by the sharp diffraction peaks. With the progress of the mechanical milling, the broadening of the diffraction peaks appeared, as shown in Fig. 5.27(b)~(g). In addition, there was no other phase but only spinel phase was detected in the milled samples.

Fig. 5.28(a) shows the Williamson-Hall plots of the $Ni_{0.5}Co_{0.5}Fe_2O_4$ samples milled for different periods of time. Based on these Williamson-Hall plots, the average grain size and the residual strain of the milled samples were derived and shown in Fig. 5.28(b). As seen from it, apparently, mechanical milling induced a large residual strain in $Ni_{0.5}Co_{0.5}Fe_2O_4$ samples after milling for 1 hour. The development of the residual strain followed the similar trend as that of H_C with milling time as shown in Fig. 5.26(b). The highest H_C corresponded to the largest residual strain. The results suggested that the high coercivity was closely related to the large residual strain

induced by mechanical milling. It was also noted that the milling-induced maximum residual strain in $Ni_{0.5}Co_{0.5}Fe_2O_4$ samples was about 0.9%, in the same order as those achieved in milled $CoFe_2O_4$ and $NiFe_2O_4$. Based on the results of XRD analysis, it is clear that a short-time mechanical milling induced a large residual strain, which should be closely related to the milling-induced high coercivity.

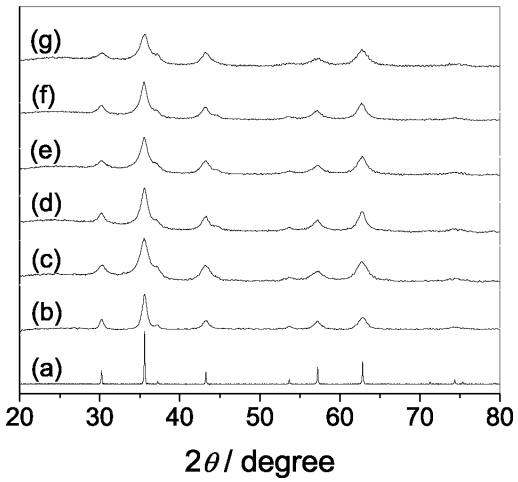

Figure 5.27 The XRD spectra of $Ni_{0.5}Co_{0.5}Fe_2O_4$ samples after milling for different periods of time: (a) before milling; (b) milled for 0.5 hour; (c) milled for 1 hour; (d) milled for 1.5 hours; (e) milled for 3 hours; (f) milled for 12 hours; (g) milled for 18 hours

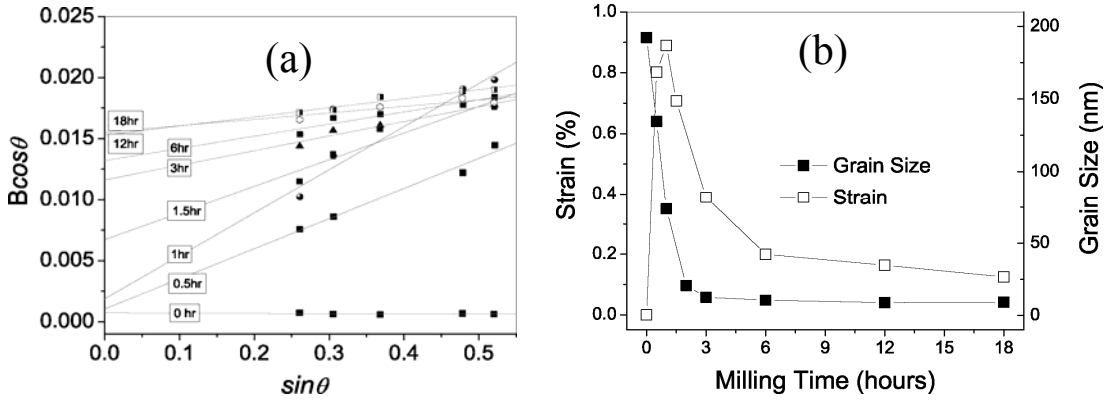

Figure 5.28 (a) Williamson-Hall Plots of $Ni_{0.5}Co_{0.5}Fe_2O_4$ samples after milling for different periods of time, and (b) the variation of strain and average grain size of $Ni_{0.5}Co_{0.5}Fe_2O_4$ samples with mechanical milling time

5.5.3. TEM analysis

Above XRD analysis revealed a large residual strain induced in the $Ni_{0.5}Co_{0.5}Fe_2O_4$ samples after a short-time milling. Therefore, it is necessary to examine the

microstructure of the highly-strained samples to see whether similar microstructure was induced as those in the milled $CoFe_2O_4$ and $NiFe_2O_4$. Thus the sample $Ni_{0.5}Co_{0.5}Fe_2O_4$ milled for 1 hour (with the highest milling-induced coercivity) was chosen for the detailed TEM analysis.

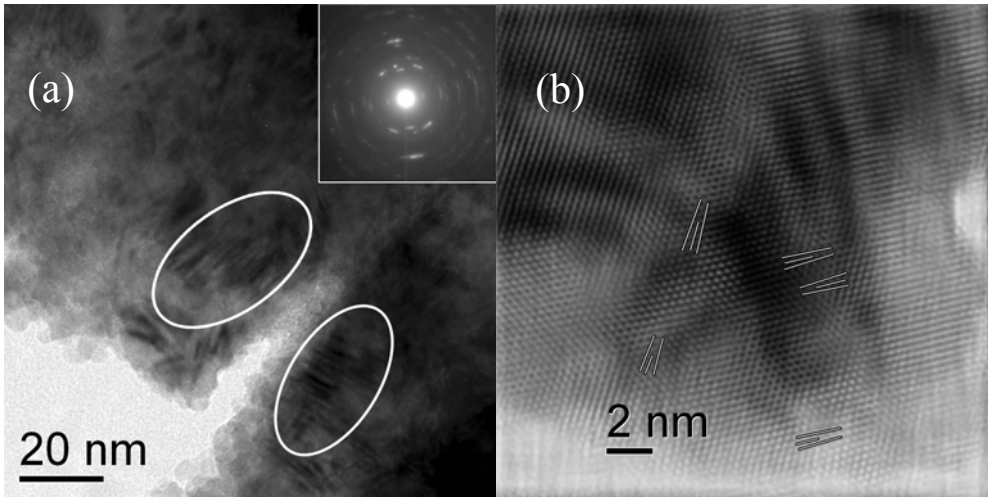

Figure 5.29 (a) The bright-filed and (b) the high-resolution TEM images of the $Ni_{0.5}Co_{0.5}Fe_2O_4$ sample milled for 1 hour

Figure 5.29 (a) and (b) show respectively the bright-field and high-resolution TEM images of the $Ni_{0.5}Co_{0.5}Fe_2O_4$ sample milled for 1 hour. As seen from Fig.5.29, the formation of bountiful shear bands was clearly evidenced (as circled in Fig. 5.29(a)). Under high-resolution TEM, a high density of dislocation-type defects was observed in these shear bands, together with strong lattice distortion. The results indicated that a highly strained defective microstructure was induced by mechanical milling.

5.5.4 Mössbauer analysis

Figure 5.30(a)~(b) show respectively Mössbauer spectra (recorded at 80K) of the $Ni_{0.5}Co_{0.5}Fe_2O_4$ samples before and after milling for 1 hour. The fitting results of the spectra are listed in Table 5.3. As seen from Fig.5.30, the spectra at 80K consisted of sextets for both samples. Comparing with the spectra before milling, the spectra of the milled samples became apparently broadened, which could be ascribed to the finite size effects, such as surface disorder.[26-29] According to the fitting results, no other

phase but only the spinel phase was identified. However, appreciable changes in the absorption area ratio (α_A/α_B) of A site to B site were observed after mechanical milling for 1 hour.

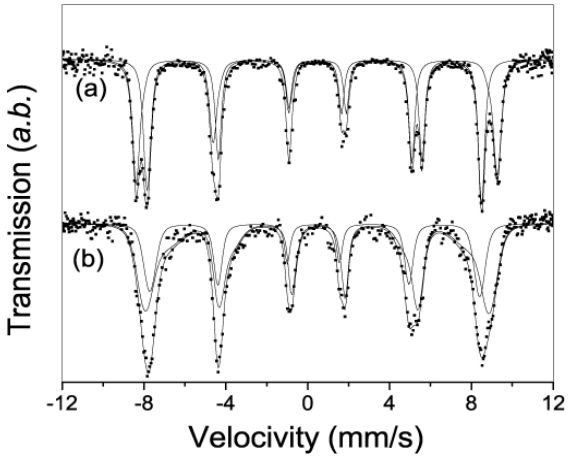

Figure 5.30 The 80K Mössbauer spectra of $Ni_{0.5}Co_{0.5}Fe_2O_4$ (a) before milling, and (b) after milling for 1 hour

Table 5.3 Mössbauer parameters (at 80K) of $Ni_{0.5}Co_{0.5}Fe_2O_4$ samples before milling and after milling (δ- Isomer shift; Δ- Quadrupole splitting, *P*-percentage; α_A/α_B –area ratio of A site to B site)

Samples	A site				B site				α_A/α_B
	δ (mm/s)	Δ (mm/s)	*H* (kOe)	*P* (%)	δ (mm/s)	Δ (mm/s)	*H* (kOe)	*P* (%)	
$Ni_{0.5}Co_{0.5}Fe_2O_4$ Before milling	0.344	-0.017	50.67	49.20	0.467	-0.029	54.52	50.80	0.969
$Ni_{0.5}Co_{0.5}Fe_2O_4$ milled for 1 hr	0.311	0.032	49.99	37.61	0.485	-0.029	50.16	62.39	0.603

As seen from Table 5.3, the area ratio α_A/α_B decrease from the value of around 1 to 0.603 after mechanical milling for 1hour. The results revealed that mechanical milling induced apparent cation redistribution in $Ni_{0.5}Co_{0.5}Fe_2O_4$, just like the milled $NiFe_2O_4$ sample as mentioned above. The decrease in α_A/α_B indicated that certain amount of Fe^{3+} ion migrated from A sites to B sites in the spinel lattice.

5.5.5 The mechanism of the milling-induced high coercivities of $Ni_{0.5}Co_{0.5}Fe_2O_4$ samples

As discussed above, mechanical milling induced apparent coercivity enhancement in $Ni_{0.5}Co_{0.5}Fe_2O_4$ samples. Both XRD and TEM analysis revealed the formation of a highly strained and defective microstructure after a short-time milling, similar to the milled $CoFe_2O_4$ and $NiFe_2O_4$ materials. Thus, the milling-induced high magnetic coercivity could be associated with the stress anisotropy and the pinning effects of the defects.

5.5.5.1 Magnetic anisotropy

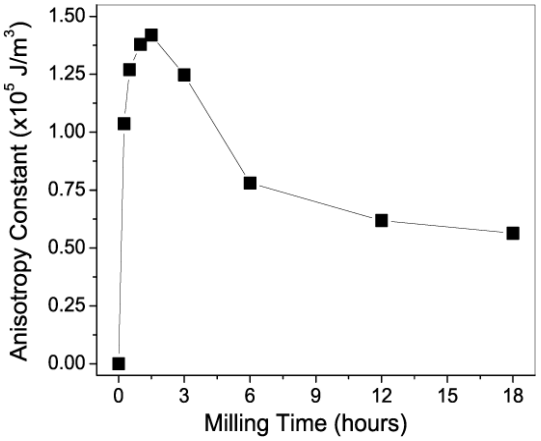

Figure 5.31 Milling-time dependent magnetic anisotropy constants of the milled $Ni_{0.5}Co_{0.5}Fe_2O_4$ samples

By using the law of approach to saturation, the magnetic anisotropies of $Ni_{0.5}Co_{0.5}Fe_2O_4$ samples milled for different periods of time were estimated, as shown in Fig.5.31. Clearly, the trend of change in anisotropy constants is similar to those of the milling-time dependent coercivity and the milling-time dependent residual strain as shown in Fig. 5.25 and Fig. 5.28 respectively. The milling-induced highest coercivities corresponded to the highest magnetic anisotropies. The results once again confirmed that the milling-induced high coercivities were closely related to the milling-induced residual strain and the associated stress anisotropies.

In order to understand the effects of mechanical milling on the magnetic anisotropies of $Ni_xCo_{1-x}Fe_2O_4$ samples, the anisotropies of $Ni_xCo_{1-x}Fe_2O_4$ samples with the highest milling-induced coercivities were estimated. Figure 5.32 showed the anisotropies/coercivities before milling and the maximum anisotropies/coercivities after the milling. As seen from it, it is clear that mechanical milling induced appreciable anisotropy increase for all the $Ni_xCo_{1-x}Fe_2O_4$ samples. In addition, large anisotropy enhancement corresponded to the large coercivity enhancement for all the $Ni_xCo_{1-x}Fe_2O_4$ samples.

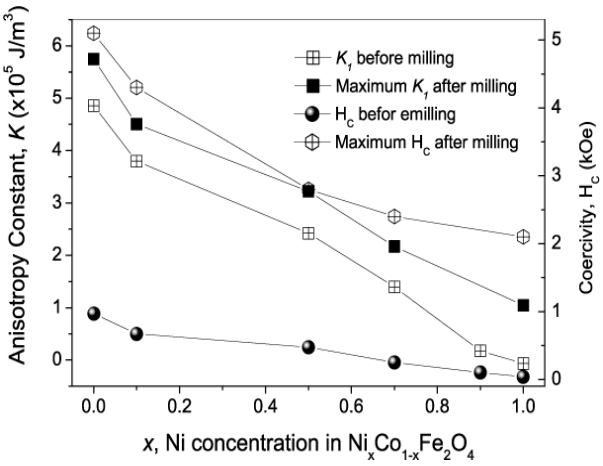

Figure 5.32 The changes in the magnetic anisotropy (K_1) and the magnetic coercivity (H_C) of $Ni_xCo_{1-x}Fe_2O_4$ samples before and after milling

It is noted that the milling-induced largest coercivity and anisotropy continuously decreased with increasing Ni^{2+} substitution. The reason could be ascribed to the effects of the Ni^{2+} substitution on the magnetostriction and the effective anisotropy of the resultant $Ni_xCo_{1-x}Fe_2O_4$ materials. As mentioned above, the magnetostriction constant of $CoFe_2O_4$ is much larger than that of $NiFe_2O_4$ due to the contribution from Co^{2+} ions. Therefore, with increasing Ni^{2+} substitution, the magnetostriction constant of the resultant $Ni_xCo_{1-x}Fe_2O_4$ should decrease. According to the XRD analysis, the milling-induced largest residual strain in $Ni_xCo_{1-x}Fe_2O_4$ samples was comparable. In terms of magnetoelastic theory, the stress anisotropy K_S can be expressed as $K_s = \frac{3}{2}\lambda \bullet \sigma$,[31] where λ is magnetostriction constant and σ is stress. Therefore, it

is expected that the milling-induced largest anisotropy will decrease with increasing Ni^{2+} substitution.

5.5.5.2 The initial magnetization and the field-dependent coercivity of the milled $Ni_{0.5}Co_{0.5}Fe_2O_4$ *sample*

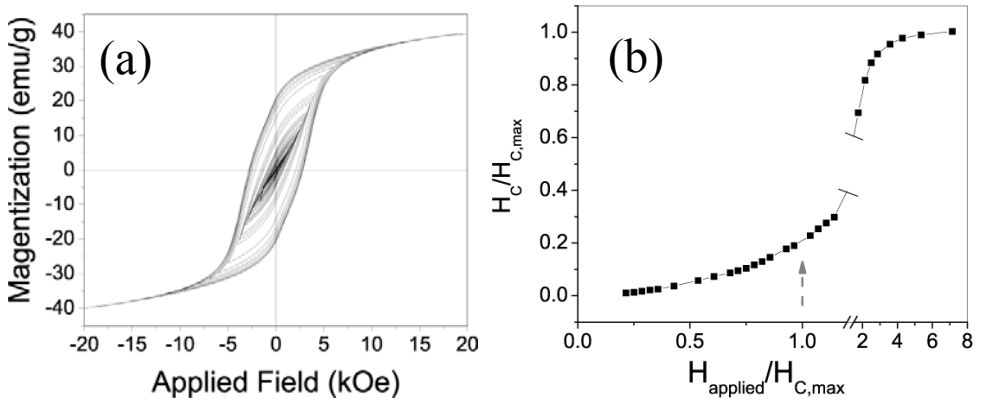

Fig. 5.33 (a) the minor loops and (b) field-dependent coercivity of the $Ni_{0.5}Co_{0.5}Fe_2O_4$ samples milled for 1 h at 296 K ($H_{C,max}$-the saturation coercivity measured at 30 kOe, $H_{applied}$-the applied magnetic field)

In order to study the coercivity mechanism behind the milling-induced high coercivity in the $Ni_{0.5}Co_{0.5}Fe_2O_4$ samples, we examined the field-dependent magnetization/demagnetization behaviors of the $Ni_{0.5}Co_{0.5}Fe_2O_4$ sample milled for 1 h. Figure 5.33(a) and (b) show respectively the minor loops and the field-dependent coercivity of the sample at room temperature (296 K). As seen from Fig. 5.33(b), the coercive force H increased slowly at low applied fields and increased rapidly when the applied field became larger than the saturation coercivity (2.8 kOe), i.e., $H_{applied}/H_{C,\,max}=1$. Such a demagnetization behaviour generally indicated the domain-wall pinning mechanism. [37] Just like the milled $CoFe_2O_4$ and $NiFe_2O_4$, the pinning centres could be the high-energy milling induced defects such as dislocations.

5.6 Mechanical milling of Fe_3O_4

5.6.1 Experiments

Commercial Fe_3O_4 powder (Fluka, 99%) was used as the raw materials for the mechanical milling. Mechanical milling was conduced in a Spex-8000 high-energy miller with a 12:1 weight ratio of ball to powder. The Fe_3O_4 powder was mechanically milled and sampled for different periods of time up to 36 hrs. The phases, grain size and residual strain of milled samples were analyzed by X-ray diffraction (Bruker XRD with Cu$K\alpha$ radiation). The microstructure of the milled samples was examined by transmission electron microscopy (TEM, JEOL JEM 3010) operated at 300kV. A VSM (Vibration Sample Magnetometer, Oxford) was used for magnetic measurements. ^{57}Fe Mössbauer spectroscopy (FAST ComTec, Germany) was used for the analysis of the site occupation of the magnetic ions in the spinel lattice before and after mechanical milling. Low temperature Mössbauer measurements were conducted in a liquid nitrogen cryostat. Spectra were analyzed with a computer program (Recoil). The area ratio of tetrahedral (A site) to octahedral (B site) subspectra was used for determination of the cation distribution.

5.6.2 Results and discussion

5.6.2.1 Starting materials

Both XRD and TEM analysis indicated that the Fe_3O_4 powder before mechanical milling was single spinel phase with well crystallized structure. Fig. 5.34(a) showed a typical bright-field TEM image of the sample before milling. As seen from it, the sample had a broad particle size distribution, ranging from 50nm to 400nm. The average grain size estimated from XRD analysis was around 120nm. The selected-area electron diffraction pattern inserted in Fig. 5.34(a) indicated only spinel

magnetite phase, consistent with XRD analysis. Fig. 5.34(b) showed a high-resolution TEM image of the sample, which indicated a well crystallized structure, consistent with both XRD and electron diffraction analysis.

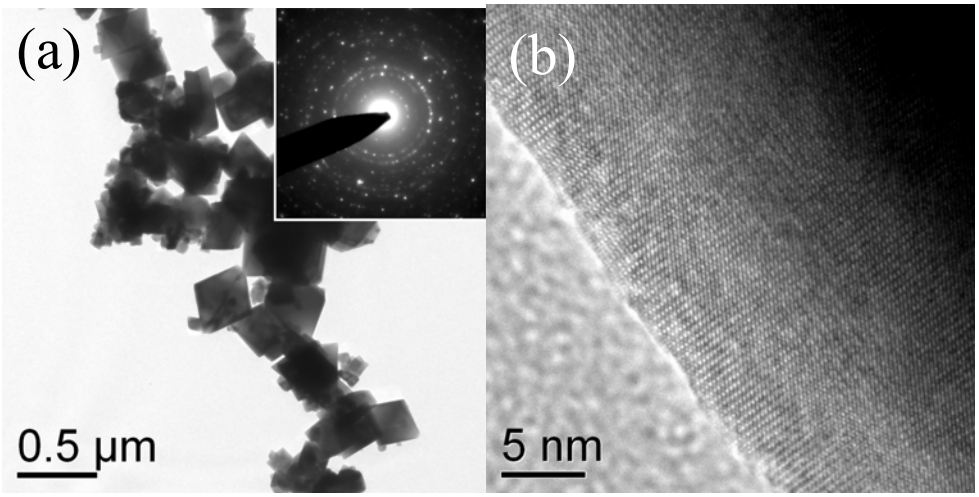

Figure 5.34 (a) Bright-field TEM image (inserted: selected-area electron diffraction pattern) and (b) high-resolution TEM image of Fe_3O_4 powder before mechanical milling

5.6.2.2 The samples after mechanical milling

A. The milling-time dependent magnetic properties of Fe_3O_4 samples

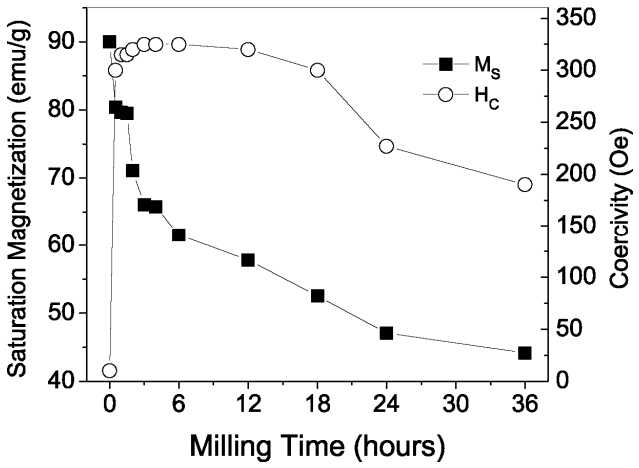

Figure 5.35 The milling-time dependent saturation magnetization and coercivity of Fe_3O_4 samples

Figure 5.35 showed the magnetic properties of Fe_3O_4 samples after milling for different periods of time. The saturation magnetization (M_S) continuously decreased

with milling of up to 36 hours. The coercivity (H_C) had a fast increase after milling for 1 hour and reached a maximum value of 330 Oe after milling for 3 hours, and then continuously decreased after prolonged milling. Such a trend of change in M_S and H_C was similar to those of milled $CoFe_2O_4$ and $Ni_xCo_{1-x}Fe_2O_4$ samples as discussed before. It was noted that the highest milling-induced coercivity (330 Oe) was much smaller than those achieved in $CoFe_2O_4$ and $Ni_xCo_{1-x}Fe_2O_4$ samples after milling. In order to understand it, the detailed phase and microstructure analysis will be presented in the following.

B. XRD analysis

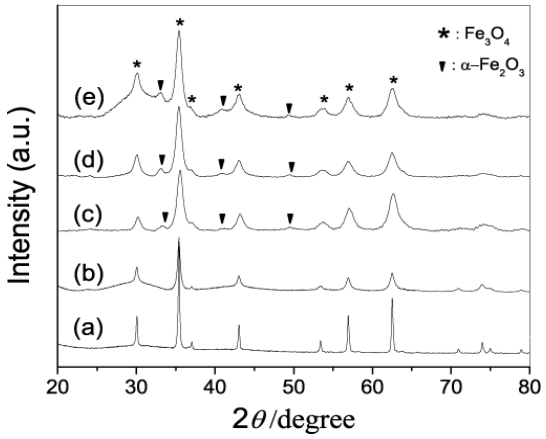

Figure 5.36 XRD spectra of Fe_3O_4 samples after milling for different periods of time: (a) before milling; (b) 1hour; (c) 3 hours; (d) 6 hours; (e) 18 hours

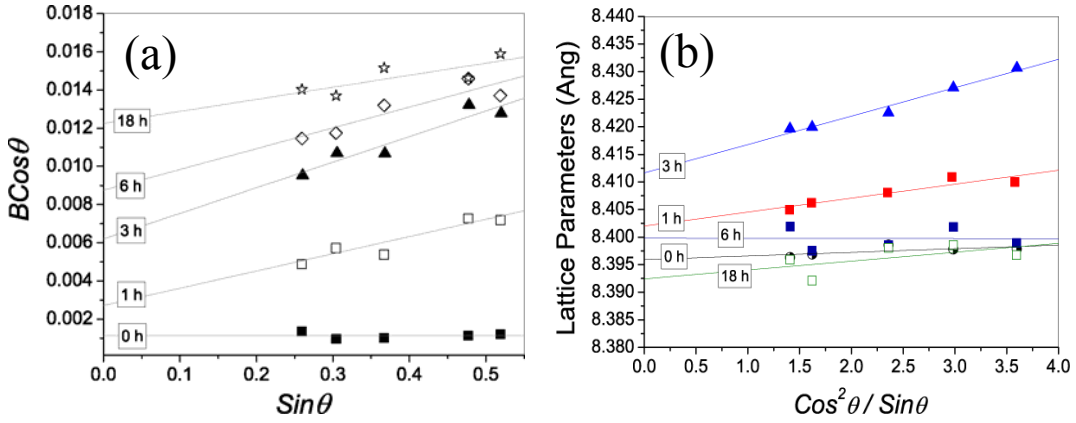

Figure 5.37 (a) Williamson-Hall plots and (b) the plots of the lattice parameters as a function of the displacement extrapolation factor ($cos^2\theta/sin\theta$) for Fe_3O_4 samples after milling for different periods of time

Fig.5.36 showed the XRD spectra of the Fe_3O_4 samples before and after milling for different periods of time. As seen from Fig. 5.36(a), the Fe_3O_4 sample was single spinel phase before milling. The sharp and strong diffraction peaks indicated its well crystallized structure. With the progress of the milling, the broadening of the diffraction peaks appeared and became enhanced with prolonged milling, as seen from Fig. 5.36(b)~(e). It was also noted that the formation of α-Fe_2O_3 phase occurred after milling for 3 hours and longer. This could be due to the oxidation of Fe_3O_4 during, although all the sampling was conducted in a glove box. Besides the α-Fe_2O_3 and Fe_3O_4 phases, no other phase could be detected according to the XRD analysis. For the milled samples, the estimation of the residual strain was done by using the Williamson-Hall plots[38] as shown in Fig. 5.37(a). The milling-time dependent residual strain in the milled samples was plotted in Fig. 5.38. In the meantime, the lattice parameters for each milled Fe_3O_4 sample were deduced by plotting lattice parameters against the displacement extrapolation factor ($cos^2\theta/sin\theta$) and extrapolating to θ=90°.[18] The plots were shown in Fig.5.37 (b).

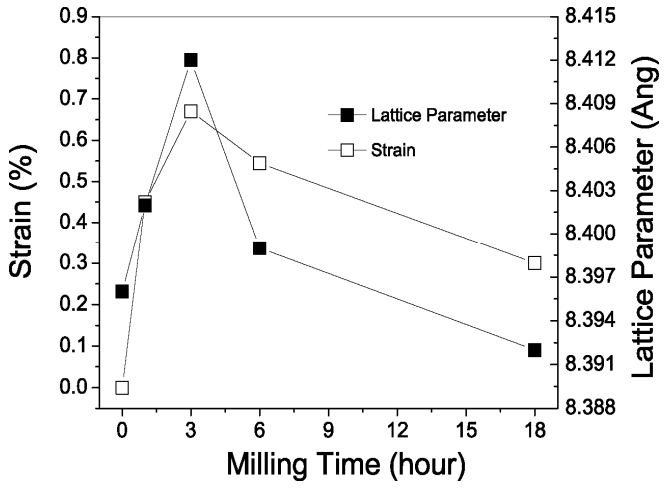

Figure 5.38 The variation of residual strain and lattice parameters of Fe_3O_4 samples after milling for different periods of time

Based on the lineal fitting results, the lattice parameters of the milled samples were shown in Fig. 5.38. As seen from it, the trend of changes in both residual strain and lattice parameters were similar to that of the milling-induced magnetic coercivity as

shown in Fig. 5.35. The highest milling-induced coercivity corresponded to the largest residual strain and lattice expansion. The results indicated that the milling-induced coercivity was closely related to the residual strain and lattice expansion, just as for the milled $CoFe_2O_4$ and $Ni_xCo_{1-x}Fe_2O_4$ samples. The milling-induced largest residual strain and lattice expansion were 0.66% and 0.19% respectively. Based on above XRD analysis, it is clear that mechanical milling did not lead to the change in the cubic symmetry of Fe_3O_4, i.e. no phase transformation.

It is also noted that the milling-induced residual strain was 0.66%, smaller than those in the milled $CoFe_2O_4$ (1.03%) and $NiFe_2O_4$ (1.18%). The reason could be ascribed to the effects of the initial grain size as discussed in Chapter 5. The grain size of the starting Fe_3O_4 powder was only around 100nm, which was smaller than those of $CoFe_2O_4$ and $NiFe_2O_4$ powders before milling. The low milling-induced residual strain may account for the low milling-induced magnetic coercivity in Fe_3O_4 samples. In addition, the oxidation during mechanical milling may also be responsible for the low coercivities of the milled Fe_3O_4 samples.

C. TEM analysis

In order to further examine whether mechanical milling could induce any phase change, two samples were selected for TEM analysis, i.e. the samples milled for 1 hour and 3 hours.

For the Fe_3O_4 sample milled for 1 hour, the microstructural features under TEM were more or less similar to those appeared in both $CoFe_2O_4$ and $NiFe_2O_4$ samples after short-time milling. The highly strained and defective structure with the formation of shear band and sub-grains was evidenced by both dark-field and high-resolution TEM analysis. Figure 5.39(a) and (b) showed respectively the typical bright-field and dark-

field TEM images of Fe_3O_4 samples after milling for 1 hour. The selected-area electron diffraction in Fig. 5.39(c) indicated a polycrystalline and textured structure.

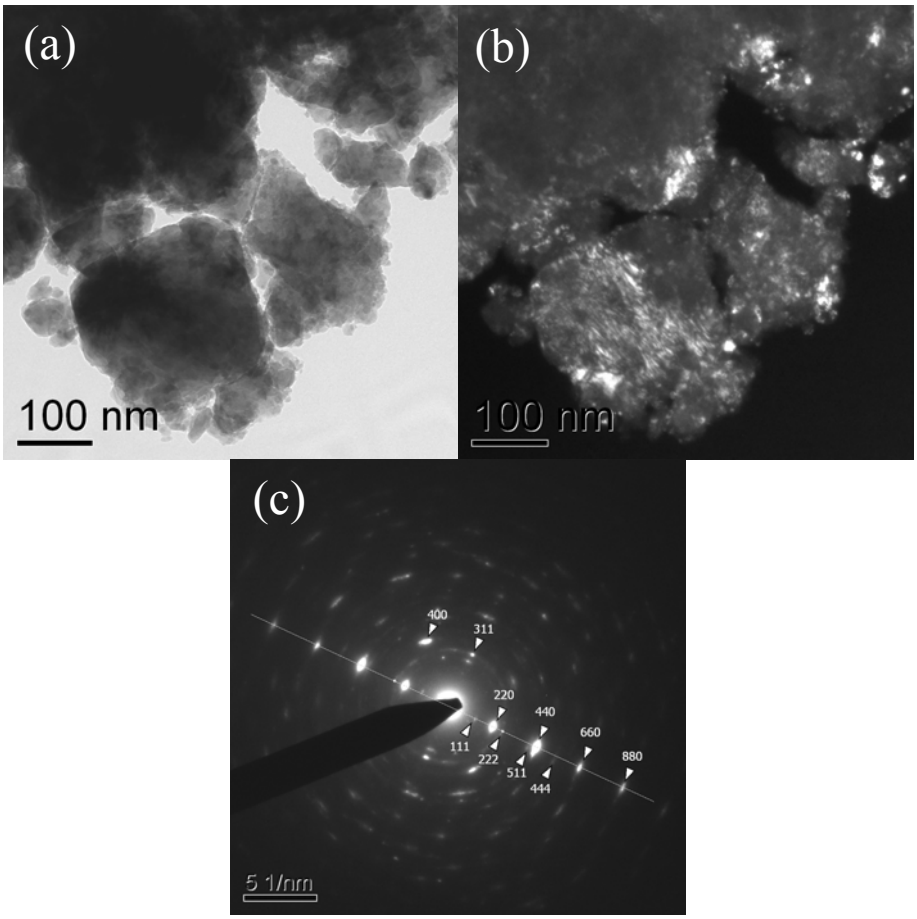

Figure 5.39 (a) The bright-field TEM image, (b) dark-field TEM image, and (c) selected-area electron diffraction of the Fe_3O_4 sample after milling for 1 hour

No other phase but only spinel Fe_3O_4 phase was detected. The results indicated that mechanical milling for 1 hour did not induce phase change in the sample. Figure 5.40(a) and (b) showed respectively a bright-field and dark-field TEM images of the Fe_3O_4 milled for 3 hours. As seen from them, appreciable amount of nanosized subgrains were formed. This was consistent with the selected-area electron diffraction in Fig. 5.40(c) which indicated a polycrystalline structure. Detailed indexing of the pattern indicated the diffraction from α-Fe_2O_3 phase beside the spinel Fe_3O_4 phase. No other phase was detected. The results were consistent with those of XRD analysis

as mentioned above. Therefore, based on both XRD and TEM analysis, mechanical milling did not result in phase transformation of spinel Fe_3O_4 phase.

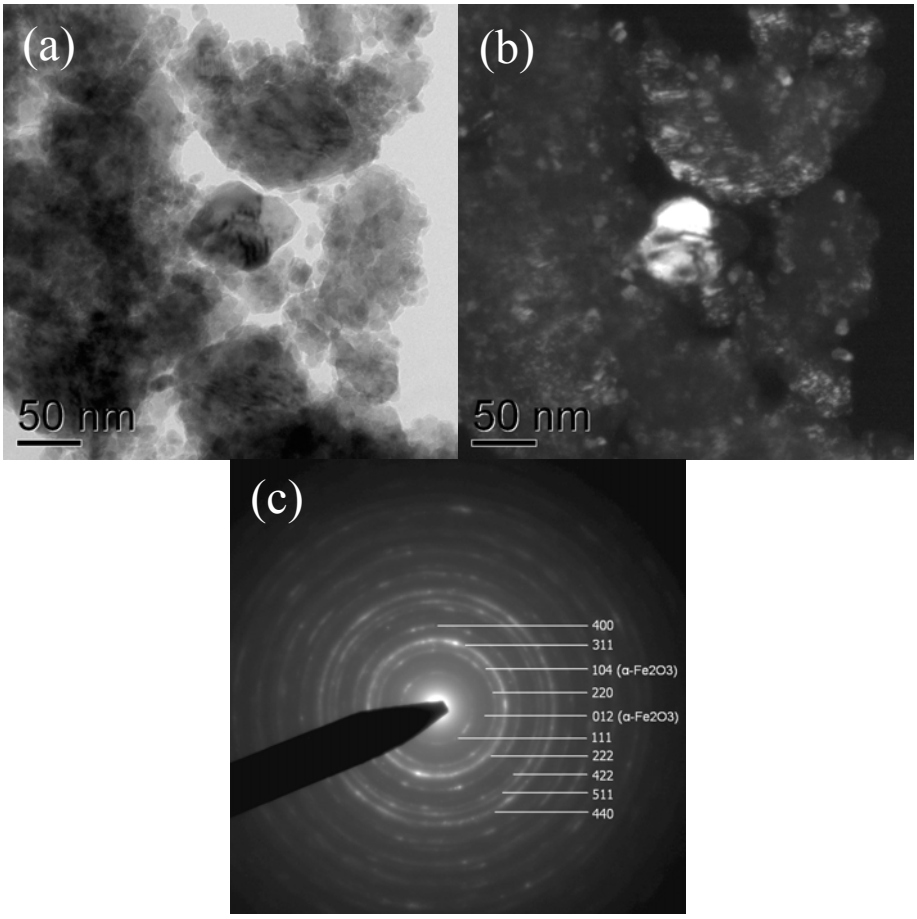

Figure 5.40 (a) The bright-field TEM image, (b) dark-field TEM image and (c) selected-area electron diffraction of the Fe_3O_4 sample after milling for 3 hours

5.7 Summary

Mechanochemical process has been proven as an effective way for synthesizing $Ni_xCo_{1-x}Fe_2O_4$ (x=0.1, 0.3, 0.5, 0.7, 0.9 and 1) powdered samples. XRD and Mossbauer analysis revealed that the $Ni_xCo_{1-x}Fe_2O_4$ samples were well-crystallized with inversed spinel structure after annealing at 1000^oC. The substitution of Co^{2+} by Ni^{2+} was evidenced by the continuous decrease in lattice parameters and the increase

in Curie temperature of $Ni_xCo_{1-x}Fe_2O_4$ samples with increasing Ni concentration. The magnetic study indicated that Ni^{2+} substitution directly led to decrease in both saturation magnetization and magnetic coercivity of the $Ni_xCo_{1-x}Fe_2O_4$ samples. It was also found that Ni^{2+} substitution readily resulted in the continuous decrease in magnetocrystalline anisotropy (K_1), following the similar tendency as that of coercivity change. Based on phase, site occupation and microstructure analysis, the decrease in magnetic coercivity should be ascribed to the decrease in K_1 with Ni^{2+} substitution. The results revealed that Co^{2+} plays a key role in the magnetocrystalline anisotropy of $Ni_xCo_{1-x}Fe_2O_4$, for which the magnetic coercivity is strongly depended on the Co^{2+} concentration.

The $Ni_xCo_{1-x}Fe_2O_4$ samples with different levels of Ni^{2+} substitution were subjected to mechanical milling for different periods of time. It was found that a short-time mechanical milling led to the notable enhancement in both magnetic coercivity and magnetic anisotropy. Detailed phase and microstructural analysis indicated that such coercivity and anisotropy enhancement was closely related to the milling-induced high-level residual strain and high-density defects. Large coercivities of up to 4.3 kOe were achieved in the $Ni_xCo_{1-x}Fe_2O_4$ materials after a short time milling. The most noteworthy is the mechanical hardening of the soft $NiFe_2O_4$ with milling and a high coercivity of 2.1 kOe was achieved. The milling-induced largest magnetic anisotropy and coercivity continuously decreased with increasing Ni^{2+} substitution, suggesting the effects of Ni^{2+} substitution on the stress anisotropy as induced. Detailed magnetic studies revealed that the domain-wall pinning mechanism also had a great contribution to the milling-induced large coercivity. The pinning sites could be low-dimensional defects such as dislocations. Therefore, both stress anisotropy and the pinning effects of defects were responsible for the milling-induced high coercivity.

To examine whether mechanical milling could induce phase changes in spinel ferrites, Fe_3O_4 powder was subjected to mechanical milling for different periods of time. Detailed phase and structure analysis indicated apparent structural distortion and lattice expansion in the milled Fe_3O_4 samples. But no phase change was found according to both XRD and TEM analysis. The oxidation of Fe_3O_4 occurred during long-time mechanical milling, which led to the formation α-Fe_2O_3 phase. Comparing with the milled $CoFe_2O_4$ and $NiFe_2O_4$ samples, the milled Fe_3O_4 samples had lower milling-induced residual strain and coercivity. The reason could be ascribed to the smaller initial grain size of the starting Fe_3O_4 powder and the oxidation during milling.

5.8 Reference

[1] B. D. Cullity, *Introduction to magnetic materials*, 266 (Reading, Mass, Addison-Wesley Pub. Co., Holland, 1972).
[2] B. D. Cullity, *Introduction to magnetic materials*, 258 (Reading, Mass, Addison-Wesley Pub. Co., Holland, 1972).
[3] D. J. Craik, *Magnetic oxides*, 241 (Wiley, London, New York 1975).
[4] C. S. Kim, S. W. Lee, S. L. Park, J. Y. Park , and Y. J. Oh, J. Appl. Phys. **79,** 5428 (1996).
[5] H. Yamamoto, IEEE Trans. Magn. **38** 3488 (2002).
[6] F. Zhang, Y. Kitamoto, M. Abe, and M. Naoe, J. Appl. Phys. **87,** 6881 (2000).
[7] Y. Kitamoto, F. Zhang, F. Shirasaki, M. Abe, and M. Naoe, IEEE Trans. Magn. **35,** 2694 (1999).
[8] J. Garc´ıa and G. Sub´ıas, J. Phys.: Condens. Matter **16,** R145 (2004).
[9] G. K. Rozenberg, M. P. Pasternak, W. M. Xu, Y. Amiel, M. Hanfland, M. Amboage, R. D. Taylor, and R. Jeanloz, Phys. Rev. Lett. **96,** 45705 (2006).
[10] F. Walz, J. Phys.: Condens. Matter **14** R285 (2002).
[11] E. J. W. Werwey, Nature **144,** 327 (1939).
[12] A. Tonejc, M. Stubicar, A. M. Tonejc, Â. K. Kosanovic, and B. S. SuboticÂ, J. Mater. Sci. Lett. **13,** 519 (1994).
[13] A. Tonejc, A. M. Tonejc, and D. DuzĬevicÂ, Scripta. Metall. Mater. **25,** 1111 (1991).
[14] C. Suryanarayana, Prog. Mater. Sci. **46,** 1 (2001).
[15] R. M. Davis, B. McDermott, and C. C. Koch, Metall. Trans. **A19,** 2867 (1988).
[16] J. Ding, P. G. McCormick, and R. Street, J. Magn. Magn. Mater. **171,** 309 (1997).
[17] B. D. Cullity and S. R. Stock, *Elements of X-ray diffraction*, 366 (Prentice Hall, Upper Saddle River, NJ, 2002).

[18] B. D. Cullity and S. R. Stock, *Elements of X-ray diffraction*, 401 (Prentice Hall, Upper Saddle River, NJ, 2002).
[19] B. D. Cullity, *Introduction to magnetic materials*, 190 (Reading, Mass, Addison-Wesley Pub. Co, Holland, 1972).
[20] B. D. Cullity, *Introduction to magnetic materials*, 128 (Addison-Wesley Publication Company, Notre Dam, 1972).
[21] R. I. Khaibullin, L. R. Tagirov, B. Z. Rameev, S. Z. Ibragimov, F. Yildiz, and B. Aktas, J. Phys.: Condens. Matter. **16,** L443 (2004).
[22] J. Navarro, C. Frontera, L. Balcells, B. Martínez, and J. Fontcuberta, Phys. Rev. B **64,** 09241 (2001).
[23] B. D. Cullity and S. R. Stock, *Elements of X-ray diffraction* (3rd edition, Prentice Hall, 2002).
[24] E. Hellstern, H. J. Fecht, C. Garland, and W. L. Johnson, Mater. Soc. Symp. Proc. **32,** 137 (1989).
[25] J. Y. Huang, Y. K. Wu, and H. Q. Ye, Acta. Mater. **44,** 1211 (1996).
[26] F. Bødker, S. Mørup, and S. Linderoth, Phys. Rev. Lett. **72,** 282 (1994).
[27] G. F. Goya, H. R. Rechenberg, and J. Z. Jiang, J. Appl. Phys. **84,** 1101 (1998).
[28] J. Z. Jiang, G. F. Goya, and H. R. Rechenberg, J. Phys.: Condens. Matter **11,** 4063 (1999).
[29] C. J. Serna, F. Bødker, S. Mørup, M. P. Morales, F. Sandiumeng, and S. Veintemillas-Verdaguer, Solid State Commun. **118,** 437 (2001).
[30] B. D. Cullity, *Introduction to Magnetic Materials*, 180 (Addison Wesley Publishing Company, University of Notre Dame, 1972).
[31] B. D. Cullity, *Introduction to magnetic materials*, 270 (Reading, Mass, Addison-Wesley Pub. Co., Holland, 1972).
[32] D. Givord, Q. Lu, and M. F. Rossignol, *Sci. and Tech. Nanostruc. Mater.* ((Plenum Press, New Yok, 1991).
[33] X. C. Kou, H. Kronmüller, D. Givord, and M. F. Rossignol, Phys. Rev. B **50,** 3849 (1994).
[34] H. Kronmüller, Phys. Stat. Sol. (b) **144,** 385 (1987).
[35] H. Kronmüller, K. D. Dust, and G. Martineck, J. Magn, Magn. Mater. **69,** 69 (1987).
[36] H. Kronmüller, K. D. Dust, and M. Sagawa, J. Magn, Magn. Mater. **74,** 291 (1988).
[37] H. W. Zhang, C. B. Rong, J. Zhang, S. Y. Zhang, and B. G. Shen, Phys. Rev. B **66,** 184436 (2002).
[38] B. D. Cullity and S. R. Stock, *Elements of X-ray diffraction*, 377 (Prentice Hall, Upper Saddle River, NJ, 2002).

CHAPTER 6

Overall Conclusions and Suggestions for Future Work

6.1 Overall conclusions

$CoFe_2O_4$ nanoparticles with relatively high coercivities were synthesized by both the modified co-precipitation process and the mechanochemical process. With the modified co-precipitation at 100^oC, one-step formation of well-crystallized $CoFe_2O_4$ nanoparticles was achieved. Systematic studies were conducted in order to understand the effects of various processing parameters on the grain size and magnetic properties of the co-precipitated nanoparticles. The results indicated that the morphologies (particle size and size distribution) of the as-obtained nanoparticles was strongly dependent on both the molar ratio of metal ions to OH^- (i.e. [Me]/[OH]) and the feeding rate of metal ions. The low [Me]/[OH] ratios and slow feeding rates were preferable for achieving high coercivities due to the formation of large-sized nanoparticles with more uniform size distribution. A relatively high coercivity of 2.1 kOe was achieved after size selection. The results indicated that the average particle/grain size and size distribution played key roles in the coercivity of the resultant nanocrystalline powdered samples. With the mechanochemical process, mechanical activation triggered the formation of $CoFe_2O_4$ spinel phase with well established nanocrystallinity at room temperature. The combination of the mechanochemical process and the low-temperature thermal annealing enabled the mass fabrication of the single-phase $CoFe_2O_4$ powdered materials with relatively high coercivity. Different post-annealing processes resulted in different magnetic properties of the resultant $CoFe_2O_4$ powdered materials. Slow-cooling process resulted in a almost fully inversed spinel structure while the quenching process led to the partially

inversed structure. The difference in the cation distribution well accorded with the difference in the saturation magnetization and magnetic coercivity as well as the magnetocrystalline anisotropy of the samples. In addition, average grain size greatly affected the coercivity of the samples. In order to achieve high coercivity of $CoFe_2O_4$ powdered materials, slow cooling process is preferred.

Milling cobalt ferrite powdered materials indicated that the initial grain/particle size greatly affected the microstructure evolutions and thus the magnetic properties of as-milled cobalt ferrite materials. While large-grained cobalt ferrite materials showed significant microstructural changes induced by milling, the nanosized cobalt ferrite samples didn't have appreciable structural changes even after long-time milling. A high coercivity of 5.1 kOe has been achieved in the cobalt ferrite powders with large grain size after milling for a short time. Our results clearly indicate that the milling-induced high coercivity in the large-grain sized cobalt ferrite materials is closely related to the formation of a unique structure with high-level strain and high-density defects as well as the large lattice expansion.

The mechanisms of milling-induced high coercivity in cobalt ferrites were first studied by analyzing the initial magnetization and demagnetization processes, which indicated the domain-wall pinning controlled mechanism. Further analysis of coercivity mechanisms was conducted based on both micromagnetic and phenomenological models. The temperature-dependent magnetization behaviors were well described by the pinning-controlled micromagnetic model in which case the size

of the pinning centers were smaller than the domain wall width. The phenomenological model analysis based on the magnetic relaxation measurements also revealed the pinning-controlled reversal magnetization behaviors. Therefore, all the results indicated that the pinning-controlled mechanisms are responsible for the milling-induced high coercivity. The associated pinning centers could be dislocation-like defects, the highly-strained areas and grain boundaries with the formation of subgrains during the mechanical milling.

To study the effects of elemental doping on the magnetic properties of cobalt ferrite materials, mechanochemical process employed for synthesizing Ni^{2+} substituted cobalt ferrites ($Ni_xCo_{1-x}Fe_2O_4$) powdered samples. The single-phased $Ni_xCo_{1-x}Fe_2O_4$ materials were successfully synthesized with the combination of the mechanochemical process and the post thermal annealing process. The magnetic studies indicated that Ni^{2+} substitution directly led to decrease in both saturation magnetization and magnetic coercivity of the $Ni_xCo_{1-x}Fe_2O_4$ samples. It was also found that Ni^{2+} substitution readily resulted in the continuous decrease in magnetocrystalline anisotropy (K_1), following the similar tendency as that of coercivity change. Based on phase, site occupation and microstructure analysis, the decrease in magnetic coercivity should be ascribed to the decrease in K_1 with Ni^{2+} substitution. The results revealed that Co^{2+} plays a key role in the magnetocrystalline anisotropy of $Ni_xCo_{1-x}Fe_2O_4$, for which the magnetic coercivity is strongly depended on the Co^{2+} concentration.

The Ni^{2+} substituted $Ni_xCo_{1-x}Fe_2O_4$ samples with different levels of Ni^{2+} substitution

were also subjected to mechanical milling. It was found that a short-time mechanical milling also led to the notable enhancement in both magnetic coercivity and magnetic anisotropy. Detailed phase and microstructural analysis indicated that such coercivity and anisotropy enhancement was also closely related to the milling-induced high-level residual strain and high-density defects. Large coercivities of up to 4.3 kOe were achieved in the $Ni_xCo_{1-x}Fe_2O_4$ materials after a short time milling. The most noteworthy is the mechanical hardening of the soft $NiFe_2O_4$ with milling and a high coercivity of 2.1 kOe was achieved. The milling-induced largest magnetic anisotropy and coercivity continuously decreased with increasing Ni^{2+} substitution, suggesting the effects of Ni^{2+} substitution on the stress anisotropy as induced. Detailed magnetic studies revealed that the domain-wall pinning mechanism accounted for the milling-induced high coercivities. The pinning sites could be low-dimensional defects such as dislocations. Therefore, both stress anisotropy and the pinning effects of defects were responsible for the milling-induced high coercivity.

In contrast, mechanical milling of Fe_3O_4 did not induce high residual strain in the milled samples. The milling-induced coercivity was very low compared with those of the milled $CoFe_2O_4$ and $Ni_xCo_{1-x}Fe_2O_4$. The reason could be ascribed to the smaller initial grain size of the starting Fe_3O_4 powder and the oxidation during milling and/or during analysis.

6.2 Suggestions for future work

Improved techniques for a better control of particle/grain size and size distribution

For the synthesis of $CoFe_2O_4$ powdered materials by both co-precipitation and mechanochemical processes, the control of the average grain size and size distribution was very challenging. The as-synthesized nanoparticles by these two processes had broad size distribution，especially for the samples synthesized by mechanochemical process. As it is well recognized, high coercivity can be achieved by controlling the average grain size near the single-domain size with uniform size distribution. The size selection based on the centrifuging method was employed in order to narrow the grain-size distribution. Although the size selection led to the apparent increase in the coercivity of the nanopowders, the resultant nanoparticles still had relatively broad size distribution. Therefore, in order to synthesize $CoFe_2O_4$ powdered materials, future work can be focused on the ways: (i) to synthesize $CoFe_2O_4$ nanoparticles with single-domain size and narrow size distribution (or even monodisperse); (ii) to explore more effective size selection methods in order to get $CoFe_2O_4$ nanoparticles with single-domain size and narrow size distribution.

A further coercivity enhancement

High-ceorcivty $CoFe_2O_4$ is promising for hard-magnetic and magneto-optical applications. In terms of the strong dependence of coercivity on the intrinsic magnetocrystalline anisotropy, future work may also be concentrated on the coercivity enhancement by the elemental substitution in $CoFe_2O_4$ materials. As shown in this

work, Ni^{2+} substitution in $CoFe_2O_4$ led to the decrease in both coercivity and magnetocrystalline anisotropy due to the much lower dipole moment of N^{2+} than that of Co^{2+}. It is possible to increase magneto-crystalline anisotropy through other elements, such as rare earth, Mn and Cr ions.

Development of novel devices

Mechanical milling induced large coercivities up to 5.1 kOe in $CoFe_2O_4$ powdered materials. Such high-coercivity powders could be promising for many hard magnetic and magneto-optical applications. We may use sol-gel, coating or other technique to fabricate thin or thick magnetic films or patterned structures for different applications. We may use the idea to fabricate high coercivity $CoFe_2O_4$ films through PVD or CVD, if large mechanical strain can be generated through suitable choice of substrate or preparation condition (substrate temperature or post-annealing).